Alignment of the ATLAS Inner Detector and probing the top quark polarization in single top t-channel production.

Tesi Doctoral

Presentada per:

Óscar Estrada Pastor

Dirigida per:

Dra. Mª José Costa Mezquita
Dr. Salvador Martí i Garcia

VNIVERSITAT DE VALÈNCIA

Departament de Física Atòmica, Molecular i Nuclear
Facultat de Física
IFIC (Universitat de València - CSIC)

Programa de Doctorat en Física

València, Febrer 2020

La Dra. **María José Costa Mezquita**, científica titular del CSIC i el Dr. **Salvador Martí i Garcia**, investigador científic del CSIC

Certifiquen:

Que la present memòria "Alignment of the ATLAS Inner Detector and probing the top quark polarization in single top t-channel production" ha sigut realitzada sota la seua direcció en el Institut de Física Corpúscular, centre mixte de la Universitat de València i del CSIC, per **Óscar Estrada Pastor** i constitueix la seua Tesi per optar al grau de Doctor en Física per la Universitat de València.

I per a que així conste, en compliment de la legislació vigent, presenten en el departament de Física Atòmica, Molecular i Nuclear de la Universitat de València la referida Tesi Doctoral, i firmen el present certificat.

València, a 25 de febrer de 2020

María José Costa Mezquita

Salvador Martí i Garcia

Amb el vist i plau del tutor, el Dr. Juan Zúñiga Roman.

A Fanny i la meua família.

La utopía está en el horizonte. Camino dos pasos, ella se aleja dos pasos y el horizonte se aleja diez pasos más. Entonces, ¿para qué sirve la utopía? Para eso, sirve para caminar.

EDUARDO GALEANO.

We're gonna get to that place
Where we really wanna go and we'll walk in the sun
But 'til then, tramps like us
Baby, we were born to run.

BRUCE SPRINGSTEEN.

Acknowledgments

Vull agrair a totes aquelles persones que han fet d'aquest llarg i de vegades tortuós camí, un camí que mirant arrere ha pagat la pena de recórrer:

En especial, als meus directors de tesi, Maria José i Salva, que em van donar de primeres l'oportunitat de realitzar la tesi de màster i la tesi al grup. Treballar amb vosaltres ha estat un plaer. Al vostre costat, he aprés molt sobre el detector ATLAS, alinear el detector intern i el quark top. Però especialment valore haver aprés amb vosaltres aquelles coses invisibles a un llibre, però que sense elles aquesta tesi hauria estat impossible de dur a terme

No em puc oblidar tampoc de Susana, per la gran ajuda que m'ha proporcionat al grup desde el primer fins al últim dia; José Enrique, per totes aquelles vesprades picant codi (i que sense ell haurien sigut moltes més); Carlos Escobar, Mercedes i Maria Moreno, per la gran acollida que vaig rebre durant les estades al CERN; Carlos Lacasta, per donar-li sentit a aquella primera estada experimental al grup i a Carmen, per la seua paciència amb la burocràcia tots aquests darrers anys. I also want to thank Judita, for being always willing to help. Igualment, gràcies a Javier, Laura i Galo pel seu recolzament en els moments de crisi. Treballar amb vosaltres és un goig. Al igual que amb Pablo, Florencia, Jesús i Dani, amb els que he compartit meetings, nervis i estrés; però sobretot, rialles. He de mencionar també a la riberenca Elena Romero, que en les etapes inicials em va presentar a la gent del grup, a Sebastián, que al màster em va salvar el TFM i a Urmila, que em va mostrar també en les etapes inicials com funcionava la sala blanca.

Al IFIC, he treballat de valent, però també he conegut meravelloses persones, amb els que he gaudit moltíssim els dinars, les sobretaules, els esmorzars i els berenars! Gràcies a tots els membres del *Escuadrón IFIC*. A tots i totes us guardaré sempre en el record.

I also want to give thanks to the people that I have worked with at CERN: Carlos, Chi, Jim, Joe, Nello, Runyu and specially Marcus, who with I have had interesting discussions that helped us to understand what we were doing. I also want to give big thanks to Regina for the aid she gave me while she was single top convener. That months would have not been the same, if it were not for the excellent company of Sergi, Laura, Florencia and Pablo. We had an amazing time travelling, playing ping-pong at 5pm, playing basketball, barbacuing at CERN and

on the usual CERN Friday beers while playing truc. Florencia and me best team ever of table tennis and truc(o)! Vamoh equipo.

This international environment always reminds me of the two fantastic summer camps that I spent in 2009 and 2010 during the International Astronomical Youth Camp with so many wonderful people. Thanks to you all, because there I realized about the awesomeness of meeting international people.

Vull donar també les gràcies als professors del Departament de Física Atòmica i Molecular: especialment a Juan Zúñiga, Santiago González, Ramon Cases i Nadia Yahali, amb els que he gaudit moltíssim donar classe. També vull agrair a Avelino i Alberto Aparici haver-me donat l'oportunitat de introduirme al fantàstic món de la divulgació científica, dintre i fora del IFIC. No em vull oblidar tampoc de la gent del Observatori Astronòmic, especialment Amelia i Alberto, amb els que ara ja fa un bon grapat de anys i ple d'il·lusió vaig poder viure la primera estada científica.

Han sigut vora cinc anys els que he passat al IFIC. Cinc anys en la mateixa "tauleta de secretari" de la *Celda 132*. L'ambient que he respirat amb els meus companys de "presó" han sigut memorables. Gràcies a Carlos, Clara, Dani, Florencia, Jesús, Joan, Luismi, Martí, Pablo, Rosa i Sergi. No hauria estat més a gust en cap despatx més que en el nostre. Amistad, música, xocolate, vacilades, bromes, festes, cartells, photoshop i potser boles del Expociencia volant ha sigut la nostra formidable senya d'identitat.

Sempre ens les hem apanyades molt bé els doctorands del IFIC per a fer esport. Sense l'esport no haguera sigut persona aquestos anys. He gaudit moltíssim amb les eixides d'escalada i vesprades de rocòdrom amb Davide i Javi. Moltes gràcies per introduir-me en aquest món. Gràcies també a Núria Fuster, Javi Barrios, Joan Climent i més recentment a Ana Peñuelas per les paxanguetes de basquet que ens marcàrem. Les partidetes de tennis i pàdel amb Ceci, Luismi, Pablo, Carlos, Judith, Joan, Florencia i Sergi també són dignes de recordar, sobre tot perquè vos rebentava en totes ;) Encara que amb el bon temps, em reventaveu vosaltres als partidets de vòlei-platja, que han sigut també fascinants amb vosaltres.

Al IFIC he pogut gaudir d'un ambient encissant que ja vaig viure a l'Erasmus a Mainz. Con Carlos, Marta e Irene compartí uno de los mejores años que he vivido, lo pasamos (en pasado y en presente cuando se puede) genial! Diego, contigo también lo pasé genial, pero tu vas a parte: porque la noche que hablamos de comunismo con el examen de *Festkorper Physik* a la mañana siguiente y la búsqueda de los *Ubungs* de teoría de cuerdas por media biblioteca, se merecen un rinconcito aquí! Això em porta també a la promoció de Grau en Física 2009-2010 de valencià. Un grupet de categoria tots, en especial, Hèctor Gisbert, Antonio, Faisel, Pacoxa, Juanjo i Hèctor Masià; amb els que vaig compartir hores memorables a classe, a les pissarres, a la biblioteca i amb Masià també al rodalia.

Ja amb el títol de físic en la mà, ens esperaven uns anys apassionants gràcies a les locures dels *frikixulis*! Anys que ens han deixat memòries inoblidables a Benimaclet i Burjassot. Hèctor, Antonio, Clara i Carlos: sou uns amics inigualables i tan valents com l'abuelo!

Gràcies també a la meua família per haver confiat en mi desde menut i pel suport que he rebut de la vostra part en els bons i mal moments.

Per últim, gràcies a Fanny per haver sigut una profe genial. Valore molt l'amistad que ara conservem. El text que hi ha en este llibre és en gran part gràcies a tu. Altres dues personetes importants que han contribuit a que este llibre siga real són *Fannyni* i Oscar: gràcies per les rialles i jocs que he compartit amb vosaltres i que m'han fet recordar quines són les coses verdaderament importants en aquesta vida, i que quan creixem de sobte oblidem.

L'últim agraïment me'l reserve per a la meua gata *Schrodi*; en gran mesura, també has teclejat alguna vegada aquest document i has contribuit a que no llançara el ordinador per la finestra més d'una vegada.

Possiblement em deixe a alguna persona que hauria d'estar en aquestes línies. Si arribes al final d'aquest llistat d'agraïments i no estàs, només dir-te que espere haver contribuit a que durant el nostre encreuament de camins hages gaudit tant com jo he gaudit de la teua companyia.

Preface

ATLAS experiment is one of the main four experiments located in the LHC ring of the CERN laboratory. ATLAS finished the data-taking period of Run 2 in 2018. Many Standard Model topics and Beyond Standard Model searches are being explored using the whole 150 fb^{-1} of data collected during the Run 2. The possibility of performing such challenging studies is mainly thanks to the excellent performance of the LHC during the Run 2, and in this particular case of the ATLAS detector. This thesis presents on the one hand performance work involved with the alignment of ATLAS Inner Detector during early Run 2. On the other hand, this thesis presents an analysis to probe the Wtb vertex using polarized single top quark events produced in the t-channel, recorded by the ATLAS detector at a center of mass energy of $\sqrt{s} = 13$ TeV, using 80.5 fb^{-1} of proton-proton collisions data collected during Run 2.

The current theoretical framework of particle physics is known as Standard Model of particle physics. The achievement of the Standard Model has involved the collaboration of theorists and experimentalists. During the 1960's and 1970's the theory development was boosted with a significant amount of mechanisms to explain the wide variety of phenomena, that later would be discovered. The Standard Model has been confronted experimentally and tested up to the TeV scale. Nowadays, the Standard Model remains as the periodic table of the subatomic world, with some of its particles discovered by CERN experiments, such as, the W and Z bosons, and more recently the Higgs boson. Nevertheless, despite the great success, the Standard Model cannot be the final theory of elementary particle physics, since there are still some phenomena that cannot be understood in this framework (e.g. dark matter, dark energy, matter-antimatter asymmetry of the universe,...). A brief description of the Standard Model will be presented in Chapter 1. As mentioned, the analysis of this thesis deals with top quark events, therefore the basics of top quark physics and the theoretical framework to develop the analysis in this thesis will be also presented in Chapter 1.

CERN has played a crucial role in the construction of the pieces involved in the Standard Model. The Large Hadron Collider (LHC) is the most powerful accelerator ever built, designed to reach unprecedented centre of mass energies and luminosities. ATLAS experiment, located at one of the four main collision points of the LHC, is the biggest particle physics experiment in the world. In Chapter 2,

the description of the LHC accelerator and the ATLAS detector that constitutes the experimental setup of this thesis, can be found. The object reconstruction that it is performed from the detector signal is also treated.

The work in this thesis has contributed to provide high quality of recorded data of the ATLAS experiment, especially during early Run 2. The tracker of the Inner Detector must be correctly calibrated in order to provide good quality tracks to the reconstruction algorithms used in the ATLAS experiment. The basics of the alignment algorithm, as well as the work developed to provide good quality alignment corrections is presented in Chapter 3.

The analysis performed to probe the Wtb vertex is presented in Chapter 4. Top quark events produced singly with one charged lepton, two jets (one of them b-tagged) and missing transverse momentum are used to probe the Wtb vertex in this analysis. The analysis consists of a measurement of angular observables asymmetries related with the top quark polarization. The dataset and the Monte Carlo samples used as well as the methodology followed to perform the measurement and the estimation of the uncertainties are explained in Chapter 4 too.

Finally, the conclusion of the thesis dissertation is presented in Chapter 5.

Contents

Chapter 1

Theoretical framework

The Standard Model (SM) of particle physics is the current theoretical framework that best describes subatomic phenomena. However, as will be explained in this chapter, this theory can not be final. Top quark physics provides the possibility of probing new physics effects, for example using the Wtb vertex. The Wtb vertex can be probed by studying the top quark decay since the top quark decays almost exclusively to Wb. This can be done using events in which top quarks were produced in pairs via the strong interaction or singly via the electroweak interaction. Moreover, the Wtb vertex is also present in the single top quark production. Several observables have been proposed in Refs. [1–4] by various theorists that are sensitive to possible anomalous couplings in the Wtb vertex. This chapter is devoted to define those that will be used in this work.

1.1 The Standard Model of particle physics

The Standard Model is a gauge theory characterized by fundamental constituents of matter (fermions). It is also able to describe very precisely the strong, weak and electromagnetic interactions of such constituent, through the exchange of the interaction carrier particles (gauge bosons).

On the one hand, fermions that constitute the matter particles are organized in leptons and quarks. Fermions are spin $1/2$ particles obeying Fermi-Dirac statistics. Each fermion has a corresponding anti-fermion, with exactly the same mass and quantum numbers, but opposite electric charge. An interesting observed property of fermions is that they are replicated in three families, as shown in Table 1.1, where each family has the same properties as the previous but with larger masses. In addition, quarks carry color charge (red, green, blue) but are confined through the strong interaction into colorless composite particles called hadrons.

On the other hand, the gauge bosons are integer spin particles obeying the Bose-Einstein statistics. The interaction mediators are known as gauge bosons. They are spin 1 bosons composed by eight gluons, that mediate the strong interaction between colored particles (quarks and gluons), one photon, that mediates

Family	Quarks	Spin	Electric charge	Leptons	Spin	Electric charge
1st	u	1/2	+2/3	e^-	1/2	-1
	d	1/2	-1/3	ν_e	1/2	0
2nd	c	1/2	+2/3	μ^-	1/2	-1
	s	1/2	-1/3	ν_μ	1/2	0
3rd	t	1/2	+2/3	τ^-	1/2	-1
	b	1/2	-1/3	ν_τ	1/2	0

Table 1.1: Fermions of the SM classified in families including the spin and the electric charge of each particle.

Gauge bosons	Spin	Electric charge	Scalar boson	Spin	Electric charge
gluons	1	0	H	0	0
Z, $W^\pm$	1	0, ±1			
γ	1	0			

Table 1.2: Bosons of the SM including the spin and the electric charge of each particle.

electromagnetic interactions between electrically charged particles, and three massive bosons mediating neutral and charged weak interactions, classified as well in Table 1.2.

The SM is a quantum gauge theory founded on a $SU(3)_C \bigotimes SU(2)_L \bigotimes U(1)_Y$ symmetry principle that describes both the strong and electroweak interactions. Under this principle the physics remains invariant under local gauge transformations. The $SU(2)_L \bigotimes U(1)_Y$ term refers to the local symmetry of electroweak interactions, whereas the $SU(3)_C$ term refers to the local symmetry of the strong interaction.

1.1.1 The path to the Standard Model

The SM constitutes an elegant theoretical framework for particle physics that has been exhaustively developed and tested along the years:

Quantum Electrodynamics (QED) was the prototype theory that would boost subsequent discoveries. QED has a $U(1)$ gauge symmetry that is invariant under local transformations mediated by a spin 1 massless field, that is, the photon field. QED predictions have been successfully tested with the lepton magnetic moments with an incredible high precision.

The open question in the 1950's was whether with a similar formalism, theories describing weak interactions phenomena could be developed. Initially, in the 1961 Glashow [5], and later in 1964 Salam and Ward [6] enlarged the gauge symmetry group to $SU(2) \bigotimes U(1)$ to explain the weak and electromagnetic interactions altogether. This work already contained the foundations of the SM. However, the gauge bosons were necessary of zero mass (known as Nambu-Goldstone bosons [7]).

In 1964, Higgs [8], Brout and Englert [9] showed that when the gauge symmetry is spontaneously broken the zero-mass Nambu-Goldstone bosons disappeared from the physical spectrum. This mechanism is the Spontaneous Symmetry Breaking mechanism (known as Brout-Higgs-Englert mechanism or Higgs mechanism too). This mechanism generates the mass of the weak interacting gauge bosons and gives rise to a scalar particle, the Higgs boson. The fermionic masses are generated through this mechanism too via the Yukawa interaction with the Higgs field.

It was in the late 1960's when Salam and Weinberg [10,11] generalized the theory incorporating the Higgs mechanism in the $SU(2)_L \bigotimes U(1)_Y$ model, mantaining the $U(1)_Y$ symmetry, and therefore protecting the zero mass of the photon.

In parallel, during the 1960's the quark concept had already been established. However, the inclusion of the quarks known by those days (up, down, strange) in the $SU(2)_L \bigotimes U(1)_Y$ electroweak model had failed. Later, on 1970 Glashow, Iliopoulos and Maiani [12] figured out a precise description of the observed flavour changing neutral current processes, this is, the GIM mechanism. Through the GIM mechanism, they proved that the latter problem could overcome if a fourth quark (charm) was included together with the up, down and strange quarks as two doblets. Indeed, the J/Ψ was a few years later discovered by Stanford and Brookhaven collaborations as a $c\bar{c}$ bound state.

On the other hand, in the 1970's, the strong interaction was deeply studied through Quantum Chromodynamics (QCD). QCD has a $SU(3)_C$ symmetry invariant under local transformations for quark field for three colors $N_C = 3$. The $SU(3)_C$ symmetry gives rise to eight massless gluons and explains the interaction between quarks and gluons, as well as, the gluon self-interaction. All interactions are given in terms of a universal strong coupling constant.

In 1973, Kobayashi and Maskawa [13] suggested the existence of a third family of fermions in the context of sheding light on the CP symmetry violation. In 1975 the lepton of the third family was discovered by the SLAC collaboration: the tau lepton [14]. Years later in 1977, the beauty (or bottom) quark composing the third family of quarks was observed through the detection of the Υ resonance [15]. Finally in 1995 the top quark was observed by the CDF and D0 collaborations [16,17]. The fermionic table in Table 1.1 was then completed with the confirmation of the tauonic neutrino in 2001 by the DONUT collaboration [18]. As for the confirmation of the bosons reported in Table 1.2, CERN reported in 1983 the discovery of the $W^{\pm}$ and Z gauge bosons by the UA1 and UA2 collaborations [19–22]. The last component of the SM puzzle was confirmed in 2012 when ATLAS and CMS collaborations announced the discovery of the Higgs boson [23, 24].

1.1.2 Why the Standard Model is not the ultimate theory

The SM has survived all the experimental tests that it has faced. It is able to describe the fundamental particle interactions with very high precision. However, the confirmed neutrino oscillations constitute the first evidence of new physics beyond

the Standard Model [25]. In addition, many open questions remain unanswered by the Standard Model, such as why there are three families of fermions, the origin of dark matter, the dark energy and the matter-antimatter asymmetry observation. That is why particle physics experiments are searching for new phenomena that can shed light on the open questions of the theory, and eventually reach a complete theoretical framework of the fundamental components of matter and its interactions.

The observation of matter-antimatter asymmetry is a key point among the remaining open questions. In the 1970's, cosmological studies already demonstrated that there is negligible primordial antimatter amount in our observable universe [26]. During the early universe equal amounts of matter and antimatter should have been created. Since matter and antimatter annihilates in pairs, all of the matter and antimatter in the universe should have already annihilated each other, and left nothing but energy behind.

Among the models that attempt to explain the matter-antimatter asymmetry, there are the electroweak baryogenesis models. Inspired by asymmetry observations in kaon systems [27], Sakharov pointed out in 1967 the three conditions that baryogenesis theoretical models should incorporate in order to assess the observed matter-antimatter asymmetry [28], and namely are:

- Baryon number (B) violation.
- Violation of C (charge conjugation) symmetry, and the combined CP (charge and parity) symmetry
- Departure from thermal equilibrium in the primitive universe.

The Standard Model includes the violation of charge-parity (CP) symmetry through an irreducible complex phase in the Cabibbo-Kobayashi-Maskawa (CKM) quark-mixing matrix [29]. The realization of the CP violation in nature has been well established in the kaons and B-meson systems by several experiments [30–33]. It has also been recently observed in the charm sector by the LHCb collaboration [34]. Nevertheless, the observed amount of CP violation is not enough to account for the observed asymmetry. This thesis searches for new sources of CP violation in the top quark production.

1.2 The top quark as a window for new physics

Since the discovery by the CDF and D0 experiments in 1995 at Fermilab's Tevatron proton-antiproton collider [16, 17], the top quark has remained a focus of study in particle physics for various reasons.

The top quark is by far the heaviest fundamental fermion in the Standard Model. In fact, it is around 40 times heavier than the b quark (its $SU(2)$ doublet companion in the Standard Model) and comparable to a Rhenium atom (with $Z = 75$)! Its discovery completed the sector of the three-generation structure of the Standard Model, which required the existence of a b quark partner that had electric charge $e = +2/3$ and isospin $T_3 = 1/2$.

Its large mass, automatically implies within the SM a large coupling to the Higgs boson because the top quark Yukawa coupling (defined as $y_t = m_t/v$ with $v = 246$ GeV) is close to 1. That means that the top quark may play a special role in the electroweak symmetry breaking, either in the context of the Higgs model or within alternative mechanisms through which elementary particles acquire mass.

Its large mass also implies that it decays rapidly through electroweak interactions before it has a chance to form hadrons (this is also unique among the quarks), and offers the possibility of studying its properties through its decay products. The decay time is also significantly smaller than the time it takes for a top quark to depolarize. Therefore the top quark transfers its polarization to the decay products. Since the top quark is much heavier than the W boson, it can decay electroweakly to $t \to Wq$, where q is the b, s or u quark; however the mode $t \to Wb$ has a branching ratio close to one: decaying almost always exclusively through a single channel is also a unique characteristic among the SM particles.

Top quark production often constitutes an important background in many searches of new physics at the LHC (as supersymmetric particles [35, 36]), so a detailed understanding of it will likely be translated into improvements in those searches. The top quark also plays an important role in many scenarios for new physics beyond the SM. Some models predict new particles that would preferentially decay to top quarks, or that could appear in top quark decays.

It is therefore essential to measure with the highest possible precision the top quark properties and confront them with the Standard Model predictions, as well as to perform direct searches for new physics in the production and decay of top quarks.

In this thesis, new physics is explored by precisely probing the Wtb vertex with top quark events singly produced via electroweak interaction in the t-channel at the LHC. The LHC is a very convenient place to carry out this measurement, actually it is usually considered as a top quark factory. The successful Run 2 operation has led to roughly 42 M top quarks singly produced and recorded by the ATLAS experiment during Run 2, allowing for even more precise measurements to be performed, of which many will no longer be dominated by statistical uncertainties but

rather systematic ones[1]. During the writing of this thesis, Run 2 p-p collisions at $\sqrt{s} = 13$ TeV at the LHC have finalised at ATLAS experiment with an impressive performance, having recorded 140.0 fb^{-1} of data ready to be used in the physics analyses. The experimental setup of LHC and the ATLAS detector will be covered with more detail in Chapter 2.

1.2.1 Probing the Wtb vertex with Effective Field Theory

The top quark being the heaviest quark, effects of new physics on its couplings are expected to be larger in many Beyond Standard Model models than for any other fermion, and deviations with respect to the SM predictions might be detectable. An adequate parametrisation of the most general interactions of the the top quark is necessary in order to search for new physics in a model independent way and interpret the results of experimental measurements.

Among the different top quark couplings to the gauge and Higgs bosons, the Wtb vertex deserves a special attention because the top quark is expected to decay almost exclusively via this interaction, $t \to Wb$. Besides, the Wtb is also present in the electroweak (EW) single top quark production. In particular, new physics effects resulting in corrections to the Wtb vertex would affect the top quark and W boson polarizations.

The SM interaction in the Wtb vertex is given by Equation 1.1 and shows the $V - A$ structure of weak interactions:

$$\mathcal{L}_{Wtb}^{SM} = -\frac{g}{\sqrt{2}}\bar{b}\gamma^{\mu}V_{tb}P_{L}tW_{\mu}^{-} + h.c, \tag{1.1}$$

where $P_L = \frac{1}{2}(1 - \gamma_5)$ is the left-chiral projector; V_{tb} is the corresponding CKM matrix element and g is the weak coupling constant; while $\bar{b}$, t and W are the corresponding fermionic and bosonic fields.

A model independent framework to study possible top quark anomalous couplings is the effective field theory, where the modifications are encoded into the coefficients of a set of higher dimensional operators that parametrise the effects of new physics at low energy. If new particles exist beyond the LHC reach, their effects at energies below the resonant threshold can be parametrised in terms of an effective Lagrangian [42–44]:

$$\mathcal{L}_{eff} = \mathcal{L}_{SM} + \sum_{x}\frac{C_x}{\Lambda^2}\mathcal{O}_x + ..., \tag{1.2}$$

where the sum is over all $\mathcal{O}_x$ dimension-six operators (higher dimension operators are suppressed, if top quark is involved). The complex coefficients C_x are the so-called Wilson coefficients and correspond to the couplings of the SM fields to the

[1] Many further Run 2 results on top quark properties and searches for BSM physics keep appearing while this thesis is being written. Some of them are recorded in Ref. [37]. An extensive review from top quark physics results of Run 1 can be found in Refs. [38–41].

new physics; while Λ is the scale at which the new physics resides. Higher-order corrections from operators of higher dimensions are suppressed by higher powers of Λ. Among the operators listed in Ref. [44], fourteen contribute to top quark electroweak anomalous couplings, as explained in Ref. [45].

In Ref. [45], the most general effective Wtb interaction arising from a minimal set of dimension-six effective operators was found to be:

$$\mathcal{L}_{Wtb} = -\frac{g}{\sqrt{2}}\bar{b}\gamma^{\mu}\left(V_L P_L + V_R P_R\right) t W_{\mu}^{-} - \frac{g}{\sqrt{2}}\bar{b}\frac{i\sigma^{\mu\nu}}{M_W}q_{\nu}\left(g_L P_L + g_R P_R\right) t W_{\mu}^{-} + h.c. \tag{1.3}$$

In this effective Lagrangian, the tensorial term $\sigma^{\mu\nu}$ also appears, apart from the $V-A$ term. We encounter both left-handed couplings (i.e. V_L, g_L) and right-handed couplings (i.e. V_R, g_R), in both terms (i.e. $V-A$ and tensorial). At tree level in the SM, the coupling V_L corresponds to the CKM matrix element $V_{tb} \simeq 1$. The rest of the couplings are anomalous and vanish at tree level in the SM. Non-vanishing anomalous couplings would provide hints of beyond the Standard Model, and complex values would imply that the the top quark has a CP violating component. Equation 1.4 shows the contributions to these couplings from the dimension-six operators:

$$\begin{aligned} \delta V_L &= C_{\phi q}^{(3,33)*}\frac{v^2}{\Lambda^2} & \delta g_L &= \sqrt{2}C_{dW}^{33*}\frac{v^2}{\Lambda^2}, \\ \delta V_R &= C_{\phi\phi}^{33}\frac{v^2}{\Lambda^2}, & \delta g_R &= C_{uW}^{33}\frac{v^2}{\Lambda^2}. \end{aligned} \tag{1.4}$$

Considering the effective Lagrangian for the Wtb vertex including SM contributions, given by [3, 4, 45], then the relevant operators in the Wtb vertex reduce to:

$$\begin{aligned} \mathcal{O}_{\phi q}^{(3,33)} &= i\left(\phi^{\dagger}\tau^I D_{\mu}\phi\right)\left(\bar{q}_{L3}\gamma^{\mu}\tau^I q_{L3}\right), \\ \mathcal{O}_{\phi\phi}^{33} &= i\left(\tilde{\phi}^{\dagger} D_{\mu}\phi\right)\left(\bar{u}_{R3}\gamma^{\mu} d_{R3}\right), \\ \mathcal{O}_{uW}^{33} &= \left(\bar{q}_{L3}\sigma^{\mu\nu}\tau^I u_{R3}\right)\tilde{\phi}W_{\mu\nu}^I, \\ \mathcal{O}_{dW}^{33} &= \left(\bar{q}_{L3}\sigma^{\mu\nu}\tau^I d_{R3}\right)\phi W_{\mu\nu}^I, \end{aligned} \tag{1.5}$$

where q_{L3}, u_{R3} and d_{R3} are the left $SU(2)_L$ weak doublet and right singlets of the quark fields for $i = 3$; that is:

$$\begin{bmatrix} u_3 \\ d_3 \end{bmatrix}_L, \qquad u_{R3}, \qquad d_{R3}, \tag{1.6}$$

with $(u_1, u_2, u_3) = (u, c, t)$ and $(d_1, d_2, d_3) = (d, s, b)$. The expressions in Equation 1.5 also depend on the covariant derivative D_{μ} acting on ϕ, which is the $SU(2)_L$ of the scalar Higgs field, whose vacuum expectation value is defined as:

$$\langle\phi\rangle = \frac{1}{\sqrt{2}}\begin{bmatrix} 0 \\ v \end{bmatrix}, \tag{1.7}$$

with $v = 246$ GeV and $\tilde{\phi} = i\tau^2\phi^*$; while the covariant derivative D_μ is :

$$D_\mu = \partial_\mu + ig_s\frac{\lambda^a}{2}G^a_\mu + ig\frac{\tau^I}{2}W^I_\mu + ig'YB_\mu, \tag{1.8}$$

where G^a_μ, W^I_μ and B_μ are the gauge fields for $SU(3), SU(2)_L$ and $U(1)_Y$; g_s, g and g' are the coupling constants for $SU(3), SU(2)_L$ and $U(1)_Y$; λ^a are the Gell-Mann matrices with $a = 1, ..., 8$; τ^I the Pauli matrices for $I = 1, 2, 3$ and Y is the hypercharge of the field to which D_μ is applied. Finally, $W^I_{\mu\nu}$ are the strength tensors for $SU(2)_L$ and $U(1)_Y$ and $\sigma^{\mu\nu} = \frac{i}{2}[\gamma^\mu, \gamma^\nu]$ is a tensor constructed from Dirac Matrices γ^μ.

The involved operators are of two different types:

- The operators $\mathcal{O}^{(3,33)}_{\phi q}$ and $\mathcal{O}^{33}_{\phi\phi}$ involve scalar field carrying covariant derivative and are relevant in new physics models in which there are mixing effects between heavy particles (predicted by new physics models) and the SM particles [46–49]. It can be generated at tree level after integrating out the new heavy particles, such as a heavy charged vector boson ($W'^{\pm}$) that mixes with SM gauge boson ($W^{\pm}$) or a heavy quark that mixes with top quark or bottom quark (see Figure 1.1).
- The operators $\mathcal{O}^{33}_{uW}, \mathcal{O}^{33}_{dW}$ involve field strength tensors, and in this case, the new physics effects would appear at loop level (within models such as two Higgs doublet model [50] or supersymmetric models [51,52]) (see Figure 1.1).

As shown in Equation 1.4, these operators give rise to a minimal set of couplings, where the anomalous terms involving V_R, g_R, g_L arise from the effective operators $\mathcal{O}^{33}_{\phi\phi}, \mathcal{O}^{33}_{uW}$, $\mathcal{O}^{33}_{dW}$ respectively, while contributions to V_L originate from $\mathcal{O}^{(3,33)}_{\phi q}$.

1.2.2 Top quark production at the LHC

At the LHC pp collisions, the top quark can be produced through two mechanisms: via Quantum Chromodynamics (QCD) in top and anti-top quark pairs ($t\bar{t}$) and via electroweak production of a single top quark associated with other particles.

1.2.2.1 Top quark pair production

In hadron colliders, the top quark is predominantly produced in pairs via the strong interaction, through gluon fusion or quark and anti-quark annihilation (see Figure 1.2). At the LHC the gluon fusion mechanism dominates in top quark pair production, with a cross-section predicted to be $933.0^{+31.8}_{-51.0}(\text{scales})^{+6.1}_{-6.2}(\text{pdf})$ at 14 TeV [54], contributing by a factor $\sim 80\%$ to the total top quark pair production cross section.

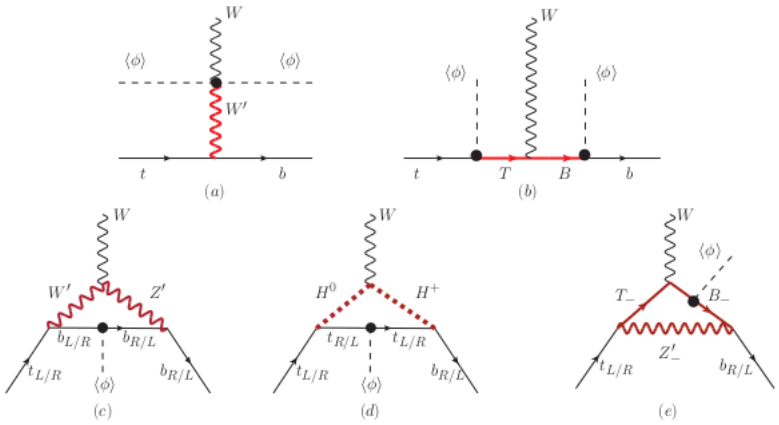

Figure 1.1: Pictorial illustration of relation between effective operators and new physics models extracted from Ref.[53]. (a) and (b) denote the tree level mixing effect between the new heavy particles and SM particles, (c)-(e) denote the possible loop-induced dimension-6 operators diagram of some extension in new physics models.

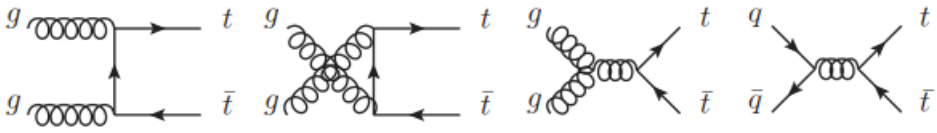

Figure 1.2: Leading Order Feynman diagrams contributing to $t\bar{t}$ pair production at LHC

The $t\bar{t}$ production cross section is predicted theoretically at next-to-next-to-leading order and include soft gluon resummation at next-to-next-to-leading logarithmic (NNLO+NNLL) [54]. Assuming a top quark mass $m_t = 172.5$ GeV, the predicted calculations are listed in Table 1.3:

$\sqrt{s}$ [TeV]	$\sigma_{t\bar{t}}$ (pb)
7	$173.3^{+4.7}_{-6.1}$
8	$252.9^{+13.2}_{-14.4}$
13	$831.8^{+40.3}_{-45.7}$

Table 1.3: Theoretical predictions for top quark pair production calculated at NNLO+NNLL at 7, 8 and 13 TeV center-of-mass energies. The uncertainties include scale and PDF variations, as well as the top quark mass uncertainty.

Figure 1.3 shows the theoretical predictions as a function of the centre-of-mass energy for the $t\bar{t}$ cross section compared to the most precise experimental measurements provided by the ATLAS and CMS experiments at 7, 8 and 13 TeV centre-of-

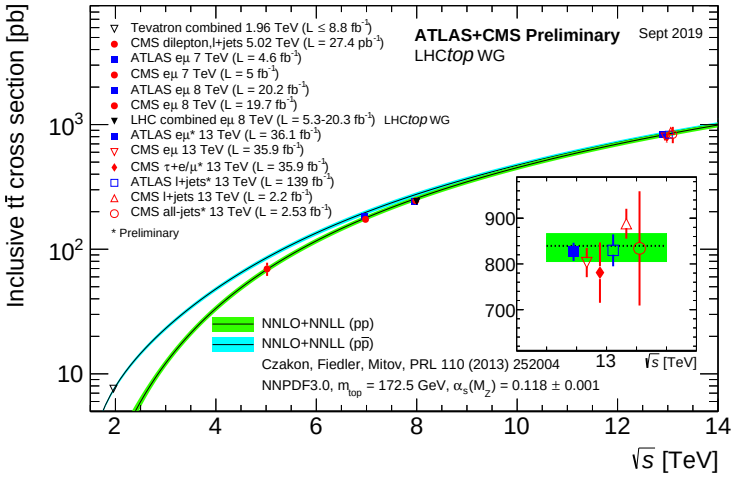

Figure 1.3: Summary of LHC and Tevatron measurements of the top-pair production cross-section as a function of the centre-of-mass energy compared to the NNLO QCD calculation complemented with NNLL resummation (top++2.0). The theory band represents uncertainties due to renormalisation and factorisation scale, parton density functions and the strong coupling. The measurements and the theory calculation is quoted at $m_t = 172.5$ GeV.

mass energies. The experimental results are in good agreement with the theoretical predictions, and are more precise than the theoretical calculations.

1.2.2.2 Production of single top quarks

Single top quarks can be produced through the electroweak interaction and almost exclusively through the Wtb vertex because $|V_{tb}| >> |V_{td}|, |V_{ts}|$[2]. At leading order (LO), there are three different production modes: s-channel, t-channel and Wt-channel, depending on whether the W boson is space-like (i.e. t-channel), time-like (i.e. s-channel) or real (i.e. Wt-channel). The Feynman diagrams representing this process at LO are shown in Figure 1.4. For anti-top quark production, the charge conjugate processes are implied. In the QCD calculation, the treatment of the b quark involved in the initial state leads to two LO schemes in the t-channel:

The $2 \to 2$ process, $b + q \to q' + t$, is the so-called 5-flavour scheme, where the proton is considered to be composed by five quark flavors (u, d, c, s and b). It is characterized by having both two particles in the initial and final state (with a b quark in the initial state).

The $2 \to 3$ process, $g + q \to q' + t + b$, is the so-called 4-flavour scheme where the proton is considered to be composed of only four light quarks (u, d, c and s)

[2]The CKM matrix values are $|V_{tb}| = 0.99915$, whereas $|V_{td}|$ and $|V_{ts}|$ respectively are 0.00875 and 0.0403

and the b quarks arise from the splitting of a virtual gluon into nearly collinear $b\bar{b}$. In this scheme, the $\bar{b}$ quark in the final state (usually called spectator b quark or second b-jet) is characterized by its soft transverse momentum spectrum, being most of the time outside the kinematic acceptance.

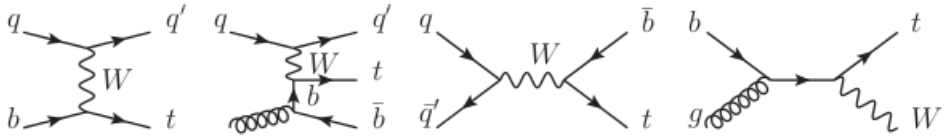

Figure 1.4: Leading Order Feynman diagrams contributing to single top production. From left to right: t-channel (5 FS), t-channel (4 FS), s-channel, Wt-channel.

The single top quark production cross section is predicted theoretically at next-to-leading order and include soft gluon resummation at next-to-next-to-leading logarithmic (NLO+NNLL) [55–60]. For a top quark mass $m_t = 172.5$ GeV, these predictions lead to the results expressed in Table 1.4:

$\sqrt{s}$ [TeV]	σ_{t-chan} (pb)	$\sigma_{Wt-chan}$ (pb)	σ_{s-chan} (pb)
7	$65.9^{+2.6}_{-1.8}$	17.0 ± 0.7	4.6 ± 0.2
8	$87.2^{+3.4}_{-2.5}$	24.0 ± 1.0	5.6 ± 0.2
13	218^{+5}_{-4}	76.2 ± 2.5	11.2 ± 0.4

Table 1.4: Theoretical predictions for single top quark production for the t-channel, Wt-channel and s-channel calculated at NLO+NNLL resummation at 7, 8 and 13 TeV center-of-mass energies. The uncertainties include scale and PDF variations, as well as the top quark mass uncertainty.

In the case of the t-channel only, the single top quark production cross section at 8 and 13 TeV is calculated at next-to-next-to-leading order (NNLO), for a top quark mass of $m_t = 172.5$ GeV and $m_t = 173.2$ GeV [61, 62] respectively, leading to:

$$\sigma_{t-chan.}(\sqrt{s} = 8 \text{ TeV}) = 83.9^{+0.8}_{-0.3} \text{ pb}, \tag{1.9}$$

$$\sigma_{t-chan.}(\sqrt{s} = 13 \text{ TeV}) = 213.6^{+2.1}_{-1.1} \text{ pb}. \tag{1.10}$$

The dominant contribution to single top quark production at LHC is, therefore, the t-channel. In this case, the NNLO calculations predict a smaller cross section compared to the NLO+NNLL values in Table 1.4. For the the three production processes, automatic calculations as a function of various parameters can be also performed with the HATHOR v2.1 program at NLO [63, 64]. The NLO+NNLL predictions are slightly larger than the NLO predictions computed with HATHOR v2.1 [65]. In order to simulate single top t-channel events, our measurement makes use of the Powheg matrix element generator at NLO in the strong coupling constant,

using the 4 flavor scheme. The HATHOR v2.1 NLO predictions are considered in the measurement computation, to estimate the signal t-channel process and the s-channel background process.

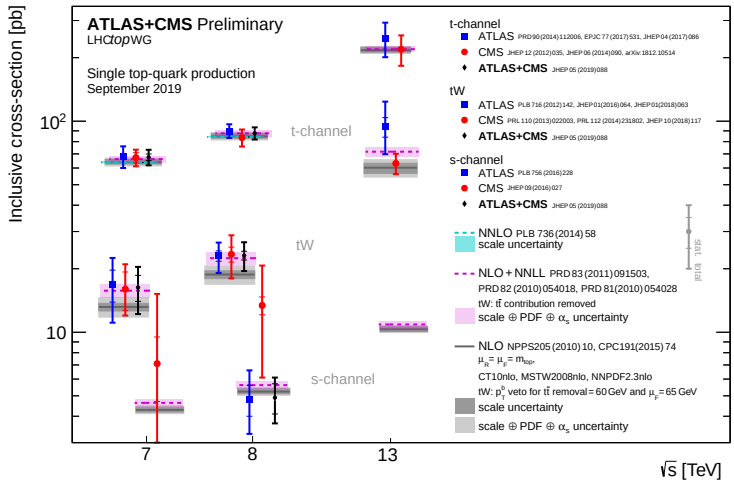

Figure 1.5: Summary of ATLAS and CMS measurements of the single top production cross-sections in various channels as a function of the center of mass energy. For the s-channel only an upper limit is shown. The measurements are compared to theoretical calculations based on: NLO QCD, NLO QCD complemented with NNLL resummation and NNLO QCD (t-channel only).

Figure 1.5 shows the theoretical predictions together with the experimental measurements obtained at 7, 8 and 13 TeV centre-of-mass energies for the single top quark cross sections in the different channels.

1.2.2.3 Top quark polarization

At the LHC, top quarks are predominantly produced in pairs, as we have seen previously. In this case, top quarks only have a small net polarization because of parity conservation in QCD [66]. On the other hand, single top quarks produced through electroweak interaction in the t-channel are expected to be highly polarized[3]: with its spin aligned along the direction of the down-type quarks [68, 69] and with its direction defined in a suitable basis. This polarization is interesting to consider because it gives access to complex phases of top quark anomalous couplings, as opposed to measurements performed with non-polarised top quarks from $t\bar{t}$ strong production. In the literature several basis are explored for t-channel single top production[4]. Here we focus on the spectator basis and the beamline basis:

[3] This is a consequence of the vector–axial (V–A) form of the Wtb vertex in the SM [67].

[4] In proton-proton colliders as the LHC, single top quarks produced via Wt-channel or s-channel do not show a high degree of polarisation in any basis.

Spectator jet basis: For top quark production, the spectator quark direction refers to the the down-type quark that comes from the up-type valence quarks of the incoming proton (see Figure 1.6 (a))[5]. Therefore, in the spectator basis the top quark spin is taken along the spectator quark (down-type quark), boosted to the top quark rest frame. In the spectator basis, the overall fraction of spin up top quarks calculated at NLO is 0.91 [70].

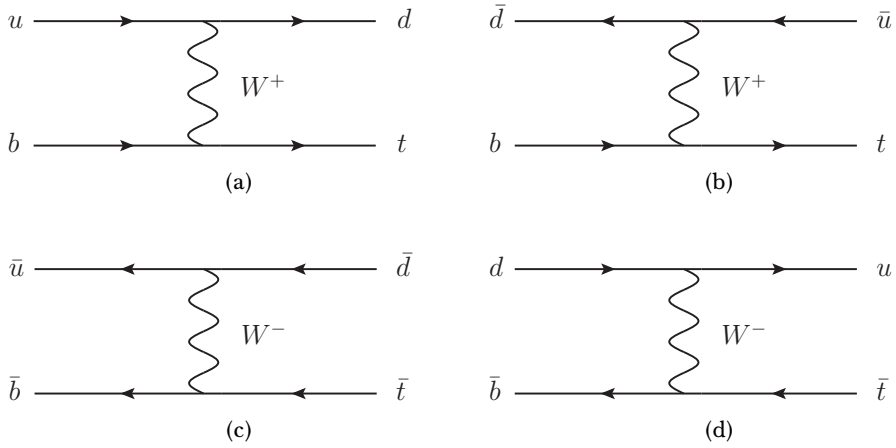

Figure 1.6: Processes contributing to the t-channel production at LO, in the 5 FS. Top production has a dominant process, in which an up-type quark from one of the colliding protons interacts with a b-quark from another proton by exchanging a virtual W boson to produce down-type spectator quark a top quark (a). In the subdominant process of top quark production, a down-antiquark from one of the colliding protons interacts with a b-quark or from another proton by exchanging a virtual W boson to produce an up-type antiquark spectator quark and a top quark (b). Antitop production has a dominant process too, in which an down-type quark from one of the colliding protons interacts with a b-antiquark from another proton by exchanging a virtual W boson to produce an up-type spectator quark and an antitop quark (d). In the subdominant process of antitop quark production, a up-type antiquark from one of the colliding protons interacts with a b-antiquark or from another proton by exchanging a virtual W boson to produce a down-type antiquark and an antitop quark (c).

For antitop production, the situation is a bit different. This is because the down-type quark is not usually the spectator quark, but rather the scattered light-quark (see Figure 1.6 (d))[6]. Therefore, a priori if we take the top quark spin in the spectator basis, we would be picking the wrong direction for the spin axis. However,

[5]The subdominant process is the scattering of a down-type antiquark from the beam from a bottom quark, to produce an up-type spectator antiquark and a top quark, as illustrated in Figure 1.6 (b). It is subdominant because the valence u-quark density of the proton is about twice as high as the valence down-quark density.

[6]The subdominant process is the scattering of a up-type antiquark from the beam from a bottom antiquark, to produce an down-type spectator antiquark and a top antiquark, as illustrated in Figure

the momentum transfer via the W boson deflects the incoming light quark just a little. Thus, the spectator quark momentum points in nearly the same direction as the original light quark momentum. Since the spectator jet and initial light quark momenta are nearly parallel, it means that the degree of spin polarization is not very much affected, when the spectator quark direction is used. In the spectator basis, the overall fraction of spin up antitop quarks calculated at NLO is -0.86 [70], very much like the top quark production but opposite in sign. Therefore, in the spectator basis the antitop quark spin can be taken along the spectator quark (light quark), boosted to the top quark rest frame as well.

Beamline basis: Since the down-type quark is dominant in the initial state in one of the two beams in the antitop production , it is worthwhile to consider the beamline basis in addition to the spectator basis. In the beamline basis, the top quark spin is measured along the direction of one of the incoming protons. However, it is unknown which of the two protons provides the light quark in each event. Therefore a choice of direction needs to be made. For that purpose, it is defined the η-beamline basis as follows: if the pseudorapidity η[7] of the spectator jet is positive, the right-moving beam is chosen as the spin axis. If the pseudorapidity of the spectator jet is negative, the left-moving beam is chosen instead. This motivated because accordingly to Ref. [71], mostly the momentum of the spectator quark in the laboratory frame follows that of the initial quark. This choice gives the correct answer 97% of the times for $ub \to dt$ ($ug \to dt\bar{b}$ in the 4FS) and 98% of the time for $d\bar{b} \to u\bar{t}$ ($dg \to u\bar{t}b$ in the 4FS), which are the main channels for single-top quark and antiquark production, respectively.

For the measurements reported on this work, the spectator jet basis is used to define the top quark spin axis . Whereas, the beam line basis is used in order to define additional directions on the top quark production frame.

1.3 Polarization observables and angular asymmetries

Following Ref. [71], three orthogonal directions can be defined. These directions are useful to express the polarization of the top quark. The $\hat{z}$ direction is the direction of the momentum of the spectator quark, $\vec{p}_s$, in the top quark reference frame. The $\hat{y}$ direction taken along $\hat{z} \times \hat{p}_q$, where $\vec{p}_q$ is the direction of the incoming light quark, in the top quark reference frame. As mentioned before, the momentum direction of the initial quark in the t-channel process cannot be determined unambiguously, though choosing the beam for which its direction is closest to the spectator quark

1.6 (c). It is subdominant because the valence u-quark density of the proton is about twice as high as the valence down-quark density.

[7] In the right-handed ATLAS coordinate system, the pseudorapidity η is defined as $\eta = -\ln\tan\theta/2$ where the polar angle θ is measured with respect to the LHC beam-line. The azimuthal angle ϕ is measured with respect to the x-axis, which points towards the centre of the LHC ring. The z-axis is parallel to the anti-clockwise beam viewed from above.

direction in the laboratory frame is a good choice. Then, the $\hat{x}$ direction lies in the plane of production, orthogonal to $\hat{y}$ and $\hat{z}$, such that $\{\hat{x}, \hat{y}, \hat{z}\}$ form a right-handed coordinate system:

$$\hat{z} = \frac{\vec{p}_s}{|\vec{p}_s|}\,, \qquad \hat{y} = \frac{\hat{z} \times \vec{p}_q}{|\hat{z} \times \vec{p}_q|}\,, \qquad \hat{x} = \hat{y} \times \hat{z}\,.$$

Considering the $qb \to dt$ process and the reference system with axes $(\hat{x}, \hat{y}, \hat{z})$ (the reference system is illustrated in Figure 1.7 :

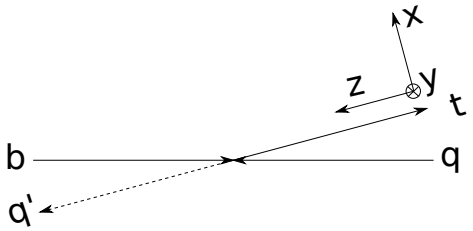

Figure 1.7: Diagram illustrating the three directions $\hat{x}$, $\hat{y}$ and $\hat{z}$ used in this analysis, as seen in the zero-momentum frame. The $\hat{z}$ direction is that of the spectator quark in the top quark rest frame. The $\hat{x}$ direction lies in the plane of production, while the $\hat{y}$ direction is perpendicular to the plane of production.

An ensemble of top quarks is characterised by a spin-density matrix ρ which depends on the three-dimensional polarization vector, $\vec{P} \equiv (P_x, P_y, P_z)$, and is expressed as

$$\rho = \frac{1}{2}\begin{pmatrix} 1+P_z & P_x - iP_y \\ P_x + iP_y & 1-P_z \end{pmatrix}\,,$$

satisfying $|\vec{P}| \leq 1$ in general, and $|\vec{P}| = 1$ if, and only if, the top quarks are produced in a pure spin state.

In the SM, the polarizations values are expected to be $P_t \simeq (0, 0, 0.90)$ and $P_{\bar{t}} \simeq (-0.14, 0, -0.86)$, for top and antitop quark respectively [71]. Such values have been computed for the $2 \to 3$ process $g + q \to q' + t + b$ with the Protos generator [72], using CTEQ6L1 [73] parton distribution functions. The longitudinal polarization is in agreement with the NLO values: $P_z = 0.91$ and $P_z = -0.86$ for top and antitop quarks, respectively [70].

The distributions of the top quark decay products are sensitive to its polarization. The general form of the angular distribution of a spin analyzer with respect to the direction i is given by:

$$\frac{1}{\Gamma}\frac{d\Gamma}{d\cos\theta_{ji}} = \frac{1}{2}\left(1 + \alpha_j P_i \cos\theta_{ji}\right)\,, \tag{1.11}$$

where θ_{ji} is the angle between the direction of motion of the chosen decay product in the top quark rest frame $j = W, b, l, \nu$ and the top quark spin axis i, α_j is the spin

analysing power associated with j, and P_i is the top-quark degree of polarization in a given direction i. The charged lepton (ℓ) is the most sensitive spin analyser and at LO its spin analysing power is $\alpha_\ell = 1$ [74]. Therefore, it is used in the measurement presented in this thesis.

In the coordinate system previously defined and considering $\theta_{\ell i}$ as the polar angle of the charged lepton momentum with respect a given axis (with $i = \hat{x}, \hat{y}, \hat{z}$) as shown in Figure 1.8, one can obtain the angular distributions associated with the three different polarization components P_x, P_y and P_z.

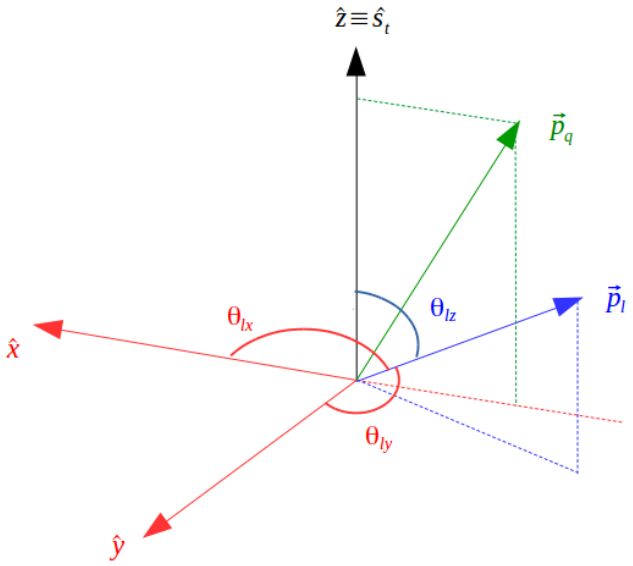

Figure 1.8: Right-handed coordinate system illustrating the angles used to define the top quark production system and their related angular asymmetries in the production and decay of polarized top quarks. The top quark spin direction $\hat{s}_t$, is taken along the spectator quark momentum in the top quark rest frame, defining the $\hat{z}$ axis. $\hat{y}$ is taken orthogonal to the top quark spin and the momentum of the initial quark $\vec{p_q}$ (in green), while $\hat{x}$ is determined by requiring that the coordinate system is right-handed. The diagram also shows the charged lepton momentum $\vec{p_l}$ in the top quark rest frame (in blue) that is used to measure the top quark polarization in the decay. The polar angle of the charged lepton momentum $\vec{p_l}$ in the top quark rest frame is labelled θ_{lz}. The polar angles between the charged lepton momentum and the $\hat{x}$ and $\hat{y}$ axis are labelled as θ_{lx} and θ_{ly} respectively and are used to construct forward-backward asymmetries.

In addition, from these angular distributions, observables related to the top quark polarization [4, 71] can be obtained as forward-backward asymmetries, A_{FB}, which are generally defined as a function of $\cos\theta_{\ell i}$ as:

$$A^i_{\text{FB}} = \frac{N(\cos\theta_{\ell i} > 0) - N(\cos\theta_{\ell i} < 0)}{N(\cos\theta_{\ell i} > 0) + N(\cos\theta_{\ell i} < 0)} = \frac{1}{2}\alpha P_i \,, \tag{1.12}$$

where N is the number of events with $i = \hat{x}, \hat{y}, \hat{z}$. Thus, three asymmetries can be measured from which P_x, P_y and P_z can be derived at parton level. As new physics in the decay vertex can enter the distributions through the α factor, the measurement of the top quark polarization is model-dependent. However, if one is just interested in new physics yielding anomalous Wtb couplings[8], i.e. $V_{L,R}$ and $g_{L,R}$, and not other dimension-six operators such four-fermion ones [76–78], limits on the anomalous couplings can be extracted from the measurements of these asymmetries, specially of A_{FB}^{X} and A_{FB}^{Y} and their respective dependence at parton level on $\text{Re}(g_R)$ and $\text{Im}(g_R)$ anomalous couplings [71], that is shown in Figure 1.9.

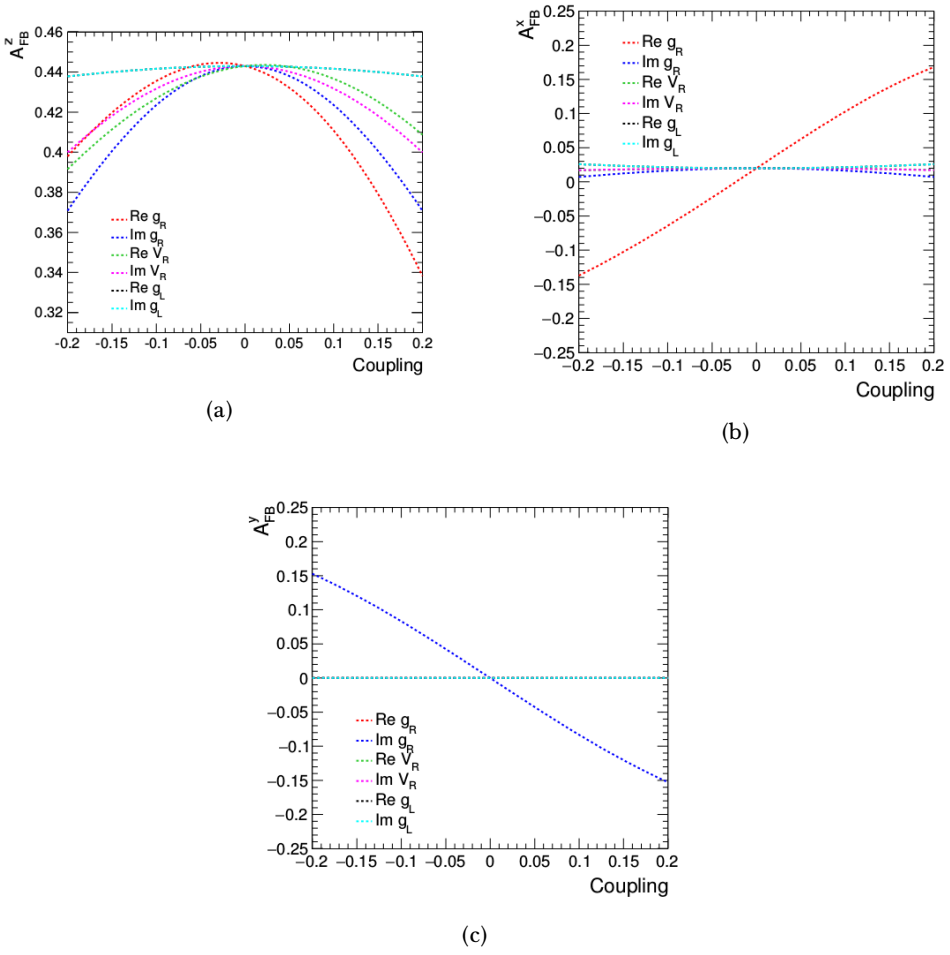

Figure 1.9: Parton level dependence on the real and imaginary parts of the Wtb anomalous couplings g_R, g_L and V_R for the asymmetries A_{FB}^{Z} (a), A_{FB}^{X} (b) and A_{FB}^{Y} (c). Figures have been extracted from Ref. [79].

[8] With anomalous couplings it is meant the four complex effective couplings $V_{L,R}$ and $g_{L,R}$, that can be identified with the dimension-six operators' Wilson coefficients [75].

In Tables 1.5 and 1.6 it is summarised the definition of the various angular observables as well as the definition of the derived asymmetries, respectively.

Angle	Definition
θ_{lz}	Angle between a decay particle (we use the lepton $\vec{p_l}$ in the t rest frame) and the chosen spin axis (in the t rest frame) (i.e the spectator quark basis in the t rest frame)
θ_{lx}	Angle between $\vec{p_l}$ (in the t rest frame) and the transverse direction to the chosen spin axis (in the t rest frame)
θ_{ly}	Angle between $\vec{p_l}$ (in the t rest frame) and the normal direction to the chosen spin axis(in the t rest frame)

Table 1.5: Angles definitions

Asymmetry	Definition
A_{FB}^{Z}	Forward-backward asymmetry (around $z = 0$) in the $\cos\theta_{lz}$ distribution
A_{FB}^{X}	Forward-backward asymmetry (around $z = 0$) in the $\cos\theta_{lx}$ distribution
A_{FB}^{Y}	Forward-backward asymmetry (around $z = 0$) in the $\cos\theta_{ly}$ distribution

Table 1.6: Summary of all the asymmetries resulting from the $\theta = \theta_{lz}, \theta_{lx}, \theta_{ly}$ angles.

1.3.1 Scope of the analysis

Previous ATLAS analyses [80, 81] extracted the value of αP_z, for an inclusive sample of events containing both top quarks and top antiquarks. In Ref. [79], the normal and transverse components of the top quark polarization ($\alpha\overline{P_x}$ and $\alpha\overline{P_y}$, respectively[9]) were obtained for the first time. The measurements provided by ATLAS but also CMS during Run 1 of the observables described in Section 1.3 are summarised in Table 1.7.

In those analyses, the observed angular distributions are corrected for detector effects to the parton level, so that the measured polarization can be compared directly with theoretical calculations. However, it has been observed that the presence of top quark anomalous couplings in general modifies the kinematics in such a way that the efficiency parton level corrections are dependent on the Wtb couplings [80]. Therefore, SM assumptions need to be considered on the parton level corrections, when unfolding to parton level. An alternative approach is to correct the measured observables to particle level in the fiducial region where events are reconstructed. In the particle level approach the measured observables are corrected for detector inefficiencies and resolution effects, avoiding extrapolations that account for the detector acceptance and the transition from partons to particles. Therefore, the uncertainties associated to the signal modelling are expected to be lower.

[9] As said before, using the spectator quark direction to choose among both beams gives the correct answer 97% and 98 % of the times for the two main production channels for single top and antitop quarks. In the remaining production channels, the estimation success rate decreases. This implies that the measured or observed polarisations $\overline{P_x}$ and $\overline{P_y}$ are slightly smaller than if the initial quark direction were certainly known.The relations between $P_{x,y}$ and the observed $\overline{P}_{x,y}$ have been calculated with a MC, resulting in a linear dependency, independent of the anomalous couplings.

	CMS	**ATLAS**
$\mathbf{A_{FB}^{Z}}$ **(8 TeV)**	$0.41 \pm 0.06(stat.) \pm 0.16(syst.)$ [82]	$0.49 \pm 0.03(stat.) \pm 0.05(syst.)$ [80]
$\alpha\mathbf{P_z}$ **(8 TeV)**	$0.82 \pm 0.12(stat.) \pm 0.32(syst.)$ [82]	$0.97 \pm 0.05(stat.) \pm 0.11(syst.)$ [80]
$\mathbf{A_{FB}^{X}}$ **(8 TeV)**	-	$-0.03 \pm 0.02(stat.)^{+0.06}_{-0.05}(syst.)$ [79]
$\alpha\overline{\mathbf{P_x}}$ **(8 TeV)**	-	$-0.05 \pm 0.04(stat.) \pm 0.11(syst.)$ [79]
$\mathbf{A_{FB}^{Y}}$ **(8 TeV)**	-	$0.01 \pm 0.02(stat.) \pm 0.03(syst.)$ [79]
$\alpha\overline{\mathbf{P_y}}$ **(8 TeV)**	-	$0.01 \pm 0.04(stat.) \pm 0.05(syst.)$ [79]

Table 1.7: Measurements performed during Run 1 by ATLAS and CMS collaborations of the single top quark polarization components and their corresponding asymmetries.

The analysis in this thesis describes a study of angular distributions in the decay of single top quarks produced in the t-channel using 80.5 fb^{-1} of data recorded in Run 2 by ATLAS detector between 2015 and 2017, containing both top quarks and antitop quarks at $\sqrt{s} = 13$ TeV. The angular distributions are unfolded to particle level in a fiducial region and the forward-backward asymmetries are extracted. This approach has been followed by the ATLAS collaboration extensively; for instance to provide a measurement of the single top t-channel cross section in a fiducial region close to the detector acceptance [83], being more precise than the inclusive measurement thanks to a reduction of the signal modelling related uncertainties. In addition, it was previously studied that the sensitivity to the Wtb anomalous couplings was retained for various forward backward asymmetries, defined at particle level within the detector acceptance [84].

The measurement in this thesis has also been the benchmark to provide a fiducial polarization measurement that is being carried out separately for top quark events, and for top antiquark events with the full Run 2 dataset. In such analysis, differential angular distributions are provided for angles $\theta_{\ell x}, \theta_{\ell y}, \theta_{\ell z}$ unfolded to particle level, for events lying within the acceptance of the analysis.

Chapter 2

The LHC and ATLAS detector at the CERN laboratory

This chapter summarizes the accelerator and the detector that constitutes the experimental setup of this thesis. The object reconstruction that is performed from the recorded signals is also described. The analysis presented in this thesis has been performed with data collected by the ATLAS experiment, using a detector located in one of the collision points within the Large Hadron Collider accelerator, located at the CERN laboratory in Geneva, Switzerland.

2.1 The CERN laboratory

CERN refers to the European Council for Nuclear Research and the acronym is adopted from the French name (*Conseil Européen pour la Recherche Nucléaire*).

CERN was born in a post-war context when in 1953 the CERN convention was signed by 12 founding states. Nowadays our understanding of the matter covers much more than the nucleus, which is why the laboratory is sometimes known as the European Laboratory for Particle Physics. Moreover, the number of CERN state members has grown until 23 and many non-European countries are involved as partners, observers or associate members.

Since the very beginning, a significant number of breakthroughs in particle physics have been achieved. For instance, the Gargamelle bubble chamber installed in the Proton Synchrotron (PS) accelerator led to the discovery in 1973 of a cornerstone of the electroweak theory, that is, the neutral currents [85, 86]. Years later the electroweak theory was confirmed in 1983; the UA1 and UA2 experiments located within the Super Proton Synchroton (SPS) discovered the $W^{\pm}$ and Z bosons [19–22]. Other important achievements followed. For example, the NA31 collaboration announced in 1993 precise results on a phenomenon known as CP violation, indicating a tiny difference between matter and antimatter [87]. Later on, the creation for the first time of antihydrogen atoms was achieved in 1995 using

Figure 2.1: The esplanade des particules located at the main entrance of the Meyrin site.

CERN's Low Energy Antiproton Ring (LEAR) facility at the PS210 experiment [88]. A major accomplishment was also achieved by using the LEP accelerator: the LEP collaborations reported at the International Europhysics Conference that the number of leptons families (including neutrinos) were exactly three [89]. More recently in 2012 ATLAS and CMS experiments discovered a new particle in the mass region around 125 GeV consistent with the Higgs boson [23, 24]. In 2015 the LHCb experiment reported a discovery of a kind of particle known as pentaquarks [90].

In addition to the development of particle physics, CERN has been also crucial in the field of nuclear physics, plasma physics and cosmology. Besides, the engineering technology required by CERN experiments has helped to expand the knowledge in superconducting materials, cryogenics, electronics and construction techniques. CERN has also helped improve our day-to-day lives including the World Wide Web.

2.2 The LHC accelerator

The Large Hadron Collider (LHC) [91] is the world's largest and most powerful particle accelerator built to the date. It started its operations in 2008 and it still remains to be the latest element of the CERN accelerator complex, which has been growing and growing since the installation of the first accelerator: the Synchrocyclotron (SC) in the late 1950's. The LHC is a synchrotron collider that consists of a 27-kilometre ring of superconducting magnets with a number of accelerating structures to boost the energy of the particles circulating along the way. Inside the accelerator, two high-energy particle beams (which can be composed of protons but also heavy ions such as ionized lead or xenon) travel (close to the speed of light) in opposite directions in two separate beam pipes. They are guided around

the accelerator ring by a strong dipole magnetic field created by superconducting electromagnets. In order to avoid collisions with gas molecules, particles are accelerated in an ultrahigh vacuum environment (10^{-13} atm). The electromagnets are built from coils of special electric cable that operates in a superconducting state, efficiently conducting electricity without resistance or loss of energy.

Figure 2.2: A panoramic view of the CERN Control Room located at Prevessin site. LHC beam is monitored from this place.

This requires cooling the magnets to $-271.3°$C. For this reason, much of the accelerator is connected to a distribution system of liquid helium, which cools the magnets. The LHC reuses the tunnel that was already built in the previous accelerator, that is, the Large Electron Positron (LEP) collider [92]. The tunnel was built $\sim$ 100 m underground. Due to geological considerations and at a slight gradient its depth varies between 175 m (under the Jura) and 50 m (towards Lake Geneva).

The LHC ring is divided into eight arcs and eight insertion regions (IR), as displayed in Figure 2.3. While four of the insertion regions are set for the placement of the experiments, the other four of the insertion regions are used to install the radio frequency (RF) cavities (that accelerate the particles and compensate the energy losses), the beam injection, the beam dump system and the beam collimator (cleaning) system. The arcs contain the dipole superconducting Niobium-Titanium magnets, with 154 in each arc, that bends the beam along the circular path of the ring; and the quadrupole magnets, that keep the beam focused. In total there are 16 RF cavities (8 per beam) operating at 400 MHz to accelerate the particle beam. When the beam has reached the required energy, a synchronised particle with exactly the required energy will not be accelerated. However, particles with slightly different energies arriving earlier or later will be accelerated or decelerated so that they obtain the desired energy. In this way, the particle beam is sorted into

packs of particles called bunches. LHC has been designed to circulate up to 2808 bunches, each one composed of 10^{11} protons, spaced every 25 ns.

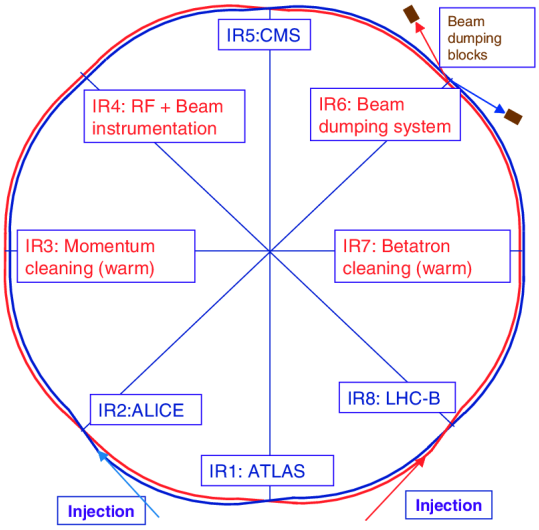

Figure 2.3: Schematic layout of the LHC.

Nevertheless, before particles collide at $\sqrt{s} = 13$ TeV in the LHC, several accelerators (both circular and linear) accelerate the particles in different sequential stages, as shown in Figure 2.4.

Although heavy ions are also used in the LHC, we will refer from now on the accelerated particles as protons, since these kind of collisions constitute the main physics program of the LHC and the analysis performed in this thesis has been carried out with proton-proton collisions too.

The proton source is just hydrogen gas, whose atoms are stripped of their electron using an electric field. The proton source is situated in the Linac 2, the first accelerator in the chain that accelerates the protons to the energy of 50 MeV. The beam is then injected into the Proton Synchrotron Booster (PSB), where protons reach an energy of 1.4 GeV. After this stage protons are transfered to the Proton Synchrotron (PS), which accelerates the beam to 25 GeV and arranges the proton in bunches. The PS was built in the 1950's and for a few years it was the accelerator that reached highest energies. It has 628 m circumference and 277 magnets operating at ambient temperature. Protons are then sent to the Super Proton Synchrotron (SPS) where they are accelerated to 450 GeV. The SPS has 1317 magnets operating at ambient temperature. With a circumference of 7 km, it started working in the 1970's and the research carried out includes the study of matter and antimatter or the inner structure of protons. W and Z bosons were discovered using proton-antiproton collisions occurring in the SPS accelerator.

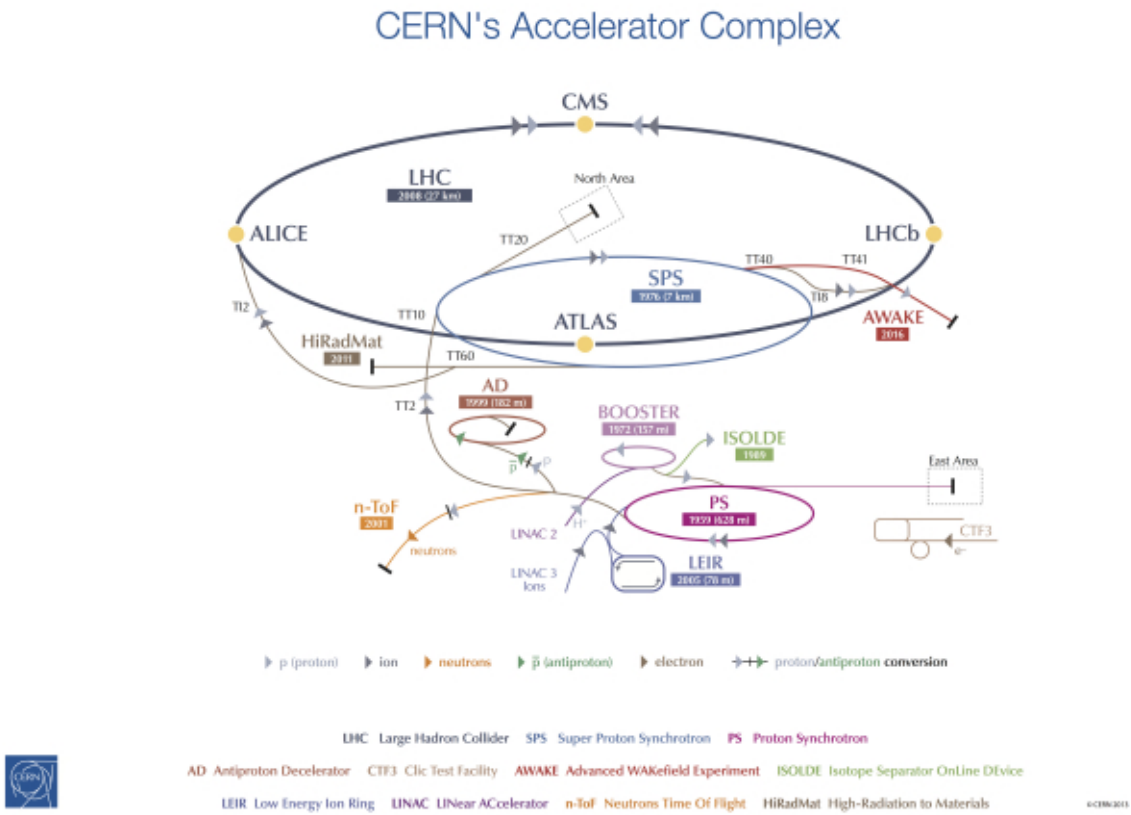

Figure 2.4: CERN accelerator complex showing the acceleraton chain and the location of the four main experiments in the LHC ring. ATLAS is located in Point 1 of the LHC in the Meyrin site of CERN. CMS is located in the Point 5 in the opposite part of the ring in the French part of the ring. LHCb is in the Point 8 near the Ferney-Voltaire village, while ALICE is located in Point 2 near the Saint-Genis-Pouilly village.

The protons are finally transferred to the two beam pipes of the LHC. The beam in one pipe circulates clockwise while the beam in the other pipe circulates anticlockwise. It takes 4 minutes and 20 seconds to fill each LHC ring, and 20 minutes for the protons to reach their maximum energy of 6.5 TeV. Beams circulate for many hours inside the LHC beam pipes under normal operating conditions.

2.2.1 LHC experiments

Finally, the two beams are brought into collision in four dedicated points in the LHC where the main detectors are placed : ATLAS (A Toroidal LHC ApparatuS) [93], CMS (Compact Muon Sollenoid) [94], ALICE (A Large Ion Collider Experiment) [95] and LHCb (LHC beauty) [96].

On the one hand, ATLAS and CMS are generic multi-purpose detectors characterized by having silicon-based tracking systems, large-coverage calorimeters, powerful magnet systems and efficient muon chambers. They are both well-known for discovering the Higgs boson in 2012, although a wide range of precise measurements featuring the Higgs and other Standard Model parameters have been studied by these detectors. ATLAS detector is covered in detail in Section 2.3.

On the other hand, ALICE and LHCb have been designed to carry out specific physics studies. ALICE uses ion collisions to study matter interacting at extreme densities, thus reproducing the quark-gluon plasma. Besides the technology of multi-purpose detector, ALICE incorporates a Time of Flight (TOF) detectors, that measure the time that a particle takes to go from one vertex to another point, to determine the momentum of the particle. LHCb has been designed to study the small asymmetries between matter and antimatter using bottom quarks. The detector is arranged as a succession of planar sub-detectors, since most of B mesons follow the beam pipe direction, when created in the proton-proton collision.

Other smaller experiments can be found in the LHC interaction point thought to cover phenomena that the main experiments do not cover. Those are namely: LHC forward (LHCf) [97] and TOTal Elastic and diffractive Meaurement (TOTEM) [98] experiments that study particles produced in the forward regions of the ATLAS and CMS respectively. The Monopole and Exotics Detector At the LHC (MoEDAL) [99] detector is installed close to the LHCb and it carries out searches for magnetic monopoles and other highly ionising particles with similar properties.

2.2.2 Luminosity

The luminosity is a collider parameter that measures its capacity to produce a certain number of scattered events. It is given by:

$$N = L \cdot \sigma, \tag{2.1}$$

where σ is the production cross-section of a certain proton-proton inelastic process, which depends on the center of mass energy. The luminosity is a collider beam parameter independent of the process, so if σ were small, it is important that the luminosity is high enough to produce a sizeable sample of events.

Equation 2.1 is often re-written per time unit as an event production rate:

$$\frac{\mathrm{d}N}{\mathrm{d}t} = L_{ins} \cdot \sigma, \tag{2.2}$$

being L_{ins} the collider instantaneous luminosity that depends only on the beam parameters and has units of $\mathrm{fb}^{-1} \cdot \mathrm{s}^{-1}$ or $\mathrm{cm}^{-2}\ \mathrm{s}^{-1}$. Assuming a Gaussian profile for the beam bunches the instantaneous luminosity is determined by the following expression:

$$L_{ins} = \frac{N_a N_b f N_{bunch}}{4\pi\sigma_x\sigma_y}, \tag{2.3}$$

where N_a and N_b represent the number of protons in each beam, f the bunch crossing frequency, N_{bunch} the number of bunches and σ_x,σ_y the Gaussian widths in the horizontal and vertical plane of the beam per bunch.

Equation 2.3 shows that there are three different ways of increasing the instantaneous luminosity:

- Increasing the number of protons in each beam.
- Increasing the number of bunches.
- Squeezing the beams to a smaller transversal size.

However, such actions affect to the event pile-up, that is the average number of particle interactions that takes place every time that the bunches cross one another. For instance, squeezing the beams or increasing the number of protons in each beam result in an increase of the number of proton-proton interactions during the same bunch crossing (i.e. in-time pile-up). Whereas increasing the number of bunches (which is the same as decreasing the spacing between them) results in an increase of collisions arising from other bunches, which are recorded when the electronics time integration is significantly larger than the crossing time between bunches (i.e. out-of-time pile-up).

In Table 2.1 a comparison of the design parameters that characterize the beams of Tevatron, SPS, LEP and LHC colliders. LHC has reached the highest energies but also has been able to squeeze the beams in the interaction points as no other collider. The number of particles per bunch is also very high.

	Energy (GeV)	L**(cm^{-2}·s^{-1})**	$\sigma_x/\sigma_y(\mu m/\mu m)$	**Particles per bunch**
Tevatron	2000	$50 \cdot 10^{30}$	30/30	$3.75 \cdot 10^{10}$
SPS	630	$6 \cdot 10^{30}$	60/30	$10 \cdot 10^{10}$
LEP	210	$100 \cdot 10^{30}$	200/2	$50 \cdot 10^{10}$
LHC	14000	$10000 \cdot 10^{30}$	17/17	$11 \cdot 10^{10}$

Table 2.1: Design energies, luminosities, beam sizes and number of particles per bunch for different colliders.

2.2.3 LHC timeline

The LHC program is divided in periods of consecutive data-taking known as *Runs*. These are separated by non-collisions periods used to consolidate, repair or upgrade the accelerator and the detectors, known as *Long Shutdowns*.

Figure 2.5 shows the tentative schedule of the LHC since 2010 until 2040, depicting the Run periods and the shut-downs. The first phase of the LHC was Run 1 and took place between 2010 and 2012, followed by the Long Shutdown 1 (LS1) during 2013 and 2014. The second phase was Run 2, from 2015 to 2018, which

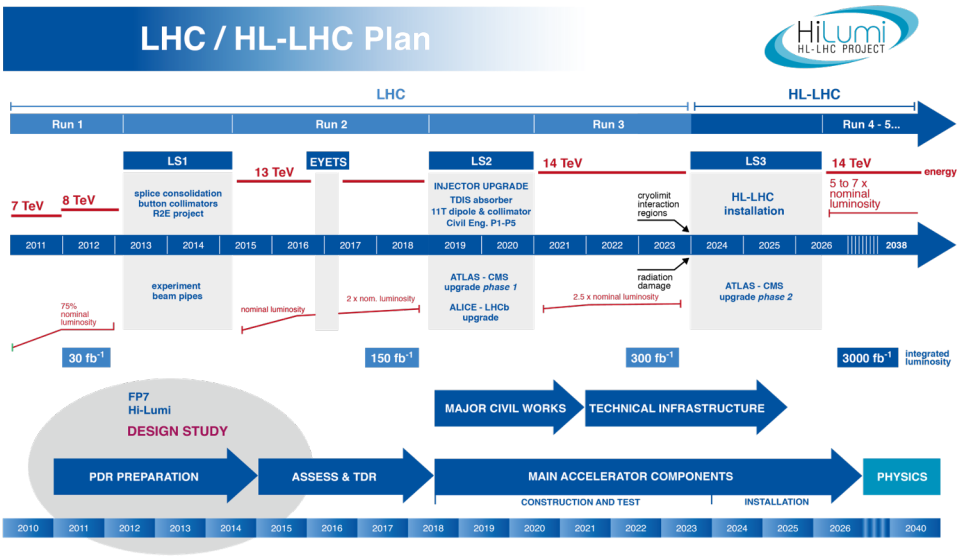

Figure 2.5: LHC and HL-LHC schedule.

is being followed by the Long Shutdown 2 (LS2) in 2019 and 2020, at the same moment of the writing of this thesis. It will be followed by Run 3, which is planned to occur from 2021 to 2023.

Afterwards the LHC is expected to enter the LS3 in 2024 to prepare the machine for a significant upgrade to achieve higher luminosity conditions during its Phase II, the so-called the High-Luminosity LHC (HL-LHC) [100].

The idea of the construction of the LHC took place in the early 1980's, when the LEP accelerator was even still not running. In December 1994, CERN Council voted to approve the construction of the LHC and it wasn't until 2008 that the LHC was finalized. The first proton-proton collisions were registered in November of 2009, although the first protons injection occured a year before. However, an electric flaw resulted in a release of helium that damaged a considerable number of magnets. Because of some concerns of the magnets safety after this incident, it was decided to set the center of mass energy to a value of 7-8 TeV, despite the nominal energy was designed to 14 TeV. During Run 1, 28.2 fb^{-1} of integrated luminosity was collected.

Run 2 started in 2015 after the upgrading period of LS1. Center of mass energy was risen until 13 TeV and the bunch spacing set to 25 ns. Run 2 was a breakthrough in the LHC history because of the very successful collection of data: a total of 150 fb^{-1} of integrated luminosity was recorded. Figure 2.6 shows the cumulative distributions per year from 2011-2018.

During Run 2, an average of 33 simultaneous proton-proton interactions was also reached, as shown in Figure 2.7.

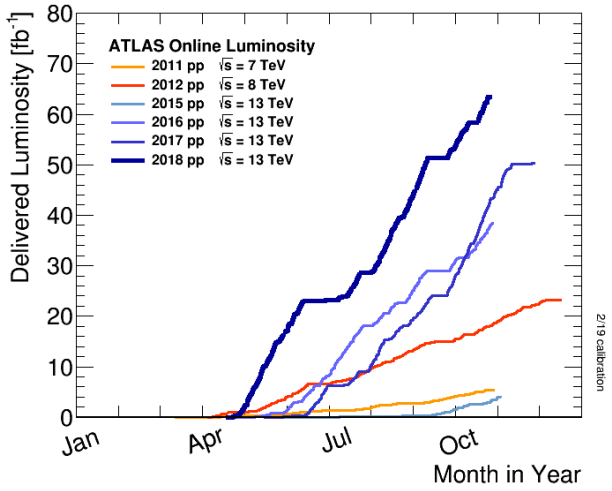

Figure 2.6: Cumulative luminosity versus day delivered to ATLAS during stable beams and for high energy p-p collisions. Run 1 (2011-2012) and Run 2 (2015-2018) are shown together in the plot.

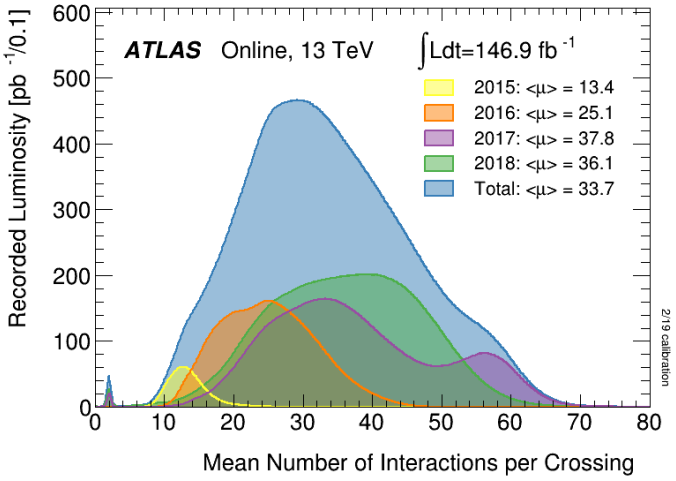

Figure 2.7: Luminosity-weighted distribution of the mean number of interactions per crossing for the 2015-2018 pp collision data at 13 TeV centre-of-mass energy.

During LS2 the LHC may be upgraded to deliver collisions at a center of mass energy of 14 TeV. During Run 3 an integrated luminosity of 300 fb^{-1} is expected to be recorded. For the next stage, the Phase-II, the HL-LHC is expected to provide up to 3000 fb^{-1} of integrated luminosity which will span from 2026 until 2040.

2.3 ATLAS detector

The ATLAS detector is a general purpose detector located 100 m underground in the Point 1 of the LHC ring at CERN. The detector is a cylinder of 46 m long and 25 m diameter. Its total weight corresponds to 7000 tones. The detector tracks and identifies particles to investigate a wide range of physics, from the study of the Higgs boson and top quark to the search for new physics at the TeV scale, such as extra dimensions and particles that could make up dark matter. Such a challenging project requires of international collaboration to maximize the quantity and the quality of the scientific results.

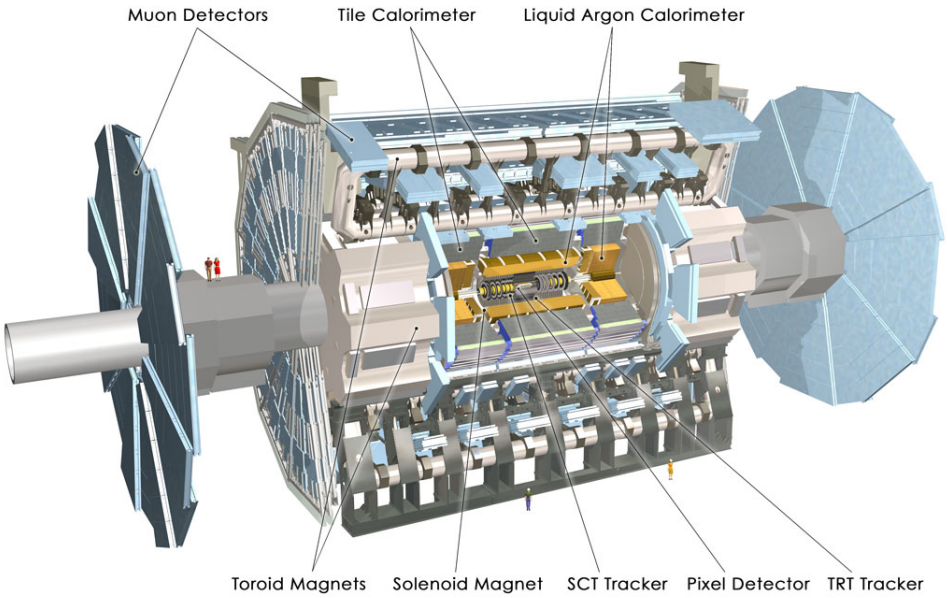

Figure 2.8: Cut-away view of the ATLAS detector. The dimensions of the detector are 25 m in height and 44 m in length. The overall weight of the detector is approximately 7000 tonnes. 100 M electronic channels instrument the detector.

ATLAS collaboration consist of roughly 3000 scientists from 183 institutions around the world, distributed across 38 countries. It is one of the largest collaborative efforts ever attempted in science. Around 1200 doctoral students are involved in detector development, data collection and analysis. The collaboration covers as well many engineers, technicians and administrative staff.

The detector itself is a many-layered-onion-like instrument, as can be seen in Figure 2.8, designed to detect the elementary particles created in the proton-proton and heavy ions collisions. It consists of six different detecting subsystems wrapped concentrically in layers around the collision point to record the trajectory, momentum, and energy of particles, allowing them to be individually identified and measured. A magnet system bends the paths of the charged particles so that their momenta

can be measured as precisely as possible. The different subsystems are explained in the Sections 2.3.2-2.3.4.

2.3.1 ATLAS coordinate system

Since for massive particles, with energies comparable to the beam constituents, scattering can occur in any direction, it is crucial to know accurately in which phase space lies each produced particle. For that purpose, a coordinate system (x, y, z) must be defined. The convention is taken with the origin in the interaction point. The beam direction defines the z-axis, so that the transverse x-y plane is where the transverse momentum (p_T) and energy (E_T) lies. The positive x-axis is defined as pointing to the center of the LHC ring, the positive y-axis is pointing upwards and the positive z-axis along the tunnel.

In the ATLAS detector, a particle is scattered with a certain polar angle θ with respect to the beam and an azimuthal angle ϕ around the beam. The phase space of such particle can be written in terms of a variable known as rapidity, defined as:

$$y = \frac{1}{2} \ln \frac{E + p_z}{E - p_z}. \tag{2.4}$$

For light particles, the rapidity can be approximated to the so-called pseudorapidity, defined as:

$$\eta = -\ln \tan \theta/2, \tag{2.5}$$

The parameter η is generally preferred over θ because it is a longitudinal boost invariant quantity. Thus, this property makes pseudorapidity interesting to perform cross-sectional calculations. The pseudorapidity is defined such that $\theta = 90^\circ$ corresponds to $\eta = 0$ and $\theta = 0^\circ$ corresponds to $\eta \to \infty$, although most of the particles are located around 5 pseudorapidity units.

The general features required by the ATLAS detector can be summarised as follows:

- Fast radiation-hard electronics and sensor elements are required due to the harsh experimental conditions at the LHC.
- Detectors with large acceptance in pseudorapidity with almost full azimuthal angle coverage.
- Trackers with a good charged-particle momentum resolution. Vertex detectors must be put close to the interaction region to reconstruct accurately secondary vertices.
- Excellent electromagnetic calorimetry performance for electron and photon identification and measurements, as well as hadronic calorimetry to measure accurately jet and missing transverse energy.

- Muon spectrometers that provide good muon identification and momentum resolution over a wide range of momenta.
- Highly efficient triggering on low transverse momentum objects is essential to achieve an acceptable trigger rate for most physics processes of interest.

2.3.2 Inner Detector

The ATLAS detector is equipped with a central tracking system, the Inner Detector. Its goal is to reconstruct the trajectories of charged particles and to estimate their kinematic parameters. For that purpose, the ID uses a 2 T magnetic field (provided by a solenoid) that bends the trajectories of the charged particles, allowing for momentum and charge measurement. The accuracy of the tracking process is limited by: the finite intrinsic resolution of the sensitive devices; the precise knowledge of the location of the sensors and the precise knowledge of the amount of material and its distribution. The location of the sensors depends significantly on the assembly tolerances accuracy and operating conditions (such as temperature effects), so it is in general different to the assembly position. Therefore, measuring the exact precise location of each of the sensors is not a straight-forward task. The detector is not even accessible while data-taking, however it is possible to fit the geometrical location of sensors using collision data. This process is known as alignment. Any error on the geometrical description are referred as misalignments. The alignment of the ID is one of the topics covered in this thesis and details of the procedure is given in Section 3.

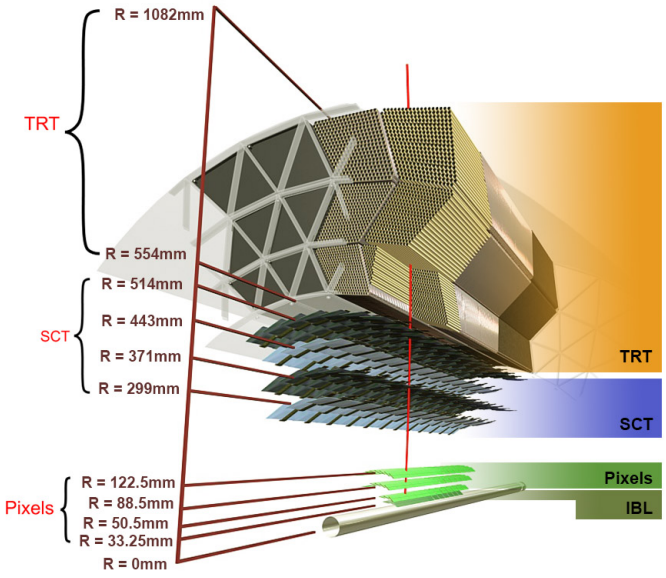

Figure 2.9: Schematic view of the ID barrel. The ID barrel is arranged in sub-detector layers. From innermost to outermost sub-detectors: IBL, Pixels, SCT and TRT.

The ATLAS Inner Detector is the innermost subsystem of the ATLAS detector allowing to measure the impact parameters in order to determine the origin of the produced particles as well as to recognize secondary vertices of quark decays and heavy leptons. It consists of three sub-detectors: the Pixel detector (including the Insertable B-Layer or IBL), the Semiconductor Tracker (SCT), and the Transition Radiation Tracker (TRT). All are embedded in a 2 T axial magnetic field as previously mentioned. Table 2.2 summarizes the main characteristics of the ID subsystems.

The ID has been designed to reconstruct the charged particles trajectories within a pseudorapidity range of $|\eta| < 2.5$ (see Figure 2.9 for a schematic view of the barrel region) and has a total length of 7 m and 2.2 m of diameter.

Sub-detector	Element size [μm]	Intrinsic resolution [μm]	Number of channels
IBL	50×250	8×40	12 M
Pixel	50×400	10×115	80 M
SCT	80	17×580	6 M
TRT	4000	130	700 k

Table 2.2: Summary of the main characteristics of the ID sub-detectors. The intrinsic resolution of the IBL, the Pixel and the SCT detectors is reported along r-ϕ and z, while only r-ϕ is considered for the TRT.

The Pixel detector consists of 1744 silicon pixel modules arranged in three barrel layers and two end-caps with three disks each. The expected hit resolution is 10 μm in r–ϕ coordinates and 115 μm in the longitudinal coordinate. Each track creates three hits on average on the Pixel detector. Due to the high resolution and the proximity to the beampipe the Pixel helps to reconstruct the interaction vertices very precisely.

During LS1, the IBL was added as an additional layer to the Pixel detector, reducing the distance from the interaction point to the first tracking layer, as IBL is placed at 33.25 mm radius while the inner layer of the rest of the Pixel is placed at 50.5 mm, becoming the nearest sub-detector to the beampipe. The IBL is composed of 280 modules, mixing planar and 3D technology, arranged on 14 azimuthal carbon fibber staves[1]. A cross-sectional view of the IBL is displayed in FIgure 2.10. The expected hit resolution is 8 μm in r–ϕ coordinates and 40 μm in the longitudinal coordinate [101]. This detector layer has improved the tracking performance in spite of effects arising from luminosity, hardware lifetime and radiation by improving the impact parameter resolution, which directly affects b-tagging and vertex operation.

[1]Each stave is built with 12 two-chip silicon planar modules, covering the region of $\eta < 2.7$, and 8 single chip modules with silicon 3D sensors, four at each end of the stave ($2.7 < |\eta| < 3$).

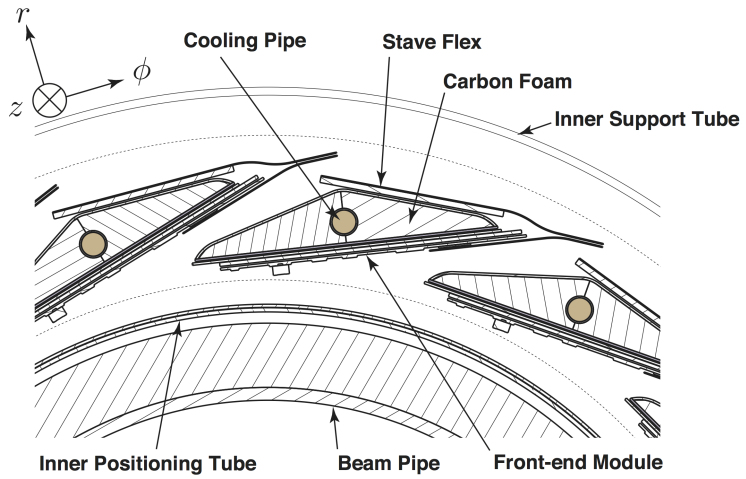

Figure 2.10: Cross-section view of the IBL Layout seen from the interaction point to +z-direction.

The SCT consists of 4088 silicon strip modules, arranged in four barrel layers and two end-caps with nine wheels each. Each module is composed by two silicon micro-strips sensors assembled back-to-back with a stereo angle of 40 mrad so that a two dimensional measurement (r–ϕ and z) can be provided. The intrinsic resolution is 17 μm in r–ϕ coordinates and 580 μm in the longitudinal coordinate. Each track leaves four hits on average on the SCT detector. 280 of the SCT modules were assembled at the IFIC clean room.

The TRT is the outermost detector of the ID sub-detectors and is made of 350848 straw tubes of 4 mm of diameter filled with a mixture of gas with a single hit resolution of 130 μm along r–ϕ only. If a charged particle passes through the TRT, it ionises the gas mixture inside the straws. The resulting free electrons drift towards the anode of the wire (located in the center of the straw) and produce a signal captured by the read-out electronics. The spaces between the straws are filled with polymer fibres in the barrel and foils in the end-caps in order to create transition radiation, that is absorbed by xenon gas and leads to significantly higher read-out signals. This allows the detector to discriminate between tracking hits and transition radiation hits. Wires are arranged longitudinally to the beam axis in the barrel region and radially in the end-caps.

2.3.3 Calorimeters

After the Inner Detector and the solenoid magnet, the next layers in the ATLAS detector are the calorimeters. Their purpose is to measure the energy of charged and neutral particles and particle jets as they pass through the calorimeters layers. For that purpose the calorimeters capture their energy within the detector. Two kind of components are used to do so: the passive and the active material. The passive material (also known as absorber) is made up of dense material and as the incident particle interacts with it, secondary particle showers are produced. The active material is interleaved in the absorbers and are able to detect the particles created in the shower creating an output signal.

The ATLAS calorimetry system is based upon two kind of calorimeters: Liquid Argon (LAr) and Tile Calorimetry (TileCal). Electromagnetic calorimeters are found in the LAr sub-detector that measure the energy of electrons and photons as they interact with matter. Hadronic calorimeters are also used in the ATLAS sub-detectors and they are in charge of measuring the energy of jets as the quarks contained interact with atomic nuclei. Muons and neutrinos are able to escape from the calorimetry systems.

The ATLAS LAr and the TileCal jointly cover the region $|\eta| < 4.9$. Whereas TileCal is fully a hadronic calorimeter, the LAr calorimeter comprises a set of detectors: the Electromagnetic LAr (EM LAr), the LAr hadronic end-caps and the LAr forward calorimeter. An overview of the full calorimeter system is depicted in Figure 2.11.

- LAr Calorimeter: the EM LAr calorimeter is a lead-and-liquid-argon detector whose main task is to measure the energy deposited by electromagnetic interacting particles, such as electrons and photons. It is divided in a barrel part ($|\eta| < 1.475$) and two end-caps ($1.375 < |\eta| < 3.2$). The barrel part is splitted in two identical halves separated by a small gap of 4 mm at z = 0. Each end-cap is mechanically divided into two coaxial wheels. In this sub-detector, the passive material consists of lead arranged in an accordion shape to ensure a complete azimuthal coverage. It is surrounded by a cryostat to ensure the needed low temperatures to operate.

  The LAr detector includes also hadronic calorimetry in the Hadronic End-Cap Calorimeters (HEC). They consist of two independent wheels per end-cap, located directly behind the end-cap electromagnetic calorimeter and sharing the same cryostats. The HEC extends out to $|\eta| = 3.2$, therefore overlapping with the forward calorimeter around $|\eta| = 3.1$. Similarly, it also overlaps with TileCal ($|\eta| < 1.7$) by extending to $|\eta| = 1.5$.

  A third sub-detector is integrated in the LAr Calorimeter, the Forward Calorimeter (FCal) that is placed in the high η region inside the LAr end-cap calorimeters. The FCal consists of three modules in each end-cap: the first, made of copper, is optimised for electromagnetic measurements, while the other two, made of tungsten, focus on hadronic interactions.

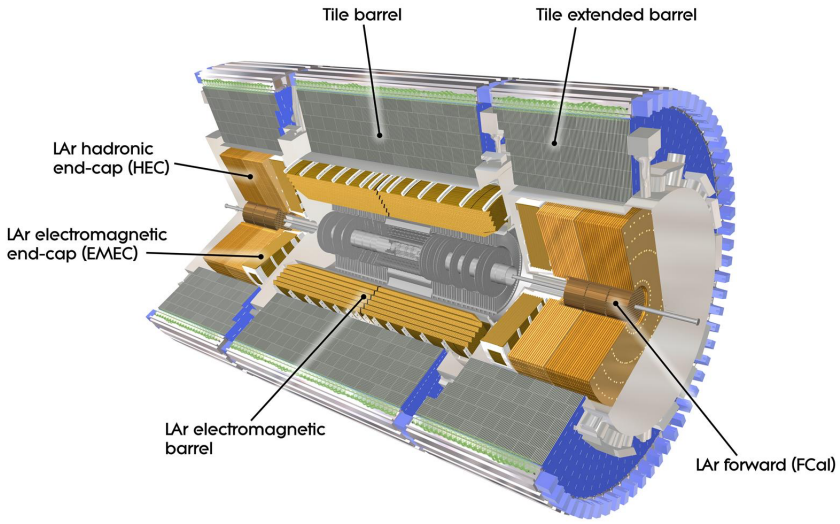

Figure 2.11: General view showing the structure of the ATLAS calorimeter system, including the TileCal long barrel (LB) and extended barrel (EB),the LAr electromagnetic barrel (EM LAr) and endcaps (EMEC), the LAr hadronic end-caps (HEC) and the LAr Forward detector (FCal). The Inner Detector is shown in gray inside the EM LAr barrel.

- TileCal: the TileCal uses scintillating-tile devices to measure the energy in hadronic particles produced in the collisions. TileCal is placed surrounding the LAr system, in the region $|\eta| < 1.7$. The detector is divided in two parts: a central barrel, called Long Barrel (LB), which covers the region $|\eta| < 1.0$, and two Extended Barrels (EB), covering the region $0.8 < |\eta| < 1.7$. Each barrel is a cylinder with an inner radius of 2.28 m and an outer radius of 4.25 m.

2.3.4 Muon spectrometer

The Muon Spectrometer (MS) forms the outer part of the ATLAS detector and is designed to detect and identify the muons exiting the barrel and end-cap calorimeters, since they barely interact with the calorimeter before escaping from them. The muon spectrometer measures the muon momentum in the pseudorapidity range $|\eta| < 2.7$. It is also designed to trigger on these particles in the region $|\eta| < 2.4$.

The way in which muons are detected is very similar to that made in the tracking. The muon momentum determination is based on the magnetic deflection of muon trajectory by the large superconducting toroid magnets.

The MS is formed by three barrel layers and six end-cap disks, which are built using four different types of detectors, optimised for different purposes. Two of them provide precision muon tracking while the other two are used for triggering muon candidates.

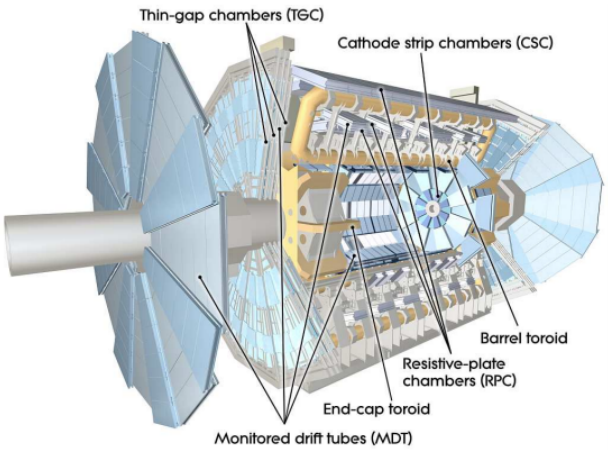

Figure 2.12: Cut away view of the Muon Spectrometer. The toroid and chambers are depicted.

Precision measurement of the track coordinates is performed by Monitored Drift Tubes (MDT) over most of the covered η range. The higher granularity Cathode Strip Chambers (CSC), which are multiwire proportional chambers with cathodes segmented into strips, are used in the innermost plane over $2.0 < |\eta| < 2.7$, to withstand the demanding rate and background conditions.

Triggers are provided by the Resistive Plate Chambers (RPC) in the barrel and the Thin Gap Chambers (TGC) in the end-cap regions. The trigger chambers for the muon spectrometer are useful to provide bunch-crossing identification, provide well-defined p_T thresholds, and measure the muon coordinate in the direction orthogonal to that determined by the precision-tracking chambers.

2.3.5 Magnet system

ATLAS features a unique hybrid system of four large superconducting magnets designed to bend the trajectory of the charged particles and thus determine their momentum from the track curvature. Both the Inner Detector and Muon Spectrometer rely on this magnet system, which consists of:

- A solenoid which is aligned to the beam axis and provides a 2 T axial magnetic field for the inner detector, but also minimising the radiation thickness in front of the EM barrel calorimeter.
- A barrel toroid and two end-cap toroids, each of them composed of eight superconducting coils, which provide in superconducting condition a peak toroidal magnetic field of approximately 3.9 T and 4 T for the muon detectors in the central and end-cap regions, respectively.

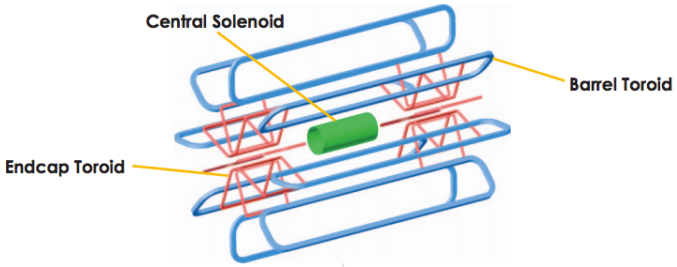

Figure 2.13: Diagram showing the structure of the Magnet system in ATLAS. The green cylinder in the middle is the central solenoid, which is placed between the Liquid Argon and the Inner Detector. The blue lines represent the toroids, both in the barrel and the end-caps.

2.3.6 Trigger system

The trigger system constitutes an essential component of any hadron collider experiment, given the limited computing resources to offline storage and data processing. The trigger system decides whether events from a certain beam crossing are interesting to keep for physics analysis or not, and thus reduce the stored event rate that is produced in the collisions.

The ATLAS trigger system [102] was designed taking into account that the LHC is able to provide a collision rate of 40 MHz, with an average 25 interactions per bunch crossing. During Run 1 it was divided in three levels: Level 1 (L1) [103], the Level 2 (L2) and the event filter (EF). In Run 2, the L2 and event filter together form the High-Level Trigger (HLT) [104]. A schematic of the trigger system used by ATLAS in Run 2 can be observed in Figure 2.14.

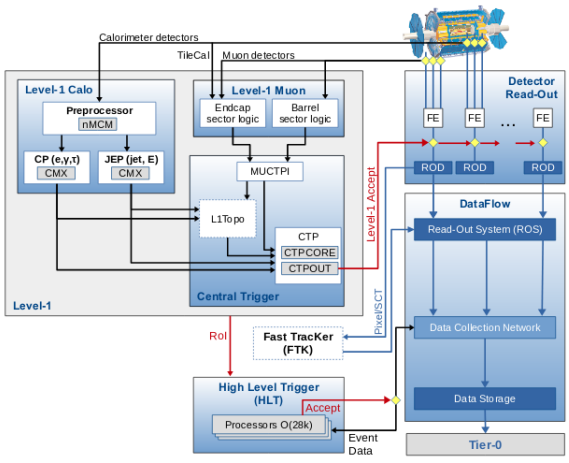

Figure 2.14: The ATLAS trigger/DAQ system used in Run 2. L1Topo and FTK systems are some of the upgrades introduced throughout Run 2.

The L1 trigger is completely hardware-based and uses information from the Muon Spectrometer for high-p_T muons and from all the calorimeter subsystems for electromagnetic clusters, jets, τ-leptons, $E_{\mathrm{T}}^{\mathrm{miss}}$ and large total transverse energy. The processing time of L1 is 2.5 μs providing an output event rate of 75 kHz. Regions of Interest (RoI's) are defined around possible physics objects by L1 trigger identification.

The L2 trigger is a software-based system that uses RoI information on coordinates, energy, and type of signatures to limit the amount of data which must be transferred from the detector readout. The L2 trigger reduces the event rate to below 3.5 kHz, with an average event processing time of approximately 40 ms. Events are then sent to EF that reduces the event to approximately 200 Hz, with an average event processing time of order 4s. EF makes use of offline algorithms with full event information. The events output by EF are finally permanently stored.

In Run 1 the ATLAS trigger system worked using distinct L2 and EF farms, however the increase in energy and the decrease in bunch spacing in Run 2 made this configuration no longer affordable. Therefore several upgrades were introduced in order to withstand such higher trigger rates during Run 2 [105]. The L2 and EF farms were merged into the HLT single farm allowing better resource sharing and thus a feasible simplification of both the hardware and software that is used in this stage.

One of the upgrades has been merging the output of L1 Calorimeter trigger and the L1 Muon trigger into to a new topological trigger processor (L1Topo). This upgrade together with improvements in the detector readout, raised the maximum L1 trigger rate from 75 kHz in Run 1 to 100 kHz in Run 2. Next, the HLT reduces the rate from the L1 output rate of 100 kHz to approximately 1 kHz on average within a processing time of about 200 ms.

2.3.7 Computing resources

LHC detectors produce a huge amount of data, even if it is filtered with the triggers. Only in 2018, around 50 petabytes of data have been produced. Moreover, this data must be stored and easily retrieved by physicists from all over the world so that they can analyse it. CERN does not have the computing or financial resources to condense all of the data on the CERN site, so in 2002 a Grid computing network was created with the intention of sharing the lattice of computer centres around the world. This requires strong collaboration between CERN institutes to dispose massive storage facilities, global networking, immense computing power and funding.

As a result, the Worldwide LHC Computing Grid (WLCG) was born with a distributed computing infrastructure arranged in tiers providing to the CERN physicists community almost real-time access to LHC data.

WLCG is arranged in four layers, known as tiers: Tier 0, 1, 2 and 3, as Figure 2.15 shows. Each tier provides a specific set of services.

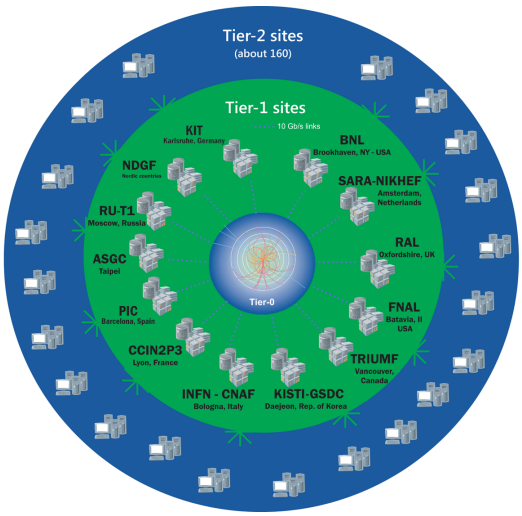

Figure 2.15: Schematic view of the computing WCLG system arranged in layers called Tiers. Tier 3 is not shown here.

There are two Tier 0 sites: one is located at CERN Data Centre and the other is located at the Wigner Research Centre for Physics in Budapest. All data from the LHC passes through the central CERN hub, but CERN provides less than 20% of the total compute capacity. Tier 0 sites are responsible for keeping the first copy of data (known as raw data), but also the first pass reconstruction, the distribution of raw data. Finally, the reconstruction output is passed to the Tier 1 centres, composed of thirteen large computer centres with sufficient storage capacity support for the Grid. They are responsible for full reconstruction of data and a proportional share of raw and reconstructed data. The corresponding output is distributed to Tier 2 centres. These centres are typically universities and other scientific institutes, which can store sufficient data and provide adequate computing power for specific analysis tasks. They handle analysis requirements and proportional share of simulated event production and reconstruction. There are currently around 160 Tier 2 sites.

Finally, Tier 3 centres are the ones that give to individual scientists access to these facilities through local computing resources, which can consist of local clusters in a home institute.

2.4 Object reconstruction

This section describes the procedures used to reconstruct, calibrate and select the physical objects (electrons, muons, jets, b-tagged jets and missing transverse momentum) required to identify events with a single top t-channel signature from the detector signals. These procedures follow recommendations of the top-quark reconstruction working group for data collected by the ATLAS detector in Run 2 during 2015–2017 [106].

2.4.1 Electrons

Electron candidates are reconstructed in the central region $|\eta| < 2.47$ from energy deposits in the EM calorimeter associated with ID tracks [107].

Several steps are followed: in the first place, clusters are formed around seeds using a clustering algorithm. A sliding window with size of 3×5 in units of 0.025×0.025 (in $\eta \times \phi$ space[2]) is used to search the electron cluster seeds. This is the so-called seed-cluster reconstruction. Next, pattern recognition and track fit is applied with the recorded ID hits. The obtained track candidates are then loosely matched to the EM clusters taking into account the energy-loss due to brehmstrahlung. Electron tracks are also required to be consistent with the beam spot within the requirements: $|d_0/\sigma(d_0)| < 5$ and $|\Delta z_0 \sin\theta| < 0.5$ mm, where d_0 and z_0 stands for the impact parameters and θ is the polar angle of the track (see Section 3.1.2 for the impact parameters definition). The candidate electrons are required to have transverse energy $E_{\mathrm{T}} > 15$ GeV.

Further requirements on the EM shower shape, calorimeter energy to tracker momentum ratio, and other discriminating variables are combined into a likelihood-based object quality requirement, optimised for strong background rejection. Specifically, three categories, based on a multi-variate likelihood, are available: `LooseLH`, `MediumLH`, and `TightLH`, in order of increasing background rejection power. Electron candidates in the analysis presented in this thesis must pass the `TightLH` selection to reject electrons from photon conversion, hadronic particle decays, and fake electrons.

Isolation criteria are also required in order to reject candidates coming from other sources than prompt W boson decays (hadrons faking an electron signature, heavy-flavour decays or photon conversions). This is achieved by applying cuts on the energy deposited in the calorimeter cells inside a cone of radius $\Delta R = 0.2$ around the electron candidate cluster. Additionally, cuts on the sum of transverse momentum of all tracks are applied to those tracks satisfying quality requirements, within a cone of $\Delta R = \min(0.2, 10)\mathrm{GeV}/E_T$, originating from the reconstructed primary vertex. To select such isolate electron candidates, a working point (known

[2]The $\eta \times \phi$ space of the EM calorimeters is divided into a grid of $N_\eta \times N_\phi = 200 \times 256$ elements of size 0.025×0.025 called towers. Inside each of these elements, the energy of cells in all longitudinal layers is summed into the tower energy.

as `Gradient`) has been defined so that the isolation is 90% efficient for electrons with $p_{\mathrm{T}} = 25$ GeV and 99% efficient for electrons with $p_{\mathrm{T}} = 60$ GeV.

The various efficiency measurements are based on the tag-and-probe method using $Z \to e^+e^-$ and $J/\Psi \to e^+e^-$ events. The efficiency to detect an electron is divided in four components, namely: reconstruction, identification, isolation and trigger. The differences between data and MC simulation have been incorporated into data-to-MC ratios as scale-factors, by combining both Z and J/Ψ measurements, as a function of the transverse energy and the pseudorapidity of the electrons. The scale-factors used in this analysis are based on the data sample collected in 2015. Figure 2.16 shows the combined electron reconstruction and identification efficiencies and data-to-MC ratios, as function of the transverse energy and pseudorapidity.

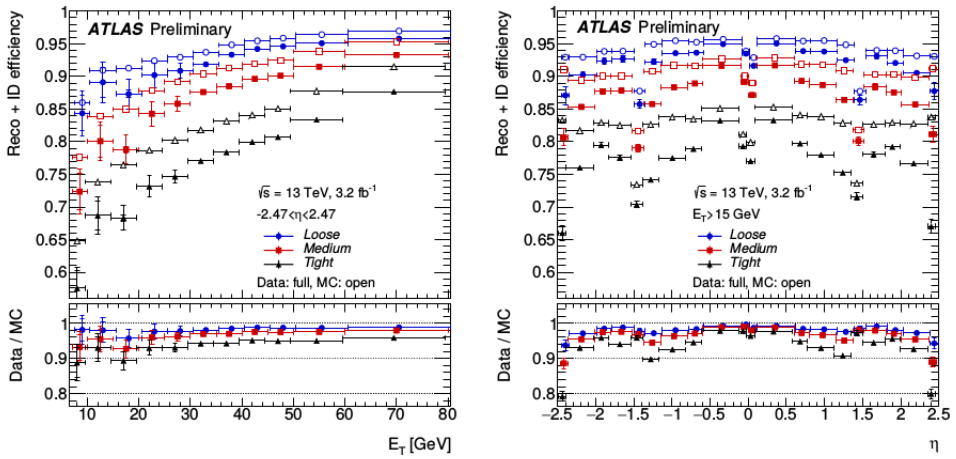

Figure 2.16: Combined electron reconstruction and identification efficiencies in $Z \to e^+e^-$ events as a function of the transverse energy E_T , integrated over the full pseudorapidity range (left), and as a function of pseudorapidity η integrated over the full E_T range (right). Figures extracted from Ref. [107].The data efficiencies are obtained using J/Ψ and Z tag-and-probe method. The ratio between data and MC efficiencies is used as a multiplicative correction factor for MC. The uncertainties are obtained with pseudo-experiments, treating the statistical uncertainties from the different (E_T, η) bins as uncorrelated. Two sets of uncertainties are shown: the inner error bars show the statistical uncertainty, the outer error bars show the combined statistical and systematic uncertainty.

2.4.2 Muons

Muon candidates are usually reconstructed combining the MS reconstruction with ID tracks [108]. Muon track candidates from the MS are built by simultaneosly fitting hits from segments in different layers, whereas the combined ID-MS muon reconstruction is performed according to various algorithms depending on which sub-detector are used in the reconstruction:

- Combined (CB) muon: a combined track is made up from a global refit that uses the hits from both the ID and the MS.
- Segment-tagged (ST) muons: an extrapolated ID track to the MS, with at least one local track segment in the MDT or CSC chambers of the MS. These are useful when muons cross only one layer of the MS, either because of their low p_T or because they fall in regions with reduced MS acceptance.
- Calorimeter-tagged (CT) muons: an extrapolated ID track matched to an energy deposit in the calorimeter compatible with a minimum-ionizing particle. These are useful because it recovers acceptance in a region of the MS which is only partially instrumented.
- Stand-alone (SA) or extrapolated muons (ME): the muon trajectory is reconstructed in this case with the MS track only, together with information of the impact parameters accounting for the energy loss of the muons in the calorimeters.

Various working points are provided: `Loose`, `Medium`, `Tight` and `High-`p_T depending on different muon identification selections. The muon candidates in the analysis presented in this thesis must pass the `Medium` identification definition, that uses only CB and ME tracks. Additionally, requirements on the compatibility between ID and MS momentum are loosely applied to get rid of fake muons. Furthermore, they must have $|\eta| < 2.5$ and $p_{\mathrm{T}} > 15$ GeV.

As in the case of electrons, isolation criteria are also required in order to reject muon candidates not originating from the decay of heavy particles, such as W, Z or Higgs bosons. Two isolation variables are used: a track-based isolation variable and a calorimeter-based isolation variable. The track-based isolation variable is defined as the sum of transverse momentum of all tracks with $p_T > 1$ GeV, within a cone of $\Delta R = \min(0.3, 10)\mathrm{GeV}/p_T^{\mu}$, around the muon transverse momentum p_T^{μ} excluding the muon track itself. The calorimeter-based isolation variable is defined as the sum of transverse energy of topological clusters in a cone of size $\Delta R = 0.2$ around the muon candidate. In order to select isolated muon candidates, a working point (known as `Gradient`) has been defined so that the isolation is 90% efficient for muons with $p_{\mathrm{T}} = 25$ GeV and 99% efficient for muons with $p_{\mathrm{T}} = 60$ GeV, considering the two isolation variables.

Similarly to the electrons, the various efficiency measurements are based on the tag-and-probe method using $Z \to \mu^+\mu^-$ and $J/\Psi \to \mu^+\mu^-$ events. The differences between data and MC simulation have been incorporated into data-to-MC ratios as scale-factors, by combining both Z and J/Ψ measurements, as a function of the transverse energy and the pseudorapidity of the electrons. The scale-factors are used in all ATLAS analyses based on the data sample collected in 2015. Figure 2.17 shows the muon reconstruction efficiencies and data-to-MC ratios, as function of the pseudorapidity and transverse energy.

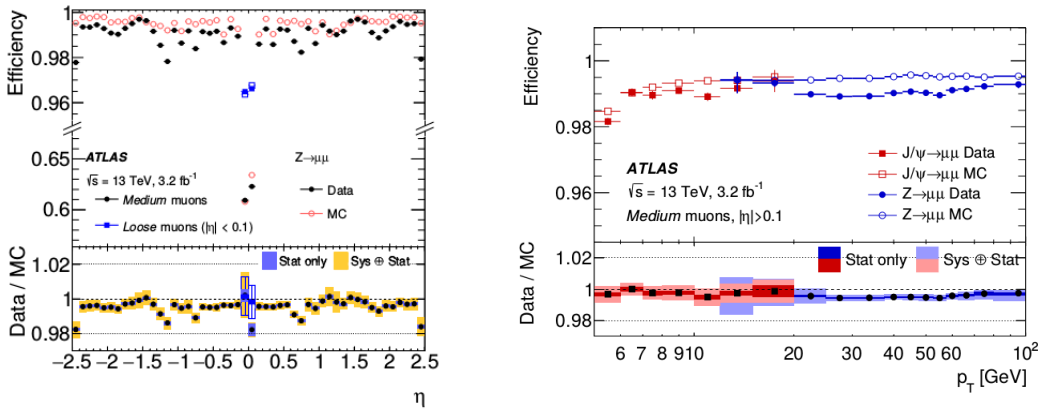

(a) (b)

Figure 2.17: Muon reconstruction efficiency as a function of η (left) measured in $Z \to \mu^+\mu^-$ events for muons with $p_T > 10$ GeV for medium muon selection. Reconstruction efficiency for the medium muon selection as a function of the p_T of the muon (right), in the region $0.1 < |\eta| < 2.5$ as obtained with $Z \to \mu^+\mu^-$ and $J/\Psi \to \mu^+\mu^-$ events. Panels at the bottom show the ratio of the measured to predicted efficiencies, with statistical and systematic uncertainties. Figures extracted from Ref. [108].

Finally, muon tracks are also required to be consistent with the beam spot applying the requirements: $|d_0/\sigma(d_0)| < 3$ and $|\Delta z_0 \sin\theta| < 0.5$ mm.

2.4.3 Jets

Jets are reconstructed from topological calorimeter clusters [109] at the EM scale using the anti-k_t algorithm [110] with radius parameter of 0.4. The topological clusters used as input by the anti-k_t algorithm are built from neighboring calorimeter cells containing significant energy (above a noise thresold estimated from measurements of calorimeter electronic noise).

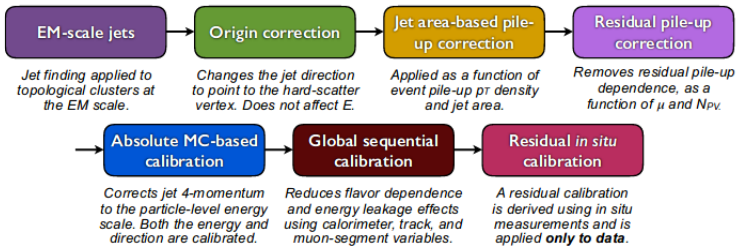

Figure 2.18: Summary of the calibration stages for EM-scale jets. Extracted from Ref. [111].

Figure 2.18 shows an overview of the ATLAS calibration scheme for EM calorimeter jets. First, the origin correction recalculates the four-momentum of jets in order

to point to the hard-process primary vertex, instead of the center of the detector. Next, the pile-up correction removes the excess of energy due to the in-time and out-of-time pile-up (consisting of an area-based p_T density substraction and a residual correction derived from MC simulation). The absolute jet energy scale calibration corrects the jet momentum to the particle-level energy scale, using truth dijet events. Further improvements are applied on the global sequential calibration, to the reconstructed energy and related uncertainties using information from the calorimeter, MS and track-based variables. Finally, a residual ***in-situ*** calibration is applied to correct jets in data using well-measured objects, e.g. photons, Z bosons and calibrated jets.

To suppress jets from in-time pileup, the jet-vertex-tagger (JVT) discriminant, which is based on a two-dimensional likelihood method, is used [112]. A JVT value of at least 0.59 is required for jets with $p_{\mathrm{T}} > 60$ GeV and $|\eta| < 2.4$, corresponding to an efficiency of 92% and a fake rate of 2%. In order to reject forward jets originating from additional proton-proton interactions, a forward-jet-vertex-tagger (fJVT) requirement is applied. This combines information about jet shapes and topological jet correlations in pile-up interactions, in order to maximise the number of selected jets coming from the hard scattering and reduce pileup jets contamination. Jets with $|\eta| > 2.5$ are required to pass the requirements of the fJVT `Medium` working point. This has an efficiency of selecting hard scattered jets of up to 97% and a pileup-jet efficiency of 53.4% for jets with p_{T} between 40 GeVand 50 GeV [113].

The final calibration of the jet energy scale includes a set of 80 systematic uncertainties (from which 29 are used in the analysis presented in this thesis). They are propagated from the individual calibration studies and are usually derived in specific regions of jet p_T and η [111]. The full combination of all uncertainties on the jet energy scale is displayed in Figure 2.19, assuming a quark-gluon composition taken from the inclusive MC dijet selection. The full set of uncertanties is reduced to a set of nuisance parameters (NPs), that has been made available in such a way that preserves as precisely as possible the correlation across jet p_T and η.

2.4.4 Identification of b-tagged jets

Jets originating from the fragmentation of b-quarks (referred as b-tagged jets, b-quark jets or simply b-jets) are identified by reconstructing secondary and tertiary vertices from the tracks associated to the jets and by combining their spatial parameters with lifetime-related information. This is because b-flavoured hadrons have a relatively long lifetime resulting in a significant flight path length which leads to measurable secondary or even tertiary vertices and impact parameters of the decay products. Different algorithms have been developed to identify b-jets exploiting several characteristics:

- Impact parameter-based algorithms: these methods make use of the transverse and longitudinal impact parameters significances. Likelihood templates are used to define the ratios of b, c and light-flavour jet hypotheses, and

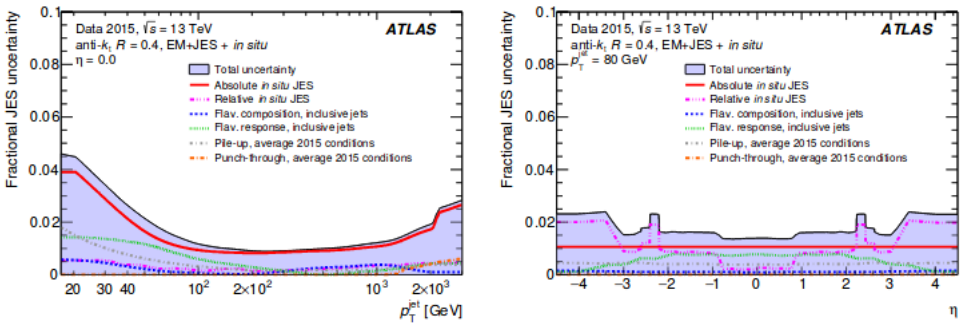

Figure 2.19: Combined uncertainty in the jet energy scale of fully calibrated jets as a function of jet p_T at $\eta = 0$ (left) and η at $p_T = 80$ GeV (right), extracted from Ref. [114]. Systematic uncertainty components include pile-up, punch-through, and uncertainties propagated from the in situ jet energy scale. The flavor composition and response uncertainties assume a quark and gluon composition taken from Pythia dijet MC simulation.

later combined in three logarithmic likelihood ratio discriminants. IP3D is the b-tagging baseline method, although methods employing neural networks to learn the dependencies between the variables are also available (such as IPRNN).

- Secondary vertex-based algorithms: they are based on the topology of the tracks associated to jets. In the SV1 algorithm, a secondary vertex is reconstructed from the accepted tracks candidates consisting of two-track vertices. Tracks are rejected if they form a secondary vertex originated from long-lived particles (beyond a B hadron), photon conversions or hadronic interactions with the detector material. The JetFitter algorithm reconstructs the topological vertex structure of heavy hadron decays inside a jet. It is based on a Kalman filter algorithm.

- Soft Muon tagger algorithms: it is based on the reconstruction of muons coming from semileptonic decays of heavy-flavor hadrons. It provides a useful complement to impact parameter-based and vertex-based taggers for jets with semileptonic decays.

In the analysis of this thesis, jets containing b-hadrons are identified and tagged as b-jets using the `MV2c` multivariate tagging algorithm [115]. In particular, the `MV2c10` variant is used. This algorithm is based on a Boosted Decision Tree (BDT) that combines the output of the low-level taggers JetFitter, IP3D and SV1 algorithms, previously described. The background sample used in the training of the BDT is composed of 7% of c-jets and 93% of light flavor jets.

The `MV2c10` algorithm is calibrated by measuring b-jet efficiency [116, 117] and the mis-tagging rates for c [118] and light-flavour [119] jets in data. It also benefits

from a re-optimisation ahead of the 2017 Run-2 data taking, improving the b-jet identification as well as the c- and light-flavoured jet rejections.

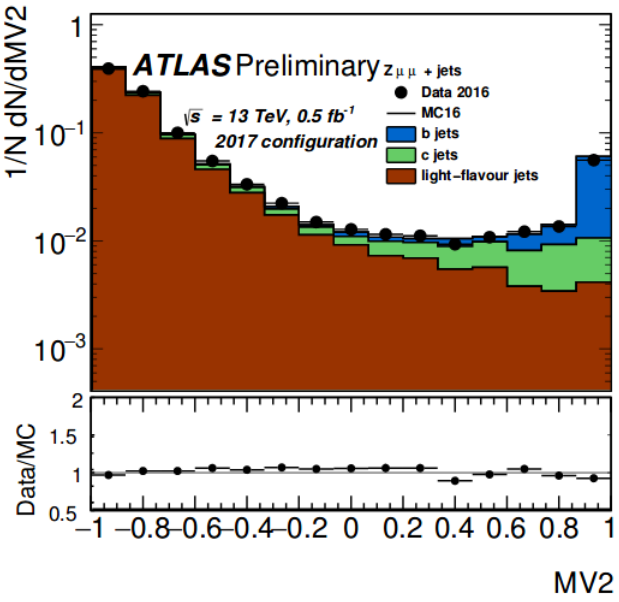

Figure 2.20: Data-MC comparison of the MV2 algorithm BDT output of the 2017 configuration using a Z+jets dominated sample. Figure extracted from Ref. [115].

The MV2c algorithm assigns to each jet a b-tagging output ranging from -1 to 1, as Figure 2.20 shows. Different working points (WPs) can be defined according to the desired b-tagging efficiency by requiring a minimum thresold on the MV2c10 output. The threshold value applied to the MV2c10 output in the analysis presented on this thesis corresponds to a b-tagging efficiency of 60%.

2.4.5 Missing transverse momentum

The missing transverse momentum, with magnitude $E_{\mathrm{T}}^{\mathrm{miss}}$, although not directly measured, can be inferred because in the transverse plane to the beam axis the transverse momentum of all particles in the final state of the collision should be zero. Any imbalance corresponds to the $E_{\mathrm{T}}^{\mathrm{miss}}$ and it indicates the presence of neutrinos in the final state. Such imbalance depends strongly on the energy scale and resolution of the reconstructed objects. The $E_{\mathrm{T}}^{\mathrm{miss}}$ is reconstructed from the negative vector sum of energy deposits of all detected particles in the calorimeter projected onto the transverse plane [120, 121].

$$E_{x(y)}^{miss} = E_{x(y)}^{e} + E_{x(y)}^{\gamma} + E_{x(y)}^{\tau} + E_{x(y)}^{jets} + E_{x(y)}^{\mu} + E_{x(y)}^{soft}. \tag{2.6}$$

Calorimeter signals are associated with the reconstructed objects shown in Equation 2.6, that is: electrons, photons, hadronically decaying tau leptons, jets and

muons. Those reconstructed signal objects not passing the corresponding object selection cuts are grouped into a soft term. These can be ID tracks (track-based soft term) or calorimeter signals (calorimeter-based soft term). During Run 2, ATLAS has based the $E_{\mathrm{T}}^{\mathrm{miss}}$ reconstruction upon the track-based soft term (TST). The TST term requires tracks that can be associated to the primary vertex. Tracks overlapping with electron or photon clusters in the calorimeter are removed. The soft term is included in order to account for low-momentum particles that are not identified among the final state objects [122].

The magnitude and azimuthal angle of the $E_{\mathrm{T}}^{\mathrm{miss}}$ are computed from its x and y components:

$$E_T^{miss} = \sqrt{(E_x^{miss})^2 + (E_y^{miss})^2} \tag{2.7}$$

$$\phi^{miss} = \arctan\left(\frac{E_x^{miss}}{E_y^{miss}}\right) \tag{2.8}$$

The $E_{\mathrm{T}}^{\mathrm{miss}}$ is taken as a measurement of the energy carried away by undetectable particles. Within the SM, the $E_{\mathrm{T}}^{\mathrm{miss}}$ is a direct measurement of neutrinos. Moreover, a large $E_{\mathrm{T}}^{\mathrm{miss}}$ is a well-known feature of many SUSY and extra-dimensions searches. Therefore, a precise measurement of the $E_{\mathrm{T}}^{\mathrm{miss}}$ is capital.

The $E_{\mathrm{T}}^{\mathrm{miss}}$ can be affected by energy losses due to detector inefficiencies and acceptance, and by energy resolution too. The $E_{\mathrm{T}}^{\mathrm{miss}}$ performance is usually checked using $Z \to \mu^+\mu^-$ events since the final state is ideal for such purpose. This is mainly because of the small background of this channel and precise measurement of the kinematics of the Z boson. $W \to e\nu$ events is also used because it provides high-p_T neutrinos from the hard-scatter interaction. Therefore, it is useful to validate the scale and direction of the reconstructed $E_{\mathrm{T}}^{\mathrm{miss}}$. Finally, $t\bar{t}$ events provide a topology with many jets and thus it is useful to check the robustness of the $E_{\mathrm{T}}^{\mathrm{miss}}$ reconstruction in multijet environments. Figure 2.21 shows the soft term of the $E_{\mathrm{T}}^{\mathrm{miss}}$ distribution for $Z \to \mu^+\mu^-$ events built with the TST method. Good data-MC agreement is observed.

2.4.6 Overlap removal

Overlap removal is a technique performed with the purpose of avoiding misidentification between the reconstructed objects. Depending on the kind of reconstructed object misidentified as another, several approaches are applied:

- Muons misidentified as electrons: An electron sharing a track with a muon is removed to avoid cases where a muon mimics an electron through radiation of a hard photon.

- Electrons misidentified as jets: Jets overlapping with selected electron candidates within an η–ϕ cone of size $\Delta R = 0.2$ are removed from the event to

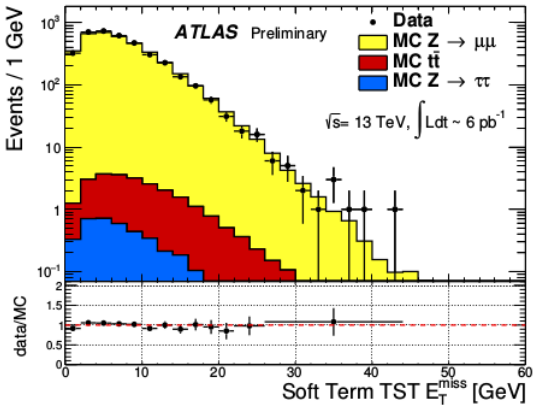

Figure 2.21: Distributions of soft term for TST $E_{\mathrm{T}}^{\mathrm{miss}}$ in $Z \to \mu\mu$ events in yellow. The expectation from MC simulation is superimposed and normalized to data, after each MC sample is weighted with its corresponding cross-section. Figure extracted from Ref. [122].

reduce the fraction of electrons being reconstructed as jets. If a remaining jet with $p_{\mathrm{T}} > 25$ GeV is found close to an electron within a cone of radius $\Delta R = 0.4$, then the electron is discarded in order to reduce backgrounds from non-prompt, non-isolated electrons coming from heavy-flavour hadron decays. This is also motivated because the electron efficiency corrections are only valid for $\Delta R > 0.4$.

- Jets misidentified as muons: Jets with fewer than three tracks originating from the primary vertex and distance $\Delta R < 0.4$ from a muon are then removed to reduce fake jets from muons depositing energy in the calorimeters. Finally, muons with a distance $\Delta R < 0.4$ from any of the surviving jets are removed as well, in order to avoid contamination of non-prompt muons from heavy-flavour hadron decays.

2.4.7 Triggers

The ATLAS event trigger system consists of hardware-based L1 trigger and software-based HLT as already mentioned in Section 2.3.6 .The analysis on this thesis uses single-lepton triggers to select the single top-quark t-channel signature.

The electron triggers select a calorimeter cluster matched to a track. Electrons must then satisfy identification criteria based on a multivariate technique using a likelihood (LH) discriminant. In 2015, electrons are triggered by requiring at L1 a transverse energy deposit E_{T} above 20 GeV, with a reduced calorimetric granularity at this stage. At the HLT, the full granularity of the calorimeter as well as tracking information are available and the reconstructed calorimeter cluster is matched to a track. The trigger electron object is then required to be isolated with medium identification and to have $E_{\mathrm{T}} > 24$ GeV. In 2016 and 2017 data, electrons had

to satisfy a tight identification at HLT together with an isolation criteria and were required to have $E_{\mathrm{T}} > 26$ GeV. During these years, to avoid efficiency losses due to identification and isolation at high p_{T}, two additional triggers were also available, selecting medium electrons with $E_{\mathrm{T}} > 60$ GeV at HLT and selecting loose electrons (i.e. without isolation requirement) with $E_{\mathrm{T}} > 120$ GeV (140 GeV in 2016 and 2017).

Muons are selected at the trigger level by matching tracks reconstructed in the Muon Spectrometer and in the Inner Detector. In 2015, muons had to satisfy a loose isolation requirement and have $p_{\mathrm{T}} > 20$ GeV. In 2016 and 2017, the isolation criterion was tightened and the threshold increased to $p_{\mathrm{T}} > 26$ GeV. During these years, to avoid efficiency losses due to isolation at high p_{T}, another muon trigger without any isolation requirement was available, selecting loose muons with $p_{\mathrm{T}} > 50$ GeV.

Chapter 3

Alignment of the ATLAS Inner Detector

The ATLAS track reconstruction system (Inner Detector or ID) aims for a precise and bias-free determination of the track parameters. The intrinsic precision of the sensor elements (Pixel, SCT modules and TRT wires) is quite good. But in order to achieve a good resolution one needs to know very precisely the actual position and orientation of the detectors and its possible changes in time. The ATLAS ID indeed has a nominal position for each of the alignable structures: surveys were done for all the different sensing devices when assembling and installing them in the ATLAS cavern. Nevertheless, the real geometry of the ID during data-taking may suffer from alterations because uncertainties can be introduced when assembling, installing and also during the operation of the detector (as a result of changes in temperature of the cooling system, ramping of magnetic field,...).

Despite all these factors, the detector is not physically accessible during data taking. Therefore performing corrections directly to each sensor every time that it moves is unfeasable. On the other hand, if no correction was performed to the ID, the reconstructed tracks of particles detected by the ID would suffer from a degradation of the track parameters (in the least of the cases), and/or introduce biases in the track parameters. Almost all physics analyses that are carried out within the ATLAS experiment rely on particle reconstruction and identification algorithms: b-tagging algorithms, primary and secondary vertex finders and lepton reconstruction are just a few of them that need an excellent track reconstruction. Using only devices with both high granularity and resolution in the ID is not enough to insure the measurements of physical quantities are as precise as possible. In addition a good calibration of the detector is needed to fully exploit the capabilities of the ID.

Consequently the availability of an algorithm that is able to determine the real position of the ID sensors and also to follow the eventual changes that happen during data taking is crucial. This is the primordial task of the ID alignment. This

chapter describes briefly the basics of the ID alignment procedure and the strategy that was followed during the Run 2.

3.1 ID alignment basics.

3.1.1 The ATLAS coordinate systems

The most relevant ATLAS frames for the ID alignment are the Global coordinate system (useful to define the position of each module in the detector) and the local coordinate system (useful to locate the hits recorded by the sensors). Both coordinate systems are depicted in Figure 3.1.

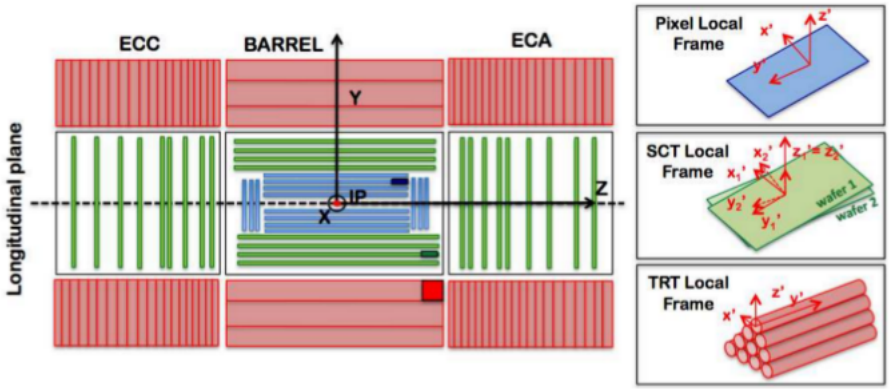

Figure 3.1: Left: Schematic view of the inner detector in the longitudinal plane. Pixels are represented in blue, the SCT in green and the TRT in red. The global coordinate system is defined at the centre of the detector. Right: Local coordinate frames are shown for different module sensors of the Pixels (up), SCT (middle) and TRT (down).

Global coordinate system

The global coordinate system (X, Y, Z) (see left Figure 3.1) is a right-handed Cartesian coordinate system with origin at the nominal interaction of the p-p collisions whose axes are defined as follows: the Z axis is defined along the beam direction in such a way that positive direction coincides with the solenoid magnetic field direction. The positive X direction is taken towards the centre of the LHC ring, while the positive Y directions points to surface of the Earth.

Local coordinate system

The local coordinate system, referred in right Figure 3.1 as (x', y', z'), is also a right-handed Cartesian system defined for each module. The origin is always taken at the centre of the considered module and the x' axis always points along the most sensitive direction of the module. Depending on the module, the axes are defined in different ways:

- In the Pixels modules (including IBL), x' and y' are defined within the detector plane. The x' direction points to the short side of the module, while y' points to the long side of the module, being the less precise direction.
- In the SCT modules, the local coordinate system is defined analagously as it is done in the Pixels, however this definition is not so straight-forward to apply because the SCT modules are sensitive in the two micro-strips wafers that are assembled back-to-back. Hence, two local coordinate systems are used instead in order to reconstruct the SCT hit. The x' and y' directions are defined within the detector plane. While the x' direction is perpendicular to the strips, the y' direction runs along the strips.
- In the TRT straws, x' points along the global $R\phi$ and it is associated to the radial distance of the track to the center of the straw, while y' runs along the wire direction.

The hits recorded by each of the itemized sub-systems in the corresponding local coordinate systems are finally used to reconstruct the tracks.

3.1.2 Track parameters

Tracks are the helical trajectories that particles describe inside the ATLAS magnetic field and can be recognized as long as sufficient hits are recorded in the ID sensors. This information is used to reconstruct the tracks and in order to distinguish them, track parameters are used. The track representation that ID alignment makes use consists of 5 parameters $\boldsymbol{\pi} = (d_0, z_0, \phi_0, \theta, q/p)$ and it is depicted in Figure 3.2.

All parameters are defined with respect to the perigee, which is the point of the closest approach of the track to the Z axis of the global coordinate system. In this representation, the transverse impact parameter d_0 is defined in the XY plane and takes the positive sign when the direction of the longitudinal component of the angular momentum is negative in z. While, the longitudinal impact parameter z_0 coincides with the z-coordinate of the perigee and it has the same sign. ϕ_0 and θ_0 are the azimuthal and the polar angle in the XY plane, respectively. And finally, the q/p parameter (where q is the charge of the particle and p its momentum) gives information about the curvature of the track.

In order to achieve the ATLAS physics goals, the degradation of the track parameters due to ID alignment should not deteriorate the resolution of the track

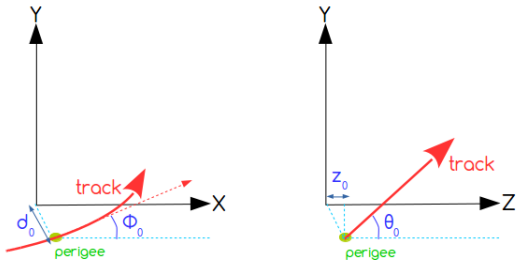

Figure 3.2: Track parameters representation in the transverse plane (left) and longitudinal plane (right).

parameters by more than 20% with respect to the intrinsic track resolution. In terms of nominal values, this means that the precision in which the silicon modules are known has to be better than 10 μm. In addition, ID alignment should correct for systematic effects that could bias the track parameters knowledge.

3.1.3 Residuals

In order to perform the reconstruction in the ID of a charged particle track, the hits recorded by each module of the tracking system are used[1]. However, as previously discussed, modules can move during data-taking and therefore performing such track reconstruction without knowing the real module location, may not be accurate enough (see Figure 3.3 to have an schematic view of the problem).

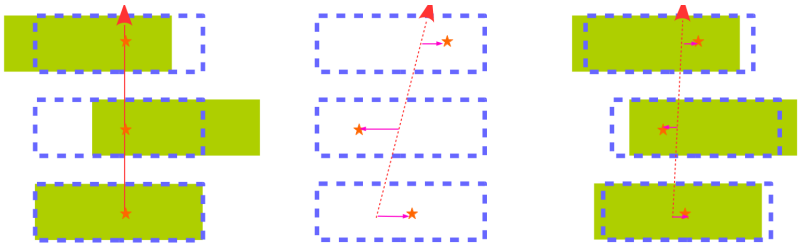

Figure 3.3: Schematic view of the alignment process. The left panel shows the real track (red line) using the installed detector geometry (green box). The apparent position (dashed blue line) is also shown. The central panel shows the reconstructed track using the apparent detector position. Finally, the right panel shows the reconstructed track obtained after the detector alignment. Initial and residual misalignment residuals are represented in pink lines.

In order to determine the modules location and to follow their eventual changes in time, the alignment method relies on the computation of the residuals, which are

[1]Hits are generated by the particles that crosses each module of the Inner Detector. The signal recorded in the pixels/strips of the Pixels systems is cluster-like, while in the TRT is drift-like.

the distance between a hit as recorded in the sensor and the extrapolation point of the reconstructed track in the sensor. Thus, we can put this mathematically as:

$$\mathbf{r} = \mathbf{m} - \mathbf{e}(\boldsymbol{\pi}, \mathbf{a}), \tag{3.1}$$

where $\mathbf{m}$ is the position of the measured hit and $\mathbf{e}$ is the intersection point in the sensor of the reconstructed track, which depends on how the track is defined, i.e. the vector of track parameters ($\boldsymbol{\pi}$) and on the corrections applied to the modules, i.e. the alignment parameters ($\mathbf{a}$)[2].

As residuals are defined in Equation 3.1, one can assess the alignment quality of the detector: residuals distributions (builded with all the recorded hits on all tracks) of a certain perfectly aligned detector are centred at zero and have a width corresponding to the specific detector and coordinate. Consequently a mandatory feature of the final set of alignment parameters is to produce centred and narrow residual distributions.

3.2 Track-based alignment

The default alignment procedure is based on the minimisation of the track-to-hit residuals for each module. Every sensor or mechanical assembly part is then considered as an alignable structure, which is treated as a rigid body with six degress of freedom (DoF) that uniquely define its position and orientation in space. These six DoF are three translations (T_x, T_y, T_z) of the centre of the object and three rotations (R_x, R_y, R_z) around the Cartesian axes and are referred to as the alignment parameters. The *alignment parameters* obtained in this minimisation of the track-to-hit residuals process are those that correspond in the description of the real geometry of the detector and will be used as *corrections* to the assumed position of each module [3].

The minimisation of the track-to-hit residuals is performed by means of minimising the χ^2 function that is referred in Equation 3.2:

$$\chi^2 = \sum_t \sum_h \left(\frac{r_{t,h}(\boldsymbol{\pi}, \mathbf{a})}{\sigma_h} \right)^2, \tag{3.2}$$

where all reconstructed tracks (denoted as t) and all recorded hits associated to each track (denoted as h) are used. The residual of each hit associated to each track is represented by $r_{t,h}$ and σ_h is the hit uncertainty.

It is convenient to write Equation 3.2 in a more compact way using matrices:

$$\chi^2 = \sum_t \mathbf{r_t}(\boldsymbol{\pi}, \mathbf{a})^T \, V^{-1} \, \mathbf{r_t}(\boldsymbol{\pi}, \mathbf{a}), \tag{3.3}$$

[2]The alignment parameters (also called corrections) are defined in Section 3.2.

[3]Not only alignment parameters can be referred as corrections, also they are often referred as *alignment constants*, specially in the context of the implementation of the alignment algorithm.

where $\mathbf{r_t}$ is the residual vector for each track and V is the covariance matrix of the detector measurements containing the hit uncertainties[4].

The χ^2 function has a minimum in the spatial configuration which corresponds to the real geometry of the detector. In order to find such geometry, one needs to derive with respect to the alignment parameters:

$$\frac{d\chi^2}{d\mathbf{a}}|_{\mathbf{a}=\mathbf{a_0}} = 2\sum_t \left(\frac{d\mathbf{r_t}(\boldsymbol{\pi},\mathbf{a})}{d\mathbf{a}}|_{\mathbf{a}=\mathbf{a_0}}\right)^T V^{-1}\,\mathbf{r_t}(\boldsymbol{\pi},\mathbf{a_0}) = 0, \tag{3.4}$$

where $\mathbf{a_0}$ is the vector of the alignment parameters which describes the initial detector geometry.

On the other hand, taking into account the dependences of the χ^2 function we arrive at:

$$\frac{d\chi^2}{d\mathbf{a}} = \boxed{\frac{d\boldsymbol{\pi}}{d\mathbf{a}}}\frac{\partial\chi^2}{\partial\boldsymbol{\pi}} + \frac{\partial\chi^2}{\partial\mathbf{a}}. \tag{3.5}$$

From the previous equation, a key point is now visible: not only the residuals depend on the track parameters and alignment parameters, but the red-squared box from previous equation shows that the track parameters depend on the alignment parameters too. This important feature is what distinguishes the two different approaches that alignment uses:

- Global χ^2 [123] : it is the general case in which $\frac{d\boldsymbol{\pi}}{d\mathbf{a}} \neq 0$ and it assumes that the track parameters depend on the alignment parameters. Thus, the minimisation of the χ^2 function is performed simultaneously for all tracks by accounting for all the correlations between the modules that participate in the reconstruction of the same track.

- Local χ^2 [124] : it is a particular case of the global χ^2 method in which one can take $\frac{d\boldsymbol{\pi}}{d\mathbf{a}} = 0$. This means that in the minimisation of the χ^2 function only the information contained in a particular module is used, leaving all the others fixed.

3.2.1 Global χ^2 alignment

For the sake of generality, we will proceed with the Global χ^2 method in the computation of the minimisation of the χ^2 function. Nevertheless, before finding the alignment parameters the track-based alignment method needs to identify the tracks that are used in the residuals. Therefore, the track parameters $\boldsymbol{\pi}$ need to be computed

[4] In general V is not a diagonal matrix because of the contribution of the Multiple Coulomb Scattering, which correlates the previous module with the next one in the particle trajectory inside the detector with the scattering angle. If no correlations are considered between the different modules, then the covariance matrix is diagonal.

for every track with an arbitrary or assumed geometry $\mathbf{a_0}$. This is based on the consideration that the alignment parameters are common to all reconstructed tracks and that the alignment parameters do not depend on the track parameters (i.e. $\frac{d\mathbf{r}}{d\boldsymbol{\pi}} = \frac{\partial \mathbf{r}}{\partial \boldsymbol{\pi}}$).

$$\frac{d\chi^2}{d\pi}|_{\pi=\tilde{\pi}} = 2\sum_t \left(\frac{d\mathbf{r_t}(\tilde{\boldsymbol{\pi}}, \mathbf{a_0})}{d\boldsymbol{\pi}}\right)^T V^{-1}\, \mathbf{r_t}(\tilde{\boldsymbol{\pi}}, \mathbf{a_0}) = 0, \tag{3.6}$$

where we have used the Equation 3.3 when applying the minimisation condition.

The solution around the minimum can be expanded through a Taylor's expansion considering an initial set of track parameters $\boldsymbol{\pi_0}$ satisfying that:

$$\tilde{\boldsymbol{\pi}} = \boldsymbol{\pi_0} + \delta(\boldsymbol{\pi}), \tag{3.7}$$

where $\delta(\boldsymbol{\pi})$ are the corrections to be applied on the assumed track parameters.

Therefore the residuals can be written as:

$$\mathbf{r} = \mathbf{r}(\boldsymbol{\pi_0}, \mathbf{a_0}) + \frac{d\mathbf{r_t}(\boldsymbol{\pi}, \mathbf{a_0})}{d\boldsymbol{\pi}}|_{\boldsymbol{\pi}=\boldsymbol{\pi_0}}\delta(\boldsymbol{\pi}), \tag{3.8}$$

where only terms up to first order have been considered in the Taylor's expansion (higher terms are neglected).

Inserting Equation 3.8 into Equation 3.6 one achieves the following corrections to the initial set of track parameters:

$$\delta\boldsymbol{\pi} = -\left[\left(\frac{d\mathbf{r}}{d\boldsymbol{\pi}}\right)^T V^{-1}\left(\frac{d\mathbf{r}}{d\boldsymbol{\pi}}\right)\right]^{-1}\left[\left(\frac{d\mathbf{r}}{d\boldsymbol{\pi}}\right)^T V^{-1}\mathbf{r}(\boldsymbol{\pi_0}, \mathbf{a_0})\right], \tag{3.9}$$

being $\frac{d\mathbf{r}}{d\boldsymbol{\pi}} = \frac{d\mathbf{r}(\boldsymbol{\pi}, \mathbf{a_0})}{d\boldsymbol{\pi}}|_{\boldsymbol{\pi}=\boldsymbol{\pi_0}}$.

In this manner we have found a set of track parameters $\tilde{\boldsymbol{\pi}}$ that accurately describe the reconstructed track and it is possible at this stage to find the set of alignment parameters that define the corrections to the assumed geometry. To that purpose, we will compute the alignment parameters corrections $\delta\mathbf{a}$ considering a set of initial alignment parameters $\mathbf{a_0}$ (in a analagous way to the track fitting procedure) close to the minimum condition, such that $\tilde{\mathbf{a}} = \mathbf{a_0} + \delta\mathbf{a}$. Therefore the residual in the alignment parameters configuration can also be written as a Taylor's expansion around the minimum of the χ^2 function as :

$$\mathbf{r} = \mathbf{r}(\tilde{\boldsymbol{\pi}}, \mathbf{a_0}) + \frac{d\mathbf{r_t}(\tilde{\boldsymbol{\pi}}, \mathbf{a})}{d\mathbf{a}}|_{\mathbf{a}=\mathbf{a_0}}\delta(\mathbf{a}), \tag{3.10}$$

Inserting Equation 3.11 into Equation 3.4 one has:

$$\mathbf{r} = \mathbf{r}(\tilde{\boldsymbol{\pi}}, \mathbf{a_0}) + \frac{d\mathbf{r_t}(\tilde{\boldsymbol{\pi}}, \mathbf{a})}{d\mathbf{a}}|_{\mathbf{a}=\mathbf{a_0}}\delta(\mathbf{a}). \tag{3.11}$$

Therefore substituting the latter equation into Equation 3.4, we reach to the following relationship:

$$\delta\mathbf{a} = -\left[\left(\frac{d\mathbf{r}}{d\mathbf{a}}\right)^T V^{-1}\left(\frac{d\mathbf{r}}{d\mathbf{a}}\right)\right]^{-1}\left[\left(\frac{d\mathbf{r}}{d\mathbf{a}}\right)^T V^{-1}\mathbf{r}(\tilde{\boldsymbol{\pi}}, \mathbf{a_0})\right], \tag{3.12}$$

where we define the alignment matrix $\mathcal{M}_a$ and vector $\mathbf{v}_a$ as:

$$\mathcal{M}_a = \left[\left(\frac{d\mathbf{r}}{d\mathbf{a}}\right)^T V^{-1}\left(\frac{d\mathbf{r}}{d\mathbf{a}}\right)\right] \quad ; \quad \mathbf{v}_a = \left[\left(\frac{d\mathbf{r}}{d\mathbf{a}}\right)^T V^{-1}\mathbf{r}(\tilde{\boldsymbol{\pi}}, \mathbf{a_0})\right]. \tag{3.13}$$

Equation 3.14 can be re-written in these terms, so it becomes:

$$\delta\mathbf{a} = -\mathcal{M}_a^{-1}\mathbf{v}_a. \tag{3.14}$$

It is clear now that the final solution $\tilde{\mathbf{a}} = \mathbf{a_0} + \delta\mathbf{a}$ for the alignment parameters is obtained after inverting the alignment matrix. This matrix relies in the first place, on the calculation of the first partial derivatives of the residuals with respect to the track parameters (track fitting) with an assumed fixed geometry. In the second place it relies on the calculation of the first partial derivatives of the residuals with respect to the alignment parameters, once each track has been fitted. We can as well take profit of the fact that the filling of the the alignment vector $\mathbf{v}_a$ and alignment matrix $\mathcal{M}_a$ are independent from the inversion of the alignment matrix $\mathcal{M}_a$. That is why the procedure to align the ATLAS ID is split in two steps:

- **Accumulation**: this is the step that takes care of reconstructing the registered tracks supposing an initial geometry. Once tracks are reconstructed, the alignment matrix and vector are computed. For that purpose, one needs to calculate the derivatives of the residuals with respect to the track parameters and with respect to the alignment parameters. The tracks that are used for the reconstruction can be selected in different ways depending on the needs for the alignment.
- **Solving**: in this final step the alignment matrix is inverted in order to find the alignment corrections from Equation 3.14.

However, there is still one important point to highlight, namely that the initially supposed alignment parameters might not be always close to the actual ones, as we have considered previously to derive the alignment parameters. Therefore, the alignment computation makes use of an iterative procedure, such that the corrections $\delta\mathbf{a}$ obtained in the final check of n-th iteration:

$$\mathbf{a_N} = \mathbf{a_{N-1}} + \delta\mathbf{a}, \tag{3.15}$$

are negligible.

It is important to point out that the size of the alignment matrix can range in a very different interval, depending on the alignable structures or modules considered. The Global χ^2 method, as previously mentioned, correlates all the alignable structures that are crossed by the same track, so in general it is preferred. On the other hand, this feature makes that alignment matrix becomes denser and denser when we start to align smaller objects. This fact might be translated in a CPU consumption time too and in this case the rounding errors can be significant. Therefore Global χ^2 is practical when aligning big structures, as for example the whole SCT barrel or end-caps or its individual layers.

3.2.2 Local χ^2 alignment

An alternative way to compute the alignment corrections that simplifies tha handling of the big matrices is the so-called local χ^2 alignment. The way to proceed in this particular case is to discard the correlations between all the modules or mathematically:

$$\frac{d\boldsymbol{\pi}}{d\mathbf{a}} = 0. \tag{3.16}$$

By substituting the latter equation in Equation 3.5, the minimisation condition from Equation 3.4 is reduced to:

$$\frac{d\chi^2}{d\mathbf{a}} = \sum_t \left(\frac{\partial \mathbf{r_t}(\boldsymbol{\pi}, \tilde{\mathbf{a}})}{\partial \mathbf{a}} |_{\mathbf{a}=\tilde{\mathbf{a}}} \right)^T V^{-1}\, \mathbf{r_t}(\boldsymbol{\pi}, \tilde{\mathbf{a}}) = 0, \tag{3.17}$$

This implies that the big alignment matrix and big alignment vector becomes:

$$\mathcal{M}_a = \left[\left(\frac{\partial \mathbf{r}}{\partial \mathbf{a}} \right)^T V^{-1} \left(\frac{\partial \mathbf{r}}{\partial \mathbf{a}} \right) \right] \quad ; \quad \mathbf{v}_a = \left[\left(\frac{\partial \mathbf{r}}{\partial \mathbf{a}} \right)^T V^{-1} \mathbf{r}(\tilde{\boldsymbol{\pi}}, \mathbf{a_0}) \right], \tag{3.18}$$

where the alignment matrix becomes $N \times N$ block diagonal, and therefore less CPU time consuming when inverted. On the other hand, this method compared to the Global χ^2 needs many more iterations in order to converge to a stable solution.

3.2.3 Alignment with constraints

The track-based alignment algorithm can profit of using additional external constraints arising from the track parameters, the alignment parameters or both of them. This is achieved modifying the Equation 3.3 by adding extra χ^2 terms:

$$\begin{aligned} \chi^2 &= \chi^2_{alignment} + \chi^2_{constraints} \\ &= \sum_t \mathbf{r_t}(\boldsymbol{\pi}, \mathbf{a})^T\, V^{-1}\, \mathbf{r_t}(\boldsymbol{\pi}, \mathbf{a}) + \sum_t \mathbf{R_t}(\boldsymbol{\pi})^T\, S^{-1}\, \mathbf{R_t}(\boldsymbol{\pi}) + \mathbf{A}(\mathbf{a})^T\, G^{-1}\, \mathbf{A}(\mathbf{a}), \end{aligned} \tag{3.19}$$

where the quantity $\mathbf{R_t}(\boldsymbol{\pi})$ determines the residuals between the track parameter and its constraint, being the matrix S^{-1} related with the track parameter constraint tolerance. Similarly, $\mathbf{A}(\mathbf{a})$ is a residual vector that encodes the dependence of the alignment parameters constraints, such that $\mathbf{A}(\mathbf{a}) = \mathbf{a} - \mathbf{a_0}$, being $\mathbf{a_0}$ the initial alignment parameters. In this case, G^{-1} is the alignment parameters tolerance matrix that satisfies $G^{-1} = \frac{1}{\sigma^2}$, where σ represents the allowed cut-off on the uncertainty of a particular alignment parameter.

An example of a track parameter constraint is the muonic decay of the Z boson, which can be used to constrain d_0 and z_0 track parameters. The information of the beam spot position is also useful to constrain d_0. Whereas, the alignment parameters constraints represent penalty terms, that are very useful to avoid large alignment corrections and are usually known as soft mode cuts.

3.3 Weak modes

The alignment algorithm just described comes in handy to provide an accurate description of the detector geometry which provides efficient and good quality track fitting, however the reconstruction of track parameters is not free of systematic uncertainties. Such systematic uncertainties are known as *weak modes* because they are "near-to-singular" solutions of Equation 3.14 in the context of the alignment problem.

Weak modes can arise from the alignment algorithm itself or from distortions of the detector that remains "invisible" in the standard track-based fitting procedure. This is because they leave the χ^2 of the reconstructed tracks and the track-to-hit residuals invariant in the minimisation procedure. However, as mentioned above, they affect ultimately to the track parameters, specially to the impact parameters d_0 and z_0, as well as to the charge over momentum q/p_T quantity (which affects the curvature radius).

If not taken into account, *weak modes* would lead to biased physics measurements. So it is very important that *weak modes* are detected and tackled. Two examples of *weak modes* are displayed in Figure 3.4.

Although there are several constraints that can be applied to reduce the impact of the *weak modes*[5], the work that has been done for this thesis has been focused on the use of well-known resonances.

3.3.1 Dimuon Resonances

The use of decays of particular mass resonances, also known as standard candles, is motivated by the fact that several weak modes introduce a bias effect on the reconstructed track momentum, therefore affecting also to the invariant mass reconstruc-

[5]Beam spot and Primary Vertex (PV) constraint considers the beam spot position to constrain the transversal impact parameter d_0 and the E/p ratio for reconstruced electrons using calorimeter information to deal with sagitta biases.

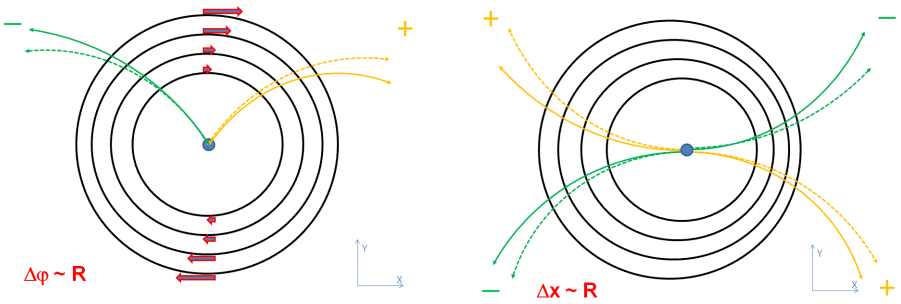

Figure 3.4: Two examples of basic distortions that bias the reconstructed track parameters. Curl (left) and radial (right) distortions that results affecting the track parameters in a charge-antisymmetric and charge-symmetric way, respectively. The true trajectory is represented in dashed lines, while the reconstructed (biased) trajectory is represented in full lines.

tion. ID alignment can exploit several standard candles, such as the reconstructed invariant mass obtained with decays of the $Z \to \mu^+\mu^-$, $J/\psi \to \mu^+\mu^-$, $\Upsilon \to \mu^+\mu^-$ or $K^0_S \to \pi^+\pi^-$. In this thesis we focus on momentum biases monitored using $Z \to \mu^+\mu^-$ events.

In order to understand how weak modes affect the momentum of reconstructed tracks, one has to bear in mind firstly that for a highly relativistic charged particle moving inside a cylindrical detector of radius R within a uniform magnetic field B along the cylinder, the p_T can be written as:

$$p_T = 0.3\, q[e]\, B[T]\, \rho[m] = 0.3\, q\, B \left(\frac{R^2}{8s} + \frac{s}{2}\right), \tag{3.20}$$

being s the sagitta of the trajectory. Moreover for medium and high p_T tracks, such as the ones considered in $Z \to \mu^+\mu^-$ decays, it satisfies that $s \leq R$. So the Equation 3.20 becomes simply:

$$p_T = 0.3\, q\, B \left(\frac{R^2}{8s}\right). \tag{3.21}$$

Equation 3.21 displays now that there are two major distortions that can result in p_T bias, namely *radial distortions* and *sagitta distortions*[6]. Whereas radial distortions alter the track curvature in an symmetric way, sagitta distortions are charge dependent, so the tracks are affected charge-antisymetrically. Examples of both can be seen in Figure 3.4, where a curl of the layers of the detector and a radial expansion of detector layers are taken as examples of charge-antisymmetric (left) and charge-symmetric (right), correspondingly.

[6]Magnetic field variations can also lead to p_T biases, but they are beyond the scope of this thesis. Detailed studies were carried out in Run 1 in Ref. [125].

Sagitta distortions: As mentioned, it is the case in which the reconstructed track differs from the true track in a charge-antisymmetric way, which is also translated to a shift of the transverse momentum p_T as:

$$\frac{q}{p_T^{reco}} \rightarrow \frac{q}{p_T^{true}} + \delta_{sagitta} \quad \text{or} \quad p_T^{reco} \rightarrow p_T^{true}\left(1 + q\, p_T^{true}\, \delta_{sagitta}\right)^{-1}, \tag{3.22}$$

where $\delta_{sagitta}$ is the parameter that describes uniquely the sagitta distortion and q the charge of the lepton decay. Moreover, the reconstructed polar angle does not vary in a transverse detector distortion, thus the total reconstructed momentum varies in the same way:

$$\frac{q}{p^{reco}} \rightarrow \frac{q}{p^{true}} + \delta_{sagitta} \quad \text{or} \quad p^{reco} \rightarrow p^{true}\left(1 + q\, p_T^{true}\, \delta_{sagitta}\right)^{-1}. \tag{3.23}$$

For cylindrical trackers this distortion may arise from rotation of the detector layers. The effect of such distortion on the reconstructed tracks can be seen in Figure 3.5 :

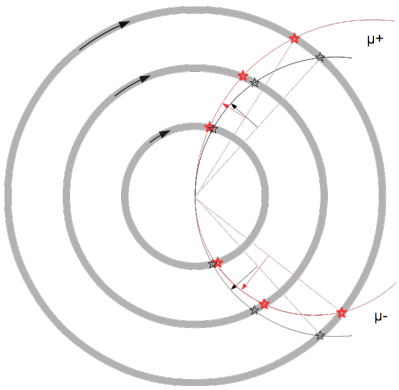

Figure 3.5: Schematic representation of how the sagitta distortion affects the reconstructed p_T of the track when the detector layers are rotated proportionally to their radius. True points are given in gray, while the reconstructed biased points in red. Therefore the apparent position of the reconstructed points (red) do no match the real ones (gray). The bias is such that for the positive muon the apparent (distorted) sagitta is smaller than the true one, and thus the reconstructed is larger than the real one ($p_T^{reco} > p_T^{true}$). For the negative muons, the effect is just the contrary.

Now let us consider the calculation of the invariant mass of the Z boson decaying to a pair of muons under the assumption that the effects of the sagitta distortion on the angular variables of the momentum can be neglected when compared to the momentum scale or the Z mass. In that case it is satisfied that:

$$m^2_{\mu\mu,true} = (p^+_{true} + p^-_{true})^2 \simeq 2p^+_{true}p^-_{true} = 2(E^+_{true}E^-_{true} - \overrightarrow{p}^+_{true}\overrightarrow{p}^-_{true}). \tag{3.24}$$

And therefore:

$$m^2_{\mu\mu,true} = 2|\overrightarrow{p}^+_{true}||\overrightarrow{p}^-_{true}|(1 - \cos\Delta\,\alpha), \tag{3.25}$$

where $|\overrightarrow{p}^{+}_{true}|$ and $|\overrightarrow{p}^{-}_{true}|$ are the total momentum of each muon and $\Delta\ \alpha$ the opening angle between them.

However, we need to use reconstructed quantities, so using Equation 3.23 we can re-write the latter equation as:

$$m^2_{\mu\mu,true} = 2|\overrightarrow{p}^{+}_{reco}||\overrightarrow{p}^{-}_{reco}|(1-\cos\Delta\ \alpha)\left(1-p^{+}_{T,reco}\,\delta^{+}_{sagitta}\right)^{-1}\left(1+p^{-}_{T,reco}\,\delta^{-}_{sagitta}\right)^{-1}. \tag{3.26}$$

On the other hand, the reconstructed invariant mass of the $\mu\mu$ system is just: $m^2_{\mu\mu,reco} = 2|\overrightarrow{p}^{+}_{reco}||\overrightarrow{p}^{-}_{reco}|(1-\cos\Delta\ \alpha)$. Therefore, the above expression becomes:

$$\begin{aligned} m^2_{\mu\mu,true} &= m^2_{\mu\mu,reco}\left(1-p^{+}_{T,reco}\,\delta^{+}_{sagitta}\right)^{-1}\left(1+p^{-}_{T,reco}\,\delta^{-}_{sagitta}\right)^{-1} \\ &\simeq m^2_{\mu\mu,reco} + m^2_{\mu\mu,reco}\left(p^{-}_{T,reco}\,\delta^{-}_{sagitta} - p^{+}_{T,reco}\,\delta^{+}_{sagitta}\right), \end{aligned} \tag{3.27}$$

where the geometric series has been applied in the last step assuming that the $\delta_{sagitta}$ biases are small together with neglecting sagitta quadratic terms.

So the relative mass difference between the true invariant mass (considered as the M_Z^{PDG}) and the biased reconstructed mass is:

$$\Delta(m^2) = \frac{m^2_{\mu\mu,reco} - m^2_{\mu\mu,true}}{m^2_{\mu\mu,reco}} = \frac{m^2_{\mu\mu,reco}}{m^2_{\mu\mu,true}}\left(p^{+}_{T,reco}\,\delta^{+}_{sagitta} - p^{-}_{T,reco}\,\delta^{-}_{sagitta}\right). \tag{3.28}$$

In principle there is no reason to assign the momentum bias to one of the muon tracks or both. The way to handle this ambiguity is to consider that the $\delta_{sagitta}$ bias is originated $1/2$ from each muon track:

$$\delta^{+}_{sagitta} = -\frac{\Delta(m^2)}{2p^{+}_{T,reco}}, \quad \delta^{-}_{sagitta} = \frac{\Delta(m^2)}{2p^{-}_{T,reco}}. \tag{3.29}$$

Then, an iterative fit process follows, in which in each iteration the muon momenta are recomputed while the computed $\delta_{sagitta}$ value is stored and used for the next iteration. This fitting process is carried out for different (η,ϕ) bins since the sagitta biases are measured covering all the ID in a (η,ϕ) map.

The iterative process to calculate the $\delta_{sagitta}(\eta,\phi)$ is repeated so that convergence is reached.

Impact parameter biases: The same $Z\to\mu^+\mu^-$ events used in the computation of sagitta biases can be used to derive constraints on the impact parameter biases of d_0 and z_0. This is because both muon tracks are expected to originate from the same production vertex, so they should share same impact parameters.

$$\delta^{+}_{d_0} = d^{+}_0 - d^{-}_0, \quad \delta^{-}_{z_0} = z^{+}_0 - z^{-}_0. \tag{3.30}$$

Any difference can be attributed to systematic distortions in the ID. Track parameter corrections are derived analogously to the sagitta biases: they are computed iteratively per (η,ϕ) bins of the ID, but re-calculating the impact parameter per iteration instead, until the impact parameters of the two muons originating from a Z boson is, on average, zero.

Radial distortions: A radial distortion is a deformation in which the detector is expanded or contracted that alters the radius of the detector as $\hat{R} = R_0 + \delta R$.

This is the case in which the reconstructed track differs from the true track in a charge-symmetric way, which is also translated to a shift of the transverse momentum p_T as:

$$p_T^{reco} \rightarrow p_T^{true}\,(1+\epsilon)\,, \tag{3.31}$$

where $\epsilon = \frac{\delta R}{R_0}$ is the magnitude of the radial distortion.

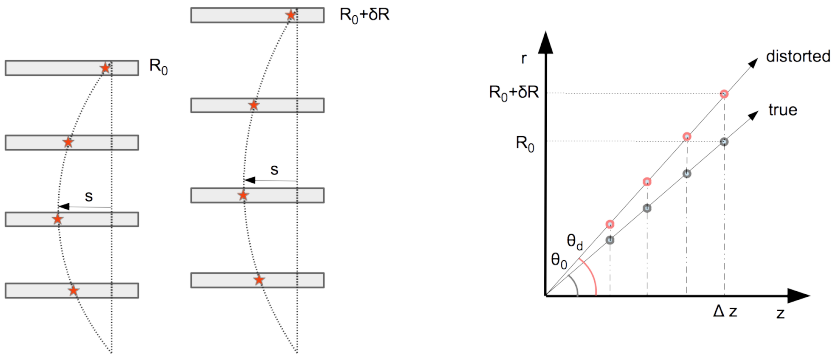

Figure 3.6: Schematic representation of the effect of a radial distortion. On the left the sagitta of the track and on the right the polar angle θ of the track. On the left the reconstructed points are located at different radius, but at the same transverse distance, leaving the sagitta invariant. On the right true points are given in grey, while the reconstructed points with the distorted geometry are shown in red. In this model, the z coordinate of the points is preserved and the radial coordinate is changed proportionally to the true radius.

The previous equation is derived under the assumption that the geometrical deformation affects the tracks only along their longitudinal direction. According to this assumption, the radial distortion does not change the sagitta of the trajectory, as shown in Figure 3.6.

Moreover, a radial distortion also introduces a bias in the polar angle θ of the reconstructed track (as shown in Figure 3.6 right), while the longitudinal component of the momentum is not affected:

$$\begin{aligned} \cot\theta_{reco} &\rightarrow \cot\theta_{true}\,(1+\epsilon)^{-1}\,, \\ p_z^{reco} &\rightarrow p_z^{true}\,, \\ p_T^{reco} &\rightarrow p_T^{true}\,(1+\epsilon) \end{aligned} \tag{3.32}$$

We can again make use of decays of several resonances to two muons: we have used $Z \rightarrow \mu^+\mu^-$, $J/\psi \rightarrow \mu^+\mu^-$, $\Upsilon \rightarrow \mu^+\mu^-$ in order to compute radial distortions and to compare the results between each other. So again, as in the sagitta distortions, it is benefitial to compute the reconstructed invariant mass using the distorted detector geometry $m^2_{\mu\mu,reco}$ and compare it with the invariant mass $m^2_{\mu\mu,true}$ of a perfectly aligned detector.

Introducing 3.32 into 3.25 and also using that $m^2_{\mu\mu,reco} = 2|\overrightarrow{p}^{+}_{reco}||\overrightarrow{p}^{-}_{reco}|(1 - \cos\Delta\ \alpha)$, it can be reached with a bit of algebra to:

$$m^2_{\mu\mu,true} = m^2_{\mu\mu,reco} + 2\left[\vec{p_T}^{+}_{reco}\vec{p_T}^{-}_{reco} - \frac{E^{-}_{reco}}{E^{+}_{reco}}\left(p^{+}_{T,reco}\right)^2\right]\epsilon^{+} + 2\left[\vec{p_T}^{+}_{reco}\vec{p_T}^{-}_{reco} - \frac{E^{+}_{reco}}{E^{-}_{reco}}\left(p^{-}_{T,reco}\right)^2\right]\epsilon^{-}, \tag{3.33}$$

where $p_{T,reco}$ and E_{reco} correspond to the momentum and energy of the muons (positive and negative) reconstructed with the distorted geometry. Radial distortion coefficients are considered separately for the positive (ϵ^{+}) and negative (ϵ^{-}) muon.

The radial distortion coefficients are locally dependent, so they are taken as function $\epsilon(\eta, \phi)$ and are computed following an iterative procedure: the momentum of each muon is left uncorrected in the first iteration, and corrected with the current values of $\epsilon(\eta, \phi)$ in the next iterations. The reconstructed invariant mass distribution $m^2_{\mu\mu,reco}$, computed with the corrected muon momenta, is also binned as function of (η, ϕ) values of each lepton, where the value of each bin is estimated with a Gaussian fit to the invariant mass spectrum. In this fit, the range is adjusted iteratively to match the standard deviation of the invariant mass distribution.

As it can be seen in Equation 3.33, the values of $m^2_{\mu\mu,reco}$ are compared to the values of $m^2_{\mu\mu,true}$, which is nothing else but the values of a perfectly aligned detector[7]. In the end, the differences between the $m^2_{\mu\mu,reco}$ and $m^2_{\mu\mu,true}$ is used to compute the $\epsilon(\eta, \phi)$ coefficients of the two muons while assuming that each muon is responsible for half of the observed difference. The computed $\epsilon(\eta, \phi)$ map is updated, and used as input to the following iteration. The procedure is repeated so that convergence is reached in the $\epsilon(\eta, \phi)$ coefficients. In order to reach convergence, it is usually required between five to ten iterations.

3.4 Inner Detector Alignment during early Run 2

One of the reason for the successes of the alignment procedure is that it is performed in hierarchical levels starting from the big structures and finishing at the module level, mimicking the mechanical assembly. Therefore the levels are treaten consecutively during the alignment procedure.

Starting with the largest physical structures at *Level 1*, the detector subsystems are aligned separating the whole detector into end-caps and barrel regions in order to correct for collective movements. These structures may suffer from relatively

[7]The true values of $m^2_{\mu\mu,true}$ can be computed using simulated samples, in which the masses of the resonances are set according to the Particle Data Group. The use of simulated samples for deriving the reference values of allows accounting for effects such as QED final-state radiation or non-Gaussian radiative tails. In the case of Z boson, it allows also accounting for the width of the Breit-Wigner distribution and Z-γ interference diagrams, as $pp \to \gamma^* \to \mu^+\mu^-$ process is indistinguishible from the $Z \to \mu^+\mu^-$ process, if $m(\gamma^*) \simeq M_Z$.

large movements. On the other hand, as they record all the tracks, they collect enough statistics, with not many events.

The next level of alignment is called *Level 2* and it treats individual barrel layers and end-cap disks as physical structures (barrel modules and end-cap wheels in case of the TRT). Since the alignable structures decrease in size, they require of more tracks (and more iterations). This can be understood easily in the context of the track-based alignment (discussed previously in Section 3), since dealing with smaller structures implies that the alignment matrix becomes bigger, and thus making matrix inversion more difficult. Finally *Level 3* corresponds to a silicon module and TRT straw level alignment and it corresponds indeed with the most challenging level that deals with the highest number of DoF.

Table 3.1 shows the number of DoF for each detector and level of alignment. As one can see, the number of alignable structures and degrees of freedom associated is very elevated and that makes the ID alignment a very challenging process. That together with the fact of the time-dependent behaviour observed in Run 2 even within the same run (see Section 3.4.1) has made ID alignment one of the most important activities contributing to the excellent ATLAS detector performance during Run 2.

As discussed in Section 2.3.2, during the Long Shutdown in which the LHC was down for repairs and upgrade between Run 1 and Run 2, the IBL was inserted in the Inner Detector and thus has become the closest detector to the beampipe. Therefore the alignment levels have been updated in order to accommodate the IBL. That is why *Level 1* in Run 2 is often referred as *Level 11*. At *Level 11* the IBL is considered a separated structure from the already existing Pixel subdetector because it has been built as a mechanically independent support structure. However for *Level 2* and *Level 3*, the IBL is considered merely as an additional Pixel layer or additional silicon modules, respectively.

Levels	Structures	DoF
L11 (large structures)	8	48
L2 (Si layers/disks, TRT modules and wheels)	208	792
L3 (Si modules)	6112	36672
L3 (TRT straws)	350848	701696

Table 3.1: Number of DoF by detector and level of alignment. Assembly structures and silicon modules use 6 DoF. TRT wires use just 2 DoF.

Level	Description	Structures	DoF	Additional constraints
11	IBL	1	All	
	Pixel detector	1	All	
	SCT end-caps (SCT barrel fixed)	2	All except T_z	
	TRT split into barrel and 2 end-caps	3	All except T_z	
Si 2	Pixel barrel split into layers	4	All	Beam spot,
	Pixel end-caps split into discs	6	All	momentum bias, and
	SCT barrel split into layers	4	All	impact parameter bias
	SCT end-caps split into disks	18	All	
Si 3	Pixel barrel modules	1736	All	Beam spot,
	Pixel end-caps modules	288	T_x, T_y, R_z	momentum bias,
	SCT barrel modules	2112	All	impact parameter bias, and
	SCT end-caps modules	1976	T_x, T_y, R_z	module placement accuracy
TRT 2	TRT barrel split into barrel modules	96	All except T_y	Momentum bias and
	TRT end-caps split into wheels	80	T_x, T_y, R_z	impact parameter bias
	Pixel and SCT detectors fixed			
TRT 3	TRT straws	351k	T_x, R_z	
	Pixel and SCT detectors fixed			

Table 3.2: Typical alignment configurations used throughout Run 2 data taking to derive baseline alignment constants.

Baseline alignment constants

The baseline alignment constants are used as a reference to compute the online alignment time-dependent corrections that are applied to the detector as the data-taking is happening. Usually baseline alignment constants are computed when ATLAS begins to record data after relatively long periods of LHC being off (end-of-year stop, technical stops, machine developments, long shutdowns,...). It is crucial that the initial baseline constants describes the detector geometry as accurately as possible, otherwise track parameter biases (such as impact parameter or momentum biases) are likely to arise during the data-taking. To that purpose, a whole alignment chain is performed using runs disposing large amount of data ($\sim 2\,\text{fb}^{-1}$) and recorded during a period of time where the detector conditions are known to be stable.

Table 3.2 shows all the different alignment levels that have been used to derive baseline alignment constants throughout all Run 2. *Level 11* and *Level 2* require between two and four iterations to converge using the Global χ^2 method. On the other hand, the Global χ^2 method requires at least four iterations to reach convergence at *Level 3* for the silicon alignable structures (SCT, Pixels and IBL). The TRT *Level 3* (straw level) uses the Local χ^2 method instead due to the high number of DoF (see Table 3.1) and requires up to 30 iterations to converge.

Despite the effort in finding accurate baseline alignment constants, during the *online or prompt alignment*) it is sometimes difficult to find a set of alignment constants that maintains the track parameter biases to zero or near to zero in a first update of the database conditions, in which it uses dedicated set of tracks from calibration streams as input. This is due to the weak modes described in Section 3.3. For each of the track parameters, weak modes are measured through 2-D maps

in which every region of the detector is splitted in (η, ϕ) coordinates. Later these maps can be used to constrain the biases and feed it into the alignment algorithm to find another set of baseline alignment constants in which the biases are almost removed in a second update of the database conditions, that uses the bulk data of already physics stream. This process is the so-called *Calibration Loop* process that takes place at the Tier 0 computing facility. In case that non-negligible biases are still found in the alignment constants, they can still be used to reprocess the data long after data-taking.

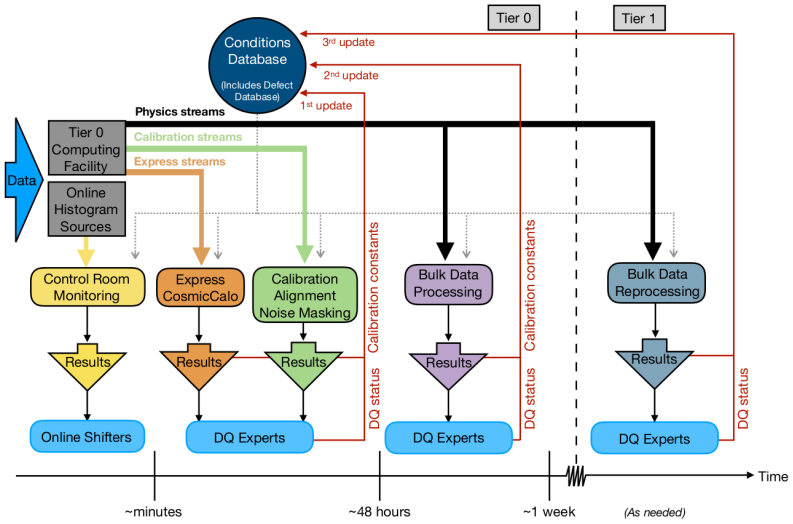

Figure 3.7: Scheme illustrating the nominal Run 2 operations workflow for the data quality assessment of ATLAS data, in which the alignment Calibration Loop algorithm is part of it. Figure extracted from Ref. [126].

3.4.1 Time-dependent alignment

During the LHC Run 1 data taking campaign, the ATLAS Inner Detector was found to be stable for long periods of time, except for some "seismic" events (magnet ramp, power-cut, cooling failure,...). Figure 2 displays the evolution of the *Level 1* global X translations of all ID sub-detectors. TRT and SCT barrel sub-detectors show a stability of a few μm, while the TRT and SCT end-caps show bigger movements of up to 20 μm. These bigger movements are related with the "seismic" events previously described and usually gradual movements attributed to mechanical relaxations to an equilibrium state take place right afterwards, which can last several weeks long. The run-by-run basis alignment procedure was fully integrated in the *Calibration Loop* process in early 2011. Two iterations of *Level 1* using the Pixels as reference were performed shortly after each run finished. If movements were detected, then the geometry of the detector was needed to be updated before

48 hours, which was the time that *Calibration Loop* process would work. This was the birth of the run-by-run alignment.

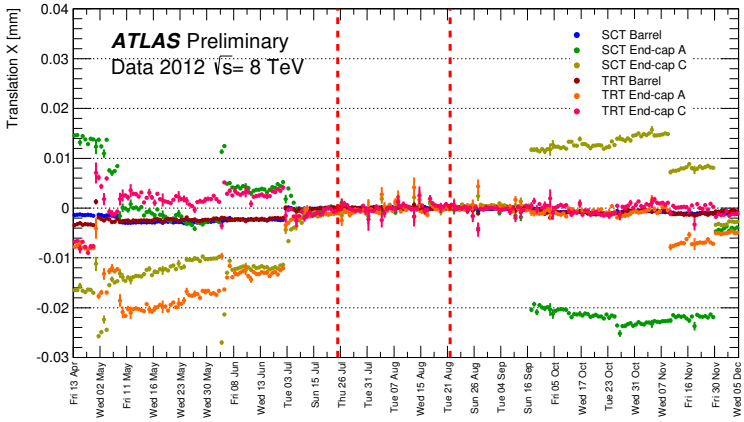

Figure 3.8: Evolution of the *Level 1* alignment constant T_x during 2012 Run 1 campaign. The vertical dashed lines stand for the data taking periods in which the baseline alignment constants were determined.

However, in Run 2 some sub-detectors have shown time-dependent deformations or movements, even within a single run, which the standard run-by-run alignment couldn't correct properly. This has required the introduction of a brand new dynamic alignment scheme.

During the period of 2015-2017, two time-dependent deformations have arisen and are assesed in the following sub-sections:

- Vertical movements of pixel sub-detector at the beginning of each run.
- IBL mechanical instabilities with temperature.

3.4.2 Pixel movements

Vertical movements of the pixel detector at the beginning of each run were registered resulting from the change in the mass of the cooling liquid after the detector is switched on until an equilibrium between vapor and liquid is reached[8]. Previously, in Run 1 no correction was applied, because only a small fraction of data was affected. During Run 2, an additional slow drift has also been observed. It takes places during all the run, in the opposite direction to the initial movement. The velocity of this slow drift depends on the peak luminosity of LHC, which was increased during 2016. Figure 3 shows that Pixel quickly lifts 6 μm during the first hour of the run, followed by a gentle descent afterwards. As it will be explained in Section 3.4.4, a new dynamic alignment procedure was introduced in August 2016 which corrects for both these effects using time-dependent alignment. This

[8]This is the most likely explanation of the Pixels detector moving upwards and downwards.

required the introduction of an improved alignment database, in which the ID geometry database was restructured in several folders.

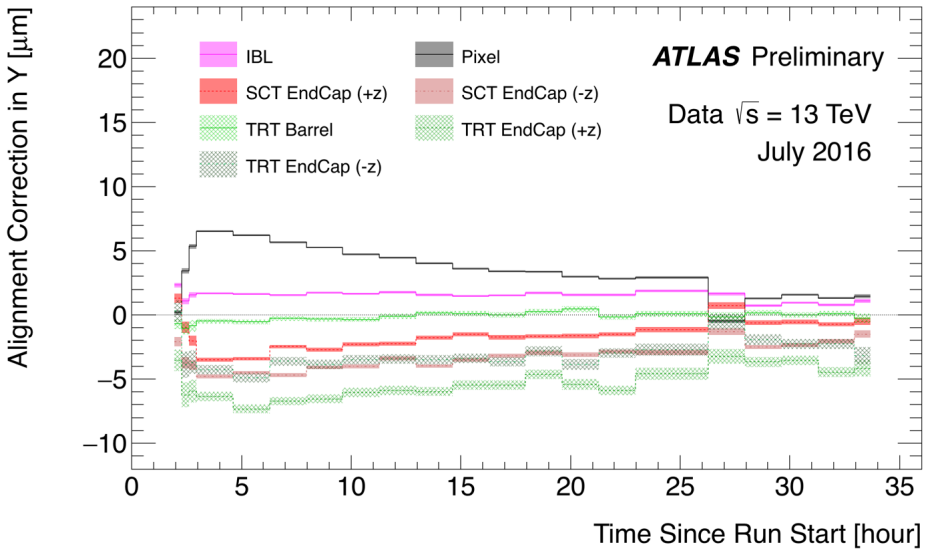

Figure 3.9: Correction in the Y vertical direction for the inner detector components as a function of time. Bands indicate statistical uncertainty. End-caps on the positive and negative side of the detector are shown separately. SCT barrel is kept fixed as a reference during the derivation of the alignment constants. While good stability was observed for all ID components in the X direction, the figure shows a fast movement of 6 μm for the Pixel sub-detector in the Y direction.

3.4.3 IBL mechanical instabilities

As mentioned in Section 2.3.2, the IBL is composed by 14 staves and each of the modules of these staves are uniquely inferred through the so-called η index[9]. The behaviour of these staves during collision data taking has been not stable, namely the staves have undergone a *bowing* deformation being more striking in the modules located in central region of the staves along the z-axis (i.e. low η indices), as left Figure 3.10 shows.

The fact that IBL wasn't stable was already observed during the commisioning of the IBL, where the IBL staves exhibited distortions with respect to the design geometry consisting on staves displacement along the local-x direction, as right Figure 3.10 shows. Understanding the instabilities of the IBL is crucial in order to ensure good quality reconstructed tracks. Further studies using cosmic-ray data from March 2015 made evident that the size of the IBL distortion depends on the operating temperature T_{set} of the IBL [127]. For theses studies, the operating

[9]High absolute values of the η index indicate that modules are closer to the extremes of the staves.

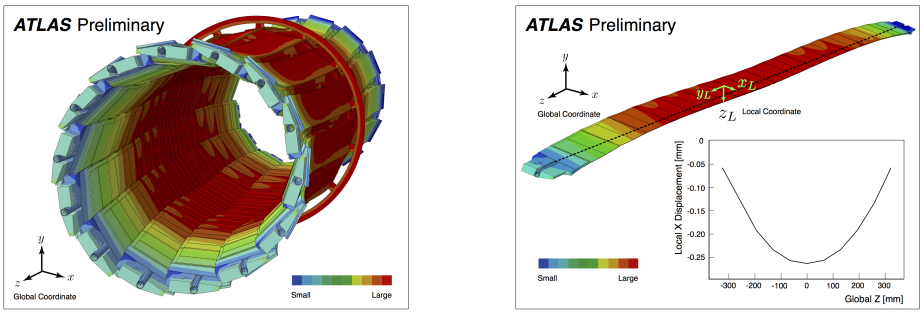

Figure 3.10: Left: Full package of the IBL staves with the central ring simulated by the 3D Finite Element Analysis (FEA) representing the distortion. The size of the distortion is magnified for visualization. The color represents the relative size of the local displacement. The temperature is set at $\delta T = -60$ K uniformly from the nominal temperature. The distortion is magnified by a factor 20. Right: Visualization of the distorted stave with magnified distortion size. The size of the distortion is magnified for visualization. The color represents the magnitude of the displacement. The right bottom graph shows the relative displacement size in local-x direction as a function of the global z-position at the face plate surface of the stave.

temperature T_{set} of the IBL vas varied in a range from $[+15°, -20°]$. The IBL distortion in local-x in terms of the operating temperature can be seen in Figure 3.11, when using 2015 and 2016 $p-p$ collisions. The local-x distortion averaged in all the 14 staves of the IBL, i.e. $\delta(x(z))$, is fitted with a parabolic function defined as:

$$\delta(x(z)) = B + M\left(1 - \frac{z^2}{z_0^2}\right), \tag{3.34}$$

where z is the position of the module along the z-axis, $z_0 = 366.5$ mm is the fixing point of each IBL stave at both ends, B is the baseline which describes a global overall translation of the stave in the local-x direction and M is the magnitude of the stave distortion. The temperature gradient after performing the fit has been found to be $\frac{dM}{dT} = -10.6 \pm -0.7$ [μm/K].

Though the scope of this thesis is not focused in correcting the IBL distortions on short time-scale, it is interesting to mention that the reason behind the ***bowing*** distortion of the IBL points to a mismatch between the thermal coefficient of the materials coupled in the staves. However, radiation effects have an impact on the low voltage (LV) currents of the IBL electronics, since leakage currents in the transistors of front-end electronics arise. The change of the LV currents depends on the total ionisation dose. In the end, a change in the LV currents results in an increase of the IBL modules temperature and therefore changes of the IBL distortion were observed on short time scales.

Figure 3.12 shows that the IBL staves bend depending on the different operating temperature conditions, while Figure 3.13 shows that distortion magnitude changes

in the same run, since the distortion varies with the integrated radiation dose and as a function of the LHC luminosity within a fill.

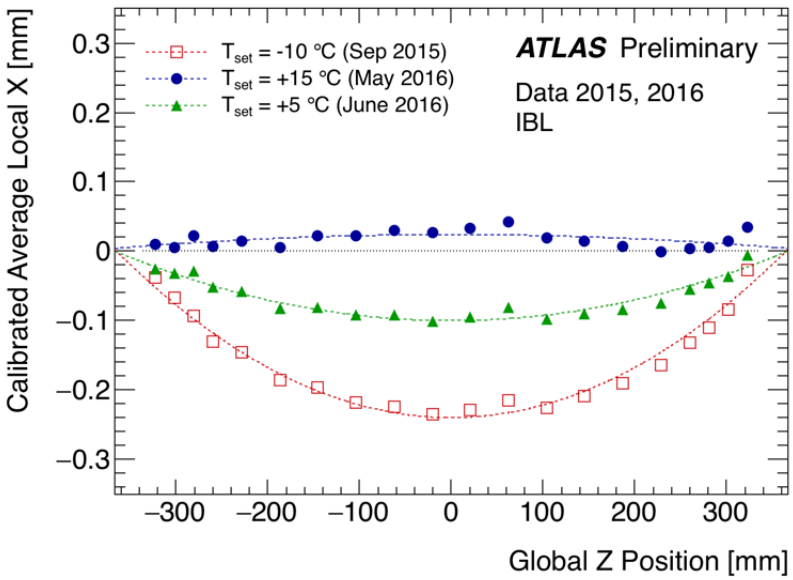

Figure 3.11: This figure shows IBL local-x correction in the transverse plane averaged over all 14 IBL staves for 2015 data (red open squares), and for 2016 data using different temperature (+15 °C, solid blue circles; +5°C, solid green triangles). No error bars associated with data are shown. Lines are presented just to highlight that trend. Here, only the correction due to the IBL distortion is shown. The baseline, which describes the overall translation of the whole stave, is subtracted using a parabolic fit function parameterizing the IBL temperature dependent distortion. In this fit the baseline is corrected so that the fitted curve is zero at the edges of the staves ± 366.5 mm.

3.4.4 Dynamic alignment scheme

Since the default alignment scheme inherited from Run 1 could not deal with the short time scale movements previously described, a new alignment scheme has been developped. The key point of this dynamic scheme is to add a new alignment degree of freedom (i.e. B_x) that absorbs the *bowing* distortion of the staves in the IBL and that is defined in Equation 3.34 as M. The *bowing* distortion can be absorbed in two different alignment levels: the first one, is the *Level 11*, in which the IBL distortion magnitude is averaged over the 14 staves and the second one, is the so-called *Level 16*, in which each stave is corrected in case that an IBL *bowing* magnitude is present. In Table 3.3 it is summarized the alignment configurations for *Level 11* and *Level 16* that has been used throughout Run 2 in the *prompt alignment* automated *Calibration Loop* process. L11 and L16 alignment constants are determined every

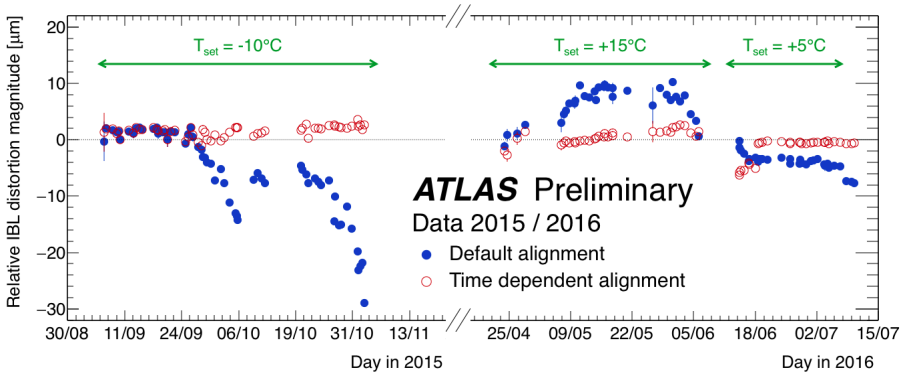

Figure 3.12: This figure shows the relative bowing magnitude of the IBL staves, averaged over its 14 staves and computed with the default alignment (blue dots) and with respect to the aligned geometry (red open circles). The IBL operation temperature (T_{set}) for each period is also shown. The runs around 18/06/2016 were poorly corrected due to a misconfiguration of the alignment procedure that slightly degraded its performance. It was expected to be fully recovered by a reprocessing. For those runs, the central modules were well aligned and the bowing only affected the outermost modules on each stave.

Level	Description	Structures	DoF
11	IBL	1	All DoF incl. B_x, except R_z
	Pixel detector	1	All
	SCT end-caps (SCT barrel fixed)	2	All except T_z
	TRT split into barrel and 2 end-caps	3	All except T_z
16	IBL staves	14	B_x
	Pixel, SCT, and TRT detectors fixed		

Table 3.3: Typical alignment configurations used throughout Run 2 data taking to derive dynamic alignment corrections.

20 LB[10] at the start of a LHC fill happening during the first hours. In this way, the rapid vertical Pixels movements at the beginning of a run can be absorbed more accurately. Alignment constants are afterwards computed every 100 LB's for the rest of the fill, happening during the slow gradual drift of the Pixels movements.

[10]One lumiblock corresponds to 1 minute of data taking.

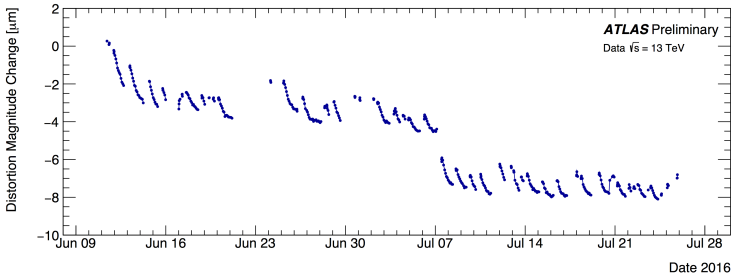

Figure 3.13: Average correction of the IBL bowing distortion magnitude with respect to the baseline alignment in 2016 $p-p$ collision runs between Technical Shutdown 1 and Machine Development 1 of the LHC. The bowing distortion magnitude is calculated every 20 minutes for the first 60 minutes of the data taking, and every 100 minutes for the rest of the run. Each chained series of points represents a continuous data-taking period. The distortion magnitude changes within a run reflecting the power consumption change of the front-end electronics due to total-ionising dose (TID) effect. The magnitude recovers between runs due to annealing effect.

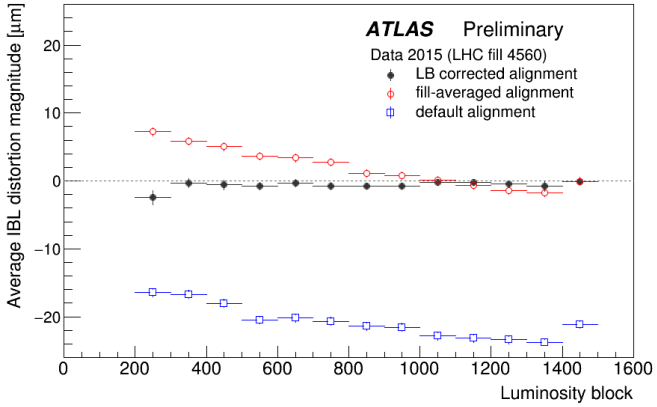

Figure 3.14: IBL distortion magnitude in the transverse plane per luminosity block range (LB) for LHC fill 4560 averaged over all 14 IBL staves. The 'default' data (open blue squares) shows the average IBL distortion in the transverse plane after the default Inner Detector (ID) alignment. Data using the 'fill-averaged ID alignment' (open red circles) include the fill-averaged correction. The 'LB corrected alignment' includes and additional time dependent alignment correction (solid black circles).

The results of the time-dependent alignment are shown in Figure 3.14. The distributions of the local-x unbiased residuals integrated over all hits of the IBL sub-detector are shown in Figure 3.15 with the default alignment constants, the run averaged alignment correction to the global IBL bowing and the time dependent corrections to the bowing of each stave.

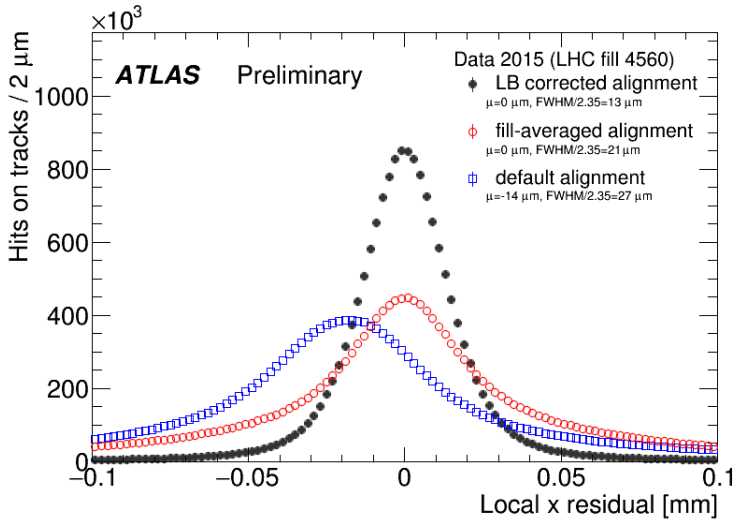

Figure 3.15: The IBL local x unbiased residual distributions for tracks that pass the Tight Primary track selection and have a transverse momentum satisfying $p_T > 3$ GeV. In blue (open squares) the distribution obtained with the default alignment compared with the one obtained with the fill-averaged alignment (open red circles) and after LB corrected alignment (solid black circles). The distributions are integrated over all hits-on-tracks in the IBL layer modules. The parameter μ represent the mean of the distributions. The distributions have been normalized to the same number of entries. The improvement between before and after alignment is quantified in terms of the Full Width Half Maximum (FWHM) of the distributions.

3.5 Run 2 alignment results

The ID alignment constants performance can be assessed using two well established techniques. One of these techniques is the study of the track-to-hit residuals and their comparison to a perfectly aligned Monte Carlo sample. A systematic misalignment of a particular sub-system would manifest itself as a bias in the mean of the corresponding track-to-hit residuals, while a random residual misalignment would leave the distribution centred on zero but with a degraded resolution. Nevertheless, track-based alignment is blind to deformations that preserves the helical paths of the tracks. Hence, the other remaining technique consists of introducing additional constraints, such as beam spot, mass resonances (Z, J/ψ, K_s) or external detector constraints (E/p). As it was already explained in Section 3.3, weak modes may introduce momentum biases. The use of standard candles such as J/ψ, K^0_S or Z that have a very precisely known mass that can be used to check, and also correct, eventual momentum or impact parameter biases.

This section comprises of alignment results in the framework of the effort of this thesis, which was involved mainly to the 2016 offline alignment (in order to spot and correct both sagitta and impact parameter biases) and initial 2017 online

alignment (in order to check the initial baseline alignment constant during the restart of data taking of the LHC in 2017). In both cases a pair of muons originated from the decay of the $Z \to \mu^+\mu^-$ was used. Additionally, this thesis dedicated also an effort to develop radial distortion studies, which were tested with $J/\Psi \to \mu^+\mu^-$, $\Upsilon \to \mu^+\mu^-$ and $Z \to \mu^+\mu^-$ events.

Data selection
Good quality tracks are mandatory to ensure samples enriched with $Z \to \mu^+\mu^-$ events because later are used to compute momentum and impact parameter biases. During the Run 2 alignment campaign in proton-proton collisions produced by the LHC at $\sqrt{s} = 13$ TeV muon candidates are selected as long as they are meet the ***Medium*** quality criteria[11], as defined in Ref. [128]. All reconstructed tracks associated with muon candidates are expected to have:

- At least one hit in the IBL, if one is to be expected.
- At least two Pixel hits and six SCT hits.
- At most one hole in the silicon sub-detectors (Pixel or SCT), including dead modules. [12]

The muon tracks are also required have transverse momentum of at least 25 GeV and to be isolated within a cone of $\Delta R = 0.4$[13] In addition, the reconstructed invariant mass of the dimuon is required to be close to the Z boson mass [29] window and that we define as:

$$70 \leq M_{\mu^+\mu^-} \leq 110\,\text{GeV}, \tag{3.35}$$

3.5.1 2016 offline alignment

In order to avoid biased physics measurements it is necessary to eliminate the present weak modes or to assess systematic uncertainties, depending on the timescale.

For the 2016 p-p collision dataset, weak modes bias sizes and uncertainties were evaluated for each baseline alignment constants change that were used during the prompt alignment algorithm, namely:

- Before TS1: from the beginning of 2016 physics data-taking until Technical Shutdown 1, with an integrated luminosity of 2.4 fb^{-1} containing runs from 297730 until 300908.

[11] Track reconstruction is performed independently in the ID and MS. If both tracks can be combined then the muon is known as *combined muon*, though later only the ID track is used.

[12] A hole is defined as a missing hit in a detector sensor where a signal is expected. Therefore dead modules do not produce holes.

[13] The isolation cone is defined as $\Delta R = \sqrt{\Delta\phi^2 + \Delta\eta^2}$.

- After TS1(a): from Technical Shutdown 1 until July 21, with an integrated luminosity of 11.1 fb^{-1} containing runs from 301912 until 304178.
- After TS1(b): from July 21 until the end of the 2016 $p-p$ runs, with an integrated luminosity of 19.6 fb^{-1} containing runs from 304198 until 311481.

Figure 3.16 shows the average size of $\delta_{sagitta}$ and δz_0 for the whole 2016 dataset, while Figure 3.17 shows the η profile of $\delta_{sagitta}$ and δz_0, averaged over ϕ component. 30×30 bins were used to derive the (η, ϕ) maps. Such decision was made to have a decent granularity taking into account the total number of $Z \rightarrow \mu^+\mu^-$ events (around 300000 in the whole 2016 dataset).

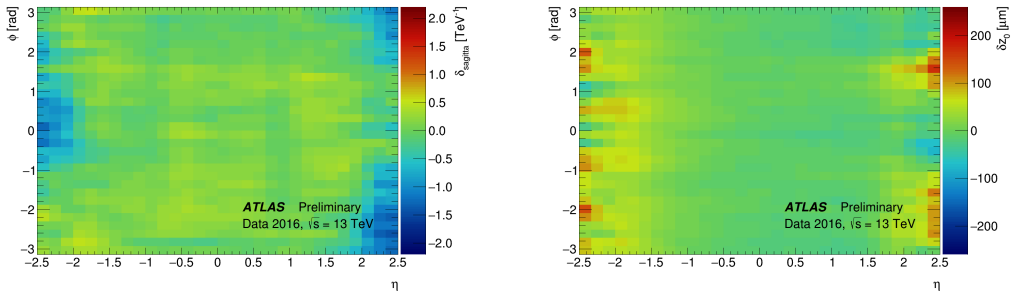

Figure 3.16: Average correction to compensate the bias of the track sagitta as a function of η and ϕ for the full 2016 proton-proton dataset (left) and average z_0 correction to compensate the bias as a function of η and ϕ for the full 2016 proton-proton dataset (right).

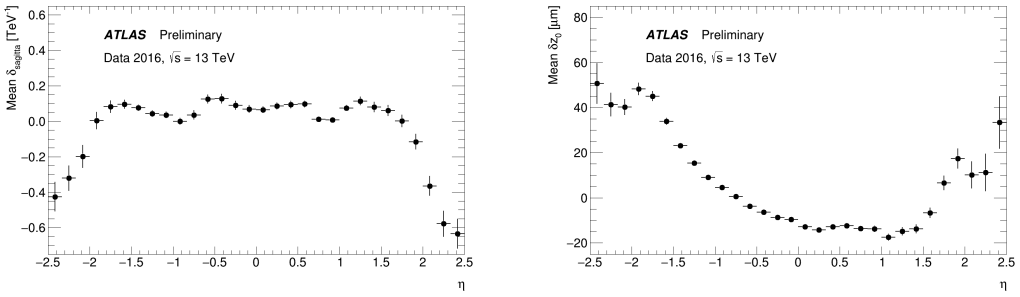

Figure 3.17: Sagitta correction to compensate the bias as a function of η for the full 2016 proton-proton dataset, averaged over ϕ. The vertical bars indicate the variance along the azimuthal direction (left) and correction to compensate the bias of the track parameter z_0 as a function of η for the full 2016 proton-proton dataset, averaged over ϕ (right).

Since the size of δd_0 differs significantly between these periods, the maps and distributions are presented separately for each period. That is presented in Figure 3.18, where 2D maps are displayed but also in Figure 3.19, that shows the η profile distribution of the δd_0 maps, averaged over ϕ component.

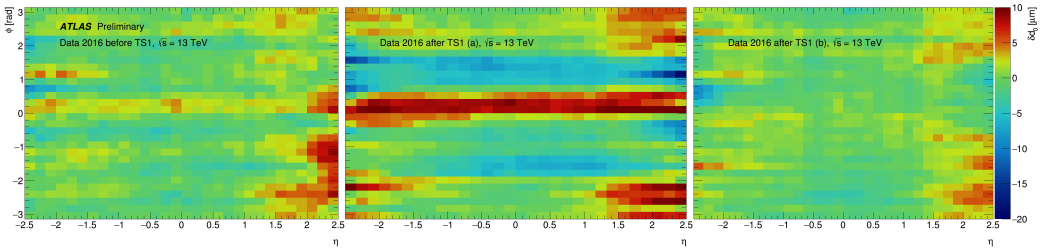

Figure 3.18: Average d_0 correction to compensate bias as a function of η and ϕ for the full 2016 proton-proton dataset. The performance differed over the year and can be separated into three distinct periods (from left to right): from the beginning of 2016 physics data-taking until Technical Shutdown 1 (before TS1); from Technical Shutdown 1 until July 21 (after TS1(a)); from July 21 until the end of the 2016 p-p data-taking (after TS1(b)).

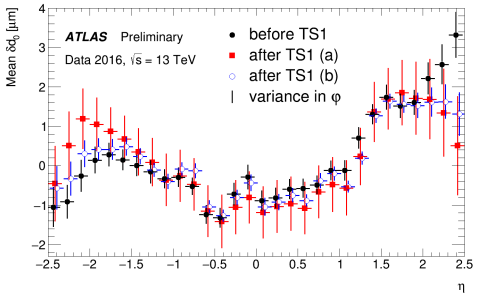

Figure 3.19: Correction to compensate the bias of the track parameter d_0 as a function of η for the full 2016 proton-proton dataset, averaged over ϕ. The vertical bars indicate the variance along the azimuthal direction. The distribution is shown separately for three periods: that is, from the beginning of 2016 physics data-taking until Technical Shutdown 1 (before TS1), from Technical Shutdown 1 until July 21 (after TS1(a)) and from July 21 until the end of the 2016 p-p data-taking (after TS1(b)).

While $Z \to \mu^+\mu^-$ events have been used to derive corrections for the impact parameters (i.e. d_0 and z_0) and sagitta biases, the E/p method with electrons is used as a cross-check for the sagitta biases, following the methods described in Section 3.3. The E/p method is described in Ref. [125].

Weak modes recommendations were provided to the ATLAS collaboration so that the weak modes maps of the sagitta and impact parameters could be applied to estimate systematic uncertainties on the residual misalignment effects of the alignment procedure in a shorter time-scale.

The uncertainty bands were calculated by adding in quadrature the statistical uncertainty with the systematic component defined in such way that takes into consideration differences observed in subperiods of the studied 2016 dataset. In the case of the uncertainty of the sagitta, an additional component was introduced to

account for the observed differences between the E/p method and the $Z \to \mu^+\mu^-$ method (due to neglection of second order terms in invariant $m^2(Z)$ calculation).

Figure 3.20 shows such uncertainties profiled over the 2D sagitta biases maps, before applying weak modes corrections. Systematic uncertainty dominates over statistical uncertainties, specially for large η regions. In the case of the sagitta the E/p component is negligible.

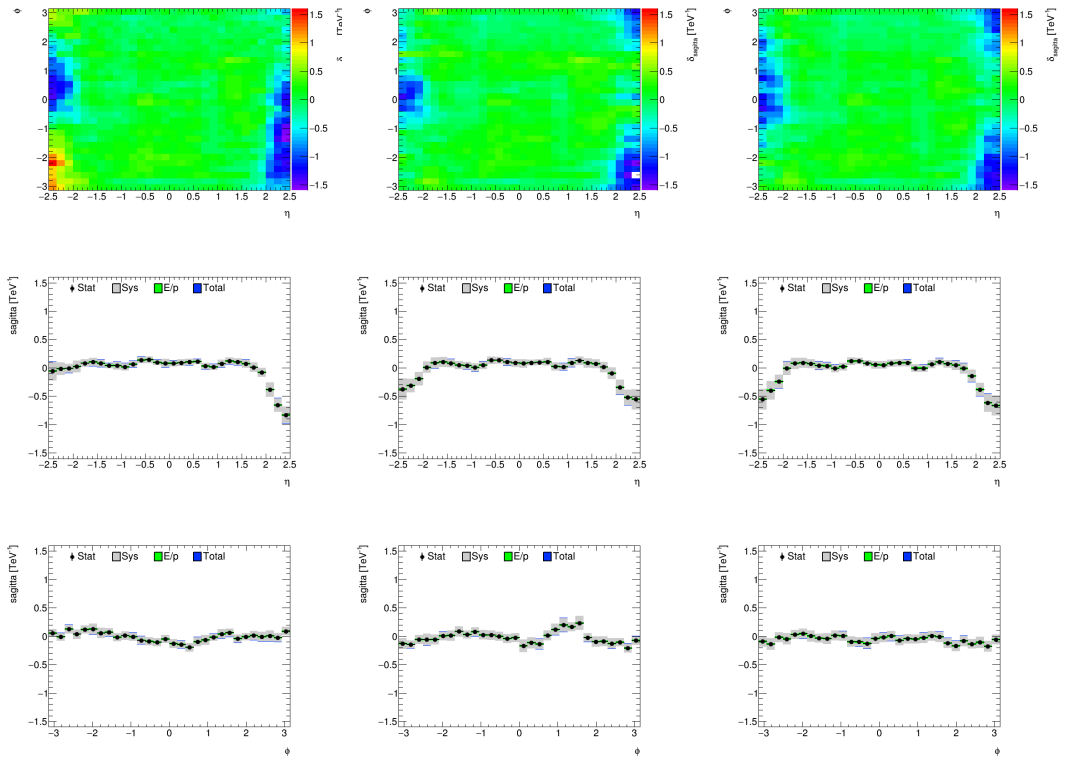

Figure 3.20: Sagitta biases in the first row before TS1 (left), after TS1(a) (middle), after TS1(b) (right). Profiles in η (second row) and ϕ (third row) with total uncertainties (blue) added in statistical (black line), E/p (green) and total systematic (gray).

In the longer time-scale, track parameters can be eventually used as additional constraints in the track-based alignment to provide new baseline alignment constants, that reduce the track parameter biases (reprocessed alignment).

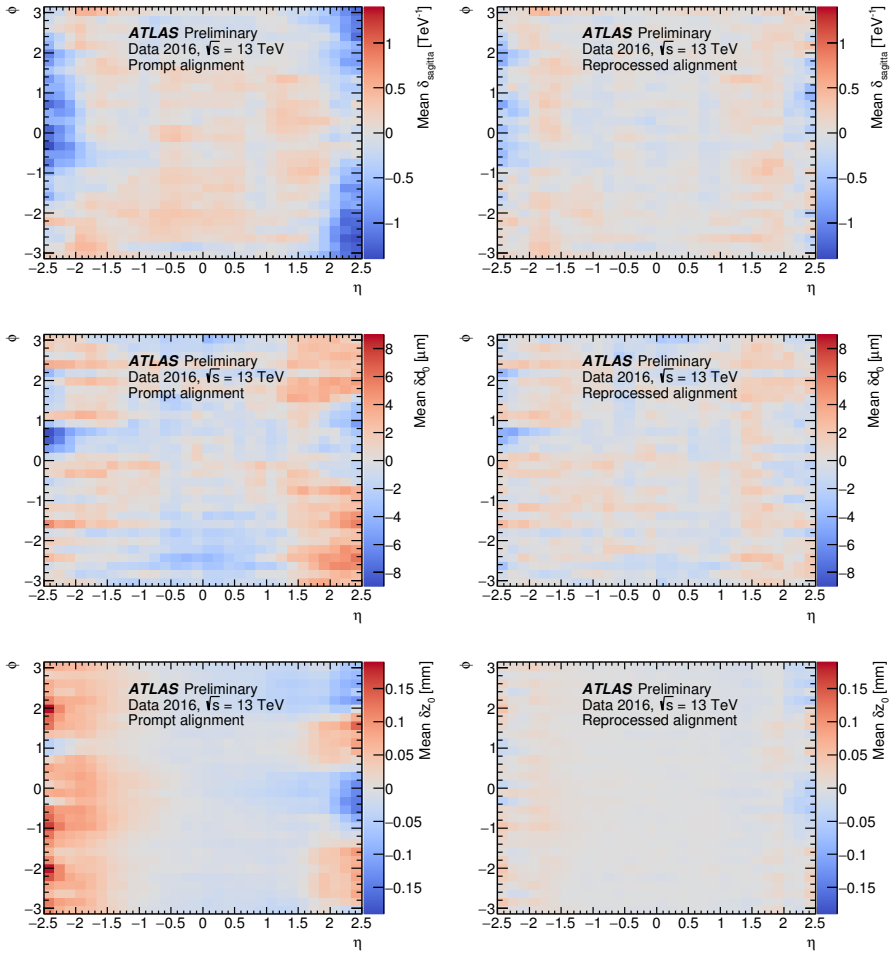

Figure 3.21: Prompt (left) and reprocessed (right) biases maps for the sagitta and impact parameters. For the reprocessed alignment the complete 30.4 fb^{-1} of proton-proton data taken after Technical Stop 1 are used, while for the prompt alignment only 20.3 fb^{-1} of data are used. Significant improvements in average biases are seen after the reprocessing with the updated alignment.

Figure 3.21 (left) shows weak modes maps using prompt alignment corrections (alignment constants derived shortly after the run has finished) and Figure 6 (right) shows corrections using reprocessed alignment (whose constants were derived after applying weak modes constraints and realigned). A clear improvement is observed for the sagitta and the impact parameters (i.e. d_0 and z_0) using reprocessed data.

The very same conclusion can be drawn when one looks at the 1D projections in the mean or RMS of the sagitta and impact parameters, shown in Figure 3.22.

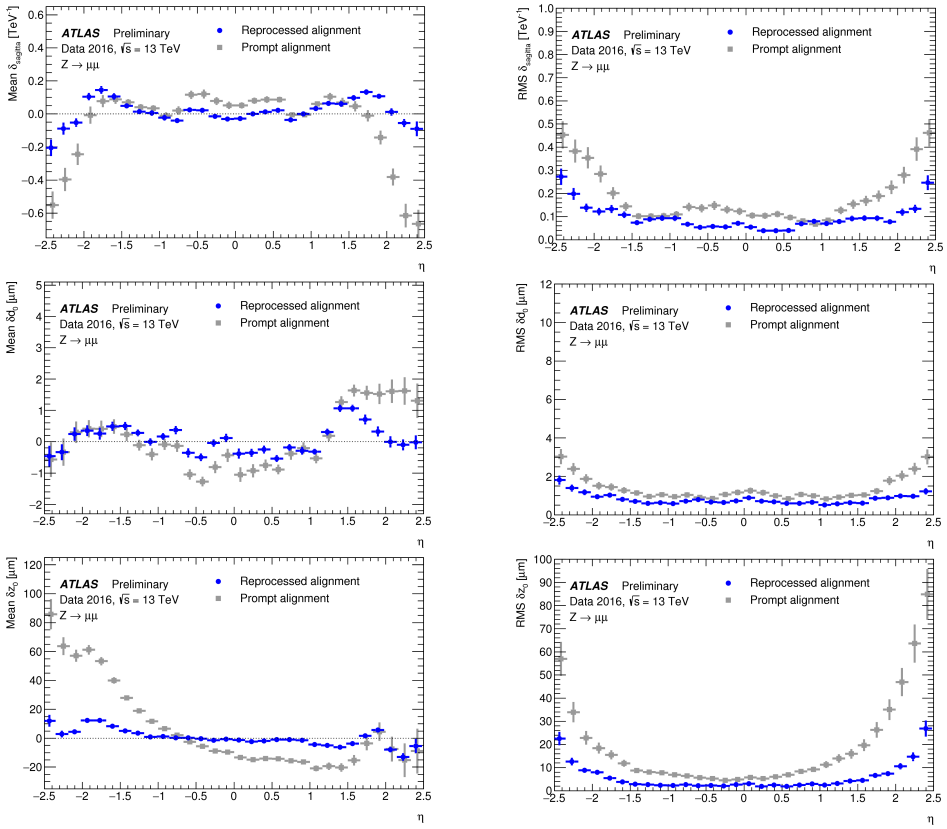

Figure 3.22: Mean (left) and RMS (right) of the sagitta bias and impact parameter biases as a function of η for the 2016 proton-proton dataset, averaged over ϕ. The vertical bars indicate the variance along the azimuthal direction. Results obtained with the reprocessed alignment (blue circles) are compared to the results obtained with the prompt alignment (gray squares).

3.5.1.1 Radial distortion studies

The radial expansion studies (see Section 3.3 for theoretical details) were performed simultaneously on J/ψ, υ, and Z decays to a pair of muons. The event selection was adapted for each case although also had common features as: request a pair of opposite charge muons, with compatible impact parameters: $|\Delta d_0| < 0.120$ mm and $|\Delta z_0| < 0.5$ mm.

- The $J/\psi \rightarrow \mu^+\mu^-$ selection consisted in requesting that both muons have $p_T > 6.5$ GeV, an opening angle of at least 0.55 radians and invariant mass between 2.6 and 4.2 GeV.
- The $\Upsilon \rightarrow \mu^+\mu^-$ selection requested a $p_T > 9$ GeV for the leading muon and $p_T > 6.5$ GeV for the sub-leading one, as well as an invariant mass between $7.25 < m_{\mu\mu} < 11.8$ GeV.
- The $Z \rightarrow \mu^+\mu^-$ consisted of an event selection with $p_T > 30$ GeV, an opening angle bigger than 1 radian and the invariant mass in the range: 70 to 110 GeV.

In all cases the p_T cut was chosen to be well above the trigger thresholds.

The advantage of using several resonances decaying to two muons is that one can study, in this case, any possible radial distortion in a quite broad p_T range.

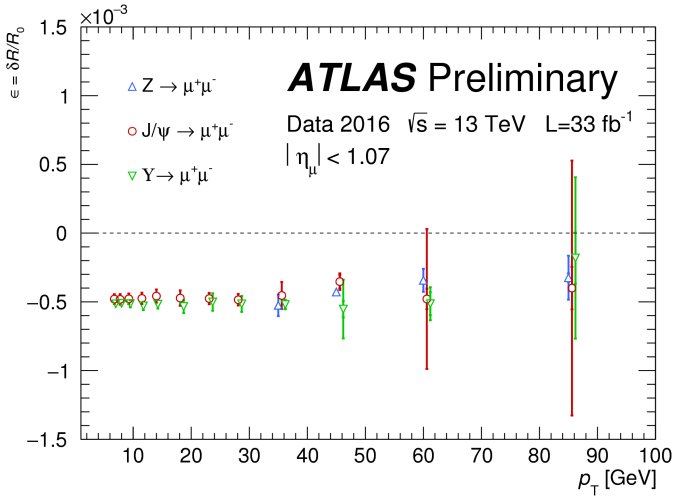

Figure 3.23: Results of the measurement of the radial distortion coefficient $\epsilon = \frac{\delta R}{R_0}$ as a function of the track p_T for 2016 data. The vertical bars represent the quadratic sum of systematic and statistical uncertainties, being the latter the dominant, specially in the high p_T range.

The observed radial distortion of $\epsilon = \frac{\delta R}{R}$ in the barrel region $|\eta| < 1.07$ in function of the p_T can be seen in Figure 3.23 and the main conclusion that can be drawn is that the radial distortion is compatible for all resonances and it is uniform

across the momentum spectrum, hinting at a geometrical deformation affecting all tracks in the same way. Such studies are explained in detail in Ref. [129].

It must be said that a bias in the magnetic field can produce a similar effect. Therefore, results displayed in Figure 3.23 show that there is a bias of the order of 5×10^{-4} in the momentum scale. At the time of writing, there are efforts to disentangle between a pure geometrical (i.e. radial) bias and a magnetic field bias.

3.5.2 2017 online alignment

In order to deliver the best possible online data quality, it is important the the online alignment performed in the calibration loop is as much accurate as possible.

During 2017, the IBL conditions were changed since the operation temperature was decreased to its nominal temperature of -20°C. This is the reason why a dedicated alignment that could account for induced bowing of the IBL was needed.

The first 2017 baseline alignment constants for 2017 data-taking were derived using 82 pb^{-1} of proton-proton collision data delivered by the LHC in June 2017, namely the Run 325713, in which the amount of tracks and their quality were sufficient (although Run 324320 was also used to start with the baseline alignment derivation).

The alignment was performed in several steps, considering different sub-detectors at increasing levels of detail, as explained in Section 3. Initially, the IBL, Pixel, SCT and TRT barrel and end-caps were aligned as one unit each (level 1 alignment). At level 2, individual barrel layers and end-cap disks of the silicon detectors were aligned. This was followed by an alignment of individual Pixel and SCT modules at level 3. The last step consisted of a level 2 (modules) alignment of the TRT. Several constraints were used in order to avoid the introduction of biases on the impact parameters or alignment weak modes: such as the beam spot constraint, null map constraint or the soft mode cut.

The alignment performance was checked by evaluating the track-to-hit residuals. A comparison between residuals in data to those of perfectly aligned Monte Carlo simulation is also crucial. Figure 3.24 shows that the modules have been aligned at $\mathcal{O}(\mu\text{m})$ level in both final reprocessed 2016 data and initial 2017 data.

Therefore, it was a major achievement that the initial 2017 alignment baseline provided a similar performance to the 2016 reprocessed constants.

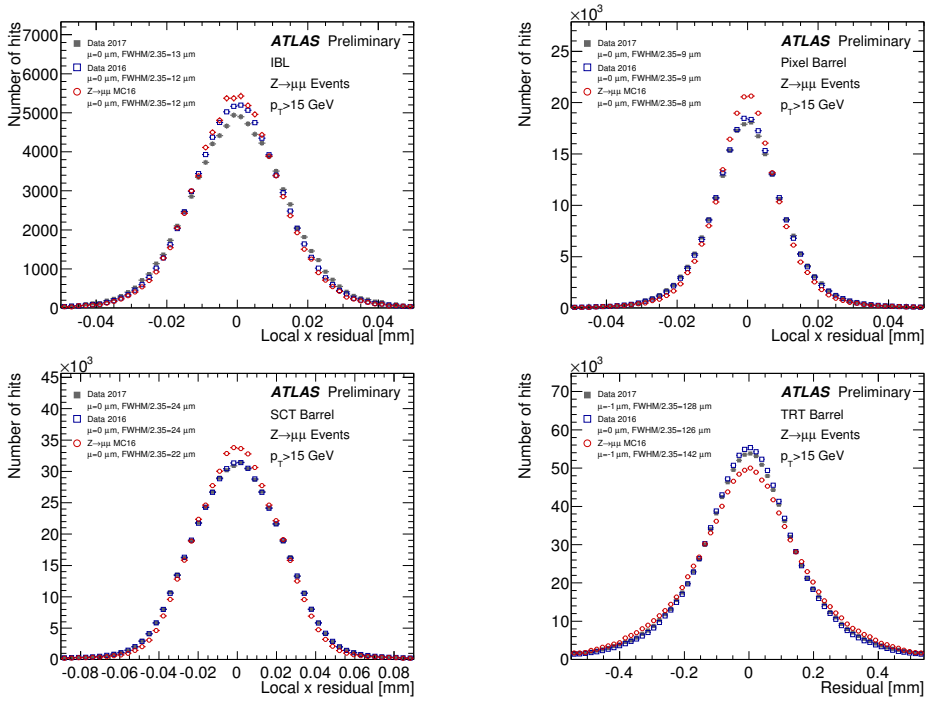

Figure 3.24: The residuals of the IBL, Pixel, SCT and TRT sub-detectors for 2017 data (gray squares) have been extracted with a sample of $Z \to \mu^+\mu^-$ events. Very similar residuals were found to the residuals obtained in the final 2016 reprocessed data (open squares) and a Monte Carlo simulated sample containing $Z \to \mu^+\mu^-$ events (open circles).

3.5.3 Run 2 alignment

Although this thesis focuses on the ATLAS Inner Detector alignment during early Run 2, it is worth highlighting that the ATLAS Inner Detector has been aligned for the whole LHC Run 2 data set, covering the Runs taken by ATLAS from 2015 until 2018 [130]. The alignment campaigns during data-taking have been splitted for each of the years in several periods, depending on the feedback of the encountered biases. Right now, the alignment process is being reapplied to process all the data in a coherent way.

Track-based alignment considers the Global χ^2 method in the alignment parameters computation, starting from big structures and finishing at modules level. Additional constraints have derived and used by the ID alignment track-based algorithm throughout the Run 2 periods in which the ATLAS detector has recorded data. For each registered run during Run 2, both short-term and long-term movements have been monitored and corrected in a lumiblock basis. Dimuon resonances have been accounted as well, in order to check whether momentum and impact parameter biases remain after applying the track-based alignment algorithm.

Chapter 4

Probing the Wtb vertex

We present in this chapter the measurement of the asymmetry observables of angular distributions described in Chapter 1. As we have discussed in previous chapters, the Wtb vertex appears in both the production and decay of the top quark singly in t-channel electroweak production. Moreover, in this case, the top quarks are produced highly polarized. Because of the extremely short lifetime of the top quark, its spin information can be inferred through its decay products. The observables explored in this thesis are asymmetries defined from angular distributions using the top quark decay in three different directions that are sensitive to the Wtb production vertex. They are related with the top quark polarization components, thus probing the vertex at the production of the polarized top quark.

The data analyzed is from pp collisions at a center of mass energy of $\sqrt{s} = 13$ TeV collected by the ATLAS detector during the years 2015, 2016 and 2017, corresponding to an integrated luminosity of 80.5 fb^{-1}.

In this chapter, we first define the signal region enriched in t-channel events, with exactly one lepton, one non-b-tagged jet, one b-tagged jet and abundant $E_{\mathrm{T}}^{\mathrm{miss}}$ in the final state. The background and signal processes are estimated via Monte Carlo (MC) simulations or data-driven techniques. Control regions are defined to check the modelling of the main backgrounds of the analysis. In order to constrain the normalization of the background processes, the signal and control regions are fitted using a maximum-likelihood fit. Afterwards, using an iterative Bayes unfolding method, the measured background-substracted angular distributions are unfolded to particle level in a fiducial region. From these distributions, the angular asymmetries A_{FB}^{X}, A_{FB}^{Y} and A_{FB}^{Z} are determined and compared with the SM predictions calculated at particle level in the fiducial region using a NLO generator for the t-channel process.

4.1 Signal and background contamination

The first step of the analysis consists on defining a signal region enriched in t-channel events. The signal and background processes are estimated via MC and data-driven techniques.

4.1.1 Signal production

The top quark at the LHC is produced when a quark from the proton interacts with a b quark from the sea through the exchange of a W boson, and thus producing a light quark and a top quark. However, there are two different ways in which the top quark can be produced singly at leading-order (LO) depending on the origin of the b quark. These are depicted in Figure 4.1:

- The $2 \to 2$ process, $b + q \to q' + t$, known also as the 5-flavour scheme, considers with a b quark in the initial state.
- The $2 \to 3$ process, $g + q \to q' + t + b$, is the so-called 4-flavour scheme where the proton is considered to be composed of only four light quarks (u, d, c and s) and the b quarks arise from the splitting of a virtual gluon into nearly collinear $b\bar{b}$. In this scheme, the $\bar{b}$ quark in the final state (usually called spectator b quark or second b-jet) is characterized by its soft transverse momentum spectrum, being most of the time outside the kinematic acceptance.

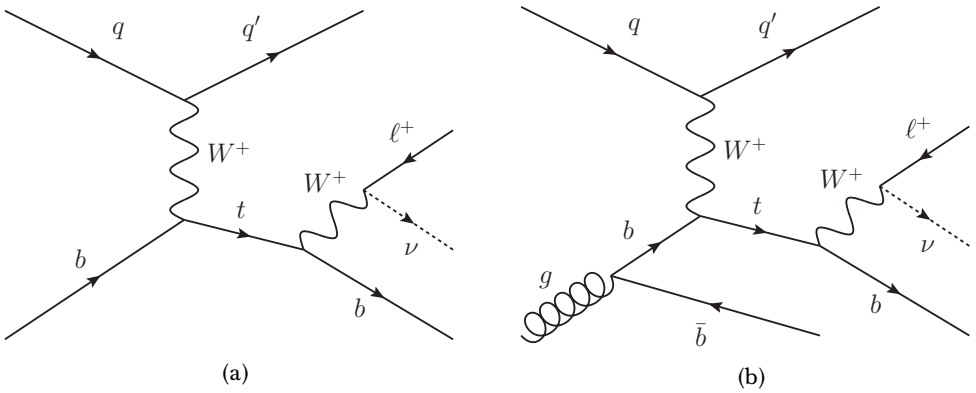

Figure 4.1: Leading-order Feynman diagrams for t-channel production of single top quarks in pp collisions: (a) $2 \to 2$ process (five-flavour scheme) and (b) $2 \to 3$ process (four-flavour scheme). The leptonic decay of the top quark ($t \to Wb$ with $W \to l\nu$) is also displayed.

The single top quark produced in the t-channel decaying to ℓ+jets (i.e. $t \to Wb$ where $W \to \ell\nu$, standing ℓ for e, μ) is our signal process. Events in which the W boson decays into a τ lepton (which happens about 30% [29] of the time in the ℓ+jets

channel) are also included if the τ lepton decays subsequently to an electron or a muon (i.e. $\tau \to e\nu_e\nu_\tau$ or $\tau \to \mu\nu_\mu\nu_\tau$)[1].

Therefore, signal events with a single top quark produced in the t-channel with a leptonic W boson decay leave a signature characterized by the presence of two jets, one of them being identified as a b-jet and a light forward jet, exactly one lepton and missing transverse momentum corresponding to the neutrino.

4.1.2 Background contamination

There are however events from other sources than the single top t-channel production that can mimic the signal signature, as shown in Figure 4.2:

- Top quark processes: these include both single top quarks created via electroweak interaction (such as s-channel or tW-channel) and $t\bar{t}$ processes strongly produced, which constitute the main background. The main feature from such processes is that they are hard to distinguish from the signal since they contain real top quarks in the final state.
- W+jets production: production of a real W boson in association with heavy flavor ($W + b\bar{b}$ and $W + c\bar{c}$) or light flavor quark jets. An example of a W+jets process is shown in Figure 4.2 (a).
- Z+jets production: production of a real Z boson in association with heavy flavor ($Z + b\bar{b}$ and $Z + c\bar{c}$) or light flavor quark jets. An example of a Z+jets process is shown in Figure 4.2 (b).
- Diboson production: electroweak production of diboson VV (WW , ZZ or ZW). An example of a ZW production process is shown in Figure 4.2 (c).
- Multijet production: events originating from QCD production in which one of the jets is misidentified as fake lepton. Such process is shown in Figure 4.2 (d) as an example.

4.2 Data and simulated event samples.

4.2.1 Data samples

This analysis is performed using data of proton-proton collisions recorded in the ATLAS detector at a center-of-mass energy of 13 TeV from 2015 until 2017, corresponding to an integrated luminosity of 80.5 fb^{-1}. The registered data must have passed through ATLAS data quality requirements for all the detectors. Table 4.1 summarizes the integrated luminosities for each year.

[1] Tau leptons decay 17.83% in an electron and 17.41% in a muon. In the remaining 64.76%, taus decay hadronically, and therefore it may be identified as a jet.

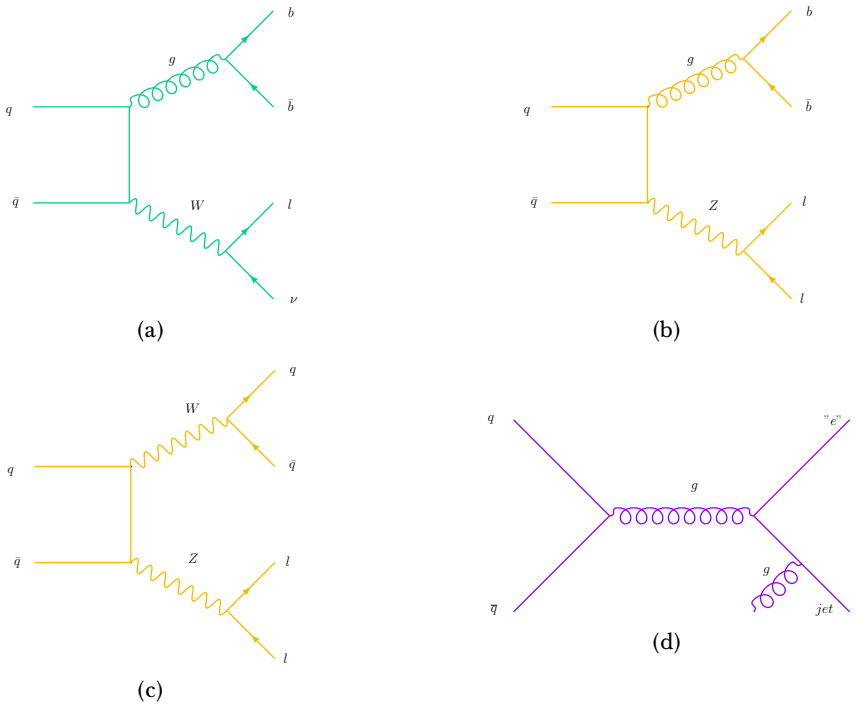

Figure 4.2: Feynman diagrams representing the main backgrounds (apart from top quark processes) of the single top t-channel signatures: (a) W+jets , (b) Z+jets, (c) Diboson and (d) Multijet production.

The electron and muon triggers impose a p_T thresold such that it requires at least one lepton with $|\eta| \leq 2.5$. On the one hand, the electron triggers impose a thresold such that $E_{\mathrm{T}} > 24$ GeV, requiring an isolation criteria with medium identification. In 2016–2017, electrons had to satisfy $E_{\mathrm{T}} > 26$ GeV together with an isolation criteria with a tight identification. Two additional triggers were also available for electrons, selecting medium electrons with $E_{\mathrm{T}} > 60$ GeV and selecting loose electrons (i.e. without isolation requirement) with $E_{\mathrm{T}} > 120$ GeV in 2015 and $E_{\mathrm{T}} > 140$ GeV in 2016–2017. On the other hand, muon triggers impose a thresold above $p_{\mathrm{T}} > 20$ GeV and had to satisfy a loose isolation requirement. In 2016–2017, the isolation criterion was tightened and the threshold increased to $p_{\mathrm{T}} > 26$ GeV. Muon trigger without any isolation requirement was available too, by selecting loose muons such that $p_{\mathrm{T}} > 50$ GeV. The corresponding single-lepton trigger configuration is summarised in Table 4.2.

4.2.2 Simulated event samples

Samples of signal and background events are generated using MC simulations using different event generators interfaced to various shower/hadronisation generators. Then, detector simulation is performed with the dedicated ATLAS software infras-

Year	Integrated luminosity [pb^{-1}]
2015	3219.56 $\pm$ 2.1%
2016	32988.1 $\pm$ 2.2%
2017	44307.4 $\pm$ 2.4%

Table 4.1: Integrated luminosity per year with their relative uncertainties. The uncertainty in the 2015, 2016 and 2017 integrated luminosities are 2.1%, 2.2% and 2.4%, respectively [131].

Year	Single-electron trigger	Single-muon trigger
2015	`HLT_e24_lhmedium_L1EM20VH`	`HLT_mu20_iloose_L1MU15`
	`HLT_e60_lhmedium`	`HLT_mu50`
	`HLT_e120_lhloose`	
2016–2017	`HLT_e26_lhtight_nod0_ivarloose`	`HLT_mu26_ivarmedium`
	`HLT_e60_lhmedium_nod0`	`HLT_mu50`
	`HLT_e140_lhloose_nod0`	

Table 4.2: HLT trigger selections of the ATLAS trigger menu per lepton flavour per year. These triggers are combined using a logical "or". The electron and muon triggers impose a p_T thresold, which is displayed in the name configuration. During 2015 the single-lepton triggers selected medium lepton, while in 2016–2017 the criterion was tightened. Muon and electron triggers without any isolation requirement were made available too in order to avoid efficiency losses.

tructure (named `Athena`) [132] and using the GEANT4 [133] framework. Some samples are however fast simulated using `ATLFASTII` [134] framework (simply named as AFII), that provides fast simulated events by considering a parametric cell response of the ATLAS calorimeters. Table 4.3 displays a summary of the baseline features in all the generated processes.

Process	Generator	Parton shower	PDF	tune	Detector
t-channel	PowhegBox	Pythia 8	NNPDF3.0NLO	A14	FullSim
t-channel	LO Protos	Pythia 8	CTEQ6L1	A14	AFII
Wt-channel	PowhegBox	Pythia 8	NNPDF3.0NLO	A14	FullSim
s-channel	PowhegBox	Pythia 8	NNPDF3.0NLO	A14	FullSim
$t\bar{t}$-channel	PowhegBox	Pythia 8	NNPDF3.0NLO	A14	FullSim
WW,WZ,ZZ	LO Sherpa	Sherpa	NNPDF3.0NLO	-	AFII
W/Z+jets	LO Sherpa	Sherpa	NNPDF3.0NLO	-	AFII

Table 4.3: Table summarising the baseline samples used in the analysis per process.

The effect of multiple interactions in the same and neighbouring bunch crossings (pile-up) is modelled by overlaying simulated minimum-bias events generated with Pythia 8 (v8.186) [135] using the NNPDF2.3LO parton distribution function (PDF) [136] and the A3 tune [137] over the original hard-scattering event.

In this analysis, samples of events generated using MC simulations were produced for t-channel signal and background processes, and were used to evaluate models of signal efficiency and resolution, and to estimate systematic uncertainties.

4.2.2.1 Simulated t-channel signal event samples

The t-channel single top quark events are produced using the PowhegBox [138–141] v2 generator which provides matrix elements (ME) at next-to-leading order (NLO) in the strong coupling constant α_S in the 4FS with the NNPDF3.0NLOnf4 [142] PDF set. Following the recommendation of Ref. [138], the functional form of the renormalisation and factorisation scale is set to $\mu_R = \mu_F = 4\sqrt{m_b^2 + p_{T,b}^2}$, where m_b is the mass of the b-quark and $p_{T,b}$ is the transverse momentum of the spectator b-quark coming from the gluon splitting. Top quarks are decayed at LO using MadSpin [143,144] to preserve all spin correlations. The events are interfaced with Pythia 8 (v8.230) [145] using the A14 tune [146] and the NNPDF23LO PDF set in order to simulate the parton showering (PS), hadronisation and underlying-event (UE) modelling. The decays of bottom and charm hadrons are simulated using the EvtGen program [147].

The signal samples have been corrected to the theoretical prediction calculated at NLO in QCD with Hathor v2.1 [63, 64]. For pp collisions at $\sqrt{s} = 13$ TeV, this cross-section corresponds to $54.9^{+2.3}_{-1.9}$ pb and $29.7^{+1.7}_{-1.5}$ pb for top quark and antiquark production, respectively, using a top quark mass of $m_t = 172.5\,\text{GeV}$. The uncertainties on the cross-section due to PDF and α_s are calculated using the

PDF4LHC prescription [148] with the MSTW2008 68% CL NLO [149, 150], CT10 NLO [151] and NNPDF2.3 NLO [136] PDF sets, and are added in quadrature to the scale uncertainty.

Additional samples of simulated t-channel single top quark events were produced with the PROTOS LO generator[2] [3] using the CTEQ6L1 PDF sets [152]. Events generated using PROTOS were produced within the 4FS. The factorisation scale is set to $\mu_F^2 = -p_W^2$ for the spectator quark and $\mu_F^2 = p_{T,b}^2 + m_b^2$ for the gluon, p_W being the three-momenta of the exchanged W boson. Apart from a SM event sample, various event samples with different configuration of anomalous couplings in both the Wtb production and the decay vertices were produced. In each of the non-SM configuration, two couplings are varied simultaneously in order to maintain the top quark width invariant, as Table 4.4 shows. The ranges of the anomalous coupling event samples were selected based on previous established limits [81].

Protos anomalous couplings samples	A_{FB}^X	A_{FB}^Y	A_{FB}^Z
$\text{Re}(g_R)/V_L = +0.18$, $\text{Im}(g_R) = \text{Re}(V_R) = \text{Re}(g_L) = 0$	0.099	-0.002	0.365
$\text{Re}(g_R)/V_L = -0.18$, $\text{Im}(g_R) = \text{Re}(V_R) = \text{Re}(g_L) = 0$	-0.178	0.012	0.413
$\text{Im}(g_R)/V_L = +0.07$, $\text{Re}(g_R) = \text{Re}(V_R) = \text{Re}(g_L) = 0$	-0.040	-0.069	0.395
$\text{Im}(g_R)/V_L = -0.07$, $\text{Re}(g_R) = \text{Re}(V_R) = \text{Re}(g_L) = 0$	-0.054	0.080	0.397
$V_R/V_L = +0.4; g_L/V_L = +0.32$, $\text{Im}(g_R) = \text{Re}(g_R) = 0$	-0.099	-0.002	0.345
$V_R/V_L = -0.4; g_L/V_L = -0.32$, $\text{Im}(g_R) = \text{Re}(g_R) = 0$	-0.104	-0.007	0.340

Table 4.4: Configuration of the produced anomalous couplings Protos samples. The particle level truth prediction of the asymmetry observables (defined in Section 1.3) is presented for each sample in the fiducial region defined in Section 4.3.2. Each anomalous coupling sample has been produced assuming the Protos SM cross-section and k factors equal to 1.

4.2.2.2 Simulated background event samples

Various background processes can mimic the single top quark t-channel signal: the most important backgrounds for single top quark t-channel process in the lepton plus jets channel are top quark pair and W+jets production. The single top quark tW and s-channel productions also contribute to the backgrounds. Less significant backgrounds are multijet, Z+jets and diboson (WW, ZZ and WZ) processes.

In order to model the kinematic distributions of the SM background processes, a set of samples of simulated events using MC simulations have been used.

This subsection describes in detail all the background simulated event samples used in this analysis, except for the multijet background, which is estimated using data-driven techniques and that is discussed in Section 4.4.1.

[2] PROTOS (PROgram for TOp Simulations) is a generator for studying new physics processes involving the top quark. It has generators for single top quark and top quark pair production with anomalous Wtb couplings.

Top processes

The production of $t\bar{t}$ events, as well as, the single top quark tW associated production and the s-channel are modelled using the PowhegBox [139–141, 153] at next-to-leading order in the strong coupling constant α_S with the NNPDF3.0NLO [142] PDF set. For the $t\bar{t}$, the h_{damp} parameter, which is in charge of regulating the high-p_T radiation , is set to 1.5 m_t [154]. In the tW associated production, the diagram removal scheme [155] is employed to handle the interference with $t\bar{t}$ production [154]. The functional form of the renormalisation and factorisation scale is set to the default scale $\sqrt{m_t^2 + p_T^2}$. The events are interfaced with Pythia 8 8.230 [145] for the parton shower and hadronisation, using the A14 set of tuned parameters [146] and the NNPDF23LO PDF set. The decays of bottom and charm hadrons are simulated using the EvtGen v1.6.0 program [147].

The NLO $t\bar{t}$ inclusive production cross-section is corrected to the theory prediction at next-to-next-to-leading order (NNLO) in QCD including the resummation of next-to-next-to-leading logarithmic (NNLL) soft-gluon terms calculated using Top++2.0 [54, 156–161]. For pp collisions at $\sqrt{s} = 13$ TeV, this cross-section corresponds to 832 ± 51 pb using a top quark mass of $m_t = 172.5$ GeV. The uncertainties on the cross-section due to PDF and α_S are calculated using the PDF4LHC prescription with the MSTW2008 68% CL NLO [149, 150], CT10 NNLO [151, 162] and NNPDF2.3 5f FFN [136] PDF sets, and are added in quadrature to the scale uncertainty.

The inclusive cross-section of the tW associated production is corrected to the theory prediction calculated at NLO in QCD with NNLL soft gluon corrections [63, 64]. For pp collisions at $\sqrt{s} = 13$ TeV, this cross-section corresponds to 71.7 ± 3.8 pb, using a top quark mass of $m_t = 172.5$ GeV. The uncertainty on the cross-section due to PDF is calculated using the MSTW2008 90% CL [149, 150] NNLO PDF set, and is added in quadrature to the scale uncertainty.

For the s-channel process, the inclusive cross-section is corrected to the theory prediction calculated at NLO in QCD with Hathor (v2.1). For pp collisions at $\sqrt{s} = 13$ TeV, this cross-section corresponds to $6.35^{+0.23}_{-0.20}$ pb and $3.97^{+0.19}_{-0.17}$ pb for top quark and top-antiquark production, respectively, using a top quark mass of $m_t = 172.5$ GeV. The uncertainties on the cross-section due to PDF and α_S are calculated using the PDF4LHC prescription with the MSTW2008 68% CL NLO , CT10 NLO and NNPDF2.3 NLO PDF sets, and are added in quadrature to the scale uncertainty

Single-boson processes

A production of a vector boson, W or Z, in association with jets production (a.k.a W/Z+jets) is another important background in this analysis and it simulated at LO with the Sherpa [163] parton shower Monte Carlo generator with its own set of tuned parton-shower parameters and NNPDF3.0 NNLO [142].

The CKKW matching procedure [164,165] is used to remove overlaps obtained during the matrix element and the parton showering for several jets multiplicities.

The $W/Z+$ jets samples are normalised to a next-to-next-to-leading order prediction [166]. A normalisation uncertainty of 20% is assigned to the W+jets background. This uncertainty is estimated from parameter variations of the SHERPA generator covering the measured W+jets cross-sections [167].

Diboson processes

Finally, diboson samples of WW, WZ and ZZ can also contribute to the t-channel signal as a non-negligible background. They are simulated with the LO SHERPA [163] parton shower MC generator. The NNPDF3.0 NNLO set [142] of PDFs as well as the dedicated set of tuned parton-shower parameters developed by the SHERPA authors for this version are used. A normalisation uncertainty of 20% is also assumed for the diboson processes.

4.2.2.3 Samples to evaluate signal and background modelling uncertainties

For the study of systematic uncertainties in the modelling of processes involving top quarks, either alternative generators from the nominal POWHEGBOX can be used, or alternative parton showering models from the nominal PYTHIA 8 can be used too. For the $t-$channel parton showering uncertainty, a POWHEGBOX sample interfaced with HERWIG 7 [168,169] were produced using the H7UE set of tuned parameters [169] and the MMHT2014LO PDF set [170]. For the $t-$channel matrix element uncertainty, MADGRAPH5_AMC@NLO sample interfaced with PYTHIA 8 was produced at next-to-leading order in the strong coupling constant α_S in the four flavour scheme with the NNPDF3.0NLOnf4 [142] parton distribution function.

For the $t\bar{t}$, s-channel and tW processes, in order to assess the uncertainty due to the choice of the matching scheme, alternative samples were produced using MADGRAPH5_AMC@NLO interfaced with PYTHIA 8. The NNPDF2.3LO PDF set is used as well as the A14 tune [146]. For the impact of the parton shower, a POWHEGBOX sample interfaced with HERWIG 7 was produced using the H7UE set of tuned parameters [169] and the MMHT2014LO PDF set [170].

The uncertainty due to radiation variations in the initial and final state (ISR and FSR, respectively) is estimated changing the hard-process and the parton shower simultaneously: to simulate higher parton radiation, the factorisation and renormalisation scales μ_F and μ_R are varied by a factor of 0.5 in the matrix element while using the Var3c up variation from the A14 tune [146]. For lower parton radiation, μ_R and μ_F are varied by a factor of 2.0 while using the Var3c down variation in the parton shower. In $t\bar{t}$ samples, h_{damp} is set to $1.5m_t$ or $3m_t$ to the Var3c up and down variations, respectively.

4.3 Event selection and fiducial region at particle level

4.3.1 Event selection

The signal event selection in this analysis is done in a two step procedure:

In the so-called *pre-selection* signal candidates are selected on the level of the basic physics objects defined in Section 4.3.1.1 according to the signal topology explained in Section 4.1.

Next, the so-called *selection* takes place. In this step requirements are defined in order to enhance the presence of the t-channel signal events over background events.

However, in order to monitor and constrain the main backgrounds of our signal, further regions with different selection need to be defined. In these so-called *control regions* the modelling of the main backgrounds (i.e. $t\bar{t}$ and W+jets) is validated for the shape of the angular distributions. They are also used to constrain the normalization of the dominant backgrounds.

4.3.1.1 Object selection

The object reconstruction was explained in detail in Section 2.4 and in the following a summary is given for the object selection done in this analysis at reconstruction level. Particle level objects are introduced afterwards, since this analysis is performed at particle level using unfolding techniques.

Reconstruction level objects definition

Electrons are reconstructed from clusters of energy deposits in the electromagnetic calorimeter cells with the corresponding matched ID track [171]. Electrons must satisfy the tight identification criteria and their tracks must point to the primary vertex [171]. They are required to have $p_T > 27$ GeV and $|\eta_{cluster}| < 2.47$, excluding $1.37 < |\eta_{cluster}| < 1.52$, being $|\eta_{cluster}|$ the pseudorapidity of the electron's energy cluster. Muons are in this analysis reconstructed by combining a track in the MS with a track in the ID [128]. They are required to meet the medium identification criteria [128] and must point to the primary vertex. They are required to have $p_T > 27$ GeV and $|\eta| < 2.5$. Selected electrons and muons must also be isolated. This is obtained when requiring that the amount of energy in nearby energy deposits in the calorimeters and the scalar sum of the transverse momenta of nearby tracks in the ID to be small.

Jets are reconstructed from topological clusters [109] in the calorimeters with a radius parameter of 0.4 through the anti-k_t algorithm [110] using FastJet [172]. The energy of the jets is calibrated with a series of simulation-based corrections and in situ techniques [111]. In addition, jets must fulfil $p_T > 25$ GeV and $|\eta| < 2.5$. In order to suppress pile-up jets, those jets with $p_T < 120$ GeV and $|\eta| < 2.4$ are required to pass a requirement on the jet-vertex-tagger (JVT) [173] . Jets are b-tagged using the MV2c10 algorithm [174], which uses a boosted decision tree based

on several b-tagging algorithms. The b-tagging efficiency for jets that originate from the hadronisation of b-quarks is 60% in simulated $t\bar{t}$ events. The mistagging rates for jets that originate from the hadronisation of c-quarks and light quarks are predicted to be 4.3% and 0.08%, respectively, in simulated $t\bar{t}$ events.

To avoid double-counting, an overlap removal technique is applied on objects. They are removed in the following order: electrons sharing a track with a muon; jets within $\Delta R = 0.2$ of an electron; electrons within $\Delta R = 0.4$ of a jet; jets within $\Delta R = 0.4$ of a muon if they have at most two associated tracks; muons within $\Delta R = 0.4$ of a jet; photons within $\Delta R = 0.4$ of an electron or muon; jets within $\Delta R = 0.4$ of a photon.

The magnitude of the missing transverse momentum $E_{\mathrm{T}}^{\mathrm{miss}}$ is reconstructed from the vector sum of the p_T of leptons, photons, and jets from information contained in the calorimeter energy deposits and ID tracks. These are combined with ID tracks that point to the primary vertex but are not associated with a reconstructed object, which is known as soft term [175].

Particle level objects definition

The particle-level objects are constructed from Monte Carlo using stable particles, that is those events with a lifetime larger than 0.310^{-10} s.

Particle-level leptons are defined as electrons or muons originate from a W boson decay, including those emerging from a subsequent tau decay. However, since certain MC generators do not include W bosons in the MC record, an implicit W-boson match is employed to assure applicability. This implicit requirement excludes leptons from hadronic decays, either directly or via a tau decay. The remaining leptons are assumed to come from a W boson decay. The selected leptons are dressed with photons within a cone of size $\Delta R = 0.1$, which implies that their final four-momenta are the vector sum of the dressing photons and their original lepton four-momenta. In order to simulate the electron/muon track match requirement (i.e. the overlap removal between electrons and muons), events are rejected if a matching in ϕ and θ of 0.005 is found between these two particle-level objects.

Particle-level neutrinos are treated as detectable particles and are considered in the same way as electrons or muons. This means that their parents are required not to be a hadron or quark. The $E_{\mathrm{T}}^{\mathrm{miss}}$ is calculated from the vector sum of all the considered neutrinos.

Particle-level jets are reconstructed using the anti-k_t algorithm with a radius parameter of 0.4 using FastJet [176]. All stable particles are used to reconstruct the jets, except the selected leptons, neutrinos and the photons associated with these leptons. A particle-level jet is identified as b-jet, if the jet is within $|\eta| < 2.5$ and a B-hadron is associated with a ghost-matching technique [177]. Events are rejected, if a selected particle-level lepton is identified within a cone of size $\Delta R = 0.4$ around a selected particle-level jet.

4.3.1.2 Signal preselection

The events contained in the pre-selection region are required to have :

- Significant missing transverse momentum.
- Exactly one isolated charged light lepton (electron or muon) with transverse momentum $p_{\mathrm{T}} > 30$ GeV and pseudorapidity $|\eta| < 2.5$.
- Exactly two jets: one of them a b-tagged jet with $|\eta| < 2.5$ and the other jet being an untagged jet with $|\eta| < 4.5$, both with $p_{\mathrm{T}} > 30$ GeV ($p_{\mathrm{T}} > 35$ GeV when $2.7 < |\eta| < 3.5$ to remove some mismodelling in the transition region between the central and forward calorimeter).

As mentioned in Section 2.4.4, the b-tagged jet is selected with the `MV2c10` tagger, with b-tagging efficiency of 60% for simulated $t\bar{t}$ events. The presence of a second b-quark originated from gluon splitting (as shown in Figure 4.1) is not considered, since this additional jet generally has a softer p_{T} spectrum and a broader η distribution compared to the b-tagged jet produced in the top-quark decay. Therefore, it is often not detected in the experiment and it is thus not required in the event selection. The magnitude of the missing transverse momentum must be $E_{\mathrm{T}}^{\mathrm{miss}} > 35$ GeV.

In addition, events are required to contain at least one good primary-vertex candidate, and no bad jets, referred to those failing to satisfy reconstruction quality criteria [178].

To further reduce the multijet background contribution, two additional multijet background rejection criteria are applied. The transverse mass of the lepton–$E_{\mathrm{T}}^{\mathrm{miss}}$ system,

$$m_{\mathrm{T}}(W) = \sqrt{2p_{\mathrm{T}}(\ell)E_{\mathrm{T}}^{\mathrm{miss}}\left(1 - \cos\Delta\phi(p_{\mathrm{T}}(\ell), E_{\mathrm{T}}^{\mathrm{miss}})\right)},$$

is required to be larger than 60 GeV. In the previous expression, $\Delta\phi\left(p_{\mathrm{T}}(\ell), E_{\mathrm{T}}^{\mathrm{miss}}\right)$ is the difference in azimuthal angle between the p_{T} of the lepton and the $E_{\mathrm{T}}^{\mathrm{miss}}$. Also, a more stringent isolation cut on the lepton p_{T} is applied to low p_{T} leptons:

$$p_{\mathrm{T}}(\ell) > 50\left(1 - \frac{\pi - |\Delta\phi(j_1, \ell)|}{\pi - 1}\right)\ \text{GeV},$$

where $\Delta\phi(j_1, \ell)$ is the difference in azimuthal angle between the lepton p_{T} and the leading jet in p_{T}.

This set of preselection requirements defines the preselected signal region.

4.3.1.3 Reconstruction of the W boson and top quark

The definition of the angular observables used in this analysis relies heavily on the kinematics of the W boson and the top quark. They are reconstructed from the identified objects at both detector and particle level.

Since the W boson decays $W \to \ell\nu$, the lepton and neutrino four-momentum are used to reconstruct the W boson:

$$\begin{aligned}(p^W)^2 = (p^\ell + p^\nu)^2 \quad \to \quad m_W^2 &= m_\ell^2 + 2(E^\ell, \vec{p}^{\,\ell})(E^\nu, \vec{p}^{\,\nu}) \\ &= m_\ell^2 + 2(E^\ell E^\nu - \vec{p}^{\,\ell} \cdot \vec{p}^{\,\nu}) \ , \end{aligned} \tag{4.1}$$

where p, m, E and $\vec{p}$ represent the four-momentum, the mass, the energy and the momentum of the mother particle (represented as W) and child particles (represented as ℓ and ν depending on if it is the lepton or the neutrino).

Since the W boson decays to a neutrino and the latter escapes undetected, the $E_{\mathrm{T}}^{\mathrm{miss}}$ of the event is assumed to correspond to the transverse momentum of the undetected neutrino (i.e. $E_{\mathrm{T}}^{\mathrm{miss}} \equiv p_{\mathrm{T}}^{\nu}$)[3].

Therefore the neutrino energy can be expressed as:

$$(E^\nu)^2 = (p_x^\nu)^2 + (p_y^\nu)^2 + (p_z^\nu)^2 = (p_{\mathrm{T}}^\nu)^2 + (p_z^\nu)^2 \ ,$$

$$E^\nu = \sqrt{(E_{\mathrm{T}}^{\mathrm{miss}})^2 + (p_z^\nu)^2} \ ,$$

and its transverse momentum components are given by:

$$p_x^\nu = E_{\mathrm{T}}^{\mathrm{miss}} \cos\phi_{\ E_{\mathrm{T}}^{\mathrm{miss}}} \quad \text{and} \quad p_y^\nu = E_{\mathrm{T}}^{\mathrm{miss}} \sin\phi_{\ E_{\mathrm{T}}^{\mathrm{miss}}} \ ,$$

where $\phi_{\ E_{\mathrm{T}}^{\mathrm{miss}}}$ is the azimuthal angle associated with the missing transverse momentum.

After substituting the latter definitions in Eq. (4.1), it becomes:

$$\begin{aligned} m_W^2 &= m_\ell^2 + 2E^\ell E^\nu - 2\left(p_x^\ell p_x^\nu + p_y^\ell p_y^\nu + p_z^\ell p_z^\nu\right) \\ &= m_\ell^2 + 2E^\ell \sqrt{(E_{\mathrm{T}}^{\mathrm{miss}})^2 + (p_z^\nu)^2} \\ &\quad - 2\left(E_{\mathrm{T}}^{\mathrm{miss}}\left(p_x^\ell \cos\phi_{\ E_{\mathrm{T}}^{\mathrm{miss}}} + p_y^\ell \sin\phi_{\ E_{\mathrm{T}}^{\mathrm{miss}}}\right) + p_z^\ell p_z^\nu\right) \ . \end{aligned} \tag{4.2}$$

The longitudinal momentum of the neutrino, p_z^ν is then derived by applying the W boson pole mass (80.399 $\pm$ 0.023 GeV [29]) as a constraint in m_W in the latter equation. A quadratic expression in p_z^ν is reached after reordering the terms of Equation 4.2 :

$$a(p_z^\nu)^2 + bp_z^\nu + c = 0 \ \to \ \left\{ \begin{array}{l} a = (E^\ell)^2 - (p_z^\ell)^2 \ . \\ \\ b = p_z^\ell \left(-m_W^2 + m_\ell^2 - 2(p_x^\ell p_x^\nu + p_y^\ell p_y^\nu)\right) \ . \\ \\ c = (E^\ell)^2 (E_{\mathrm{T}}^{\mathrm{miss}})^2 - \frac{1}{4}\left(m_W^2 - m_\ell^2 + 2(p_x^\ell p_x^\nu + p_y^\ell p_y^\nu)\right)^2 \ . \end{array} \right\}$$

[3] Although it is true that the neutrino is the main contributor to the $E_{\mathrm{T}}^{\mathrm{miss}}$ at LO, there are more contributors, such as extra neutrinos (from B-hadrons and τ decays), additional p_{T} contributions (ISR/FSR effects, etc), miscalibration of $E_{\mathrm{T}}^{\mathrm{miss}}$, fake missing $E_{\mathrm{T}}^{\mathrm{miss}}$ due to the detector energy resolution and acceptance, etc.

whose solutions are namely the longitunal neutrino momentum p_z^ν:

$$p_z^\nu = \frac{p_z^\ell \left(m_W^2 - m_\ell^2 + 2(p_x^\ell p_x^\nu + p_y^\ell p_y^\nu)\right) \pm \sqrt{\Delta}}{2\left((E^\ell)^2 - (p_z^\ell)^2\right)} \,, \tag{4.3}$$

where:

$$\Delta \equiv (E^\ell)^2 \left[\left(m_W^2 - m_\ell^2 + 2(p_x^\ell p_x^\nu + p_y^\ell p_y^\nu) \right)^2 - 4(E_{\mathrm{T}}^{\mathrm{miss}})^2((E^\ell)^2 - (p_z^\ell)^2 \right] \,.$$

Depending on the values that Δ can take, there are three different solutions:

- $\Delta = 0$: a single p_z^ν value is chosen.
- $\Delta > 0$: the lower p_z^ν value of the two obtained solutions is chosen.
- $\Delta < 0$: the magnitude of the measured $E_{\mathrm{T}}^{\mathrm{miss}}$ is re-scaled until a physical solution is obtained by decreasing the $E_{\mathrm{T}}^{\mathrm{miss}}$ (i.e. p_{T}^ν) step by step until the Δ term becomes positive so that a real pair of solutions is found. This decreasing is performed while preserving the $E_{\mathrm{T}}^{\mathrm{miss}}$ direction $(\cos\phi\ _{E_{\mathrm{T}}^{\mathrm{miss}}}, \sin\phi\ _{E_{\mathrm{T}}^{\mathrm{miss}}})$ and using the $m_{\mathrm{T}}(W)$ pole mass constraint. In other words, one can solve the discriminant equation (i.e. $\Delta = 0$) in terms of $E_{\mathrm{T}}^{\mathrm{miss}}$. The solution of this equation is denoted as $E_{\mathrm{T}}^{\mathrm{miss}\prime}$:

$$E_{\mathrm{T}}^{\mathrm{miss}\prime} = \frac{-(-m_W^2+m_\ell^2)(p_x^\ell \cos\phi\ _{E_{\mathrm{T}}^{\mathrm{miss}}} + p_y^\ell \sin\phi\ _{E_{\mathrm{T}}^{\mathrm{miss}}}) \pm (-m_W^2+m_\ell^2)\sqrt{(E^\ell)^2-(p_z^\ell)^2}}{2\left[(E^\ell)^2-(p_z^\ell)^2-(p_x^\ell \cos\phi\ _{E_{\mathrm{T}}^{\mathrm{miss}}} + p_y^\ell \sin\phi\ _{E_{\mathrm{T}}^{\mathrm{miss}}})^2\right]}. \tag{4.4}$$

If just one solution for $E_{\mathrm{T}}^{\mathrm{miss}\prime}$ is positive, this is the one which is chosen. If the two solutions for $E_{\mathrm{T}}^{\mathrm{miss}\prime}$ are positive, the one closer to the initial $E_{\mathrm{T}}^{\mathrm{miss}}$ is taken. Once this new $E_{\mathrm{T}}^{\mathrm{miss}\prime}$ is calculated it is increased by few eV so that $\Delta > 0$. This new $E_{\mathrm{T}}^{\mathrm{miss}}$ value is used to obtain the final value of p_z^ν.

Once the four-momentum of the neutrino is fully determined, the four-momentum of the W boson can be reconstructed. The kinematics of the top-quark candidate is reconstructed by combining the four-momentum of the reconstructed W boson with the four-momentum of the selected b-tagged jet. Events with exactly two jets are selected, one of them being b-tagged, therefore there is no ambiguity in the association of jets to quarks.

$$t \quad \rightarrow \quad Wb \quad \rightarrow \quad (p^t)^2 = (p^W + p^b)^2. \tag{4.5}$$

4.3.1.4 Event selection in the signal region

In addition to the signal event preselection, further discrimination between single top-quark t-channel events and background events can be achieved by applying additional requirements:

- The invariant mass of the lepton–b-jet system, $m_{\ell b}$, is required to be lower than 153 GeV, to reject background events from processes not involving top quarks.
- The invariant mass of the reconstructed top quark from its decay products, $m(\ell\nu b)$, is required to be within 134–206 GeV, to also reject background events from processes not involving top quarks.
- A trapezoidal requirement is also requested in order to reject background events, which have leptons in the forward region in events with central reconstructed top-quarks. These requirements are:

$$\eta_j < \eta_{top}4 + a \cap \eta_j > \eta_{top}4 - a \tag{4.6a}$$
$$\eta_j > \eta_{top}0.44 + b \cup \eta_j < \eta_{top}0.44 - b \tag{4.6b}$$

  where parameters a and b are 9 and 2, respectively. The trapezoidal cut procedure can be seen in Figure 4.4.
- The mass of the spectator jet–top-quark system, m_{jt}, is required to be greater than 280 GeV, to reject also background events from processes not involving top quarks.
- The sum of the p_{T} of all final-state objects, H_{T}, must be larger than 170 GeV.

These selection requirements have been obtained optimising the expected signal-to-background ratio at $\sqrt{s} = 13$ TeV, by mantaining the statistical significance [179]. These criteria and the basic event selection together define the t-channel signal region of the analysis.

Figure 4.3 shows the shape comparison between the t-channel signal and the main backgrounds at preselection level for the variables used in the selection requirements, except for the trapezoidal cut performance, whose performance is shown in Figure 4.4.

Figure 4.5 shows the same distributions, comparing data to the predicted signal and background distributions normalized to the results of the maximum-likelihood fit discussed in Section 4.4.2. The multijet background estimate shown in the Figure 4.5 is discussed in Section 4.4.1.

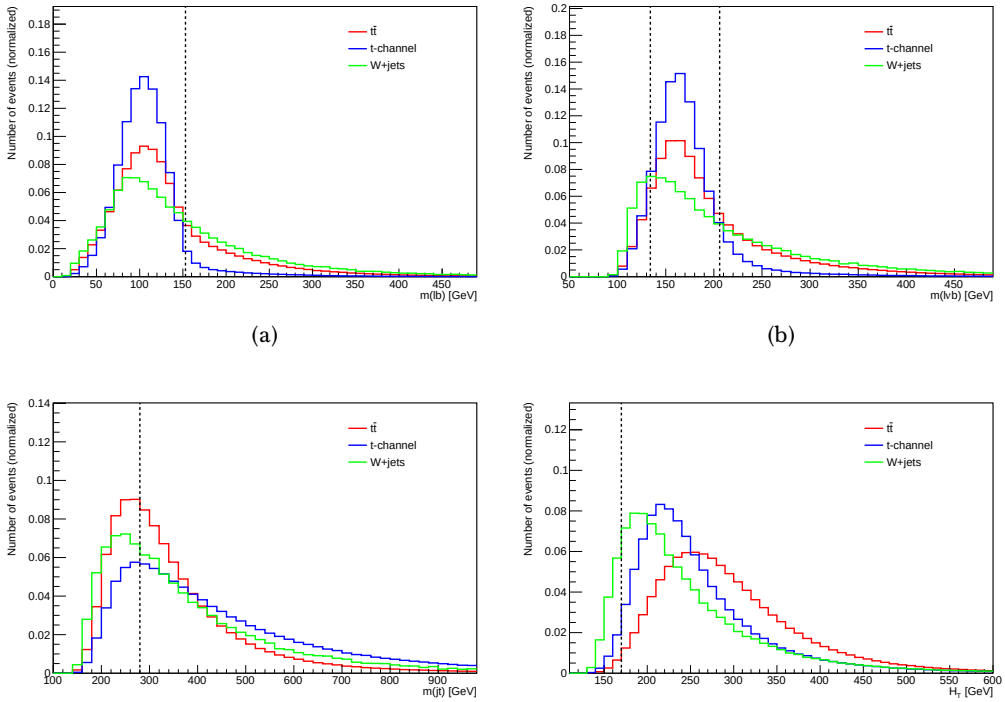

Figure 4.3: Shape distributions of the selection variables in the pre-selection region for the signal and main backgrounds: (a) the invariant mass of the lepton-b-jet system, (b) the invariant mass of the reconstructed top quark, (c) the invariant mass of the spectator jet-top-quark system, (d) the scalar sum of the lepton, the jets and the $E_{\mathrm{T}}^{\mathrm{miss}}$ The distributions are normalized to one. The vertical dashed line represents the thresolds required for each distribution.

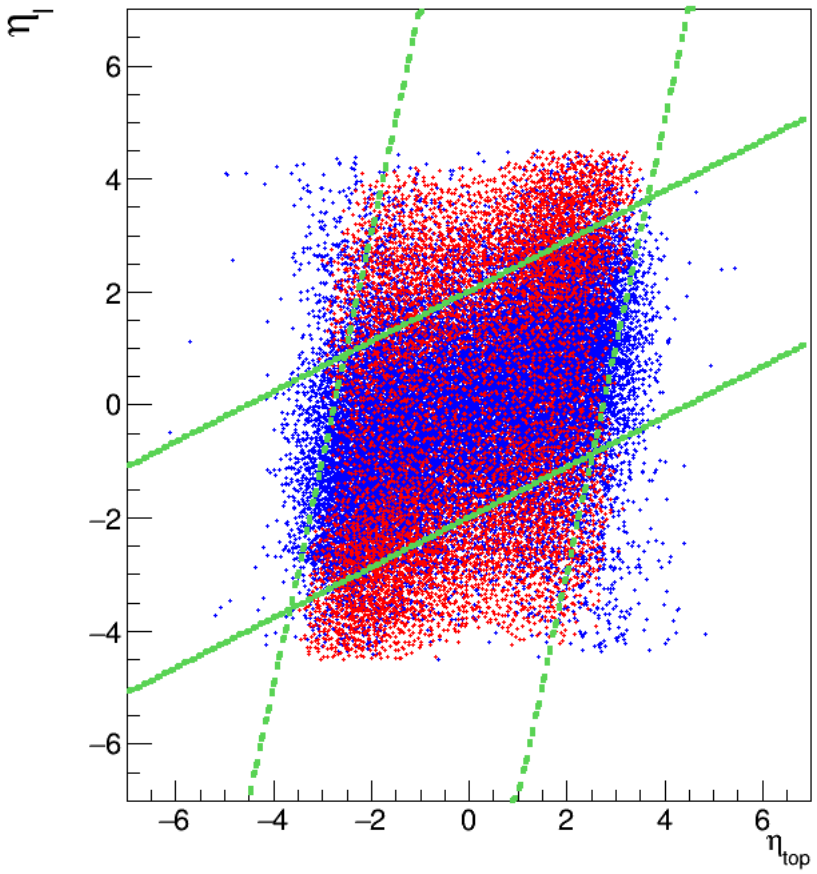

Figure 4.4: Two dimensional correlations among the pseudorapidity of the light forward jet η_j and the one of the reconstructed top quark η_{top}. Trapezoidal cut with optimised intercepts: $a = 9$ and $b = 2$ overlaid has a significant power of optimizing the signal (red dots) and reducing the background (blue dots).

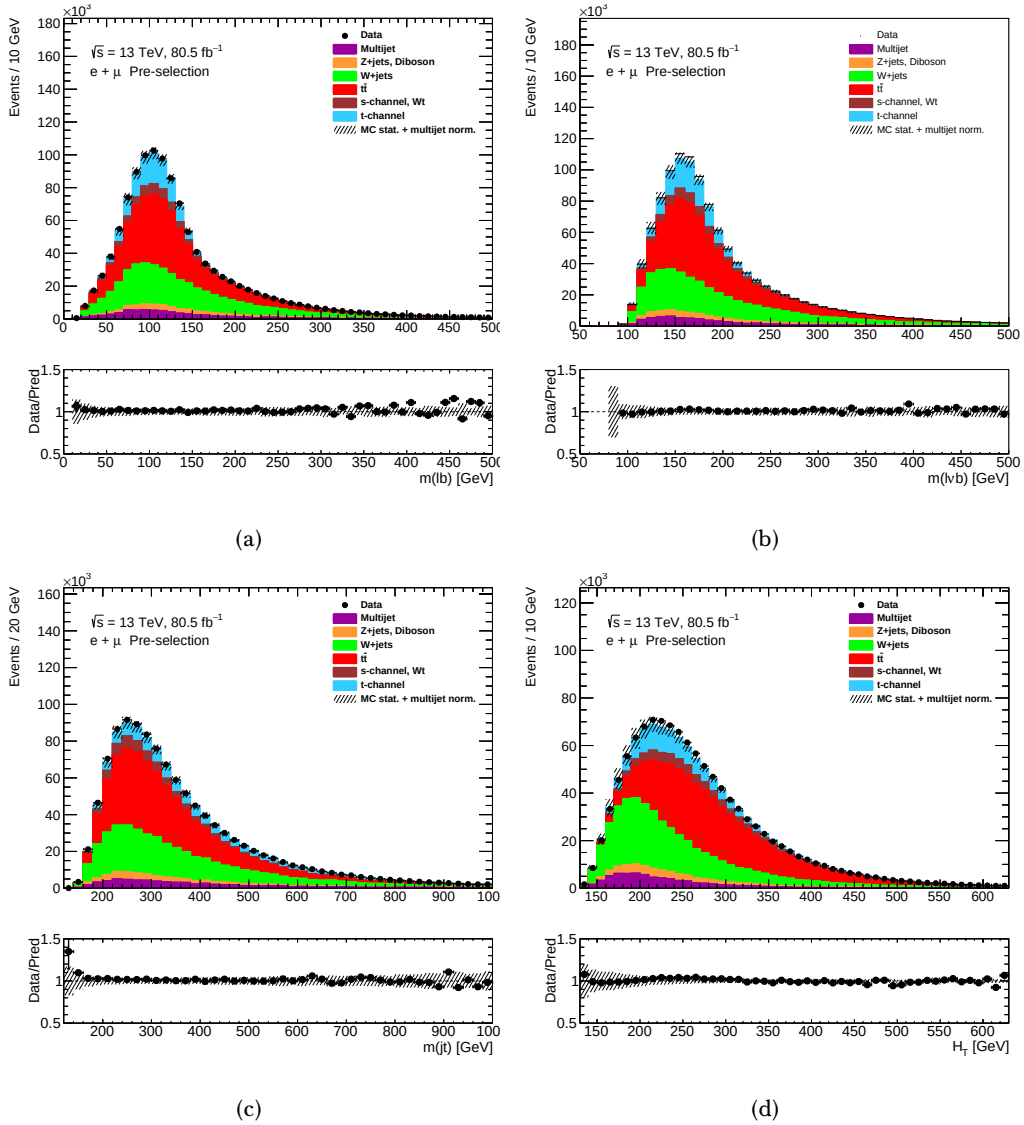

Figure 4.5: Kinematic distributions of the selection variables in the pre-selection region: (a) the invariant mass of the lepton-b-jet system, (b) the invariant mass of the reconstructed top quark, (c) the invariant mass of the spectator jet-top-quark system, (d) the scalar sum of the lepton, the jets and the $E_{\mathrm{T}}^{\mathrm{miss}}$. The uncertainty bands correspond to the errors due to the limited size of the simulation samples added in quadrature with the normalization uncertainty estimated for the multijet contribution. The lower panel shows the ratio of data to prediction.

4.3.1.5 Event selection in the control regions

In order to check the modelling shape of the main background contributions (i.e. $t\bar{t}$ and W+jets backgrounds) and to constrain their normalisation from data, dedicated background-enriched regions are defined.

These two specific background–enriched regions are:

- A control region enriched in $t\bar{t}$ events is defined by considering preselected events containing two jets being b-tagged. This definition guarantees that the dilepton $t\bar{t}$ composition is similar to that in the signal region.
- An enriched control region in W+jets events is defined in order to control the modelling of the W+jets background. This control region has a similar W+jets flavour composition to that of the signal region (in terms of W+light-jets and W+heavy-jets contribution). Events in this control region are selected by considering the preselection criteria and vetoing all the requirements of the signal selection shown in Section 4.3.1.4.

Figure 4.6 summarizes the relative expected contribution of the t-channel signal and different background processes in the signal and control regions. The expected contribution of the t-channel signal process in the signal region is about 42% as shown in Figure 4.6. The two main backgrounds, $t\bar{t}$ and W+jets contributions, that are expected to represent about almost 30% and 20%, respectively, in the signal region. In the W+jets control region the main contributions come from top quark pair production, representing around 41% of the total yield, and the W+jets production, with a contribution of 31%. In the $t\bar{t}$ control region, top quark pair events are expected to represent 77% of the total yield.

4.3.2 Fiducial region definition at particle level

The particle-level event selection uses the particle-level objects previously defined in Section 4.3.1.1. With the idea of defining a fiducial region as close as possible to the measured phase space (i.e. signal region at reconstruction level as discussed in Section 4.3.1.4), the particle-level event selection (i.e. fiducial region) requires exactly one particle-level lepton with $p_{\mathrm{T}} > 30$ GeV. Electrons must have $|\eta| < 2.47$ and not be in the calorimeter barrel—end-cap transition region, corresponding to $1.37 < |\eta| < 1.52$. Muons must have $|\eta| < 2.5$. Any additional lepton with $p_{\mathrm{T}} > 10$ GeV is rejected. There must be two particle-level jets with $p_{\mathrm{T}} > 30$ GeV and $|\eta| < 4.5$; exactly one of these jets must be b-tagged using the ghost-matching technique [177]. The particle $E_{\mathrm{T}}^{\mathrm{miss}}$ object is required to be larger than 35 GeV and the $m_{\mathrm{T}}(W)$ larger than 60 GeV. Finally, all the selection requirements discussed in Section 4.3.1.4 are also required at particle level.

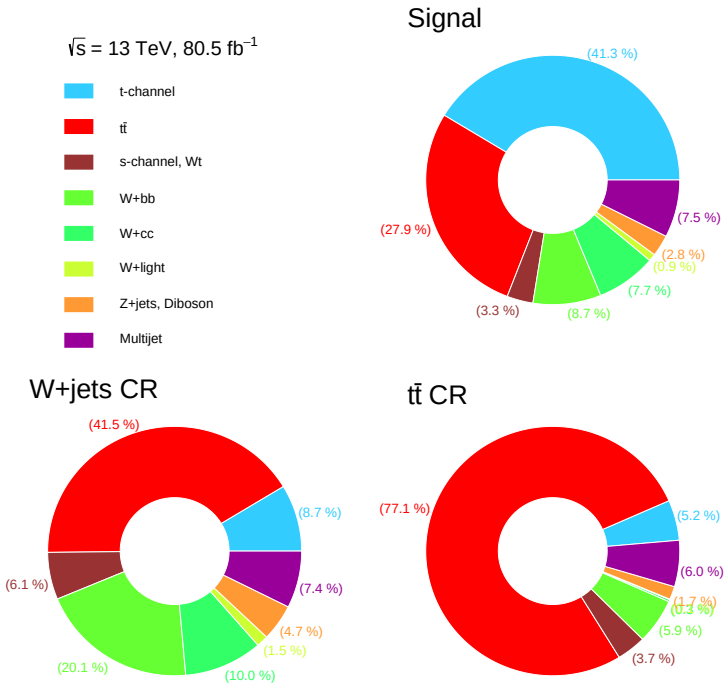

Figure 4.6: Comparison of the expected composition in the different control and signal regions. The contribution of W+jets is split in heavy flavor (W+bb and W+cc) and light flavor being displayed in green colors. s-channel and tW contributions are merged in brown, while Z+jets and dibosons are merged in orange.

4.4 Background estimation

For all the contributing processes, except multijet production, their MC predictions are initially normalised to their corresponding theoretical cross-sections predictions. The shape modelling is taken from the simulations. For the multijet production, the normalisation as well as the shape distribution is extracted by different means depending on whether the lepton signature is electron-like or muon-like. Next section covers the estimation of the multijet background in more detail.

4.4.1 Estimation of the multijet background

Multijet events can pass the t-channel selection if a jet is mis-identified as an isolated fake lepton, or a non-prompt lepton appears to be isolated. The normalisation of the multijet background can be extracted using a binned likelihood fit performed on the $E_{\mathrm{T}}^{\mathrm{miss}}$, where the shape of the multijet contribution is modelled either using the jet-electron model [180], which is built from a simulated di-jet sample, or using a purely data-driven anti-muon method [180]. The fitted parameters are the

normalisation factors associated with the multijet, W+jets and merged top quark contributions (i.e. $t\bar{t}$ and single top quark processes, including t-channel), where the shapes of these processes in the distribution of $E_{\mathrm{T}}^{\mathrm{miss}}$ are given by MC simulations. The Z+jets and diboson background components are fixed to their predicted values for both normalizations and shapes, which means that they are not allowed to vary in the fit. The used likelihood function is the same used in Section 4.4.2 and it includes Gaussian priors to constrain the normalisations of the W+jets and all top quark production processes, which are taken to their associated theoretical uncertainties: for the merged top quark processes, a constraint value of 6%, combining the theoretical cross-section uncertainties in proportion to the contribution of each individual process, is applied (a relative uncertainty of 4% is taken for the t-channel cross-section when combining its contribution); for the W +jets contribution, a constraint of 20% is considered. The multijet scale factor is a free (unconstrained) parameter of the fit.

In the jet-electron model, simulated events containing exactly one jet that fakes a signal (real) electron are selected, no additional signal leptons are required. This jet should have the same p_T thresold and the same η acceptance as a signal candidate electron and, in addition, it should deposit 80-100% of its energy in the electromagnetic calorimeter. The jet should also contain at least four tracks to reduce the contribution from converted photons. Additionally, no special trigger requirement is applied. Finally, a positive or negative charge, randomly drawn, is assigned to the jet-electron (a charge symmetric electron faking is assumed). The jet-electron selection is applied to simulated di-jet events in order to build a multijet model in the electron channel

For the muon channel, the anti-muon method allows to build a multijet model from pure collision data highly enriched in non-prompt muons mostly originated from the decay of heavy flavour hadrons. This is done by relaxing or inverting some of the muon identification cuts to select muons which are non-isolated. Events containing exactly one anti-muon candidate, without any signal leptons, are selected.

4.4.1.1 Fitting procedure

The binned likelihood fit is performed on the $E_{\mathrm{T}}^{\mathrm{miss}}$ distribution separately for two regions after having applied all the event selection requirements, but leaving out the $E_{\mathrm{T}}^{\mathrm{miss}}$ cut and the additional multijet rejecting cut in order to guarantee the highest number of multijet events (referred as *extended* regions). These extended regions are namely the pre-selection and $t\bar{t}$ regions. In the $t\bar{t}$ extended control region, the low contributions coming from W+jets processes are kept fixed to their theoretical predictions. Both W+jets and top processes are fitted in the extended preselection region. The $E_{\mathrm{T}}^{\mathrm{miss}}$ distribution shapes for the W+jets and top quark processes ($t\bar{t}$ and single-top quark, including t-channel) are given by the Monte Carlo simulations. The number of estimated multijet events is then determined in the region $E_{\mathrm{T}}^{\mathrm{miss}} > 30$ GeV. For the electron channel, as real electrons with a pseudorapidity falling in the electromagnetic crack region cannot be faked by the jet-electron model, the multijet normalisation estimates are derived separately for events with a central jet-electron ($|\eta| < 1.5$) and for events with a forward jet-electron ($|\eta| > 1.5$). Although the multijet estimates are extracted separately for the electrons and muon channels, the fitted W+jets and top quark scale factors are constrained to be the same for both channels.

The number of multijet events in the $t\bar{t}$ control region and in the the preselected signal containing exactly one jet-electron (central or forward) or exactly one anti-muon (estimated from the likelihood fit of the corresponding extended $E_{\mathrm{T}}^{\mathrm{miss}}$ distributions) are given in Table 4.5 for the $t\bar{t}$ region and preselected signal region. For the W+jets control region and signal region, the normalisation factors derived from the fit of the preselected signal events are used. The corresponding event yields are also listed in Table 4.5.

Channel	W+jets CR	$t\bar{t}$ CR	Preselection	Signal
Electron	36319	3004	39555	3234
Muon	39396	5934	43017	3620

Table 4.5: Multijet event yields estimated in the electron and muon channel with the jet-electron and anti-muon models. They are given for the W+jets control region, for the $t\bar{t}$ control region, and for the preselection and signal regions.

The fitted distributions of the $E_{\mathrm{T}}^{\mathrm{miss}}$ are displayed in Figures 4.7 and 4.8. They are shown for the $t\bar{t}$ enriched region, and for the enriched preselected signal events; the distributions associated with the central and forward jet-electrons are both fitted and thus displayed separately. The scale factors associated with the W+jets and the merged top quark contributions are reported in Table 4.6 with their statistical uncertainties, even though these scale factors are not extended to the next steps of the analysis (they are only used to estimate the multijet normalization).

By comparing the fit results in the preselected signal region and in the $t\bar{t}$ control region (without the $E_{\mathrm{T}}^{\mathrm{miss}}$ and the additional multijet rejecting cuts) with the results obtained by fitting an alternative distribution (m_{T}(W) in this analysis), an uncertainty of 70% is assigned for the fake leptons normalisation. The choice of the MC generator for $t\bar{t}$ processes leads to uncertainties of 50% for fake-electrons and 20% for fake-muons. These studies, together with the comparison of the predictions with data in different distribution shapes, indicate that a systematic uncertainty of 70% is representative of the overall impact of these sources. Such value is therefore used in both channels and all regions.

Process	$t\bar{t}$ CR	Preselection
W+jets	fixed	1.182±0.018
$t\bar{t}$,t-channel,Wt,s-channel	1.008±0.005	0.923±0.005

Table 4.6: Scale factors extracted for the W+jets and merged top quark contributions from the maximum-likelihood fit of the distributions of the $E_{\mathrm{T}}^{\mathrm{miss}}$ observed in the pre-selection extended region and in the $t\bar{t}$ extended control region. The uncertainty corresponds to statistical uncertainties provided by the likelihood fit.

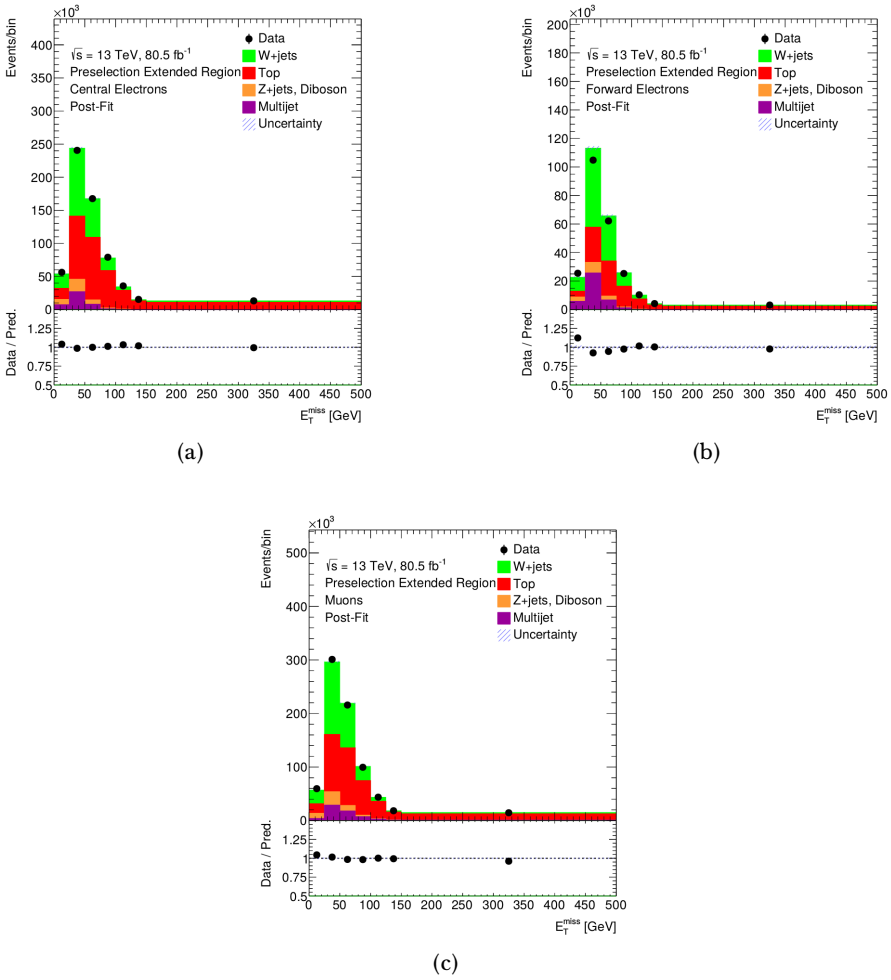

Figure 4.7: Distributions of the missing transverse momentum in the extended preselected signal region for (a) the central electron channel, (b) the forward electron channel, and (c) the muon channel. The observed distributions are compared to the predicted signal and background distributions. The predicted distributions are re-scaled using the fitted scale factors and the uncertainty bands correspond to the post-fit errors. The lower panel shows the ratio of data to prediction.

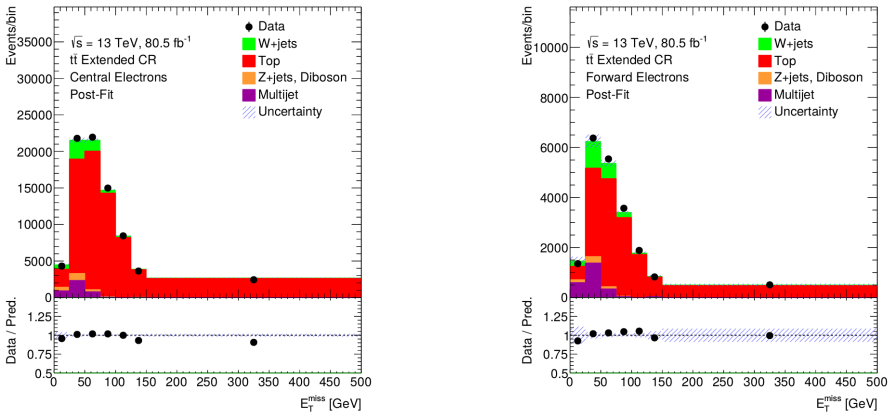

Figure 4.8: Distributions of the missing transverse momentum in the extended $t\bar{t}$ control region for (a) the central electron channel, (b) the forward electron channel, and (c) the muon channel. The observed distributions are compared to the predicted signal and background distributions. The predicted distributions are re-scaled using the fitted scale factors and the uncertainty bands correspond to the post-fit errors. The lower panel shows the ratio of data to prediction.

4.4.2 Overall normalisation constraints

The event yields of the signal and background processes are determined through a maximum-likelihood fit to the number of data events observed in the $t\bar{t}$ and W+jets control regions.

In the fit the top quark background ($t\bar{t}$, single top Wt and s-channel) contributions are merged with their relative fractions taken from simulation, and the applied constraint is derived from the combination of their cross-section uncertainties presented in Section 4.2.2. The W+light jets and W+heavy-flavour jets are also merged together, the W+heavy-flavour being the dominant contribution to the W+jets background, which is also considered a constrained parameter of the fit.

Moreover, the fit also includes the number of events observed in the signal region, in order to constrain the low, but non-negligible contribution of t-channel events in the two control regions.

All other background contributions (Z+jets, diboson and multijet productions) are minor and therefore fixed to their simulated or data-driven predictions. The used likelihood function [181] is given by:

$$L(\beta^s;\beta_j^b) = \prod_{i=1}^{N_{\text{selections}}} \frac{e^{-\mu_i}\cdot\mu_i^{n_i}}{n_i!} \cdot \prod_{j=1}^{N_{\text{backgrounds}}} G\left(\beta_j^b;1,\Delta_j\right) \tag{4.7}$$

$$\text{with}\quad \mu_i = \mu_i^s + \sum_{j=1}^{N_{\text{backgrounds}}} \mu_{ij}^b \quad , \quad \mu_i^s = \beta^s\cdot\tilde{\nu}_i^s \quad \text{and} \quad \mu_{ij}^b = \beta_j^b\cdot\tilde{\nu}_{ij}^b, \tag{4.8}$$

which corresponds to the product of two blocks:

- The Poisson distributions of the individual signal and background event yields for the three different selections (i.e signal selection and control regions selections).
- Gaussian priors useful to constrain the background rates, according to their theoretical cross-section uncertainties presented in Section 4.4[4].

The index i in the Poisson term runs over the three regions used in the fit, being n_i the observed number of events; while μ_i is the sum of each expected contribution from both signal and all simulated or data-driven backgrounds.

The index j runs over the background processes and it represents the constraint applied to the normalisation performed in the Gaussian prior constraints, represented by Δ_j.

For a given process, the expectation value in each selection is given by the the product combining the predicted number of events ($\tilde{\nu}_i^s$ for signal or $\tilde{\nu}_{ij}^b$ for backgrounds) in the considered sample and a scale factor (β^s or β_j^b).

[4] 6% for the merged top quark background processes; 20% for the W+jets contribution and 4% for the t-channel. Remaining processes are not allowed to vary.

The results of the maximum-likelihood fit are shown in Table 4.7 separately for the electron and muon channels as well as for the combined merged channel. They are reported in terms of scale factors with their corresponding fit uncertainty to be applied to the expected event yields.

Values very close to 1.0 are found for the merged top quark background which are dominated by $t\bar{t}$ production and for the W+jets processes. This means that the evaluated data-driven normalisations are consistent with the cross section calculations, whose central values are used to normalise the corresponding simulations samples, and whose theoretical uncertainties are used to constrain the fit.

Process	e-channel	μ-channel	e+μ-channels
t-channel	1.00±0.04	0.99±0.06	0.99±0.004
W+jets	0.98±0.04	1.03±0.17	1.003±0.029
$t\bar{t}$,Wt,s-channel	1.019±0.021	0.99±0.06	1.007±0.015

Table 4.7: Scale factors extracted for the t-channel signal contribution, and for the W+jets and top quark background processes from the simultaneous maximum-likelihood fit of the number of data events observed in the signal region and in the $t\bar{t}$-enriched and W+jets control regions. The uncertainties come from the likelihood fit and are related to the Poissonian and Gaussian terms of the likelihood function of Equation 4.7.

4.4.3 Signal and background event yields

In Section 4.3.1.5, the pre-fit pie chart shows the relative expected contributions of the t-channel signal and their different background processes in the signal and control regions. Table 4.8 now shows the event yields for the combined electron and muon channels after the pre-selection and the selection requirements. The $t\bar{t}$ and W+jets control regions are included too. The signal to background ratio is 0.7, being $t\bar{t}$ and W+jets the two main background contributions.

Process	Pre-selection	$t\bar{t}$ CR	W+jets CR	Selection
t-channel	131145 ± 205	7889 ± 50	91877 ± 172	39269 ± 112
Diboson	10167 ± 106	606 ± 8	9805 ± 104	362 ± 20
Multijet	82572 ± 40907	7496 ± 4295	75716 ± 37509	6856 ± 3399
W+bb jets	221899 ± 702	8855 ± 113	213641 ± 681	8259 ± 168
W+cc jets	114095 ± 1571	417 ± 100	106787 ± 1504	7308 ± 452
W+light jets	17177 ± 637	95 ± 11	16239 ± 614	939 ± 170
Wt-channel	62648 ± 137	3555 ± 32	59719 ± 134	2929 ± 30
Z+bb jets	35598 ± 223	1861 ± 34	33503 ± 213	2094 ± 67
Z+cc jets	5138 ± 185	53 ± 20	4928 ± 179	210 ± 45
Z+light jets	2004 ± 159	35 ± 17	1970 ± 156	34 ± 33
s-channel	5291 ± 14	2084 ± 8	5055 ± 14	236 ± 3
$t\bar{t}$	466269 ± 387	116325 ± 190	439789 ± 376	26479 ± 92
Total expected	1154004 ± 40952	149271 ± 4303	1059030 ± 37554	94976 ± 3441
Data	1156332	151521	1061520	94812
S/B	0.13	0.06	0.09	0.70

Table 4.8: Event yields for the t-channel signal and all the background contributing processes in the combined electron and muon channel for the pre-selection, selection and the control regions of the analysis. The predictions are derived from simulated event samples together with their theoretical cross-section except multijet which normalisation is estimated from a data-driven likelihood fit. No overall normalisation scale factors are considered to compute these event yields. The uncertainties shown are statistical only. Multijet events are quoted with an uncertainty of 70%. The expected S/B ratios are also given.

Good overall data-prediction agreement is found in pre-selection and signal regions for relevant kinematic variables, such as the $E_{\mathrm{T}}^{\mathrm{miss}}$, the transverse mass of the W boson and lepton p_{T}. Figures 4.12 and 4.9 show respectively the combined electron and muon selected and pre-selected events in terms of these three kinematic variables. Figures 4.10 and 4.11 show the same kinematic distributions for the $t\bar{t}$ and W+jets control regions, respectively. Good overall data-prediction is observed too. The distributions in all figures are normalized to the results of the maximum likelihood fit explained in Section 4.4.2.

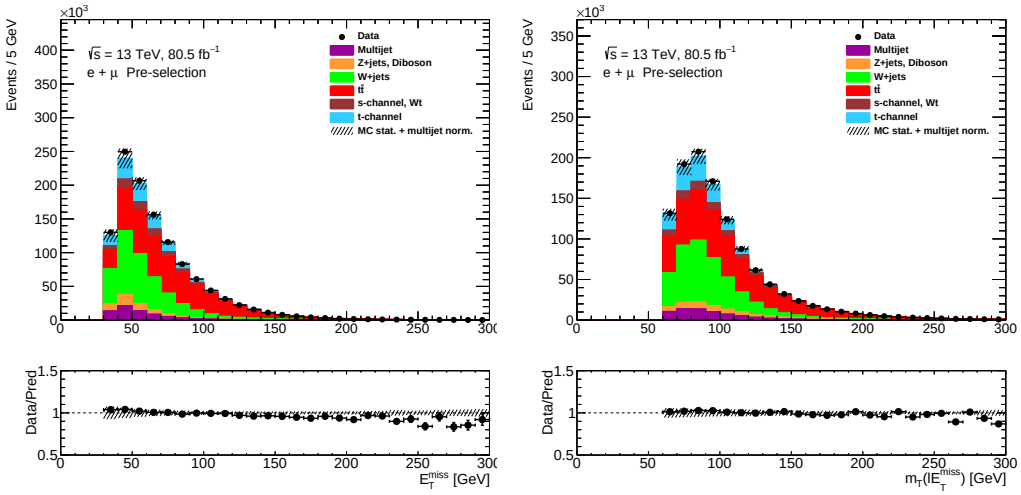

(a) (b)

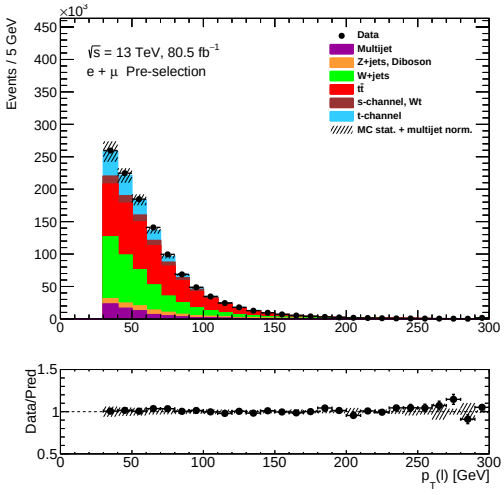

(c)

Figure 4.9: Kinematic distributions in the pre-selection: (a) missing transverse momentum, (b) W boson transverse momentum, and (c) lepton transverse momentum. The observed distributions are compared to the predicted signal and background distributions. The predicted multijet distributions are re-scaled using the values given in Table 4.7. The uncertainty bands correspond to the errors due to the limited size of the simulation samples added in quadrature with the normalization uncertainty estimated for the multijet contribution. The lower panel shows the ratio of data to prediction.

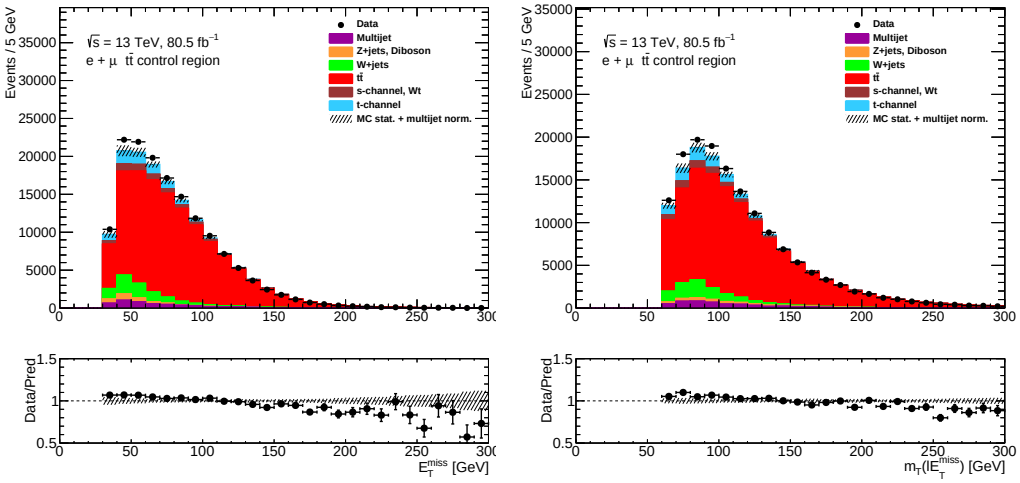

(a) (b)

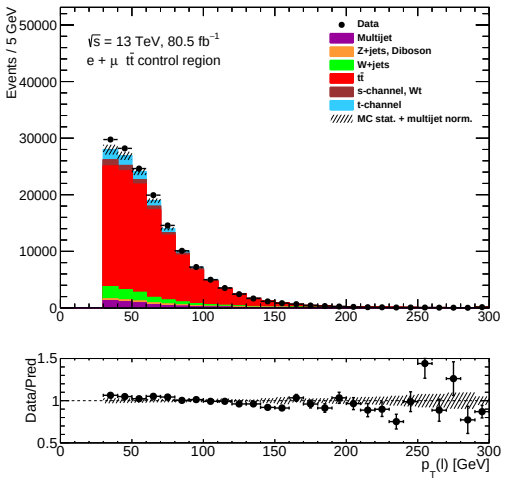

(c)

Figure 4.10: Kinematic distributions in the $t\bar{t}$ control region: (a) missing transverse momentum, (b) W boson transverse momentum, and (c) lepton transverse momentum. The observed distributions are compared to the predicted signal and background distributions. The predicted multijet distributions are re-scaled using the values given in Table 4.7. The uncertainty bands correspond to the errors due to the limited size of the simulation samples added in quadrature with the normalization uncertainty estimated for the multijet contribution. The lower panel shows the ratio of data to prediction.

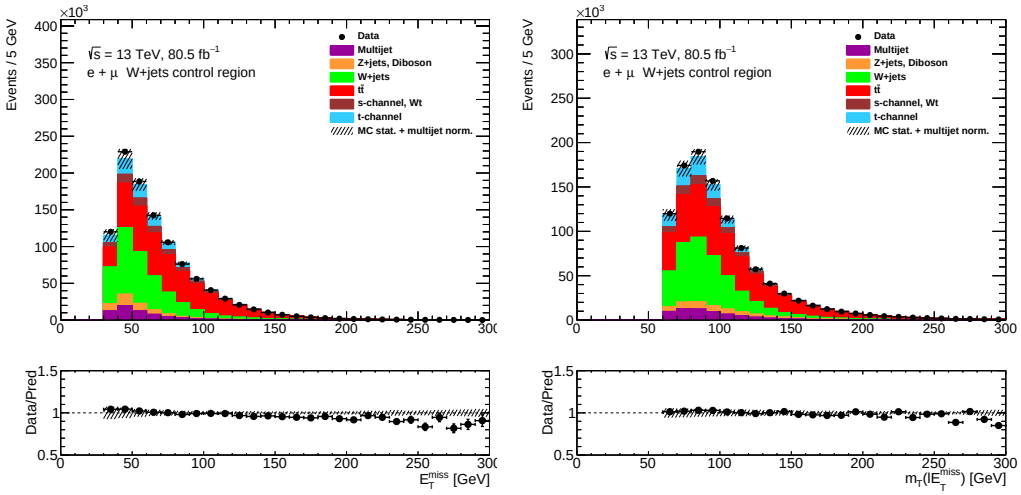

(a) (b)

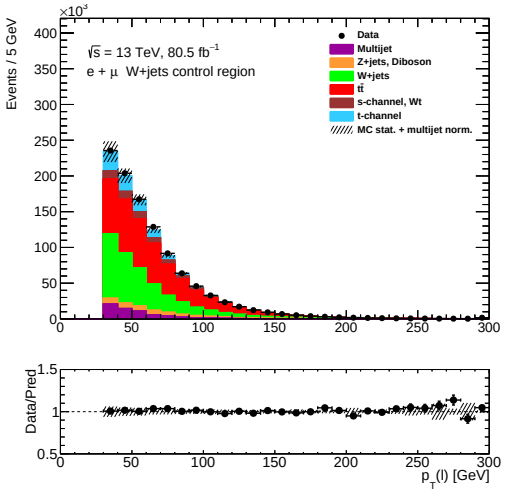

(c)

Figure 4.11: Kinematic distributions in the W+jets control region: (a) missing transverse momentum, (b) W boson transverse momentum, and (c) lepton transverse momentum. The observed distributions are compared to the predicted signal and background distributions. The predicted multijet distributions are re-scaled using the values given in Table 4.7. The uncertainty bands correspond to the errors due to the limited size of the simulation samples added in quadrature with the normalization uncertainty estimated for the multijet contribution. The lower panel shows the ratio of data to prediction.

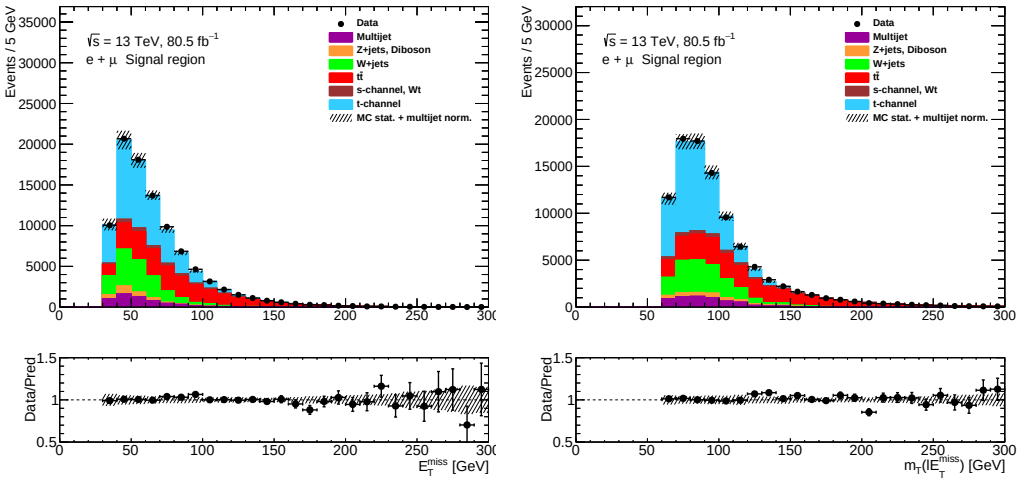

(a) (b)

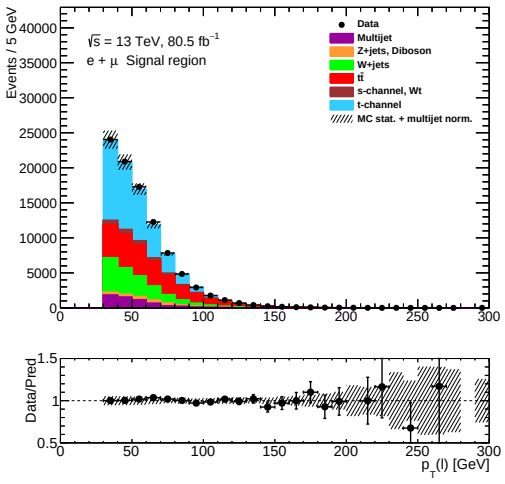

(c)

Figure 4.12: Kinematic distributions in the signal region: (a) missing transverse momentum, (b) W boson transverse momentum, and (c) lepton transverse momentum. The observed distributions are compared to the predicted signal and background distributions. The predicted multijet distributions are re-scaled using the values given in Table 4.7. The uncertainty bands correspond to the errors due to the limited size of the simulation samples added in quadrature with the normalization uncertainty estimated for the multijet contribution. The lower panel shows the ratio of data to prediction.

4.5 Measurement of the angular distributions

As explained in Section 1.3, various forward-backward asymmetries can be obtained from the angular distributions defined in the coordinate system of Figure 1.8. A_{FB}^{Z} is derived from $\cos(\theta_{lz})$ angular distribution. Similarly, A_{FB}^{X} and A_{FB}^{Y} are derived from the $\cos(\theta_{lx})$ and $\cos(\theta_{ly})$ angular distributions, respectively.

The angular distributions measured at reconstruction level in the signal region, used to measure the various asymmetries, are presented in Figures 4.14. They are compared to the predicted signal and background distributions, normalized to the results of the maximum-likelihood fit. Four bins are chosen for the angular distributions[5].

These distributions are unfolded to particle level in the fiducial volume defined in Section 4.3.2, with the purpose of being independent to assumptions on Wtb couplings of the signal process. During this process of unfolding, detector effects as well as reconstruction and selection efficiencies are corrected. The unfolding corrections are computed from simulated events of the signal process by generating a migration matrix of particle and reconstructed events. In the end, the unfolding process is applied to the angular distributions after substracting the background contributions. A schematic view of the whole process is displayed in Figure 4.13.

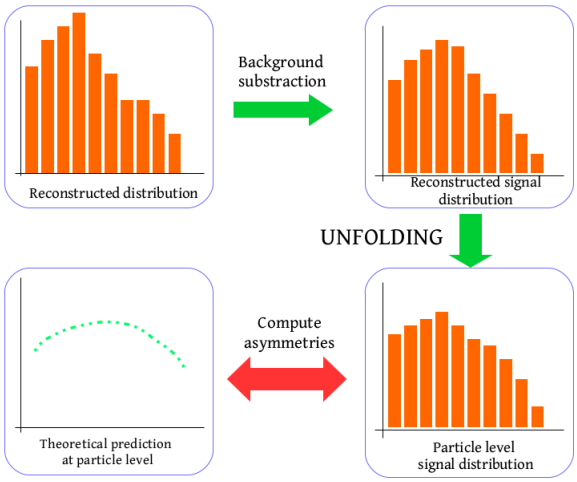

Figure 4.13: Schematic view summarising the unfolding process: the estimated background is substracted to the measured reconstructed distribution. The unfolding process is applied to the signal distribution obtained after the background substraction and a particle level unfolded distribution is achieved. The forward-backward asymmetry is then computed from the unfolded angular distribution and compared to the forward-backward asymmetry extracted from the theoretical predicted angular distribution at particle level.

[5]This will be motivated in Section 4.6.

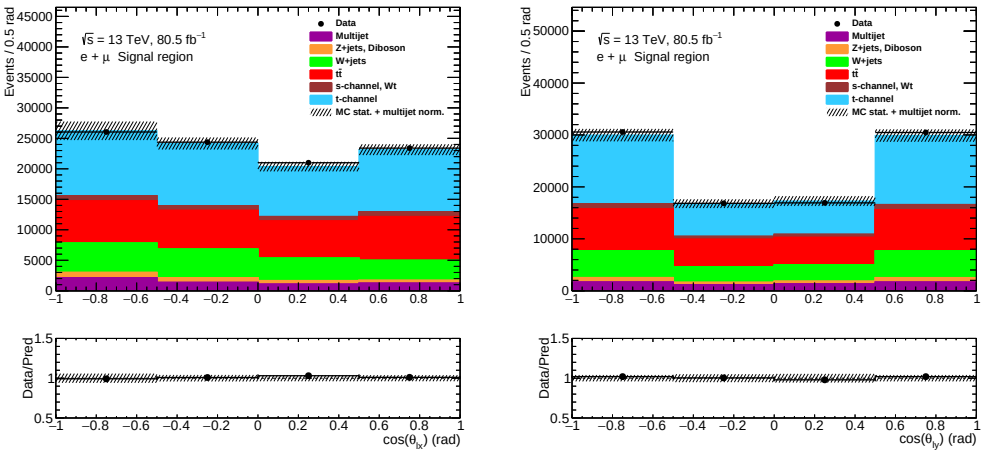

(a) (b)

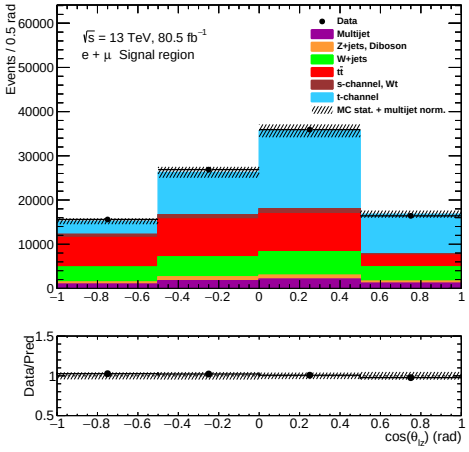

(c)

Figure 4.14: Angular distributions in the signal region for the combined electron and muon channels (a) $\cos(\theta_{lx})$, (b) $\cos(\theta_{ly})$, and (c) $\cos(\theta_{lz})$. The predicted distributions are re-scaled using the fitted scale factors given in Table 4.7 and the uncertainty bands correspond to the limited size of the simulation samples added in quadrature with uncertainty estimated for the multijet contribution.

4.6 Unfolding procedure

The unfolding procedure starts from the reconstructed measured angular distributions. The aim is to correct these distributions for resolution and efficiency effects and to perform an inversion of the migration matrix M. However, in most of the cases, the nverse matrix M^{-1} cannot be found such as $M \cdot M^{-1} = I$, where I is the identity matrix. Hence, approximations are needed to perform the matrix inversion to acceptable accuracy. In addition, to suppress spurious fluctuations in the inversion result, a regularization procedure has to be applied. An iterative Bayesian approach [182] is used to unfold the angular distributions presented in Section 4.5. In this approach, the simulated angular distribution of the t-channel events obtained after having applied all the selection requirements is taken as initial prior. This prior is updated with the resulting unfolded angular distribution. The obtained prior is used as prior for the next iteration step. In the iterative Bayesian unfolding method, the number of iterations is the regularization parameter and it depends on the angular distribution.

The observed number of events in each bin j of the measured angular distribution can be described by:

$$N_j^{\text{data}} = \sum_k M_{jk}\epsilon_k L_{\text{int}} d\sigma_k + B_j \,, \tag{4.9}$$

where $d\sigma_k$ is the estimated cross-section in each bin k, M_{jk} is the migration matrix that describes the probability of migration of particle level events in bin k to bin j after detector reconstruction of the event, L_{int} is the integrated luminosity and B_j is the sum of all background contributions. The efficiency correction, ϵ_k , is the efficiency for an event to be selected in bin k and it considers signal acceptance and detector efficiencies:

$$\epsilon_k = S_k^{\text{sel,MC}} / S_k^{\text{tot,MC}}, \tag{4.10}$$

where $S_k^{\text{tot,MC}}$ is the number of generated MC events in bin k and $S_k^{\text{sel,MC}}$ is the number of selected MC events in bin k after all cuts are applied.

The reconstructed observables and angular distributions are unfolded to the particle level within the fiducial volume. The detector efficiency and resolution effects are corrected using:

$$N_k^{\text{particle}} = C_k^{\text{particle!reco}} \sum_j M_{jk}^{-1} C_j^{\text{reco!particle}} (N_j^{\text{data}} - B_j), \tag{4.11}$$

where N_k^{particle} represents the number of t-channel events at particle level in bin k of the fiducial volume, M_{jk}^{-1} represents the migration matrix inverted with Bayesian unfolding procedure, and $C_j^{\text{reco!particle}}$ is a correction factor that accounts for events that pass reconstruction selection but not particle level selection. It is defined as:

$$C_j^{\text{reco!particle}} = \frac{S_j^{\text{reco}} - S_j^{\text{reco!particle}}}{S_j^{\text{reco}}}, \tag{4.12}$$

where S_j^{reco} is the number of reconstructed signal events in bin j and $S_j^{\text{reco!particle}}$ is the number of events that pass the reconstruction level selection but not the particle level selection.

$C_k^{\text{particle!reco}}$ is a correction factor that accounts for signal events that pass particle level selection but not the reconstruction level selection:

$$C_k^{\text{particle!reco}} = \frac{1}{\epsilon_k} = \frac{S_k^{\text{particle}}}{S_k^{\text{particle}} - S_k^{\text{particle!reco}}}, \tag{4.13}$$

where S_k^{particle} is the number of signal events at particle level and $S_k^{\text{particle!reco}}$ is the number of events that pass the particle level selection but not the reconstruction level selection.

The unfolded results presented in this thesis are obtained using the Bayes unfolding algorithm implemented in the `RooUnfold` package [183]. The validation of the Bayes unfolding procedure includes first convergence tests in order to define the optimal number of iterations of the algorithm. Tests are then performed to check the closure and the linearity of its response. These tests are performed using the various t-channel event samples generated with the POWHEG-BOX, AMC@NLO and PROTOS generators interfaced with PYTHIA for parton showering and hadronization. The next subsections present the convergence, closure and linearity tests, as well as, the migration matrix and corrections of the baseline sample.

4.6.1 Migration matrix and corrections for baseline

For the three angular distributions $\cos(\theta_{lx})$, $\cos(\theta_{ly})$ and $\cos(\theta_{lz})$, Figure 4.15 and Figures 4.16 and 4.17 respectively show the migration matrices and efficiency corrections for the baseline POWHEG-BOX+PYTHIA Full Simulation (FS) sample. The migration matrices exhibit in all cases that the fraction of simulated events lies in the diagonal elements between 75% and 97% of the times. In order to have a stable unfolding response, the possible binning configurations are restrained to those for which at least 70% of the events are in the diagonal elements of the migration matrix. Thus, 4 bins is the binning configuration chosen for all the elements present in Equation 4.11. Regarding the correction factors, whereas the $C_j^{\text{reco!particle}}$ correction factor vary between 40% and 50%, the $C_j^{\text{particle!reco}}$ efficiency is situated around 20%. Such predictions are consistent between different generators.

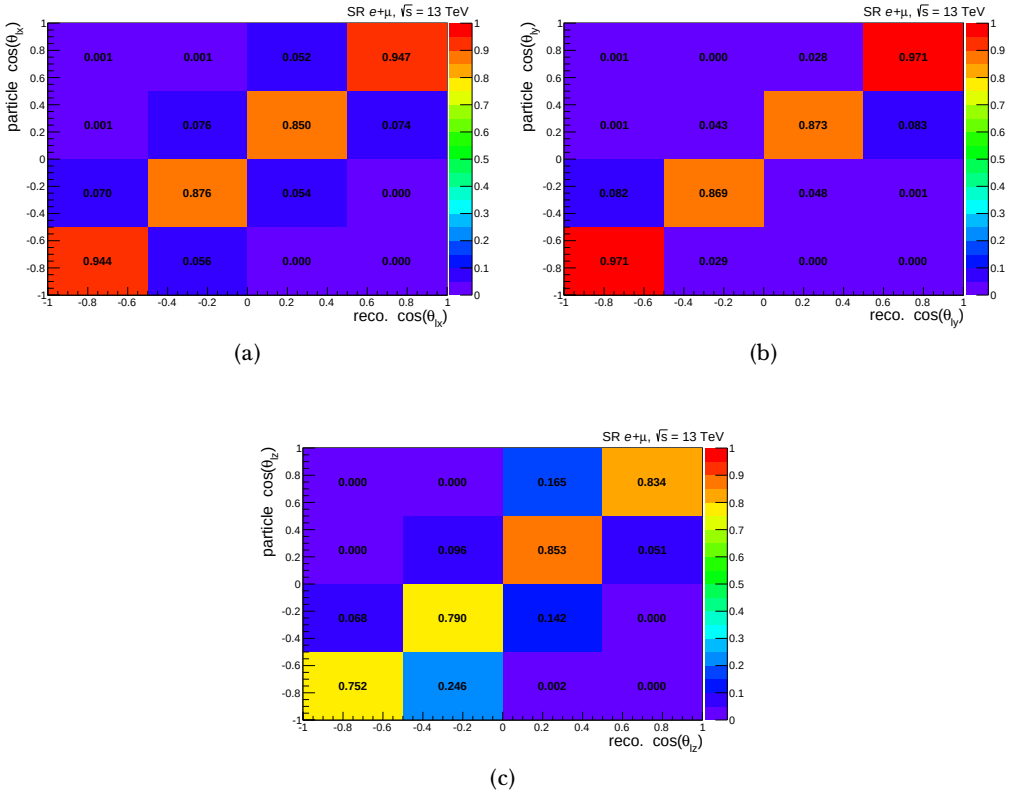

(a) (b)

(c)

Figure 4.15: Migration probability matrices for the measured angular distributions: $\cos(\theta_{lx})$ (a) , $\cos(\theta_{ly})$ (b) and $\cos(\theta_{lz})$ (c) . They have been computed from the baseline POWHEG-BOX+PYTHIA FS sample.

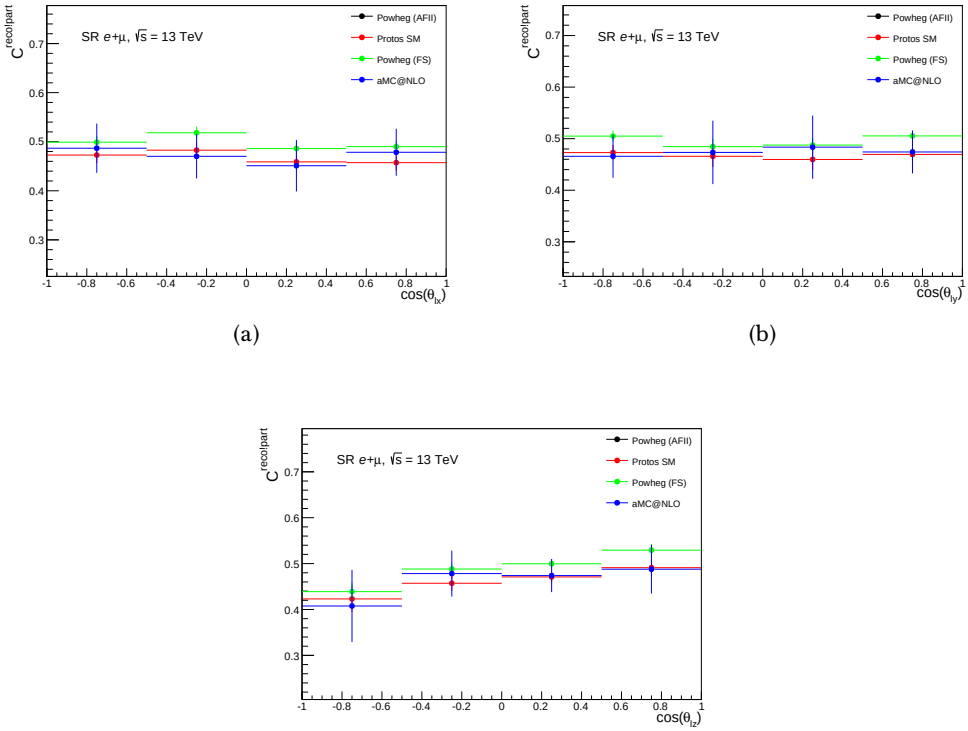

(a) (b)

(c)

Figure 4.16: Efficiency accounting for signal events that pass particle level selection but not the reconstruction level selection for each bin as a function of the measured angular distributions : $\cos(\theta_{lx})$ (a) , $\cos(\theta_{ly})$ (b) and $\cos(\theta_{lz})$ (c) . The correction factor used in the unfolding is the one obtained from baseline POWHEG-BOX+PYTHIA FS sample. The baseline predictions are compared with POWHEG-BOX AFII, aMC@NLO and PROTOS generators interfaced with PYTHIA.

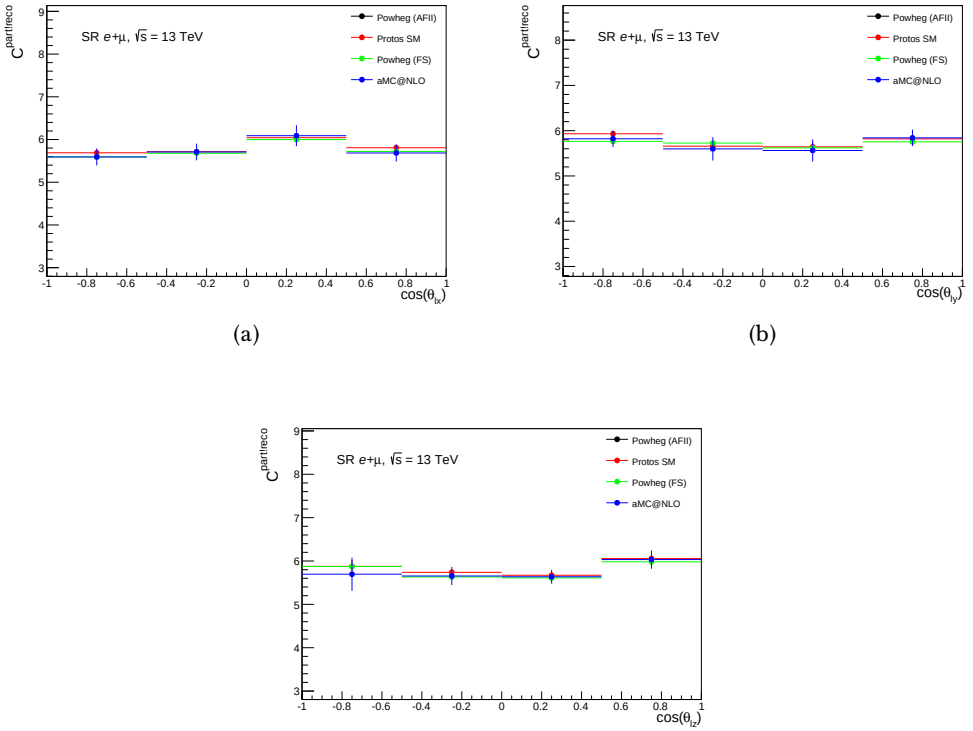

(a) (b)

(c)

Figure 4.17: Correction accounting for signal events that pass particle level selection but not the reconstruction level selection for each bin as a function of the measured angular distributions : $\cos(\theta_{lx})$ (a) , $\cos(\theta_{ly})$ (b) and $\cos(\theta_{lz})$ (c) . The correction factor used in the unfolding is the one obtained from baseline POWHEG-BOX+PYTHIA FS sample. The baseline predictions are compared with POWHEG-BOX AFII, AMC@NLO and PROTOS generators interfaced with PYTHIA.

4.6.2 Convergence test

To define the optimal number of iterations of the Bayesian unfolding algorithm, convergence tests are performed. The convergence studies presented in this subsection are performed using the baseline POWHEG-BOX+PYTHIA FS sample (sample with the Standard Model couplings and processed with the full detector simulation), and other t-channel generators, such as PROTOS+PYTHIA, POWHEG+PYTHIA and AMC@NLO+PYTHIA, interfaced with AFII.

Figure 4.18 shows the evolution, as a function of the number of iterations, of the asymmetries extracted from the unfolded angular distributions. The optimal number of iterations is derived with respect to a well-defined convergence criterion. For a given asymmetry, the unfolding procedure is considered to have converged when the absolute change between two successive steps becomes negligible (of the order of 0.0001). One can see in all the plots that the convergence is very fast for the unfolded POWHEG-BOX FS distributions (only one iteration is necessary). The fast convergence for these distributions is due to the fact that the same event sample is used to build the unfolded angular distributions and to compute the resolution and efficiencies corrections. When unfolding the distributions reconstructed from the other t-channel generator samples, the convergence for the extracted asymmetry values is in general notably slower. Figure 4.18 also shows that even if convergence is reached, there is a difference between the unfolded asymmetry values in each of the samples. This means that the unfolding response is sensitive to the modelling of NLO the generators (AMC@NLO or POWHEG-BOX)[6] and the detector simulation (FS vs AFII). Such differences between the unfolded asymmetry values are accounted in a systematic uncertainty. Three to five iterations are indeed needed for all asymmetries, as shown in Table 4.9.

Asymmetry	Number of iterations
A_{FB}^{X}	5
A_{FB}^{Y}	3
A_{FB}^{Z}	5

Table 4.9: Numbers of Bayes iterations chosen for the measured asymmetries.

[6]The difference between NLO generators(i.e. AMC@NLO, POWHEG-BOX) with respect to the PROTOS sample is mainly due to the fact that the PROTOS sample is simulated at LO.

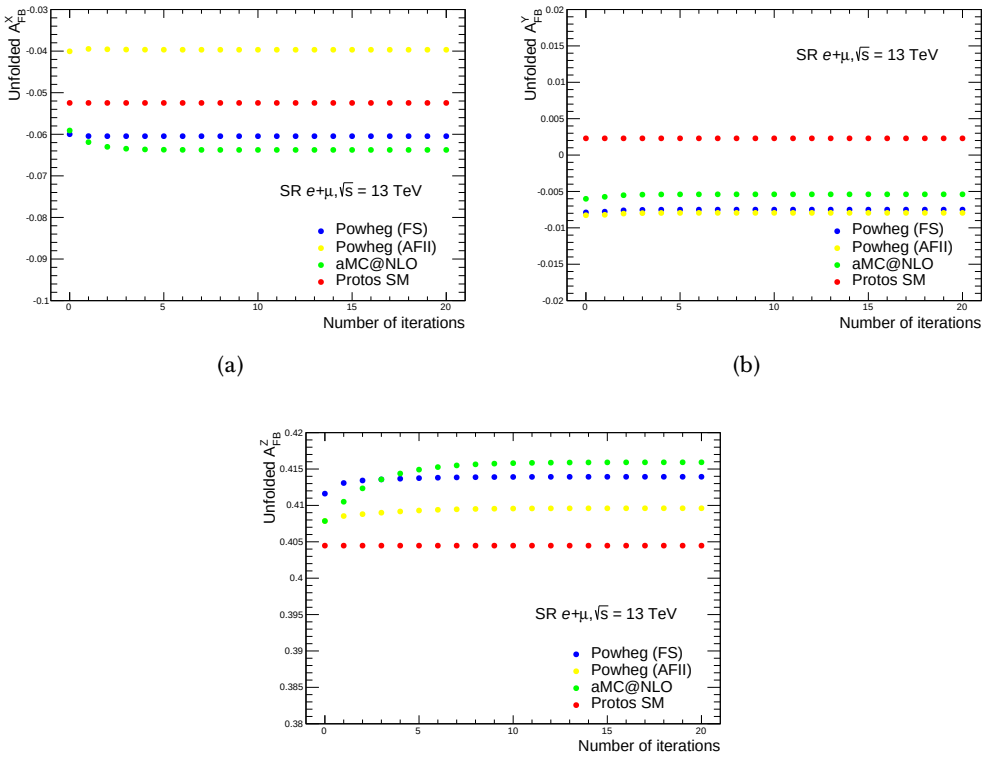

Figure 4.18: Unfolded values of the asymmetries A_{FB}^{X} (a), A_{FB}^{Y} (b) and A_{FB}^{Z} (c); as a function of the number of iterations obtained after unfolding the angular distributions predicted by the nominal POWHEG-BOX (blue points), the AFII POWHEG-BOX (yellow points), the aMC@NLO (green points) and the PROTOS SM (red points). The unfolding has been performed in all cases using the baseline POWHEG-BOX unfolding matrix and efficiency corrections.

4.6.3 Closure test

The goal of the closure test is to check the accuracy (i.e. the intrinsic bias) of the unfolding algorithm using statistically independent event samples for the unfolded angular distributions and for the resolution and efficiency corrections. To that end, the baseline POWHEG-BOX FS sample is split into two sub-sets of same size: one sub-set is used to determine the corrections applied to unfold the angular distributions built from the second sub-set of events. The measurement results are then compared to the particle level values taking into account the expected statistical uncertainties related to the limited size of the Monte Carlo simulation samples (statistics of the two sub-sets).

The results of the closure test obtained for the different angular distributions are shown in Figure 4.19. One can see that the truth angular distribution represented in the dashed line is compatible with the unfolded angular distribution, within the statistical uncertainty of the unfolded angular distribution of the splitted samples.

Moreover, the difference between the unfolded and particle level truth values is shown in Figure 4.20 for each measured asymmetry with the statistical uncertainty associated with the limited sizes of the splitted POWHEG-BOX FS event samples. One can see a good closure of the results, whatever the measured asymmetry: within the expected statistical uncertainties, all the measurement results are compatible with the truth particle level values (represented by the horizontal dashed line in the plot). Therefore, no bias will be considered in the measurement of all asymmetries.

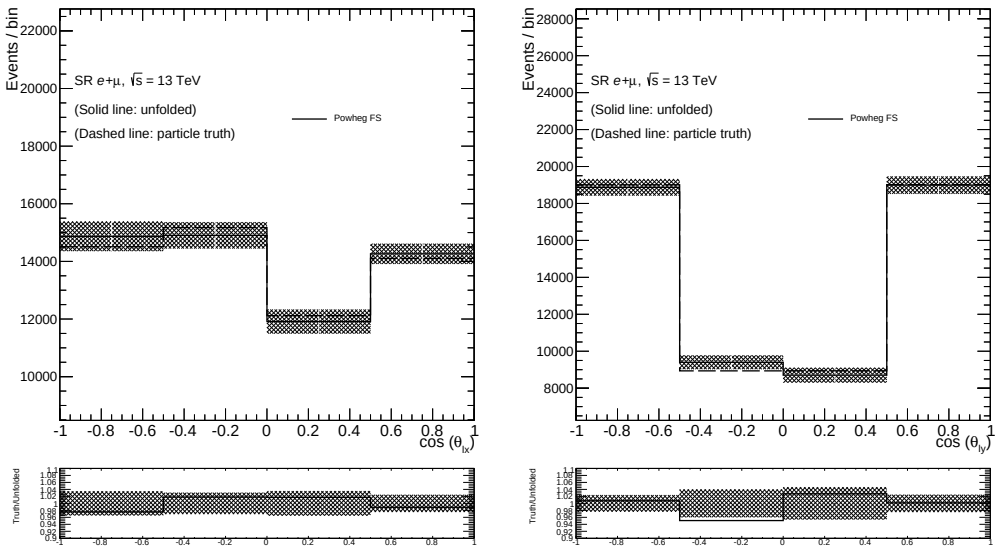

(a)

(b)

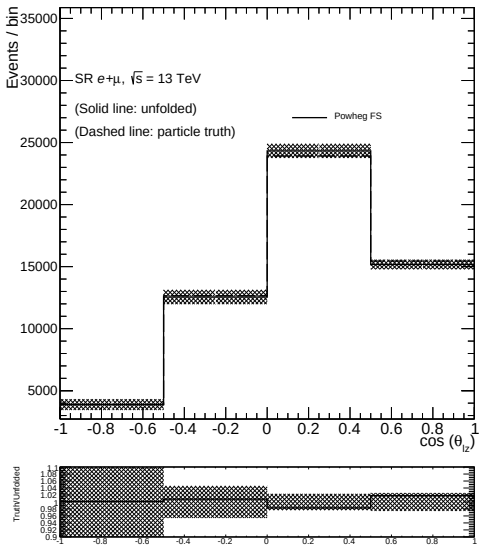

(c)

Figure 4.19: Relative differences between the unfolded (solid) and particle level truth (dashed) angular distributions for $\cos(\theta_{lx})$ (a) $\cos(\theta_{ly})$ (b) and $\cos(\theta_{lz})$ (c). The POWHEG-BOX FS event sample is divided into two sub-sets, from which the unfolding corrections and the unfolded distributions are derived. The error bars represent the statistical uncertainties due to the limited sizes of the two t-channel simulation sub-samples.

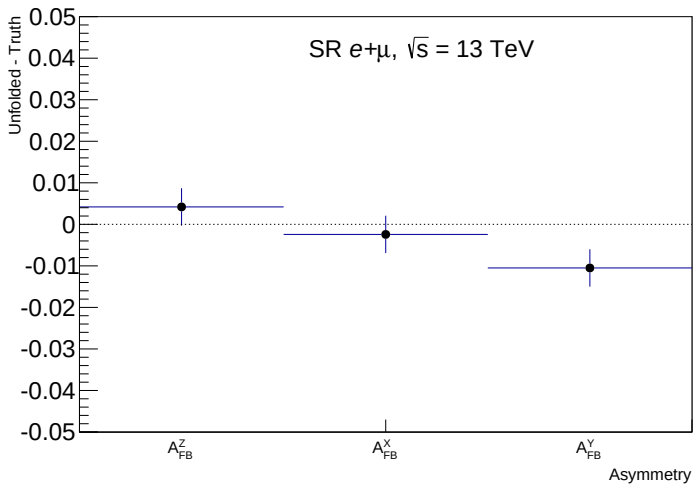

Figure 4.20: Differences between the asymmetry values derived from the unfolded and particle level angular distributions. The POWHEG-BOX FS event sample is divided into two sub-sets, from which the unfolding corrections and the unfolded distributions are derived. The error bars represent the statistical uncertainties due to the limited sizes of the two t-channel simulation sub-samples.

4.6.4 Linearity test

Since our measurement relies on probing the Wtb anomalous couplings, it is important to check that the unfolding response is independent of non-vanishing anomalous coupling. To that end, the linearity test is implemented in the unfolding validation. It consists of measuring the unfolded distributions of several non-Standard ModelWtb anomalous coupling samples using the SM efficiencies and migration corrections and compare them with the corresponding particle level truth measurement. If the unfolding depends on the anomalous couplings assumptions, they would be different.

The PROTOS non-Standard Model values chosen in this test are summarized in Table 4.4 and can be categorized in three types: samples with non-vanishing Im(g_R) (i.e Im(g_R)/V_L = $\pm$0.07), samples with non-vanishing Re(g_R) (i.e. Re(g_R)/V_L = $\pm$0.18) and samples combining non-vanishing V_R and g_L (i.e. $V_R/V_L = \pm 0.4; g_L/V_L = \pm 0.32$). The values were chosen to have a more complete coverage of possible variations with respect to the Standard Model configuration and considering the current limits on the non-Standard Model anomalous couplings [81]. The PROTOS sample used to calculate the baseline unfolding corrections is generated with the Standard Model parameterization of the Wtb couplings: $V_{\mathrm{L}} = 1$, $V_{\mathrm{R}} = g_{\mathrm{L}} = g_{\mathrm{R}} = 0$.

The results of the linearity tests obtained for the various asymmetries is shown in Figure 4.21. The plotted graphs represent the extracted unfolded asymmetries as a function of their particle level truth values for each set of anomalous couplings samples of Table 4.4. The lines corresponding to a perfect response (slope=1 and offset=0) are displayed in the figures. The plotted error bars represent the uncertainties due to the limited sizes of the tested PROTOS samples, estimated through the generation of pseudo-experiments.

The black dots correspond to the PROTOS sample with SM couplings, and exhibit a perfect response, as expected. The rest of the points, in which the anomalous couplings configuration is implemented, are distributed around the perfect linearity represented with the dashed line. Therefore, a good linearity is found for the asymmetries A_{FB}^{X}, A_{FB}^{Y} and A_{FB}^{Z} taking into account the statistical uncertainty associated to each sample.

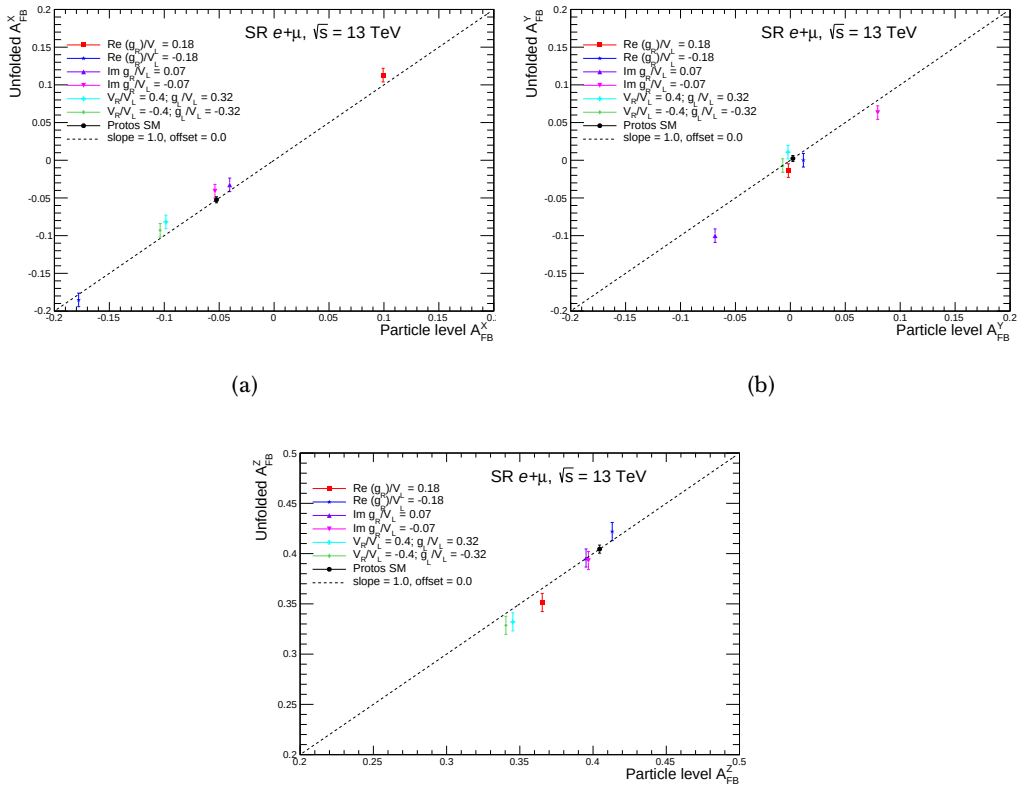

(a) (b)

(c)

Figure 4.21: Unfolded asymmetries A_{FB}^{X} (a), A_{FB}^{Y} (b) and A_{FB}^{Z} (c); as a function of their particle level truth values using different new physics samples. The PROTOS event samples with the Standard Model Wtb parameterization (black points) and with anomalous couplings, corresponding to non-zero values of $\mathrm{Im}(g_R)$ (pink and purple points), $\mathrm{Re}(g_R)$ (red and blue points), and $V_R/V_L; g_L/V_L$ (green and cyan points). The error bars represent the uncertainties due to the limited statistics of the unfolded event distributions. The dashed line corresponds to the perfect linearity response.

4.7 Sources of systematics and data statistical uncertainties

Various sources of systematic uncertainty are considered in this analysis. Such sources of systematics are classified in two main groups: experimental uncertainties related with detector modelling and theoretical uncertainties related with the signal and background modelling. These different systematic uncertainties affect the normalisation and shape of the angular distributions, that are used to extract the angular asymmetries. The impact of systematic uncertainties are estimated separately and are propagated in a correlated way to the signal region and to the two control regions. All systematic uncertainties components are then added in quadrature to get the total systematic uncertainty. The effect due to the statistics of the data and simulated event samples is also taken into account.

4.7.1 Treatment of uncertainties.

In order to dispose a conservative approach in the total uncertainty estimation, each individual systematic uncertainty in which only the up or the down contribution has an impact on the measurement has been symmetrised. The varied samples are used to estimate the effect of each source of uncertainty in the expected and observed measured asymmetries. Afterwards, the systematic contributions, that arises from the experimental uncertainties, theoretical modelling uncertainties and due to the limited size of simulation samples, are merged. However, both expected and observed methods differ slightly in the computation.

4.7.1.1 Expected uncertainties

For each source of systematic uncertainty, up and down variations are constructed as accordingly explained in the next section. The expected uncertainty on each asymmetry is then computed with the following procedure:

- Add all the varied background and signal samples for all the control and signal regions. This defines the so-called pseudo-data sample.
- The nominal simulated samples are fitted to the pseudo-data sample with the procedure explained in Section 4.4.2, to account for the correlations of the varied samples in the different regions.
- After scaling the nominal backgrounds with the obtained scale factors, those scaled backgrounds are subtracted to the pseudo-data. The remaining distribution is known as pseudo-signal.
- Such pseudo-signal distribution, on which the effect of the systematic source has been propagated, is unfolded using the nominal migration matrices and efficiency corrections. When computing the PDF signal modelling systematic

uncertainty, nominal migration matrices are not used in the unfolding procedure. In that particular case, the migration matrix is obtained with the central eigenvalue of the PDF4LHC30 set instead.

- For all the systematic sources, except the signal modelling uncertainties, the final effect of the uncertainty source on the asymmetry is given by the difference between the nominal asymmetry and the value obtained from the varied pseudo-data samples. For the signal modelling uncertainties, the value obtained from the varied sample is directly compared with its corresponding particle level truth value.

4.7.1.2 Observed uncertainties

A similar procedure is used to evaluate the observed systematic uncentainties.

- The nominal signal and background samples yields are re-scaled with the scale factors obtained from the fit to the data explained in Section 4.4.2, i.e. SF^{data}. Then, a pseudo-data sample is created by adding all the varied background and signal samples for control and signal regions, after having re-scaled them as well with the SF^{data}.

- Since the shape of the simulated signal sample is not in general the same as the shape of the signal obtained from data, bin-by-bin scale factors are derived for the t-channel simulated samples by comparing the shapes of the nominal (re-scaled) simulated signal sample and the measured signal distribution (obtained from the nominal background subtracted to data). An analogous bin-by-bin scale factor is derived using the unfolded measured signal distribution and the nominal simulated signal sample at particle level, which is applied when computing the signal modelling uncertainties that use particle level truth spectrum.

- The nominal simulated background samples scaled with SF^{data} are fitted to the corresponding pseudo-data sample to obtain a set of scale factor, SF^{syst}. Later, those are used to obtain the pseudo-signal, as in the expected uncertainties method.

- Once the pseudo-signal is obtained, it is re-weighted using the bin-per-bin scale factors described previously, before performing the unfolding. Finally, the difference between the asymmetry extracted from the pseudo-signal and the measured asymmetry is taken as the observed uncertainty. For the signal modelling uncertainties, the value obtained from the varied sample is directly compared with the particle level truth value instead, re-weighted using the bin-per-bin scale factors described above.

4.7.2 Experimental uncertainties

Luminosity
The individual uncertainties in the 2015, 2016 and 2017 integrated luminosities are 2.1%, 2.2% and 2.4%, respectively [131], as mentioned already in Section 4.2.1. This uncertainty is propagated to the asymmetries by varying accordingly the overall normalizations of all simulated samples.

Pile-up reweighting
All MC simulated event samples are reweighted to match the observed distribution of the average number of interactions per bunch-crossing in data [184], as discussed in Section 4.2.2. The uncertainties related to the pile-up scale factors are propagated into the measured asymmetries.

Lepton reconstruction
The reconstruction, identification, isolation and trigger performances differ between data and MC for electrons and muons. Similarly, the lepton momentum scale and resolution can be different between the simulated events and the observed data as well. In either case, so as to correct such differences, scale factors are applied. They are estimated with the tag-and-probe method with dedicated electrons and muons from Z boson, W boson and J/ψ decays [128, 171]. The uncertainties on these scale factors are propagated to the measured asymmetries.

Jet vertex fraction efficiency
Scale factors, used to account for differences between the JVT efficiency in simulation and data, are derived using Z+jets events [185]. From these studies, a conservative uncertainty of 30% is used to cover a potential mismodelling.

Jet Energy Scale
The jet energy scale (JES) takes into account jet calibrations together with the calorimeter response and other sources. The goal is to calibrate the jet energy measured in the calorimeter with that predicted at particle level. The JES and the corresponding uncertainty is derived using information from test-beam data, LHC collision data and simulation [111]. A parametrisation of 29 uncorrelated components is considered in this analysis [186], which can have different jet p_{T} and η dependencies.

Jet energy resolution
The jet energy resolution (JER) is extracted from di-jet events by measuring the width of the dijet asymmetry distribution across p_{T} and η [186, 187]. The jet energy resolution uncertainty is propagated by smearing the jet p_{T} in MC simulation.

The comparison of the nominal and smeared prediction is made by eight components: a data/MC comparison term and seven modelling/theory components. Such parametrisation defines the JER uncertainty.

Heavy- and light-flavour tagging
Since this measurement makes use of a b-tagging algorithm, the b-tag and c-tag efficiencies are considered and the mistag rate for light-flavour jets as well. They are measured and scale factors derived from data are applied to the simulation [118, 119,174]. Uncertainties are propagated into the analysis via 9 components for b-jets, 4 components for c-jets and 17 components for light-flavour jets, respectively. All of those are later on merged into the analysis in one jet flavor tagging uncertainty.

Missing transverse momentum
The uncertainty on $E_{\mathrm{T}}^{\mathrm{miss}}$ due to a possible miscalibration of the soft-track component of the $E_{\mathrm{T}}^{\mathrm{miss}}$ is derived from data–MC comparisons of the p_{T} balance between the hard and soft $E_{\mathrm{T}}^{\mathrm{miss}}$ components to the overall $E_{\mathrm{T}}^{\mathrm{miss}}$ [175].

4.7.3 Signal and background modelling uncertainties

The systematic uncertainties associated with the modelling of the t-channel signal and background processes (i.e. top quark pairs, s-channel and tW-channel) are estimated by comparing the nominal samples with respect to alternative MC simulated samples, for which either specific parameters or the whole event generator is changed. Up and down variations are symmetrised.

- **Matrix element modelling**: in order to assess the uncertainty due to the choice of the matching scheme in the ME generation, the nominal MC generator Powheg-Box is compared to aMC@NLO. The parton showering and hadronisation are simulated with Pythia8 in both cases.
- **Parton shower modelling**: in order to estimate the uncertainty due to the choice of parton shower and hadronisation model, the nominal sample which uses Pythia8 is compared to another sample using Herwig7. The ME generator for both samples is Powheg-Box.
- $t\bar{t}$ **and** tW **interference**: in the case of tW associated production, the interference between tW and $t\bar{t}$ processes constitutes another source of systematic uncertainty. The impact is estimated by comparing samples using either the diagram removal scheme or the diagram substraction scheme, both generated with Powheg-Box + Pythia8 .
- **Initial/Final State Radiation**: the uncertainty originating from Initial/Final State Radiation (ISR/FSR) modelling is evaluated for the t-channel signal process and the other two single top processes, as well as for top quark pair production. For the signal and all backgrounds, the matrix element simulated

with the POWHEG-BOX+PYTHIA8 sample is used. To simulate higher parton radiation, the renormalisation and factorisation scales μ_{R} and μ_{F} are varied by a factor of 0.5 in the matrix element while using the Var3c up variation from the A14 tune. For lower parton radiation, μ_{R} and μ_{F} are varied by a factor of 2.0 while using the Var3c down variation in the parton showering. In the $t\bar{t}$ samples, h_{damp} is set to m_t or to $2m_t$ in combination with the lower and higher parton radiation parameterizations, respectively.

- **PDF uncertainty**: PDF uncertainties are evaluated for the t-channel and background processes using the PDF4LHC15 uncertainty set, which consists of 30 nuisance parameters (NP) [188]. Internal reweighting in the nominal POWHEG-BOX+PYTHIA8 sample is used. It is reweighted to the PDF4LHC15 PDF and its uncertainty set on an event-by-event basis. The differences between the 30 eigenvalues are found to be smaller than 1% in both reconstruction and particle level spectra. The PDF uncertainty is assessed for each eigenvalue. In the case of the t-channel signal, the unfolded result is compared with respect to the corresponding particle level result. The impact of the PDF uncertainty on top-quark pairs, s-channel and tW-channel has been also assessed. In that case, the unfolded result (obtained with the nominal unfolding configuration) is compared with the corresponding unfolded result, achieved by employing in the unfolding configuration the central eigenvalue of the PDF4LHC15 set.

- **Normalisation**: The event yields associated with the simulated top-quark pair events, single top-quark, W/Z+jets and diboson processes are estimated using the selection acceptances and the theoretically predicted cross-sections as reported in Section 4.2.2. Theoretical relative uncertainties of 6%, 7% and 4% are assigned to the $t\bar{t}$, associated tW and s-channel processes, respectively. For vector boson in association with jets and diboson processes, a normalisation uncertainty of 20% is considered. The multijet background normalisation is obtained from data, as described in Section 4.4.1. A relative systematic uncertainty of $\pm$70% is assigned to this data-driven overall normalisation.

4.7.4 Limited size of data and simulation samples

The statistical uncertainties associated to the limited size of the simulated samples are evaluated using pseudo-experiments. The bins of the nominal angular distributions are varied, for each process in each pseudo-experiment, by a random number generated through a Gaussian distribution of the same width as the statistical error associated with the bin content. The whole analysis chain is performed so as to obtain the asymmetry observables in each pseudo-experiment. The final statistical uncertainty is assigned as the standard deviation associated with the distribution resulting from the measured asymmetries provided by the ensemble of pseudo-experiments.

The statistical uncertainties due to the limited sizes of the data samples are estimated from pseudo-experiments by varying the rates and the shapes analogously through bin-by-bin Poisson fluctuations on the expected signal and background angular distributions (in this case the data-driven multijet contribution is not fluctuated). Finally, the standard deviation is obtained in the same way as the simulation statistical uncertainty.

4.7.5 Uncertainties breakdown

Table 4.10 shows the contribution of each source of systematic uncertainty to the measured asymmetries, together with the statistical uncertainty. All measurements are systematic dominated. Depending on the asymmetry, the largest contribution rises from the uncertainties in the jet energy scale and jet energy resolution. But also the $t\bar{t}$ and signal modelling have a sizeable impact.

Uncertainty Source	$\Delta A_{\mathrm{FB}}^{X}$	$\Delta A_{\mathrm{FB}}^{Y}$	$\Delta A_{\mathrm{FB}}^{Z}$
Statistical uncertainty	± 0.008	± 0.008	± 0.009
Simulation statistics	± 0.015	± 0.015	± 0.017
Pile-up	0.008	0.002	± 0.008
Lepton reconstruction	± 0.012	± 0.006	± 0.013
MET reconstruction	± 0.008	± 0.002	± 0.008
Jet Flavor Tagging	± 0.017	± 0.017	± 0.010
Jet Energy Scale	± 0.075	± 0.027	± 0.024
Jet Energy Resolution	± 0.033	± 0.027	± 0.071
Multijet Normalisation	± 0.015	± 0.002	± 0.007
PDF	± 0.002	< 0.001	± 0.009
t-channel radiation	< 0.001	< 0.001	± 0.005
$t\bar{t}$ radiation	± 0.022	< 0.001	± 0.006
s-channel radiation	< 0.001	< 0.001	< 0.001
tW-channel radiation	< 0.001	< 0.001	< 0.001
t-channel parton shower	± 0.028	± 0.002	± 0.017
$t\bar{t}$ parton shower	± 0.019	± 0.007	± 0.009
s-channel parton shower	< 0.001	< 0.001	< 0.001
t-channel generator	± 0.032	± 0.007	± 0.018
$t\bar{t}$ generator	± 0.011	± 0.002	± 0.012
s-channel generator	< 0.001	< 0.001	< 0.001
Wt-channel DS	± 0.001	± 0.002	± 0.003
Total systematic uncertainty	± 0.100	± 0.046	± 0.085

Table 4.10: Breakdown of the contributions to the observed statistical and systematic uncertainties on the A_{FB}^{X}, A_{FB}^{Y} and A_{FB}^{Z} of the distributions in $\cos(\theta_{lx})$, $\cos(\theta_{ly})$ and $\cos(\theta_{lz})$, respectively. The total systematic uncertainty is computed from the sum in quadrature of the individual sources.

4.8 Results

The initial step of this measurement relies on the angular distributions sensitive to the top quark polarization components (i.e. $\cos(\theta_{lx})$, $\cos(\theta_{ly})$ and $\cos(\theta_{lz})$) presented in Section 4.5, from which the different asymmetries A_{FB}^{X}, A_{FB}^{Y} and A_{FB}^{Z} are measured. Having performed a simultaneous likelihood fit to the signal and control regions (see Section 4.4.2), the normalized background contributions are substracted from the data in the signal region. Next, the angular distributions are unfolded using the iterative Bayes unfolding method to particle level in a fiducial region. The efficiencies and migration matrices used as input for the unfolding method are determined from the t-channel POWHEG-BOX + PYTHIA8 Standard Model sample, generated with Full Simulation.

From the unfolded angular distributions the A_{FB}^{X}, A_{FB}^{Y} and A_{FB}^{Z} asymmetries are computed at particle level and found to be:

$$A_{\text{FB}}^{X} = -0.042 \pm 0.008(\text{stat.}) \pm 0.100(\text{syst.})$$
$$A_{\text{FB}}^{Y} = -0.011 \pm 0.008(\text{stat.}) \pm 0.046(\text{syst.})$$
$$A_{\text{FB}}^{Z} = 0.380 \pm 0.009(\text{stat.}) \pm 0.085(\text{syst.})$$

The results presented here are extracted from angular distributions combining both the electron and muon channels. The top quark and top-antiquark productions are also merged.

Finally, the asymmetry results obtained in this thesis are summarised in Figure 4.22, in which the measured asymmetries at particle level in a fiducial region are compared to the NLO SM predictions at particle level in the same fiducial region, provided by the POWHEG-BOX + PYTHIA8 sample. The measurements are also compared with the predictions given by PROTOS + PYTHIA8 for various configurations of Wtb anomalous couplings. The results provided in this thesis are consistent with the SM predictions.

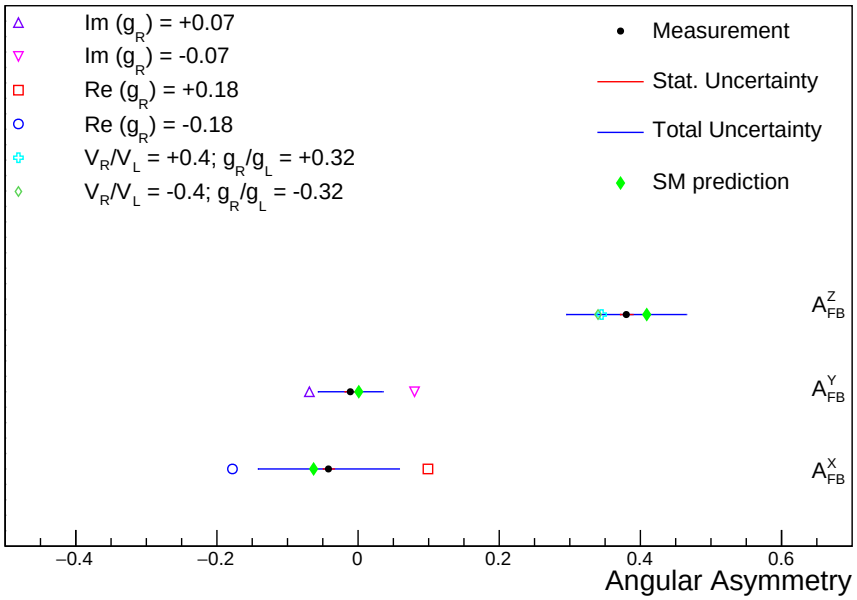

Figure 4.22: Summary of the measured asymmetries (black points) with their corresponding statistical uncertainty (red lines) and total uncertainty (blue lines). The measured asymmetries are compared with the SM predictions provided by the NLO POWHEG-BOX sample (green diamonds), but also with new physics predictions provided by LO PROTOS samples, corresponding to different settings of Wtb anomalous couplings . Good agreement is found between the measurement and the SM prediction.

Chapter 5

Conclusions

This thesis has been elaborated with the $p-p$ collisions data collected by the ATLAS experiment at the CERN LHC collider. It is divided into two well differentiated parts: one devoted to the alignment of the ATLAS Inner Detector, and another part dedicated to the measurement of top quark polarization observables sensitive to Wtb anomalous couplings in single top t-channel production.

The purpose of the Inner Detector is to reconstruct the trajectory of charged particles. For that purpose, it is composed of modules with high intrinsic resolution. However, if the location of the modules less well-known than the intrinsic module resolution, this may worsen the track parameter resolution, in the least of the cases, or even bias them. Therefore, the primordial task of the Inner Detector alignment is to determine the sensor positions and orientations and follow its eventual changes. Although the alignment work presented in this thesis corresponds to the early Run 2 period, the ATLAS Inner Detector has been aligned for the whole LHC Run 2 data set. It uses a track based procedure that minimizes the track-hit residuals. The alignment procedure acts in a hierarchical level, from the big structures assembly to individual modules or sensor elements. In total the system deals with more than 36,000 degrees of freedom for the silicon modules (IBL, Pixel and SCT) and more than 700,000 for the TRT.

Although the majority of the Inner Detector structure has remained quite stable, it was observed during the early Run 2, that the operational conditions affect the actual geometry of some parts the Inner Detector, namely the Pixels and the IBL. The Inner Detector alignment framework has been successfully upgraded to cope with time-dependent deformations observed during Run 2 in order to correct for IBL and Pixel rapid movements.

The alignment work performed in this thesis has studied the effect of the track-based alignment weak modes (i.e. distortions of the detector that corresponds to systematic uncertainties of the track-based alignment minimization method) through the computation of track sagitta and impact parameters biases. Radial distortions studies have also been performed. With the aim of assessing the weak modes or bias in the track parameters, dimuon resonances have been used.

In spite of the very challenging conditions, the alignment has been able to reach very precise results in a fully automatized process. Weak modes misalignments were identified and corrected for 2016 data. During this thesis, the initial 2017 alignment has also been validated.

The second part of this thesis, corresponds to the physics analysis. This analysis makes use of 80.5 fb^{-1} of data collected by the ATLAS detector at the LHC between 2015 and 2017, at a center-of-mass energy of $\sqrt{s} = 13$ TeV. The goal of the analysis is to probe the Wtb vertex which appears at the production of t-channel single top quark events and also at the decay of the top quark. In order to select t-channel single top quark events, the selected events are required to contain exactly one lepton, exactly two jets (one being b-tagged) and large missing transverse energy. A cut-based strategy is used to discriminate the signal events from the background contributions. The main background sources after the selection arise from $t\bar{t}$ and W+jets events.

The analysis uses top quark polarization observables sensitive to top quark couplings, with special focus on g_R, have been proposed in Ref. [71]. Such new physics observables are measured from asymmetries of various angular distributions, accounting for the top quark spin direction, and its normal and transverse direction.

Previous ATLAS analyses [79–81] have obtained the value of the three top quark polarization components. In those analysis the observed angular distributions are corrected for detector effects to the parton level, so that the measured polarization can be compared directly with theoretical calculations. However, the correction performed to parton level typically introduces large systematic uncertainties coming from the signal modelling understanding. The measurements at parton level are generally model dependent and therefore only valid for a consistency check of the Standard Model, which is the model asssumed when correcting to parton level. In this thesis, the observed angular distributions are unfolded to particle level in a fiducial region matching the detector acceptance, with the purpose of having a measurement independent of any model assumption.

From the unfolded angular distributions the A_{FB}^{X}, A_{FB}^{Y} and A_{FB}^{Z} asymmetries are computed at particle level and found to be:

$$
\begin{aligned}
A_{\text{FB}}^{X} &= -0.042 \pm 0.008(\text{stat.}) \pm 0.100(\text{syst.}) \\
A_{\text{FB}}^{Y} &= -0.011 \pm 0.008(\text{stat.}) \pm 0.046(\text{syst.}) \\
A_{\text{FB}}^{Z} &= 0.380 \pm 0.009(\text{stat.}) \pm 0.085(\text{syst.})
\end{aligned}
$$

The results provided in this thesis are consistent with the SM predictions. The dominant systematic uncertainties are: jet energy scale and jet energy resolution, although $t\bar{t}$ and signal modelling uncertainties are also found to be non-negligible.

It must also be said, that the measurement in this thesis has been the benchmark to provide a fiducial polarization measurement, using the whole 140.0 fb^{-1} Run 2 dataset. In such analysis, differential angular distributions are provided for angles $\theta_{\ell x}, \theta_{\ell y}, \theta_{\ell z}$ unfolded to particle level, for events lying within the acceptance of the analysis. During the writing of this thesis, the corresponding paper is being considered for publication by the ATLAS collaboration [189].

Capítol 6

Resum en valencià

De què està feta la matèria? Com interaccionen els seus constituents? Aquesta mena de preguntes han format part de la nostra societat des de temps molt remots en l'antiguitat. De fet, els savis de l'antiga Grècia van ser els primers en tractar de donar una explicació a aquestes qüestions. No obstant això, ho van fer en termes filosòfics, malgrat que aquestes explicacions serien aprofitades posteriorment per la ciència en el procés d'el·laboració dels models atòmics. Aquest procés va ser dut a terme a principis del segle XX i és considerat avui en dia como una vertadera revolució científica de la física del món subàtomic. Aquesta revolució científica va ser possible gràcies a la col·laboració de la física teòrica i la física experimental, i tanmateix va suposar el naixement de la física de partícules.

El Model Estàndard (SM) de la física de partícules és el marc teòric que millor descriu el món subatòmic en l'actualitat i la culminació de la revolució científica adés mencionada. Tot i que el SM és una teoria extremadament precisa, a la natura s'hi observen fenòmens que el SM no pot explicar. És per això, que el SM és una teoria que roman incompleta. El laboratori de física de partícules CERN (*Conseil Européen pour la Recherche Nucléaire*) hi va ser molt rellevant en la configuració del SM de física de partícules. Tanmateix, avui en dia el CERN juga un paper clau en la cerca de física més enllà del SM, el que hom coneix com nova física.

Aquesta tesi fa ús de dades enregistrades pel detector ATLAS (*A Toroidal LHC ApparatuS*), que es troba a l'accelerador LHC (*Large Hadron Collider*) i pertany a les instal·lacions del CERN. La tesi s'organitza en dues parts ben diferenciades. D'una banda, aquesta tesi tracta les tasques de maquinari realitzades amb el propòsit de mantindre el detector intern d'ATLAS correctament alineat mentres hi enregistra dades. D'altra banda, aquesta tesi presenta una anàlisi de dades que empra esdeveniments del quark cima [1], que és sensible a nova física i n'és la partícula fonamental més massiva fins ara detectada. En qualsevol cas, ambdues anàlisis s'enquadren en el segon període de funcionament de l'LHC, anomenat Run 2 i que abasta des de l'any 2015 fins al 2018.

[1] D'ara endavant ens referirem al quark cima emprant el terme anglès *top*.

Els treballs d'alineament del detector intern d'ATLAS es van dur a terme per a dades enregistrades a l'any 2016 i inicis del 2017, mentres que l'anàlisi de física utilitza dades preses durant els anys 2015, 2016 i 2017.

6.1 Marc teòric

6.1.1 El Model Estàndard de física de partícules

El Model Estàndard de física de partícules és una teoria quàntica de camps que descriu de manera molt precisa les interaccions dels fermions (els constituents fonamentals de la matèria) mitjançant l'intercanvi de bosons, que són com es coneixen les partícules portadores de la corresponent força d'interacció.

Família	Quarks	Espín	Càrrega elèctrica	Leptons	Espín	Càrrega elèctrica
1a	u	1/2	+2/3	e^-	1/2	-1
	d	1/2	-1/3	ν_e	1/2	0
2a	c	1/2	+2/3	μ^-	1/2	-1
	s	1/2	-1/3	ν_μ	1/2	0
3a	t	1/2	+2/3	τ^-	1/2	-1
	b	1/2	-1/3	ν_τ	1/2	0

Taula 6.1: Fermions presents al SM classificats en famílies. S'inclou l'espín i la càrrega elèctrica de cada partícula.

Bosons	Espín	Càrrega elèctrica
g	1	0
Z, $W^\pm$	1	0, ± 1
γ	1	0
H	1	0

Taula 6.2: Bosons presents al SM. S'inclou l'espín i la càrrega elèctrica de cada partícula.

D'una banda, els bosons mediadors de les interaccions (anomenats bosons de *gauge*) són partícules d'espín enter, que obeeixen l'estadística de Bose-Enstein. Hi ha tres tipus de bosons: vuit gluons (g) sense massa (responsables de la mediació de la interacció forta entre partícules quarks i gluons), un fotó (γ) sense massa (responsable de la interacció entre partícules carregades) i tres bosons (Z, $W^\pm$) massius (que intervenen en interacciones febles neutres i carregades, respectivament).

D'altra banda, els fermions es classifiquen en leptons i quarks. El seu espín és $1/2$, doncs obeeixen l'estadística de Fermi-Dirac. Cadascun dels fermions conté una antipartícula associada, amb sengles propietats, però carrega elèctrica oposada. Com mostra la Taula 6.1, els fermions a la natura s'observen replicats en tres famílies, ordenades segons l'escala de masses de les partícules que les composen. La primera família, formada per les partícules que conformen la matèria estable de l'univers, és la més lleugera; mentres que la tercera família és la més massiva.

Tanmateix, els quarks disposen d'una propietat addicional que es coneix com càrrega de color (que pren tres valors: roig, blau i verd). No obstant això, els quarks es combinen per a formar partícules sense color, anomenades hadrons. Amb una parella de quark-antiquark formen un mesó i amb tres quarks formen un barió. Aquest confinament és possible gràcies a que els quarks intervenen mitjançant l'interacció forta. Igualment, aquest procés es pot repetir successivament, donant lloc a un doll d'hadrons que es propaga en la mateixa direcció que el hadró primitiu (d'ara endavant, ens referirem a aquest procés amb el terme anglès, és a dir, *jet* de partícules).

El principi de simetria sobre el que es recolza aquesta teoria quàntica de camps del SM és l'$SU(3)_C \bigotimes SU(2)_L \bigotimes U(1)_Y$, que concentra les interaccions fortes i electrofebles: el terme $SU(2)_L \bigotimes U(1)_Y$ fa referència a la simetria local de les interaccions electrofebles, entretant que el terme $SU(3)_C$ descriu la simetria local de les interaccions fortes. Sota aquest principi, les lleis físiques associades a les interaccions fortes i electrofebles romanen invariants sota transformacions locals.

Tot plegat, el SM constitueix un model teòric molt elegant, que ha sigut desenvolupat i testat fil per randa al llarg dels anys. Amb tot, el formalisme matemàtic originari del SM prediu només partícules sense massa. Llavors, durant el seu desenvolupament inicial mancava un mecanisme apte per descriure les partícules electrofebles massives. El mecanisme de ruptura espontània de la simetria, realitzat al 1964 per Higgs [8], Brout i Englert [9], donà finalment sentit al fet d'observar els bosons massius Z i $W^{\pm}$. Ho feia a través de la predicció d'una nova partícula, el bosó de Higgs H, l'interacció de la qual (interacció de Yukawa) és l'origen dels fermions i els bosons massius observats a la natura. El descobriment del bosó de Higgs al 2012 per les col·laboracions ATLAS [23] i CMS [24], encara és avui en dia un dels majors assoliments del SM.

Malgrat l'elevada quantitat de proves que validen el SM, encara resten interrogants que fan pensar que ha d'haver-hi una teoria més general, capaç d'aglutinar-ne alguns fenòmens que no s'expliquen mitjançant el SM en la seua descripció actual. A tall d'exemple, les oscil·lacions de neutrinos constitueixen la primera evidència de nova física més enllà del SM. Tanmateix, l'origen de les tres famílies de fermions, l'origen de la matèria fosca i de l'energia obscura (que constitueixen el 25 % i el 68 % del contingut de l'univers respectivament); així com l'asimetria matèria-antimatèria de l'univers (per a la qual la violació de CP que prediu el SM és insuficient) són preguntes que manquen d'una explicació satisfactòria avui en dia.

6.1.2 La física del quark *top*

El quark *top* és la partícula fonamental més pesada descoberta fins al moment. La seua massa equival fins i tot a la d'un àtom d'or! El seu descobriment va ser realitzat pels experiments CDF i D0 al 1995 en les instal·lacions del Fermilab, utilitzant el col·lisionador de protons i antiprotons conegut com Tevatron. El seu descobriment va culminar l'estructura de tres famílies del SM.

Com que té una massa tan gran, el quark *top* és la partícula que més interacciona amb el bosó de Higgs, i possiblement també amb partícules de nova física. Tanmateix, tindre'n una massa tant elevada li permet desintegrar-se abans d'hadronitzar, oferint així la possibilitat d'estudiar les seues propietats amb els seus productes de desintegració. El 99,8 % de les vegades el quark *top* es desintegra electrofeblement en un bosó W i un quark b. A continuació, el bosó W també es desintegra a partícules més estables.

L'estudi de la física associada al quark *top* és interessant, doncs hi apareix en escenaris teòrics de física més enllà del SM, on noves partícules apareixen en la producció o desintegració del quark *top*. En qualsevol cas, és cabdal mesurar amb la màxima precissió possible les propietats del quark *top* per poder confrontar-les amb aquelles predites pel SM.

Al col·lisionador d'hadrons LHC, la producció del quark *top* pot ocórrer o bé en parelles mitjançant la interacció forta, o bé en solitari associat amb altres partícules mitjançant la interacció electrofeble. Tot i que la producció en parelles és la predominant, la producció del quark *top* en solitari també resulta interessant d'estudiar, doncs permet estudiar l'estructura del vèrtex Wtb tant en la producció com en la desintegració del quark *top*. A més a més, en la producció en solitari el quark *top* està polaritzat. A primer ordre, hi ha tres modes de produir el quark *top* en solitari i es troben representats en la Figura 6.1.

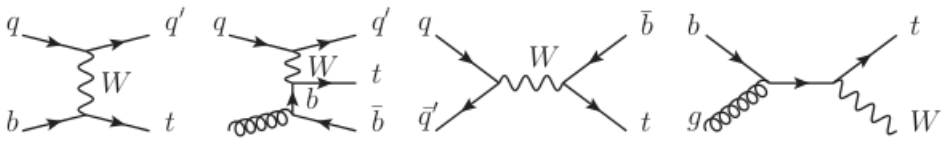

Figura 6.1: Modes de producció del quark *top* en solitari representats amb diagrames de Feynman. De esquerra a dreta: canal t (5 FS), canal t (4 FS), canal s i canal Wt.

6.2 Dispositiu experimental

6.2.1 LHC: Gran Col·lisionador d'Hadrons

Per tal de dur a terme els estudis associats al quark *top*, descrits a la secció anterior, és necessari produir un gran nombre d'esdeveniments de senyal per tal de acumular suficient estadística. Açò va ser possible amb la posada en marxa del Gran Col·lisionador d'Hadrons (LHC) a l'any 2009 a les instal·lacions del CERN. Considerat com una "factoria" del quark *top*, el LHC va suposar una nova era experimental de la física de del quark *top*.

L'LHC és un anell de 26,7 km de circumferència. Es situa 100 m davall del terra, a les rodalies de la frontera franco-suïssa. Empra un complex sistema de imants que generen camps magnètics molt potents, per tal de corbar els dos feixos de protons (o ions pesats) que circulen per dintre. Tanmateix, diverses cavitats

de ràdio-freqüènciadistribuïdes al llarg de l'anell proporcionen camps elèctrics per accelerar els feixos de partícules. Durant el primer periode d'operació de l'LHC (Run 1), el feixos de l'LHC han sigut accelerats a energies de $\sqrt{s} = 7$ i 8 TeV. Durant el Run 2, periode de operació recentment finalitzat, l'energia assoliada ha sigut de $\sqrt{s} = 13$ TeV. A més a més, la luminositat (paràmetre que caracteritza el nombre de col·lisions per unitat de temps) durant el Run 2 ha superat el valor de disseny nominal de l'LHC de $10^{34}\mathrm{cm}^{-2}\mathrm{s}^{-1}$

Al llarg de l'LHC, es van dissenyar quatre punts d'interacció dels feixos, on es disposen quatre detectors de partícules. ATLAS i CMS són experiments de propòsit general, dissenyats per cobrir un ventall molt ampli d'estudis (on s'inclou la física del quark *top*); mentres que LHCb i ALICE són experiments dedicats a un tema en concret.

6.2.2 ATLAS: *A Toroidal LHC Apparatus*

Una vegada descobert el bosó de Higgs, ATLAS investiga un espectre molt ampli de la física de partícules, desde l'estudi de les propietats del bosó de Higgs fins a l'evidència de física més enllà del SM (com dimensions extra i partícules supersimètriques). La Figura 6.2 mostra una visió esquemàtica dels components del detector ATLAS, que com s'observa es troben arranjats a mode de capes, com si fós una ceba cilíndrica. Les seues dimensions són 46 m de llargària, 25 metres d'amplària i 25 m d'altura, amb un pes de vora 7000 tones.

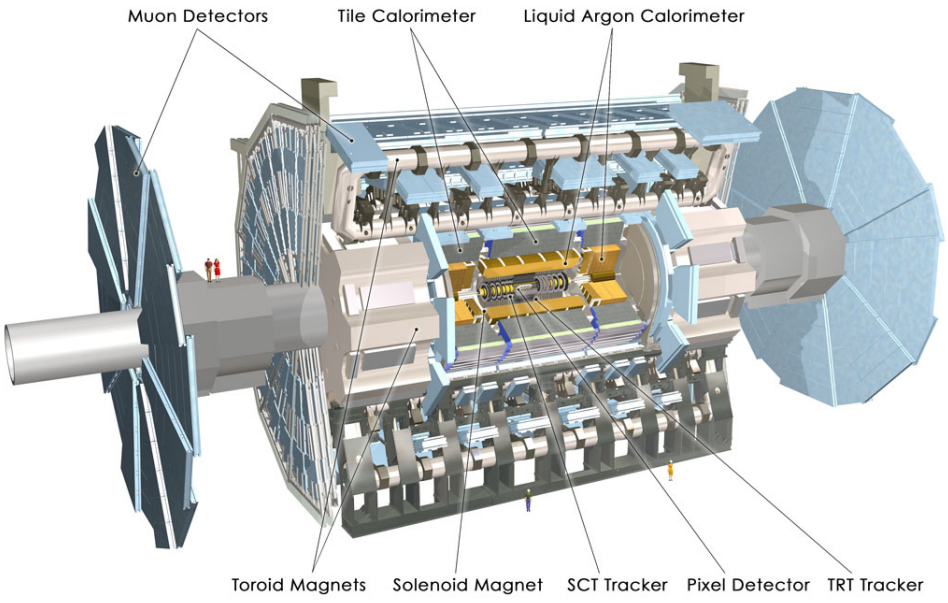

Figura 6.2: Esquema d'ATLAS.

Una vegada produïdes les partícules en la col·lisió, i a partir del rastre que deixen aquestes en els mòduls que composen el detector, cadascun dels subdetectors s'hi encarrega d'una funció específica per tal de caracteritzar les partícules amb la mesura de dues quantitats físiques: l'energia i el moment. Els neutrinos són les úniques partícules conegudes que no deixen cap senyal al seu pas pels detectors, però podem intuir la seua presència si hi ha un dèficit en l'energia transversal total. De dins cap a fóra trobem el següents subdetectors:

- Detector intern: determina les càrregues, posicions i moments de totes les partícules carregades produïdes, mesurant trajectòries corbes de partícules càrregades a partir del rastre de senyals que deixa en cadascun dels mòduls que el composen. La corbatura de les trajectòries s'aconsegueix emprant un camp magnètic axial constant de 2 T, proporcionat per un solenoide que envolta el detector intern.

- Calorímetre electromagnètic: mesura l'energia i posició d'electrons i fotons aturant-los en el seu interior. L'energia es mesura iniciant una interacció amb les partícules elèctricament carregades del medi, provocant una cascada electromagnètica.

- Calorímetre hadrònic: mesura l'energia i posició de gluons i quarks produïts per interacció forta absorbint els hadrons formats (com protons i neutrons), doncs els hadrons interaccionen amb els nuclis atòmics. En els calorímetres es poden absorbir quasi totes les partícules, exceptuant muons i neutrinos, que precissen d'altres mètodes per a la seua mesura.

- Cambra de muons: com que els muons travesen el ferro del calorímetre sense interaccionar gaire, la cambra de muons es col·loca a l'extrem del detector. La manera de detectar els muons és molt semblant a la del detector intern. Bàsicament, són un cert nombre d'estacions que enregistren el seu pas en un camp magnètic que corba la trajectòria del muó, permitint calcular el moment del muó. El camp magnètic que s'empra en aquest punt és proporcionat per un sistema de vuit imants toroïdals.

Així mateix, degut a les limitacions en l'emmagatzematge de la ingent quantitat de dades produïdes, cal fer un filtratge de aquelles que són rellevants. El sistema necessari per a fer-ho és l'anomenat *trigger*, en anglés. Cada nivell du a terme una selecció de dades; de tal manera que d'uns 40 milions d'esdeveniments per segon, se'n guarden uns pocs milers. El CERN empra una potent xarxa de superordinadors (coneguda com *Grid*) per guardar i analitzar totes aquestes dades.

Una vegada les dades es troben en disposició de ser analitzades, els senyals enregistrats pels diferents subdetectors han de ser traduïts a objectes físics reconstruïts; açò és: electrons, muons, *jets*, *jets* originats d'un quark b i energia transversal faltant. La reconstrucció en el cas dels electrons es fa combinant informació de la

traça al detector intern juntament amb el dipòsit d'energia al calorímetre electromagnètic. La reconstrucció dels muons empra traces obtingudes tant al detector intern com a la cambra de muons. D'altra banda, els *jets* es reconstruixen a partir de les topologies dels dipòsits d'energia del calorímetre amb l'algoritme *anti-*k_t [110]. Per a identificar *b-jets* és necessari fer ús d'algoritmes que analitzen les propietats d'aquestes partícules, com per exemple el paràmetre d'impacte o la presència de vèrtexs secundaris. Finalment, per a poder confirmar la presència de neutrinos, s'ha de trobar un desequilibri en la energia transversal total (que en una col·lisió hauria de ser zero); és que el que hom coneix per energia transversal faltant.

6.3 Alineament del detector intern d'ATLAS

El detector intern ATLAS consta de tres subdetectors, dos basats en silici i un basat en tecnologia de tubs de deriva. El detector de Pixels és aquell més proper al punt d'interacció dels feixos. Està format per 1744 mòduls de silici arranjats en tres capes de barril i dues tapes de tres discs cadascuna. Per al Run 2, se li va afegir als Pixels una capa addicional, anomenada IBL. L'IBL es situa a 33.25 mm del feix i es troba en la part més propera a aquest. La seua tecnologia barreja sensors planars i i sensors 3D. A continuació trobem l'SCT, format per milers de sensors de silici disposats en quatre capes de barril i dues tapes de nou discs cadascuna. Finalment, la capa més externa del detector intern la conforma el TRT, que està format per uns 350.000 tubs de deriva farcits d'argó, disposats de manera anàloga a l'SCT en un barril central i dues tapes als extrems.

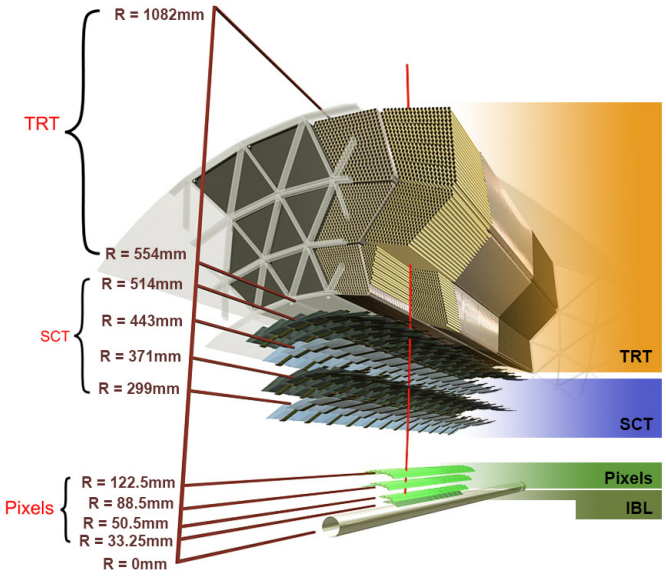

Figura 6.3: Vista esquemàtica de la part central del barril del detector intern. De la part interna a la més externa trobem els subdetectors IBL, Pixel, SCT i TRT.

Amb l'objectiu de reconstruir la trajectòria de les partícules carregades, s'empra la informació que capten cadascun dels mòduls quan els recorre una partícula. No obstant això, la geometria real del detector pot variar durant la presa de dades degut a canvis en les condicions d'operació. Així doncs, la finalitat del procediment d'alineament del detector intern és conéixer la posició de cadascun dels mòduls amb major precisió que la resolució intrínseca d'aquests i la seua evolució temporal. A més a més, en cas de detectar alguna mena de moviment del detector intern, l'alineament ha d'introduir-hi correccions per evitar degradar la resolució dels paràmetres de les traces, o inclús esbiaixar-los en el pitjor dels casos.

6.3.1 Algoritme d'alineament

Com que el detector és inaccessible durant la presa de dades i es precisa d'una gran precisió, l'alineament del detector es fonamenta en un mètode indirecte que minimitza distàncies dels senyals enregistrats pels diferents mòduls del detector. Les distàncies que es minimitzen, o residus, es defineixen entre el punt del senyal mesurat per un sensor i el mateix punt reconstruït a partir de la extrapolació de la traça. Llavors, cada mòdul o estructura mecànica és considerat com un sòlid rígid de 6 graus de llibertat (tres translacions i tres rotacions), per poder definir la seua posició i orientació a l'espai; i així doncs, poder ser alineats. La Figura 6.4 mostra una visió bàsica del funcionament de l'algoritme.

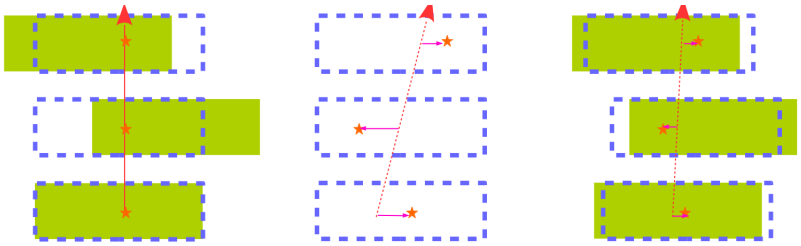

Figura 6.4: Visió esquemàtica de l'algoritme d'alineament. A l'esquerra es mostra una traça real (en roig) representant el detector com una caixa verda. La posició aparent es representa com una línia discontínua blava. Al centre, es mostra la traça reconstruïda emprant la posició aparent del detector. Per últim a la dreta, es mostra la traça reconstruïda que s'obté després d'aplicar l'algoritme d'alineament. Els residus es representen amb línies roses.

La minimització de les distàncies es realitza emprant la funció χ^2 que s'observa en l'equació 6.1:

$$\chi^2 = \sum_{tracks} \sum_{hits} \left(\frac{\vec{r}_h(\boldsymbol{\pi}, \mathbf{a})}{\sigma_h} \right)^2 = \sum_{tracks} \vec{r}(\boldsymbol{\pi}, \mathbf{a})^T \, V^{-1} \, \vec{r}(\boldsymbol{\pi}, \mathbf{a}), \tag{6.1}$$

on V és la matriu de covariança que conté les incerteses de les mesures del detector[2], $\mathbf{r}$ són els residus, $\mathbf{a}$ els paràmetres d'alineament i $\boldsymbol{\pi}$ els paràmetres de les traces.

En efecte, la funció χ^2 hi té un mínim en l'espai que es correspon amb la geometria real del detector. Només es necessita derivar respecte els paràmetres d'alineament:

$$\frac{d\chi^2}{d\mathbf{a}}|_{\mathbf{a}=\tilde{\mathbf{a}}} = 2\sum_t \left(\frac{d\mathbf{r_t}(\boldsymbol{\pi},\tilde{\mathbf{a}})}{d\mathbf{a}}|_{\mathbf{a}=\tilde{\mathbf{a}}}\right)^T V^{-1}\,\mathbf{r_t}(\boldsymbol{\pi},\tilde{\mathbf{a}}) = 0. \tag{6.2}$$

Cal destacar però, que els residus depenen de les traces i la posició dels sensors, i que a més a més les traces depenen de la posició dels sensors a través dels paràmetres d'alineament. Tot açò queda reflectit en l'equació 6.3:

$$\frac{d\chi^2}{d\mathbf{a}} = \boxed{\frac{d\boldsymbol{\pi}}{d\mathbf{a}}}\frac{\partial\chi^2}{\partial\boldsymbol{\pi}} + \frac{\partial\chi^2}{\partial\mathbf{a}}. \tag{6.3}$$

Aquesta important característica distingeix dos maneres d'aplicar l'algoritme. El primer cas es coneix com *Global* χ^2. Ocorre quan $\frac{d\boldsymbol{\pi}}{d\mathbf{a}} \neq 0$ i l'algoritme s'aplica simultàniament considerant tots els mòduls que intervenen en la reconstrucció d'una traça. El segon cas és el *Local* χ^2, que ocorre quan $\frac{d\boldsymbol{\pi}}{d\mathbf{a}} = 0$; és a dir, a la reconstrucció només s'empra informació d'un mòdul en concret (deixant la resta fixes). De qualsevol manera, l'algoritme es basa en l'inversió d'una matriu. A banda, necessita assumir una geometria del detector, aleshores és important que els paràmetres d'alineament inicial siguen tan precissos com siga possible. Com que no sempre és possible proporcionar una geometria del detector semblant a la vertadera, l'algoritme s'aplica de forma iterativa fins que convergeix a una sol·lució.

Tanmateix, cal nombrar que la implementació de l'algoritme es realitza de forma jeràrquica en diferent nivells que permet alinear des de les estructures més grans fins a cadascun del sensors individuals. La Taula 6.3 mostra els diferents nivells d'alineament, començant pel nivell 1 (estructures grans) i finalitzant amb el nivell 3 (sensors). En total el sistema consta de 36.000 graus de llibertat per als mòduls de silici (IBL, Pixel i SCT) i més de 700.000 per al TRT.

[2]En general la matriu V no és diagonal degut al fenòmen de dispersió coulombiana múltiple, que relaciona mòduls subsegüents en la trajectòria d'una partícula i l'angle de dispersió. Si no es consideren correlacions entre mòduls, aleshores la matriu de covariança és diagonal.

Nivells	Estructures	Graus de llibertat
L1 (estructures grans)	8	48
L2 (capes/discs, mòduls del TRT)	208	792
L3 (mòduls)	6112	36672
L3 (cables del TRT)	350848	701696

Taula 6.3: Nivells d'alineament emprats a l'algoritme, juntament amb el corresponent nombre de graus de llibertat. El nivell 1 es correspon amb les estructures més grans (barril, tapes). El nivell 2 es correspon amb els discs i capes del barril i les tapes. El nivell 3 fa referència als mòduls i als cables del TRT.

6.3.2 Deformacions depenent del temps

Malgrat que la major part de la estructura del detector intern ha estat prou estable (especialment al Run 1); a principis del Run 2 es va observar que les condicions d'operació introduiren moviments depenent del temps, que afectaven sobretot al Pixel i al IBL. Per tant, el marc de referència en què s'aplica l'algoritme va haver-hi de ser modificat per tal de poder corregir-ne aquests ràpids moviments. Dos tipus de moviments van ser identificats durant el Run 2:

- Moviments verticals del Pixel al començament de cada presa de dades.
- Inestabilitats mecàniques depenents de la temperatura de l'IBL.

6.3.2.1 Moviments del Pixel

Els moviments verticals del Pixel durant el Run 2 tenien lloc quan el detector mamprenia a enregistrar les dades[3]. Prèviament, durant el Run 1, aquest efecte a penes era observable en una petita fracció de les dades. La raó d'aquest moviment subjau en què una vegada s'inicien els sistemes del detector, el líquid refrigerant s'evapora i causa una diferència de massa del líquid refrigerant, fins que s'equilibren de nou el vapor i el líquid. A continuació, després de inicialment ascendre, s'observava que el Pixel descenia lentament fins estabilitzar-se, tal i com mostra la Figura 6.5. L'equip d'alineament va determinar que la velocitat de descens depenia de la lluminositat instantània en què operava el LHC durant la presa de dades. Llavors, un nou esquema dinàmic va ser introduït a l'agost del 2016 per tal de corregir aquests efectes variants al llarg de la presa de dades.

6.3.2.2 Inestabilitats mecàniques de l'IBL

El segon tipus de moviment del detector intern identificat al Run 2 es tracta de l'arquejat de les dogues de l'IBL en la direcció "x" del sistema referència local; inclús durant una mateixa presa de dades. Es va determinar que aquest arquejament

[3]També conegut en anglés com *run*, en minúscula.

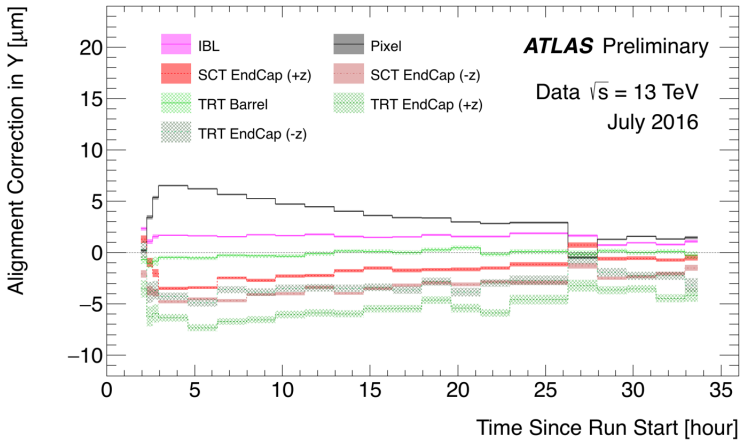

Figura 6.5: Correccions en la component vertical Y per a components del detector intern en funció del temps. La figura mostra inicialment un ràpid moviment vertical de 6 μm per al subdetector Pixel en la component vertical Y, seguit d'un subtil descens.

és depenent amb la temperatura i es manifesta quan les dogues es refreden, com s'observa a la Figura 6.6. Per a aquest estudi, es van usar dades de 2015 i 2016 i l'IBL es va a sotmetre a diferents temperatures d'operació, en el interval de $[+15°$ C , $-20°$ C$]$.

La distorsió global promediada sobre les 14 dogues de l'IBL s'extrau amb un ajust parabòlic:

$$\delta(x(z)) = B + M\left(1 - \frac{z^2}{z_0^2}\right), \tag{6.4}$$

on z és la posició del mòdul en eixa mateixa direcció, $z_0 = 366.5$ mm és el punt d'anclatge a ambdós extrems, B és la base que descriu una translació global en la direcció local-x i M la magnitud de la distorsió de les dogues. Després de realitzar l'ajust, el gradient de temperatures obtingut va ser der: $\frac{dM}{dT} = -10.6 \pm -0.7$ [μm/K].

L'origen d'aquesta corbatura és mecànica, doncs existix una diferència en el coeficient tèrmic dels materials que composen les dogues de l'IBL. Un augment sobtat de la lluminositat, com el que es va produir al 2016, causa un augment del consum dels mòduls per la major irradiació al que estan sotmesos. Eventualment, un augment del consum dels mòduls es manifesta com un augment de la temperatura dels mòduls respecte a la temperatura nominal de $-20°$C ; que resulta en el vinclament de les dogues de l'IBL.

Com hem dit adés, un nou esquema dinàmic va ser introduït al *Calibration Loop*, que és com es coneix el procés on es calculen algoritmes de calibració; un d'ells és és l'algoritme d'alineament on es calculen les correccions als paràmetres d'alineament. En primer lloc, un nou grau de llibertat va ser definit per tal de poder corregir la distorsió de l'IBL. En un primer nivell anomenat *Nivell 11*, es corregix la distorsió promediada sobre les 14 dogues i en un segon nivell, *Nivell 16*, es tracta la

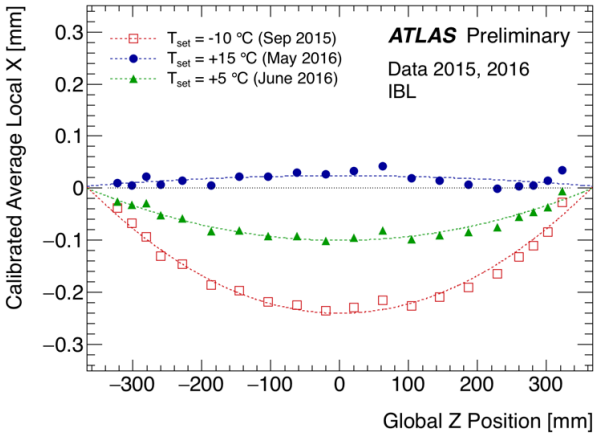

Figura 6.6: Arquejat de l'IBL promediat sobre les 14 dogues usant dades de 2015 i 2016. L'arquejat és depenent de la temperatura (+15 °C, cercles blaus; +5°C, triangles verds; -10 °C, quadrats rojos).

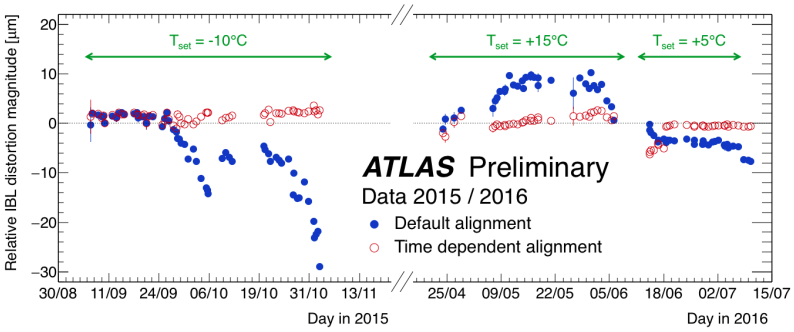

Figura 6.7: Arquejat de l'IBL obtingut amb el equema d'alineament previ (punts blaus) i amb l'esquema dinàmic (cercles rojos). Amb el nou esquema, l'arquejat és correctament corregit.

corbatura de cada doga. A més a més, les correccions als nivels L11 i L16 passaren a ser determinades cada 20 minuts durant les primeres hores de presa de dades. D'aquesta manera, els ràpids moviments verticals del Pixel es poden corregir més acuradament. A continuació, durant el lent procés de descens del Pixel, el càlcul es realitza cada 100 minuts.

6.3.3 Resultats d'alineament al Run 2

A la vista dels resultats del apartat anterior, l'algoritme d'alineament utilitzat durant els inicis del Run 2 ha resultat ser un èxit per proporcionar una descripció precisa de la geometria del detector. No obstant això, per construcció, l'algoritme no es pot aplicar en aquelles deformacions que preserven l'estructura helicoïdal

de les traces, deixant invariant la funció χ^2. Aquestes deformacions, si no són tractades, suposen la introducció de biaixos sistemàtics (anomenats modes febles) que afecten a la descripció de la geometria del detector. Llavors, és menester l'ús de restriccions adicionals com per exemple l'ús de la posició del feix, o la massa de les resonàncies Z i J/ψ (que disposen d'una massa coneguda mesurada molt precissament) per poder detectar i corregir els biaixos associats als modes febles. De fet, quan es produixen desplaçaments ortogonals dels senyals reconstruïts en el detector, la reconstrucció del moment i dels paràmetres d'impacte es veu afectada segons:

$$p_T^{reco} = p_T^{true}\left(1 + q p_T^{true}\delta_{sagita}\right)^{-1} \tag{6.5}$$

on δ_{sagita} és el paràmetre universal del biaix per als moments mesurats.

Per tal de discernir l'impacte dels modes febles, s'han utilitzat parelles muons provinents de la desintegració del bosó Z, per així calcular els biaixos de la sagita i dels paràmetres impactes durant la presa de dades del 2016. Els biaixos de la sagita i dels paràmetres d'impacte es mesuren per a cada regió del detector, i per això, es proporcionen com mapes 2D en funció de les coordenades η i ϕ del detector. Una vegada calculats els biaixos per a cada regió, aquesta informació s'aplica en l'algoritme d'alineament i es re-calculen uns nous paràmetres d'alineament.

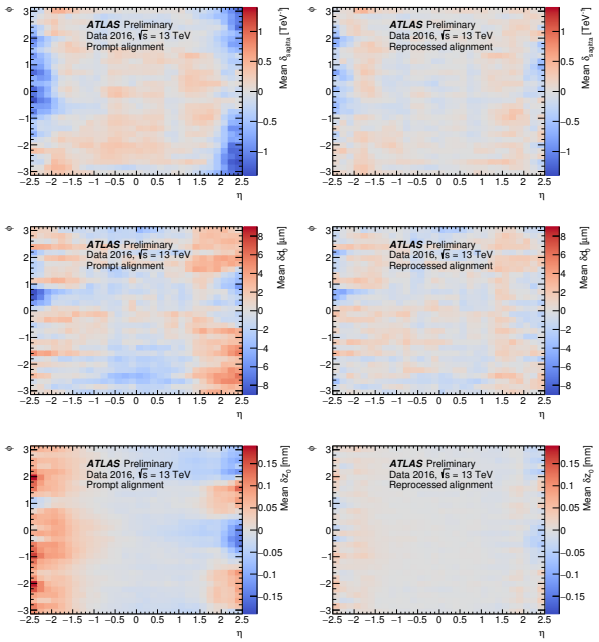

Figura 6.8: Mapes dels biaixos abans (esquerra) i després (dreta) d'haver aplicat aquests a l'algoritme d'alineament, tant per a la sagita com per als paràmetres d'impacte. Es poden apreciar millores considerables després de reprocessar els dades amb la nova configuració d'alineament.

La Figura 6.8 de la part esquerra mostra els mapes de modes febles usant les correccions que proporciona l'algoritme d'alineament poc després de la finalització de cada *run*. La Figura 6.8 de la part dreta en canvi mostra les correcciones obteses en el reprocessat, una vegada s'han aplicat els mapes de biaixos dels modes febles en l'algoritme. Una clara millora s'observa tant per a la sagita com per als paràmetres d'impacte, això és d_0 and z_0, usant dades reprocessades.

Finalment, es va poder comprovar mitjançant els residus de la Figura 6.9 que els mòduls van ser alineats a l'ordre de les $\mathcal{O}(\mu\text{m})$ tant a finals de 2016, però també a inicis de 2017, la qual cosa és tot un èxit.

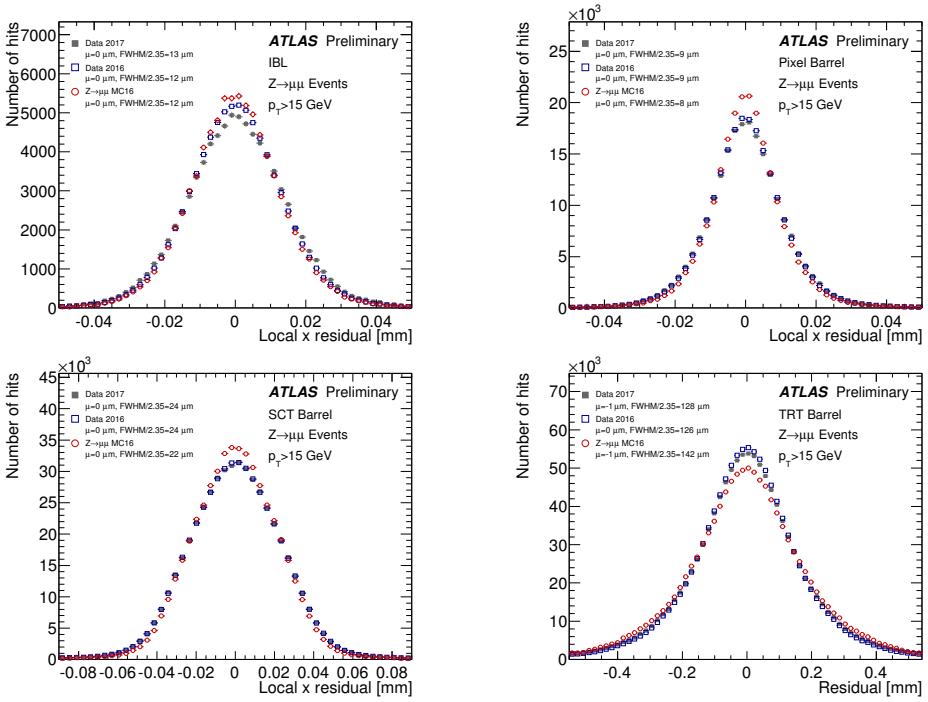

Figura 6.9: Residus de l'IBL, Pixel, SCT i TRT extrets amb esdeveniments provinents de una mostra de $Z \to \mu^+\mu^-$. Es mostren per a un dels primers *runs* enregistrats al 2017 (quadrats grisos) i per a les dades de 2016 reprocessades (quadrats blaus). Tots dos són comparats amb una mostra de Monte Carlo d'esdeveniments $Z \to \mu^+\mu^-$ (cercles rojos).

Aquesta manera de procedir, aplicada ací durant 2016, també va ser aplicada per a la presa de dades efectuada durant la resta del Run 2 (2015-2018). Al cap i a la fi, disposar de dades de qualitat ha resultat fonamental per als anàlisis de física que les utilitzen.

6.4 Estudi del vèrtex Wtb

El quark *top* pot ser produït en solitari en el canal t a través del vèrtex Wtb, quan un quark de valència del protó interactua amb un quark b mitjançant l'intercanvi d'un bosó W, produïnt un quark lleuger (conegut com quark espectador) i el quark *top*, tal i com es mostra a la Figura 6.10. El quark *top* produït d'aquesta manera presenta un alt grau de polarització en la direcció del quark espectador. Com que a més a més, el quark *top* es desintegra ràpidament sense hadronitzar, la informació de seu espín es trasllada als seus productes de desintegració.

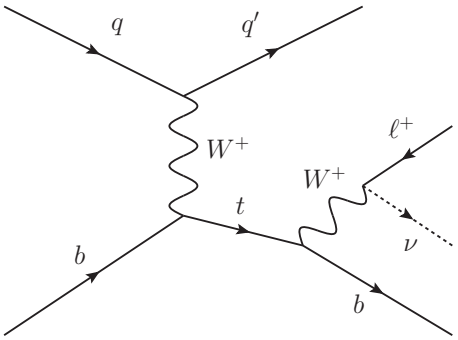

Figura 6.10: Diagrama de Feynman que representa la producció del quark *top* en solitari en el canal t mitjançant col·lisions protó-protó.

L'interés de la mesura d'observables relacionats amb la polarització del quark *top* radica en què, en presència de nova física, les correccions que s'introduïrien en el vèrtex Wtb afectarien a la polarització del quark *top*. Aleshores, disposar d'una parametrització general de les interaccions del quark *top* és cabdal per cercar efectes de nova física d'una manera independent. En el context d'una teoria quàntica de camps efectiva, el lagrangià més general possible en el vèrtex Wtb és el següent:

$$\mathcal{L}_{Wtb} = -\frac{g}{\sqrt{2}}\bar{b}\gamma^{\mu}\left(V_L P_L + V_R P_R\right) t W^{-}_{\mu} - \frac{g}{\sqrt{2}}\bar{b}\frac{i\sigma^{\mu\nu}}{M_W}q_{\nu}\left(g_L P_L + g_R P_R\right) t W^{-}_{\mu} + h.c., \tag{6.6}$$

on trobem acoblaments anomals levògirs (i.e. V_L, g_L) i dextrògirs (i.e. V_R, g_R), en ambdós termes. A primer ordre en el SM, l'acoblament V_L es correspon amb l'element de la matriu CKM $V_{tb} \simeq 1$. La resta d'acoblaments són anòmals i s'esvaeixen en el SM. Aleshores, la presència d'acoblaments anòmals diferents de zero, implicaria la presència de física més enllà del SM. En particular, si es mesuraren valors complexos, a més a més, es tractaria d'una component que viola la simetria CP.

Aquests tipus d'observables relacionats amb la polarització del quark *top* són ni més ni menys que asimetries avant-arrere (*forward-backward en anglés*):

$$A^{i}_{\text{FB}} = \frac{N(\cos\theta_{\ell i} > 0) - N(\cos\theta_{\ell i} < 0)}{N(\cos\theta_{\ell i} > 0) + N(\cos\theta_{\ell i} < 0)} = \frac{1}{2}\alpha P_i\,, \tag{6.7}$$

on N és el nombre d'esdeveniments, éssent $i = \hat{x}, \hat{y}, \hat{z}$.

Les asimetries es construeixen a partir de diverses distribucions angulars que consideren la direcció de la polarització del quark espectador, la direcció normal i la transversal, tal i com es proposa en la referència [71]. La Figura 6.11 il·lustra les direccions mencionades.

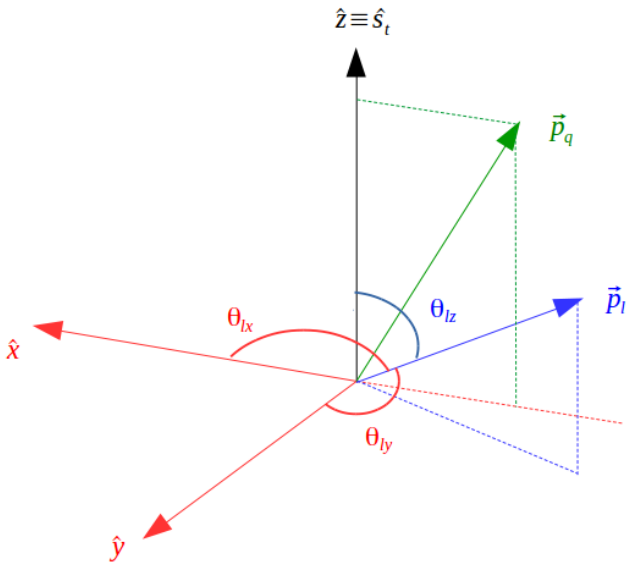

Figura 6.11: Sistema de coordenades cartesià emprat per definir les distribucions angulars en el sistema de producció de quarks *top* i les corresponents asimetries angulars. La direcció de polarització del quark *top* $\hat{s}_t$, es pren al llarg de la direcció del quark espectador, definit a l'eix $\hat{z}$. La direcció $\hat{y}$ es definix ortogonalment al quark espectador i al quark inicial $\vec{p_q}$ (en verd), mentre que $\hat{x}$ es determina mitjançant el requeriment que el sistema de coordenades és cartesià. El diagrama també mostra la direcció del leptó carregat $\vec{p_l}$ en el sistema de referència del quark *top* (en blau). L'angle polar del leptó carregat està etiquetat com θ_{lz}. Els angles polars entre el moment de lepton carregat i els eixos $\hat{x}$ i $\hat{y}$ s'identifiquen amb θ_{lx} i θ_{ly} respectivament.

Els angles θ_{lx} i θ_{ly} són molt sensibles a valors anòmals del vèrtex Wtb, en particular a la part real i imaginària de g_R, respectivament. L'angle θ_{lz} és igualment sensible a ambdues parts reals i imaginària. La Taula 6.4 resumeix la definició de les asimetries angulars juntament amb les corresponent distribucions angulars.

Prèviaments, algunes anàlisis d'ATLAS [79–81] han obtés el valor de la polarització del quark *top* en les tres components a nivell de partons, per així poder comparar directament la mesura amb les prediccions teòriques. No obstant això, s'ha observat que la presència d'acoblaments anòmals modifica la cinemàtica de tal forma que les eficiències de correccions que s'apliquen a les dades a nivell de partons deixen de ser independents dels acoblaments anòmals [80]. Altrament, si

Asimetria	Definició
A_{FB}^{Z}	Asimetria avant-arrere (al voltant de $z = 0$) en la distribució $\cos\theta_{lz}$
A_{FB}^{X}	Asimetria avant-arrere (al voltant de $z = 0$) en la distribució $\cos\theta_{lx}$
A_{FB}^{Y}	Asimetria avant-arrere (al voltant de $z = 0$) en la distribució $\cos\theta_{ly}$

Taula 6.4: Resum de les asimetries resultants dels angles $\theta = \theta_{lz}, \theta_{lx}, \theta_{ly}$.

els observables es mesuren a nivell de partícules en una regió fiducial (tot just abans d'hadronitzar), com es fa en en aquesta anàlisi, les correccions romanen independents dels acoblaments anòmals, doncs no es corrigeix per la transició de partons a partícules.

Aquesta anàlisi fá ús de 80.5 fb^{-1} de dades recollides pel detector ATLAS del LHC entre 2015 i 2017, a una energia en el centre de masses de $\sqrt{s} = 13$ TeV.

6.4.1 Sel·lecció d'esdeveniments

És menester una sel·lecció d'esdeveniments que disposen en l'estat final la mateixa topologia que quarks *top* produïts en solitari mitjançant el canal t i desintegrats de forma leptònica: açò és, exactament un leptó (electró o muó) provinent del bosó W[4], exactament dos *jets* (un d'ells b-jet i l'altre generat per un quark lleuger) i abundant energia transversal faltant. Cal esmentar que en les col·lisions de protons es produeixen esdeveniments semblants al senyal i que es poden confondre amb el senyal. Aquest tipus de processos s'anomenen fons. Els principals fons que hi trobem a la nostra anàlisi són els següents:

- Parelles de quarks *top*.
- Quarks *top* produïts en solitari mitjançant el canal s i Wt.
- Producció de bosons W i Z associats amb *jets*.
- Producció de processos dibosònics (WW, ZZ i ZW).
- Esdeveniments de dolls múltiples de quarks (multijet), generats al interaccionar per QCD, la reconstrucció dels quals es confón amb un leptó.

[4]Si el bosó es desintegra a un tau, també es considera senyal si aquest últim es desintegra leptònicament.

Apliquem dos talls per tal de desfer-nos-en d'esdeveniments de multijet :

$$m_{\mathrm{T}}(W) = \sqrt{2p_{\mathrm{T}}(\ell)E_{\mathrm{T}}^{\mathrm{miss}}\left(1 - \cos\Delta\phi(p_{\mathrm{T}}(\ell), E_{\mathrm{T}}^{\mathrm{miss}})\right)} > 60 \text{ GeV},$$

on $\Delta\phi\left(p_{\mathrm{T}}(\ell), E_{\mathrm{T}}^{\mathrm{miss}}\right)$ és la diferència de l'angle azimutal entre el moment del leptó (p_{T}) i la $E_{\mathrm{T}}^{\mathrm{miss}}$.

$$p_{\mathrm{T}}(\ell) > 50\left(1 - \frac{\pi - |\Delta\phi(j_1, \ell)|}{\pi - 1}\right) \text{ GeV},$$

on $\Delta\phi(j_1, \ell)$ és la diferència azimutal entre l'angle entre el moment del leptó (p_{T}) i el jet amb moment més alt.

La sel·lecció del senyal en aquesta anàlisi es realitza en dues passes mitjançant l'aplicació de talls. La sel·lecció duta a terme fins a aquest punt defineix la regió de preselecció i considera bàsicament la topologia del senyal així com la rejecció d'esdeveniments de multijet. La Figura 6.12 mostra el bon acord que s'obté entre dades i simulacions de Monte Carlo per a la massa invariant del sistema format pel leptó i el b-jet (a) i la massa invariant del quark *top* (b), per a tots aquells esdeveniments que satisfan els criteris de la regió de preselecció.

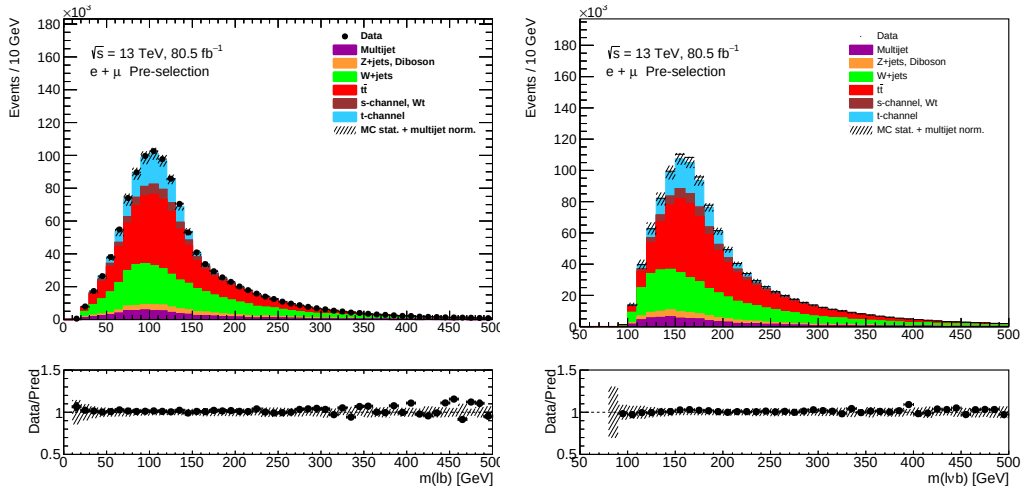

(a) (b)

Figura 6.12: Distribucions de dues variables en la regió de presel·lecció: (a) la massa invariant del sistema format pel leptó i el b-jet, (b) la massa invariant del quark *top*; on es compara les prediccions de simulacions i de les dades.

D'altra banda, la regió de sel·lecció de senyal aplica talls més restrictius per tal de garantir la presència d'esdeveniments de senyal alhora que rebutjar esdeveniments de fons:

- La massa invariant del sistema leptó–b-jet, $m_{\ell b}$, ha de ser menor de 153 GeV, per a rebutjar esdeveniments que no involucren el quark *top*.

- La massa invariant del quark ***top*** reconstruït[5], $m(\ell\nu b)$, ha d'estar en la finestra de 134–206 GeV.

- S'apliquen les següents condicions trapezoidals per tal de rebutjar esdeveniments amb leptons paral·lels al feix i quarks ***top*** en la regió central:

$$\eta_j < \eta_{top} * 4 + a \cap \eta_j > \eta_{top} * 4 - a \tag{6.8a}$$

$$\eta_j > \eta_{top} * 0.44 + b \cup \eta_j < \eta_{top} * 0.44 - b, \tag{6.8b}$$

  éssent els paràmetres a i b 9 i 2, respectivament.

- La massa del sistema format pel ***jet*** espectador i el quark ***top***,m_{jt}, ha de ser superior a 280 GeV.

- La suma de p_{T} de tots els objectes d'estat final, H_{T}, ha de ser superior a 170 GeV.

6.4.2 Regió fiducial a nivell de partícules

Els talls fins ara presentats són útils per sel·leccionar els objectes reconstruïts amb els senyals que enregistra el detector. No obstant això, la nostra mesura es realitza en un pas previ, açò és a nivell de partícules. Com que la regió fiducial ocupada a nivell de partícules ha de ser el més semblant possible a la regió en la qual es mesura els senyals, cal aplicar una sel·lecció a nivell de partícules igualment semblant a la sel·lecció dels objectes reconstruïts. Per tant, és menester requirir a nivell de partícules extactament un leptó amb un moment $p_{\mathrm{T}} > 30$ GeV. Qualsevol leptó addicional amb $p_{\mathrm{T}} > 10$ GeV és rebutjat. Cal tindre exactament dos ***jets*** (éssent un d'aquest b-jet) que satisfan que el seu moment $p_{\mathrm{T}} > 30$ GeV i la seua posició en el detector siga $|\eta| < 4.5$. Tanmateix, cal que l'energia transversal faltant, $E_{\mathrm{T}}^{\mathrm{miss}}$, siga major de 35 GeV i la massa transversal del bosó W, $m_{\mathrm{T}}(W)$, més gran de 60 GeV. Finalment, els mateixos talls propis de la regió de sel·lecció de la senyal hi són també requirits a nivell de partícules.

6.4.3 Estimació del fons

Per constrényer les normalitzacions dels fons dominants i assegurar-se'n d'una descripció adient de les principals contribucions dels processos de fons (com són $t\bar{t}$ i W+jets), es defineixen regions enriquides amb esdeveniments d'aquests dos fons:

- Una regió de control enriquida en esdeveniments $t\bar{t}$ es defineix considerant esdeveniments preseleccionats que contenen dos $b - jets$.

[5] El quark ***top*** es detecta a partir de la informació del b-jet i del bosó W (igualment reconstruït amb informació del leptó i del b-jet).

- A més a més, es defineix una regió de control enriquida en esdeveniments de W+jets. Els esdeveniments d'aquesta regió de control es seleccionen considerant els criteris de preselecció malgrat vetant tots els requisits de la selecció del senyal.

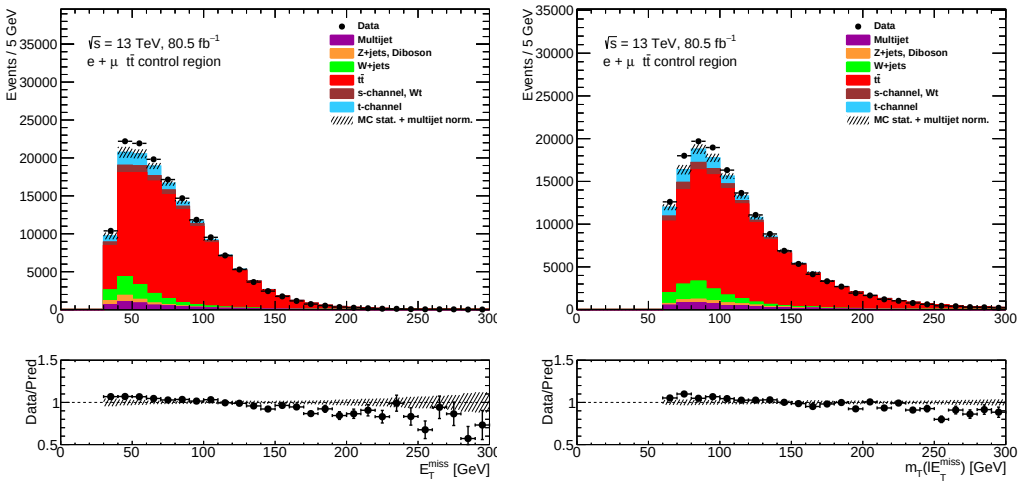

(a) (b)

Figura 6.13: Distribucions en la regió de control de $t\bar{t}$ de dues variables: (a) energia transversal faltant, (b) moment del bosó W; on es compara l'acord entre dades i simulacions de Monte Carlo del senyal i els fons considerats en l'anàlisi.

Les Figures 6.13, 6.14 i 6.15 mostren el bon acord entre dades i simulacions obtés en ambdues regions de control, així com en la regió de senyal. La normalització de tots els processos que es mostren en les figures s'extrauen amb càlculs teòrics i simulacions de Monte Carlo; a excepció del multijet, que empra a més a més dades reals. No obstant això, cal extraure uns factors d'escala, a mode d'una normalització adicional per als principals fons (parelles de $t\bar{t}$ i W+jets). Aquesta normalització adicional s'obté realitzant un ajust múltiple amb una funció que considera el nombre d'esdeveniments dels diferents processos en les regions de control i de senyal. Els paràmetres lliures d'aquest ajust hi són precisament el nombre d'esdevinements del senyal i de les parelles de $t\bar{t}$ i W+jets.

6.4.4 Mesura d'asimetries

Una vegada es sel·leccionen els esdeveniments interessants per a la mesura i es considera de forma adequada els principals fons; el següent pas consistix en mesurar els observables sensibles a la polarització del quark *top*. Donat que les asimetries es mesuren a partir de les distribucions angulars són obteses a nivell de reconstrucció del detector (observar Figura 6.16), cal emprar una tècnica de desdoblament, que

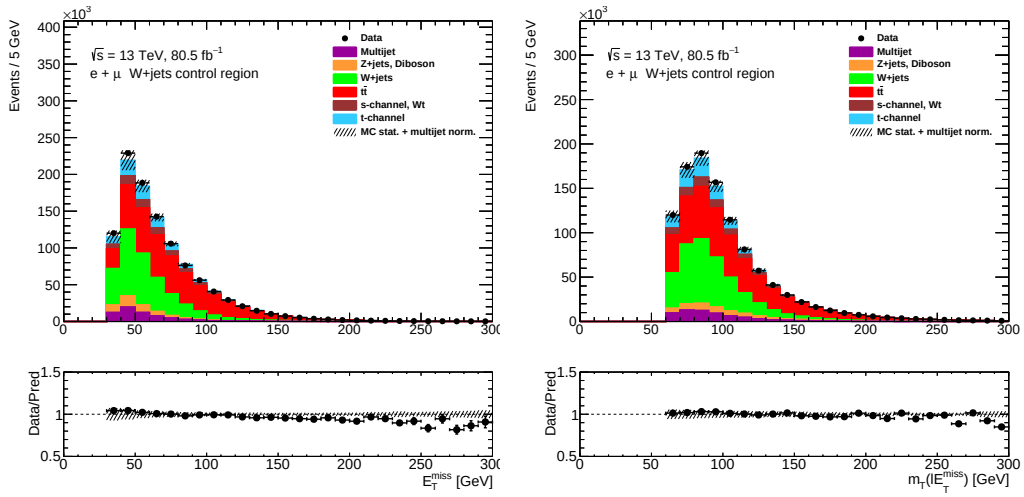

(a) (b)

Figura 6.14: Distribucions en la regió de control de W+jets de dues variables: (a) energia transversal faltant, (b) moment del bosó W; on es compara l'acord entre dades i simulacions de Monte Carlo del senyal i els fons considerats en l'anàlisi.

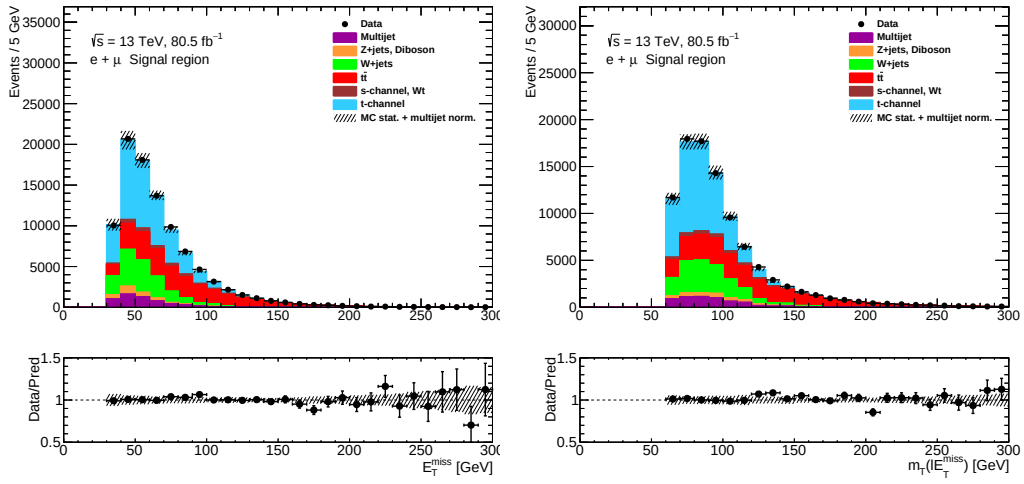

(a) (b)

Figura 6.15: Distribucions en la regió de senyal de dues variables: (a) energia transversal faltant, (b) moment del bosó W; on es compara l'acord entre dades i simulacions de Monte Carlo del senyal i els fons considerats en l'anàlisi.

permeta transformar a nivell de partícules les distribucions angulars a nivell de detector.

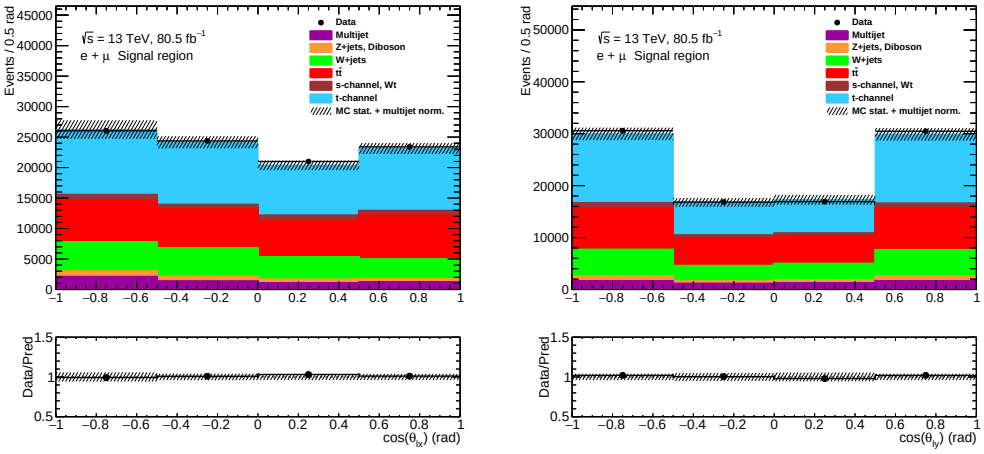

(a) (b)

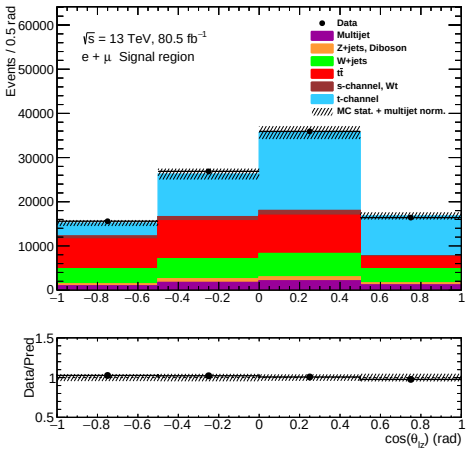

(c)

Figura 6.16: Distribucions angulars reconstruïdes en la regió de senyal (a) $\cos(\theta_{lx})$, (b) $\cos(\theta_{ly})$, and (c) $\cos(\theta_{lz})$.

Aquest mètode és de tipus iteratiu i durant el procediment corregeix pels efectes dels components del detector sobre la mesura, al tindre en compte diverses eficiències de sel·lecció, tant a nivell de partícules com de reconstrucció. El seu mode d'operació es resumix en la següent equació:

$$N_k^{\text{particle}} = C_k^{\text{particle!reco}} \sum_j M_{jk}^{-1} C_j^{\text{reco!particle}} (N_j^{\text{data}} - B_j), \tag{6.9}$$

on N_k^{particle} representen els esdeveniments de senyal a nivell de partícules en el bin k del volum fiducial, M_{jk}^{-1} és la matriu de migració a invertir iterativament i els

factors $C_j^{\text{reco!particle}}$ ($C_k^{\text{particle!reco}}$) són correccions que consideren esdeveniments que passen la sel·lecció a nivell de reconstrucció (partícules) però no a nivell de partícules (reconstrucció).

En l'extracció de les asimetries a nivell de partícules s'empra una mostra de Monte Carlo produïda a NLO amb el generador POWHEG, amb els valors que prediu el SM per als acoblaments. En presència de nova física (per exemple a través d'acoblament anòmals), les asimetries es manifestarien amb valors lleugerament diferents als que prediu el SM. És per això important validar el mètode de desdoblament emprat no esbiaixa els valors de les asimetries, mitjançant mostres simulades amb acoblaments anòmals. Aquest test de linealitat es troba representat a la Figura 6.17, que mostra un bon acord entre els valors desdoblats i vertaders de les asimetries, en el ventall que proporciona les mostres de nova física emprades. Llavors, la mesura que proporcionem serà independent dels valors dels acoblaments anòmals assumits en la mostra utilitzada per extraure les correccions. A banda de comprovar la resposta del mètode, també s'han estudiat (tant per a la mostra nominal emprada en l'anàlisi com per a les mostres de nova física) els valors òptims de convergència del mètode, i s'ha verificat el que les mostres emprades no estiguen intrínsicament esbiaixades.

6.4.5 Fonts d'incertesa

En aquesta anàlisi es consideren diverses fonts d'incertesa sistemàtica. Aquestes fonts de sistemàtica es classifiquen en dos grups principals: incerteses experimentals relacionades amb el modelat de detector i incerteses teòriques relacionades amb el modelat del senyal i dels fons. Aquestes diferents incerteses sistemàtiques afecten la normalització i la forma de les distribucions angulars, que s'utilitzen per extreure les asimetries angulars. L'impacte d'incerteses sistemàtiques s'estima per separat i es propaga de manera correlacionada a la regió de senyal i a les dues regions de control. Tots els components d'incerteses sistemàtiques s'afegeixen llavors en quadratura per obtenir la incertesa sistemàtica total. També es té en compte l'efecte degut a la estadística de les dades i a les mostres d'esdeveniments simulats. Les incerteses dominants provenen del modelatge dels procesos del canal t i parelles de $t\bar{t}$, així com, incerteses experimentals relacionades amb els *jets*.

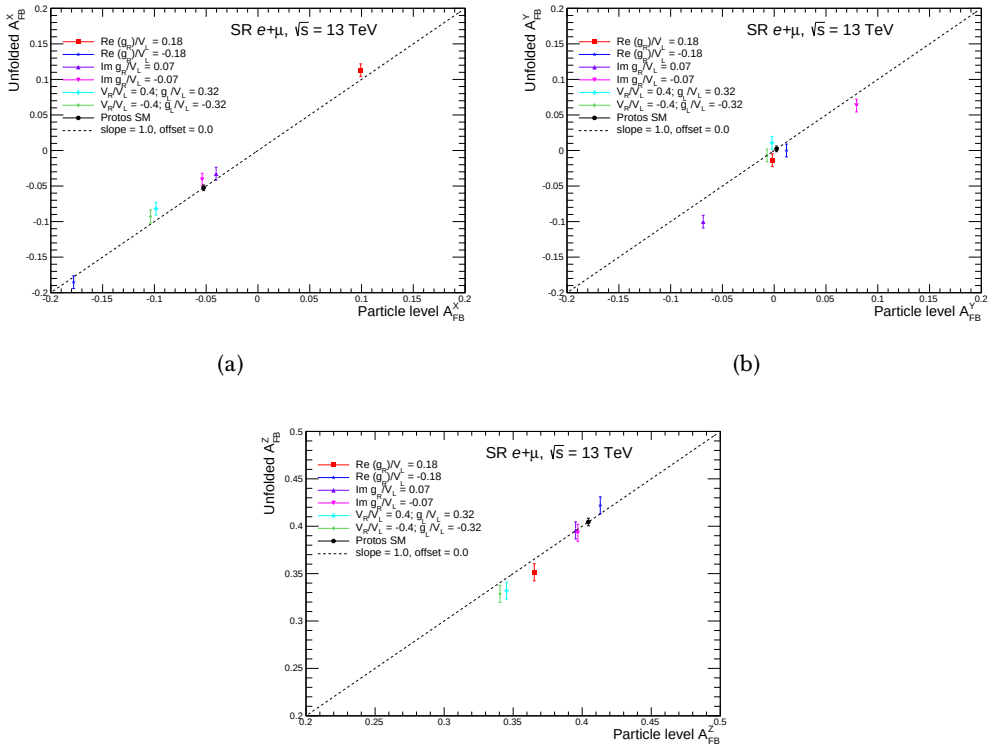

(a) (b)

(c)

Figura 6.17: Asimetries desdoblades A_{FB}^X (a), A_{FB}^Y (b) i A_{FB}^Z (c); en funció dels seus valors a nivell de partícules vertaders emprant mostres de nova física generades amb PROTOS. Els punts negres són aquells generats amb la configuració del SM, mentres que valors distints de zero de l'acoblament $\mathrm{Im}(g_R)$ es representen en rosa i púrpura. Tanmateix els punts rojos i blaus es referixen a mostres generades per a valors distints de zero en l'acoblament $\mathrm{Re}(g_R)$. En el cas de l'acoblament $V_R/V_L; g_L/V_L$ es tracta dels punts verds i blau clar.

6.4.6 Resultats

Finalment, els diferents observables proposats són mesurats després de llevar els diferents fons simulats a les dades, en les distribucions angulars de la Figura 6.16. A continuació, disposant ja del senyal interessant per a la mesura, la distribució angular reconstruïda es corregeix a nivell de partícules (tal i com havem explicat en anterioritat) i es calculen les tres asimetries que considerem a aquesta tesi: A_{FB}^X, A_{FB}^Y i A_{FB}^Z. Trobem que els seus valors, amb les incerteses estadístiques i sistemàtiques, són els seguents:

$$A_{FB}^X = -0.042 \pm 0.008(\text{stat.}) \pm 0.100(\text{syst.})$$
$$A_{FB}^Y = -0.011 \pm 0.008(\text{stat.}) \pm 0.046(\text{syst.})$$
$$A_{FB}^Z = 0.380 \pm 0.009(\text{stat.}) \pm 0.085(\text{syst.})$$

Finalment, els resultats de les asimetries obtinguts en aquesta tesi es resumeixen a la Figura 6.18, en què es comparen les asimetries mesurades a nivell de partícules en una regió fiducial amb les prediccions vertaderes a nivell de partícules a la mateixa regió fiducial, mitjançant la mostra POWHEG-BOX + PYTHIA8 de simulació completa a NLO en la configuració del SM. També es tenen en compte les prediccions de nova física proporcionades per PROTOS + PYTHIA8. Els resultats proporcionats en aquesta tesi són consistents amb les prediccions de SM.

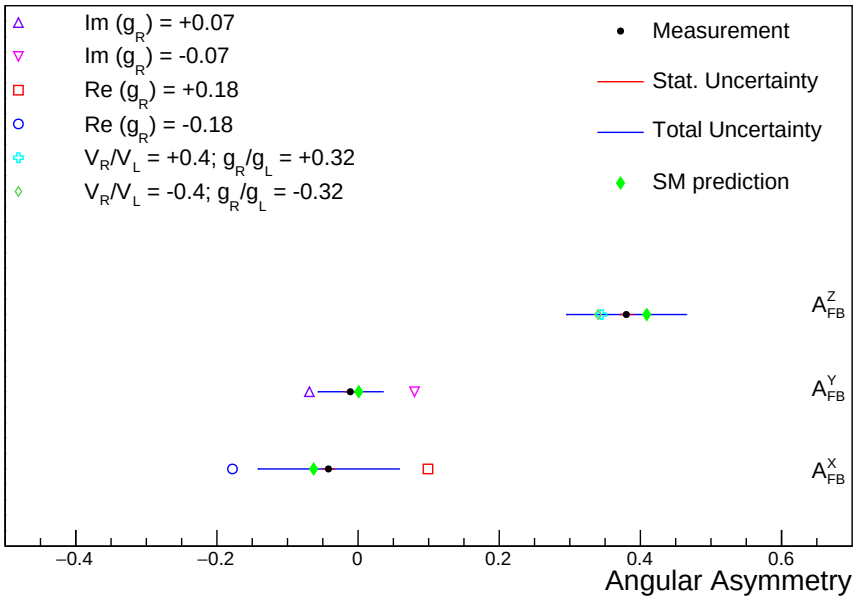

Figura 6.18: Resum de les asimetries mesurades (punts negres) amb la seua corresponent incertesa estadística (línies rojes) i incertesa total (línies blaves). Les asimetries mesurades es comparen amb les prediccions de SM que proporciona la mostra NLO POWHEG-BOX (diamants verds), així com mostres de nova física. Es troba un bon acord entre la mesura i la predicció de SM.

Bibliography

[1] J. H. Kuhn and K. H. Streng, *Measurement of Weak Couplings Through Toponium Decays*, Nucl. Phys. **B198** (1982) 71.

[2] J. A. Aguilar-Saavedra, J. Carvalho, N. F. Castro, F. Veloso, and A. Onofre, *Probing anomalous Wtb couplings in top pair decays*, Eur. Phys. J. **C50** (2007) 519–533, arXiv:hep-ph/0605190 [hep-ph].

[3] J. Aguilar-Saavedra, *Single top quark production at LHC with anomalous Wtb couplings*, Nucl.Phys. **B804** (2008) 160–192, arXiv:0803.3810 [hep-ph].

[4] J. Aguilar-Saavedra and J. Bernabeu, *W polarisation beyond helicity fractions in top quark decays*, Nucl.Phys. **B840** (2010) 349–378, arXiv:1005.5382 [hep-ph].

[5] S. L. Glashow, *Partial Symmetries of Weak Interactions*, Nucl. Phys. **22** (1961) 579–588.

[6] A. Salam and J. C. Ward, *Electromagnetic and weak interactions*, Phys. Lett. **13** (1964) 168–171.

[7] J. Goldstone, A. Salam, and S. Weinberg, *Broken Symmetries*, Phys. Rev. **127** (1962) 965–970.

[8] P. W. Higgs, *Broken Symmetries and the Masses of Gauge Bosons*, Phys. Rev. Lett. **13** (1964) 508–509. [,160(1964)].

[9] F. Englert and R. Brout, *Broken Symmetry and the Mass of Gauge Vector Mesons*, Phys. Rev. Lett. **13** (1964) 321–323. [,157(1964)].

[10] A. Salam, *Weak and Electromagnetic Interactions*, Conf. Proc. **C680519** (1968) 367–377.

[11] S. Weinberg, *A Model of Leptons*, Phys. Rev. Lett. **19** (1967) 1264–1266.

[12] S. L. Glashow, J. Iliopoulos, and L. Maiani, *Weak Interactions with Lepton-Hadron Symmetry*, Phys. Rev. **D2** (1970) 1285–1292.

[13] M. Kobayashi and T. Maskawa, *CP Violation in the Renormalizable Theory of Weak Interaction*, Prog. Theor. Phys. **49** (1973) 652–657.

[14] M. L. Perl et al., *Evidence for Anomalous Lepton Production in e+ - e- Annihilation*, Phys. Rev. Lett. **35** (1975) 1489–1492. [,193(1975)].

[15] S. W. Herb et al., *Observation of a Dimuon Resonance at 9.5-GeV in 400-GeV Proton-Nucleus Collisions*, Phys. Rev. Lett. **39** (1977) 252–255.

[16] CDF Collaboration, F. Abe et al., *Observation of top quark production in $\bar{p}p$ collisions*, Phys. Rev. Lett. **74** (1995) 2626–2631, arXiv:hep-ex/9503002 [hep-ex].

[17] D0 Collaboration, S. Abachi et al., *Observation of the top quark*, Phys. Rev. Lett. **74** (1995) 2632–2637, arXiv:hep-ex/9503003 [hep-ex].

[18] DONUT Collaboration, K. Kodama et al., *Observation of tau neutrino interactions*, Phys. Lett. **B504** (2001) 218–224, arXiv:hep-ex/0012035 [hep-ex].

[19] UA1 Collaboration, G. Arnison et al., *Experimental Observation of Isolated Large Transverse Energy Electrons with Associated Missing Energy at s**(1/2) = 540-GeV*, Phys. Lett. **122B** (1983) 103–116. [,611(1983)].

[20] UA2 Collaboration, M. Banner et al., *Observation of Single Isolated Electrons of High Transverse Momentum in Events with Missing Transverse Energy at the CERN anti-p p Collider*, Phys. Lett. **122B** (1983) 476–485. [,7.45(1983)].

[21] UA1 Collaboration, G. Arnison et al., *Experimental Observation of Lepton Pairs of Invariant Mass Around 95-GeV/c**2 at the CERN SPS Collider*, Phys. Lett. **126B** (1983) 398–410. [,7.55(1983)].

[22] UA2 Collaboration, P. Bagnaia et al., *Evidence for Z0 —> e+ e- at the CERN anti-p p Collider*, Phys. Lett. **129B** (1983) 130–140. [,7.69(1983)].

[23] ATLAS Collaboration, G. Aad et al., *Observation of a new particle in the search for the Standard Model Higgs boson with the ATLAS detector at the LHC*, Phys. Lett. **B716** (2012) 1–29, arXiv:1207.7214 [hep-ex].

[24] CMS Collaboration, S. Chatrchyan et al., *Observation of a New Boson at a Mass of 125 GeV with the CMS Experiment at the LHC*, Phys. Lett. **B716** (2012) 30–61, arXiv:1207.7235 [hep-ex].

[25] Super-Kamiokande Collaboration, Y. Fukuda et al., *Evidence for oscillation of atmospheric neutrinos*, Phys. Rev. Lett. **81** (1998) 1562–1567, arXiv:hep-ex/9807003 [hep-ex].

[26] G. Steigman, *Observational tests of antimatter cosmologies*, Ann. Rev. Astron. Astrophys. **14** (1976) 339–372.

[27] J. H. Christenson, J. W. Cronin, V. L. Fitch, and R. Turlay, *Evidence for the 2π Decay of the K_2^0 Meson*, Phys. Rev. Lett. **13** (1964) 138–140.

[28] A. D. Sakharov, *Violation of CP Invariance, C asymmetry, and baryon asymmetry of the universe*, Pisma Zh. Eksp. Teor. Fiz. **5** (1967) 32–35. [Usp. Fiz. Nauk161,no.5,61(1991)].

[29] Particle Data Group Collaboration, M. Tanabashi et al., *Review of Particle Physics*, Phys. Rev. **D98** no. 3, (2018) 030001.

[30] BaBar Collaboration, B. Aubert et al., *Observation of direct CP violation in $B^0 \to K^+\pi^-$ decays*, Phys. Rev. Lett. **93** (2004) 131801, arXiv:hep-ex/0407057 [hep-ex].

[31] Belle Collaboration, Y. Chao et al., *Evidence for direct CP violation in B0 —> K+ pi- decays*, Phys. Rev. Lett. **93** (2004) 191802, arXiv:hep-ex/0408100 [hep-ex].

[32] LHCb Collaboration, R. Aaij et al., *First observation of CP violation in the decays of B_s^0 mesons*, Phys. Rev. Lett. **110** no. 22, (2013) 221601, arXiv:1304.6173 [hep-ex].

[33] LHCb Collaboration, R. Aaij et al., *Observation of CP violation in $B^\pm \to DK^\pm$ decays*, Phys. Lett. **B712** (2012) 203–212, arXiv:1203.3662 [hep-ex]. [Erratum: Phys. Lett.B713,351(2012)].

[34] LHCb Collaboration, R. Aaij et al., *Observation of CP Violation in Charm Decays*, Phys. Rev. Lett. **122** no. 21, (2019) 211803, arXiv:1903.08726 [hep-ex].

[35] H. P. Nilles, *Supersymmetry, Supergravity and Particle Physics*, Phys. Rept. **110** (1984) 1–162.

[36] H. E. Haber and G. L. Kane, *The Search for Supersymmetry: Probing Physics Beyond the Standard Model*, Phys. Rept. **117** (1985) 75–263.

[37] U. Husemann, *Top-Quark Physics: Status and Prospects*, Prog. Part. Nucl. Phys. **95** (2017) 48–97, arXiv:1704.01356 [hep-ex].

[38] W. Bernreuther, *Top quark physics at the LHC*, J.Phys. **G35** (2008) 083001, arXiv:0805.1333 [hep-ph].

[39] F.-P. Schilling, *Top Quark Physics at the LHC: A Review of the First Two Years*, Int.J.Mod.Phys. **A27** (2012) 1230016, arXiv:1206.4484 [hep-ex].

[40] Top Quark Working Group Collaboration, K. Agashe et al., *Working Group Report: Top Quark*, arXiv:1311.2028 [hep-ph].

[41] K. Kröninger, A. B. Meyer, and P. Uwer, *Top-Quark Physics at the LHC*, arXiv:1506.02800 [hep-ex].

[42] C. J. C. Burges and H. J. Schnitzer, *Virtual Effects of Excited Quarks as Probes of a Possible New Hadronic Mass Scale*, Nucl. Phys. **B228** (1983) 464.

[43] C. N. Leung, S. T. Love, and S. Rao, *Low-Energy Manifestations of a New Interaction Scale: Operator Analysis*, Z. Phys. **C31** (1986) 433.

[44] W. Buchmuller and D. Wyler, *Effective Lagrangian Analysis of New Interactions and Flavor Conservation*, Nucl. Phys. **B268** (1986) 621–653.

[45] J. Aguilar-Saavedra, *A Minimal set of top anomalous couplings*, Nucl.Phys. **B812** (2009) 181–204, arXiv:0811.3842 [hep-ph].

[46] K. Hsieh, K. Schmitz, J.-H. Yu, and C. P. Yuan, *Global Analysis of General SU(2) x SU(2) x U(1) Models with Precision Data*, Phys. Rev. **D82** (2010) 035011, arXiv:1003.3482 [hep-ph].

[47] Q.-H. Cao, Z. Li, J.-H. Yu, and C. P. Yuan, *Discovery and Identification of W' and Z' in SU(2) x SU(2) x U(1) Models at the LHC*, Phys. Rev. **D86** (2012) 095010, arXiv:1205.3769 [hep-ph].

[48] G. Cacciapaglia, A. Deandrea, D. Harada, and Y. Okada, *Bounds and Decays of New Heavy Vector-like Top Partners*, JHEP **11** (2010) 159, arXiv:1007.2933 [hep-ph].

[49] J. Aguilar-Saavedra, R. Benbrik, S. Heinemeyer, and M. Pérez-Victoria, *Handbook of vectorlike quarks: Mixing and single production*, Phys.Rev. **D88** no. 9, (2013) 094010, arXiv:1306.0572 [hep-ph].

[50] B. Grzadkowski and W. Hollik, *Radiative corrections to the top quark width within two Higgs doublet models*, Nucl. Phys. **B384** (1992) 101–112.

[51] A. Dabelstein, W. Hollik, C. Junger, R. A. Jimenez, and J. Sola, *Strong supersymmetric quantum effects on the top quark width*, Nucl. Phys. **B454** (1995) 75–85, arXiv:hep-ph/9503398 [hep-ph].

[52] J.-j. Cao, R. J. Oakes, F. Wang, and J. M. Yang, *Supersymmetric effects in top quark decay into polarized W boson*, Phys. Rev. **D68** (2003) 054019, arXiv:hep-ph/0306278 [hep-ph].

[53] Q.-H. Cao, B. Yan, J.-H. Yu, and C. Zhang, *A General Analysis of Wtb anomalous Couplings*, arXiv:1504.03785 [hep-ph].

[54] M. Czakon, P. Fiedler, and A. Mitov, *The total top quark pair production cross-section at hadron colliders through $O(\alpha_S^4)$*, Phys. Rev. Lett. **110** (2013) 252004, arXiv:1303.6254 [hep-ph].

[55] N. Kidonakis, *Two-loop soft anomalous dimensions for single top quark associated production with a W- or H-*, Phys. Rev. **D82** (2010) 054018, arXiv:1005.4451 [hep-ph].

[56] N. Kidonakis, *NNLL resummation for s-channel single top quark production*, Phys. Rev. **D81** (2010) 054028, arXiv:1001.5034 [hep-ph].

[57] N. Kidonakis, *Next-to-next-to-leading-order collinear and soft gluon corrections for t-channel single top quark production*, Phys. Rev. **D83** (2011) 091503, arXiv:1103.2792 [hep-ph].

[58] N. Kidonakis, *Top Quark Production*, arXiv:1311.0283 [hep-ph].

[59] N. Kidonakis, *High-precision theory for top-quark production*, PoS **HQL2016** (2017) 041, arXiv:1607.08892 [hep-ph].

[60] N. Kidonakis, *Soft-gluon corrections for tW production at N^{3}LO*, Phys. Rev. **D96** no. 3, (2017) 034014, arXiv:1612.06426 [hep-ph].

[61] M. Brucherseifer, F. Caola, and K. Melnikov, *On the NNLO QCD corrections to single-top production at the LHC*, Phys. Lett. **B736** (2014) 58–63, arXiv:1404.7116 [hep-ph].

[62] E. L. Berger, J. Gao, C. P. Yuan, and H. X. Zhu, *NNLO QCD Corrections to t-channel Single Top-Quark Production and Decay*, Phys. Rev. **D94** no. 7, (2016) 071501, arXiv:1606.08463 [hep-ph].

[63] M. Aliev, H. Lacker, U. Langenfeld, S. Moch, P. Uwer, and M. Wiedermann, *HATHOR: HAdronic Top and Heavy quarks crOss section calculatoR*, Comput. Phys. Commun. **182** (2011) 1034–1046, arXiv:1007.1327 [hep-ph].

[64] P. Kant, O. M. Kind, T. Kintscher, T. Lohse, T. Martini, S. Mölbitz, P. Rieck, and P. Uwer, *HatHor for single top-quark production: Updated predictions and uncertainty estimates for single top-quark production in hadronic collisions*, Comput. Phys. Commun. **191** (2015) 74–89, arXiv:1406.4403 [hep-ph].

[65] A. Giammanco and R. Schwienhorst, *Single top-quark production at the Tevatron and the LHC*, Rev. Mod. Phys. **90** no. 3, (2018) 035001, arXiv:1710.10699 [hep-ex].

[66] G. Mahlon and S. J. Parke, *Angular correlations in top quark pair production and decay at hadron colliders*, Phys. Rev. **D53** (1996) 4886–4896, arXiv:hep-ph/9512264 [hep-ph].

[67] M. Jezabek and J. H. Kuhn, *V-A tests through leptons from polarized top quarks*, Phys. Lett. **B329** (1994) 317–324, arXiv:hep-ph/9403366 [hep-ph].

[68] G. Mahlon and S. J. Parke, *Improved spin basis for angular correlation studies in single top quark production at the Tevatron*, Phys. Rev. **D55** (1997) 7249–7254, arXiv:hep-ph/9611367 [hep-ph].

[69] G. Mahlon and S. J. Parke, *Single top quark production at the LHC: Understanding spin*, Phys. Lett. **B476** (2000) 323–330, arXiv:hep-ph/9912458 [hep-ph].

[70] R. Schwienhorst, C. P. Yuan, C. Mueller, and Q.-H. Cao, *Single top quark production and decay in the t-channel at next-to-leading order at the LHC*, Phys. Rev. **D83** (2011) 034019, arXiv:1012.5132 [hep-ph].

[71] J. A. Aguilar-Saavedra and S. Amor Dos Santos, *New directions for top quark polarization in the t-channel process*, Phys. Rev. **D89** no. 11, (2014) 114009, arXiv:1404.1585 [hep-ph].

[72] "Protos - PROgram for TOp Simulations." http://jaguilar.web.cern.ch/jaguilar/protos/.

[73] P. M. Nadolsky, H.-L. Lai, Q.-H. Cao, J. Huston, J. Pumplin, D. Stump, W.-K. Tung, and C. P. Yuan, *Implications of CTEQ global analysis for collider observables*, Phys. Rev. **D78** (2008) 013004, arXiv:0802.0007 [hep-ph].

[74] A. Brandenburg, Z. G. Si, and P. Uwer, *QCD corrected spin analyzing power of jets in decays of polarized top quarks*, Phys. Lett. **B539** (2002) 235–241, arXiv:hep-ph/0205023 [hep-ph].

[75] K. G. Wilson, *Nonlagrangian models of current algebra*, Phys. Rev. **179** (1969) 1499–1512.

[76] Q.-H. Cao, J. Wudka, and C. P. Yuan, *Search for new physics via single top production at the LHC*, Phys. Lett. **B658** (2007) 50–56, arXiv:0704.2809 [hep-ph].

[77] C. Zhang and S. Willenbrock, *Effective-Field-Theory Approach to Top-Quark Production and Decay*, Phys. Rev. **D83** (2011) 034006, arXiv:1008.3869 [hep-ph].

[78] J. A. Aguilar-Saavedra, *Effective four-fermion operators in top physics: A Roadmap*, Nucl. Phys. **B843** (2011) 638–672, arXiv:1008.3562 [hep-ph]. [Erratum: Nucl. Phys.B851,443(2011)].

[79] J. Jimenez Pena, *ATLAS Inner Detector alignment and analysis of the Wtb vertex structure with single top quarks*, Jul, 2018. https://cds.cern.ch/record/2644636. Presented 05 Oct 2018.

[80] ATLAS Collaboration, *Probing the Wtb vertex structure in t-channel single-top-quark production and decay in pp collisions at $\sqrt{s} = 8$ TeV with the ATLAS detector*, JHEP **04** (2017) 124, arXiv:1702.08309 [hep-ex].

[81] ATLAS Collaboration, *Analysis of the Wtb vertex from the measurement of triple-differential angular decay rates of single top quarks produced in the t-channel at $\sqrt{s}$ = 8 TeV with the ATLAS detector*, JHEP **12** (2017) 017, arXiv:1707.05393 [hep-ex].

[82] CMS Collaboration, C. Collaboration, *Measurement of top quark polarization in t-channel single-top production*, CMS-PAS-TOP-13-001 (2013).

[83] ATLAS Collaboration, M. Aaboud et al., *Fiducial, total and differential cross-section measurements of t-channel single top-quark production in pp collisions at 8 TeV using data collected by the ATLAS detector*, Eur. Phys. J. **C77** no. 8, (2017) 531, arXiv:1702.02859 [hep-ex].

[84] O. Estrada Pastor, *Probing the Wtb structure at the LHC.*, Sep, 2015. Presented 23 Sep 2015.

[85] F. J. Hasert, H. Faissner, W. Krenz, J. Von Krogh, and D. Lanske, *Search for elastic muon neutrino electron scattering*, Phys. Lett. B **46** (1973) 121–124. https://cds.cern.ch/record/243640.

[86] Gargamelle Neutrino Collaboration, F. J. Hasert et al., *Observation of Neutrino Like Interactions Without Muon Or Electron in the Gargamelle Neutrino Experiment*, Phys. Lett. **46B** (1973) 138–140. [,5.15(1973)].

[87] NA31 Collaboration, G. D. Barr et al., *A New measurement of direct CP violation in the neutral kaon system*, Phys. Lett. **B317** (1993) 233–242.

[88] G. Baur et al., *Production of anti–hydrogen*, Phys. Lett. **B368** (1996) 251–258.

[89] J. Mnich, *Tests of the standard model*,.

[90] LHCb Collaboration, R. Aaij et al., *Observation of $J/\psi p$ Resonances Consistent with Pentaquark States in $\Lambda_b^0 \to J/\psi K^- p$ Decays*, Phys. Rev. Lett. **115** (2015) 072001, arXiv:1507.03414 [hep-ex].

[91] L. Evans and P. Bryant, *LHC Machine*, JINST **3** (2008) S08001.

[92] *LEP design report.* CERN, Geneva, 1984. https://cds.cern.ch/record/102083. Copies shelved as reports in LEP, PS and SPS libraries.

[93] ATLAS Collaboration, G. Aad et al., *The ATLAS Experiment at the CERN Large Hadron Collider*, JINST **3** (2008) S08003.

[94] CMS Collaboration, S. Chatrchyan et al., *The CMS Experiment at the CERN LHC*, JINST **3** (2008) S08004.

[95] ALICE Collaboration, K. Aamodt et al., *The ALICE experiment at the CERN LHC*, JINST **3** (2008) S08002.

[96] LHCb Collaboration, A. A. Alves, Jr. et al., *The LHCb Detector at the LHC*, JINST **3** (2008) S08005.

[97] LHCf Collaboration, O. Adriani et al., *Technical design report of the LHCf experiment: Measurement of photons and neutral pions in the very forward region of LHC*,.

[98] TOTEM Collaboration, V. Berardi et al., *TOTEM: Technical design report. Total cross section, elastic scattering and diffraction dissociation at the Large Hadron Collider at CERN*,.

[99] MoEDAL Collaboration, J. Pinfold et al., *Technical Design Report of the MoEDAL Experiment*,.

[100] G. Apollinari, I. Béjar Alonso, O. Brüning, M. Lamont, and L. Rossi, *High-Luminosity Large Hadron Collider (HL-LHC): Preliminary Design Report*. CERN Yellow Reports: Monographs. CERN, Geneva, 2015. https://cds.cern.ch/record/2116337.

[101] *ATLAS Insertable B-Layer Technical Design Report*, tech. rep., ATLAS Collaboration, Sep, 2010. https://cds.cern.ch/record/1291633.

[102] ATLAS Collaboration, G. Aad et al., *Performance of the ATLAS Trigger System in 2010*, Eur. Phys. J. **C72** (2012) 1849, arXiv:1110.1530 [hep-ex].

[103] ATLAS Collaboration Collaboration, *ATLAS level-1 trigger: Technical Design Report*. Technical Design Report ATLAS. CERN, Geneva, 1998. https://cds.cern.ch/record/381429.

[104] ATLAS Collaboration Collaboration, P. Jenni, M. Nessi, M. Nordberg, and K. Smith, *ATLAS high-level trigger, data-acquisition and controls: Technical Design Report*. Technical Design Report ATLAS. CERN, Geneva, 2003. https://cds.cern.ch/record/616089.

[105] *2015 start-up trigger menu and initial performance assessment of the ATLAS trigger using Run-2 data*, Tech. Rep. ATL-DAQ-PUB-2016-001, CERN, Geneva, Mar, 2016. https://cds.cern.ch/record/2136007.

[106] ATLAS Collaboration, *TopCommonObjects13TeV twiki*,. https://twiki.cern.ch/twiki/bin/view/AtlasProtected/TopCommonObjects13TeV.

[107] ATLAS Collaboration, "Electron efficiency measurements with the ATLAS detector using the 2015 LHC proton–proton collision data." ATLAS-CONF-2016-024, 2016. https://cds.cern.ch/record/2157687.

[108] ATLAS Collaboration, *Muon reconstruction performance of the ATLAS detector in proton–proton collision data at* $\sqrt{s} = 13$ *TeV*, Eur. Phys. J. C **76** (2016) 292, arXiv:1603.05598 [hep-ex].

[109] ATLAS Collaboration, *Topological cell clustering in the ATLAS calorimeters and its performance in LHC Run 1*, Eur. Phys. J. C **77** (2017) 490, arXiv:1603.02934 [hep-ex].

[110] M. Cacciari, G. P. Salam, and G. Soyez, *The anti-*k_t *jet clustering algorithm*, JHEP **04** (2008) 063, arXiv:0802.1189 [hep-ph].

[111] ATLAS Collaboration, M. Aaboud et al., *Jet energy scale measurements and their systematic uncertainties in proton-proton collisions at* $\sqrt{s} = 13$ *TeV with the ATLAS detector*, Phys. Rev. **D96** no. 7, (2017) 072002, arXiv:1703.09665 [hep-ex].

[112] ATLAS Collaboration, "Constituent-level pile-up mitigation techniques in ATLAS." ATLAS-CONF-2017-065, 2017. https://cds.cern.ch/record/2281055.

[113] ATLAS Collaboration, *Identification and rejection of pile-up jets at high pseudorapidity with the ATLAS detector*, Eur. Phys. J. C **77** (2017) 580, arXiv:1705.02211 [hep-ex].

[114] ATLAS Collaboration, *Jet energy scale measurements and their systematic uncertainties in proton–proton collisions at* $\sqrt{s} = 13$ *TeV with the ATLAS detector*, Phys. Rev. D **96** (2017) 072002, arXiv:1703.09665 [hep-ex].

[115] ATLAS Collaboration Collaboration, *Optimisation and performance studies of the ATLAS* b*-tagging algorithms for the 2017-18 LHC run*, Tech. Rep. ATL-PHYS-PUB-2017-013, CERN, Geneva, Jul, 2017. https://cds.cern.ch/record/2273281.

[116] ATLAS Collaboration, *Measurements of* b*-jet tagging efficiency with the ATLAS detector using* $t\bar{t}$ *events at* $\sqrt{s} = 13$ *TeV*, JHEP **08** (2018) 089, arXiv:1805.01845 [hep-ex].

[117] ATLAS Collaboration, "Calibration of the ATLAS b-tagging algorithm in $t\bar{t}$ semileptonic events." ATLAS-CONF-2018-045, 2018. https://cds.cern.ch/record/2638455.

[118] ATLAS Collaboration, "Measurement of b-tagging efficiency of c-jets in $t\bar{t}$ events using a likelihood approach with the ATLAS detector." ATLAS-CONF-2018-001, 2018. https://cds.cern.ch/record/2306649.

[119] ATLAS Collaboration, "Calibration of light-flavour b-jet mistagging rates using ATLAS proton–proton collision data at $\sqrt{s} = 13$ TeV." ATLAS-CONF-2018-006, 2018. https://cds.cern.ch/record/2314418.

[120] ATLAS Collaboration, *Performance of missing transverse momentum reconstruction with the ATLAS detector using proton–proton collisions at* $\sqrt{s} = 13$ *TeV*, Eur. Phys. J. C **78** (2018) 903, arXiv:1802.08168 [hep-ex].

[121] ATLAS Collaboration, "$E_{\mathrm{T}}^{\mathrm{miss}}$ performance in the ATLAS detector using 2015–2016 LHC pp collisions." ATLAS-CONF-2018-023, 2018. https://cds.cern.ch/record/2625233.

[122] *Performance of missing transverse momentum reconstruction for the ATLAS detector in the first proton-proton collisions at at* $\sqrt{s}$*= 13 TeV*, Tech. Rep. ATL-PHYS-PUB-2015-027, CERN, Geneva, Jul, 2015. https://cds.cern.ch/record/2037904.

[123] P. Brückman, A. Hicheur, and S. J. Haywood, *Global chi2 approach to the Alignment of the ATLAS Silicon Tracking Detectors*, tech. rep., CERN, 2005. http://cds.cern.ch/record/835270.

[124] T. Göttfert, *Iterative local Chi2 alignment algorithm for the ATLAS Pixel detector*, May, 2006. https://cds.cern.ch/record/1511043. Presented 26 May 2006.

[125] ATLAS Collaboration Collaboration, *Study of alignment-related systematic effects on the ATLAS Inner Detector tracking*, Tech. Rep. ATLAS-CONF-2012-141, CERN, Geneva, Oct, 2012. https://cds.cern.ch/record/1483518.

[126] ATLAS Collaboration, *ATLAS Data Quality Operations and Performance for 2015–2018 data-taking*,.

[127] *Study of the mechanical stability of the ATLAS Insertable B-Layer*, Tech. Rep. ATL-INDET-PUB-2015-001, CERN, Geneva, Jun, 2015. http://cds.cern.ch/record/2022587.

[128] ATLAS Collaboration, G. Aad et al., *Muon reconstruction performance of the ATLAS detector in proton–proton collision data at* $\sqrt{s}$ *=13 TeV*, Eur. Phys. J. **C76** no. 5, (2016) 292, arXiv:1603.05598 [hep-ex].

[129] ATLAS Collaboration Collaboration, *Studies of radial distortions of the ATLAS Inner Detector*, Tech. Rep. ATL-PHYS-PUB-2018-003, CERN, Geneva, Mar, 2018. http://cds.cern.ch/record/2309785.

[130] M. Danninger, P. Bruckman de Renstrom, S. Marti i Garcia, H. Oide, P. Butti, A. K. Morley, J. Jimenez Pena, S. Henkelmann, W. K. Di Clemente,

S. Camarda, J. Wollrath, J. Guerrero Rojas, and G. R. Gonzalvo Rodriguez, *Alignment of the ATLAS Inner Detector*, Tech. Rep. ATL-COM-PHYS-2019-953, CERN, Geneva, Jul, 2019. https://cds.cern.ch/record/2684129.

[131] ATLAS LUCID Collaboration, *Measurement of the luminosity with the new LUCID-2 detector in 2015*, Tech. Rep. ATL-COM-FWD-2016-008, 2016. https://cds.cern.ch/record/2154368.

[132] ATLAS Collaboration, *The ATLAS Simulation Infrastructure*, Eur. Phys. J. C **70** (2010) 823, arXiv:1005.4568 [physics.ins-det].

[133] GEANT4 Collaboration, S. Agostinelli et al., *GEANT4: A Simulation toolkit*, Nucl. Instrum. Meth. A **506** (2003) 250.

[134] E. Richter-Was, D. Froidevaux, and L. Poggioli, *ATLFAST 2.0 a fast simulation package for ATLAS*,.

[135] T. Sjostrand, S. Mrenna, and P. Skands, *A brief introduction to PYTHIA 8.1*, Comput. Phys. Commun. **178** (2008) 852–867, arXiv:0710.3820 [hep-ph].

[136] R. D. Ball et al., *Parton distributions with LHC data*, Nucl. Phys. B **867** (2013) 244, arXiv:1207.1303 [hep-ph].

[137] ATLAS Collaboration Collaboration, *A study of the Pythia 8 description of ATLAS minimum bias measurements with the Donnachie-Landshoff diffractive model*, Tech. Rep. ATL-PHYS-PUB-2016-017, CERN, Geneva, Aug, 2016. https://cds.cern.ch/record/2206965.

[138] R. Frederix, E. Re, and P. Torrielli, *Single-top t-channel hadroproduction in the four-flavour scheme with POWHEG and aMC@NLO*, JHEP **09** (2012) 130, arXiv:1207.5391 [hep-ph].

[139] P. Nason, *A new method for combining NLO QCD with shower Monte Carlo algorithms*, JHEP **11** (2004) 040, arXiv:hep-ph/0409146.

[140] S. Frixione, P. Nason, and C. Oleari, *Matching NLO QCD computations with parton shower simulations: the POWHEG method*, JHEP **11** (2007) 070, arXiv:0709.2092 [hep-ph].

[141] S. Alioli, P. Nason, C. Oleari, and E. Re, *A general framework for implementing NLO calculations in shower Monte Carlo programs: the POWHEG BOX*, JHEP **06** (2010) 043, arXiv:1002.2581 [hep-ph].

[142] NNPDF Collaboration, R. D. Ball et al., *Parton distributions for the LHC Run II*, JHEP **04** (2015) 040, arXiv:1410.8849 [hep-ph].

[143] S. Frixione, E. Laenen, P. Motylinski, and B. R. Webber, *Angular correlations of lepton pairs from vector boson and top quark decays in Monte Carlo simulations*, JHEP **0704** (2007) 081, arXiv:hep-ph/0702198.

[144] P. Artoisenet, R. Frederix, O. Mattelaer, and R. Rietkerk, *Automatic spin-entangled decays of heavy resonances in Monte Carlo simulations*, JHEP **03** (2013) 015, arXiv:1212.3460 [hep-ph].

[145] T. Sjöstrand, S. Ask, J. R. Christiansen, R. Corke, N. Desai, P. Ilten, S. Mrenna, S. Prestel, C. O. Rasmussen, and P. Z. Skands, *An Introduction to PYTHIA 8.2*, Comput. Phys. Commun. **191** (2015) 159, arXiv:1410.3012 [hep-ph].

[146] *ATLAS Run 1 Pythia8 tunes*, Tech. Rep. ATL-PHYS-PUB-2014-021, CERN, Geneva, Nov, 2014. https://cds.cern.ch/record/1966419.

[147] D. J. Lange, *The EvtGen particle decay simulation package*, Nucl. Instrum. Meth. A **462** (2001) 152.

[148] M. Botje et al., *The PDF4LHC Working Group Interim Recommendations*, arXiv:1101.0538 [hep-ph].

[149] A. D. Martin, W. Stirling, R. S. Thorne, and G. Watt, *Parton distributions for the LHC*, Eur. Phys. J. C **63** (2009) 189, arXiv:0901.0002 [hep-ph].

[150] A. D. Martin, W. Stirling, R. Thorne, and G. Watt, *Uncertainties on α_S in global PDF analyses and implications for predicted hadronic cross sections*, Eur. Phys. J. C **64** (2009) 653–680, arXiv:0905.3531 [hep-ph].

[151] H.-L. Lai, M. Guzzi, J. Huston, Z. Li, P. M. Nadolsky, J. Pumplin, and C. P. Yuan, *New parton distributions for collider physics*, Phys. Rev. **D82** (2010) 074024, arXiv:1007.2241 [hep-ph].

[152] J. Pumplin et al., *New generation of parton distributions with uncertainties from global QCD analysis*, JHEP **07** (2002) 012, arXiv:hep-ph/0201195.

[153] S. Frixione et al., *A positive-weight next-to-leading-order Monte Carlo for heavy flavour hadroproduction*, JHEP **09** (2007) 126, arXiv:0707.3088 [hep-ph].

[154] ATLAS Collaboration Collaboration, *Studies on top-quark Monte Carlo modelling for Top2016*, Tech. Rep. ATL-PHYS-PUB-2016-020, CERN, Geneva, Sep, 2016. https://cds.cern.ch/record/2216168.

[155] S. Frixione, E. Laenen, P. Motylinski, B. R. Webber, and C. D. White, *Single-top hadroproduction in association with a W boson*, JHEP **07** (2008) 029, arXiv:0805.3067 [hep-ph].

[156] M. Beneke, P. Falgari, S. Klein, and C. Schwinn, *Hadronic top-quark pair production with NNLL threshold resummation*, Nucl. Phys. B **855** (2012) 695–741, arXiv:1109.1536 [hep-ph].

[157] M. Cacciari, M. Czakon, M. Mangano, A. Mitov, and P. Nason, *Top-pair production at hadron colliders with next-to-next-to-leading logarithmic soft-gluon resummation*, Phys. Lett. B **710** (2012) 612–622, arXiv:1111.5869 [hep-ph].

[158] P. Bärnreuther, M. Czakon, and A. Mitov, *Percent Level Precision Physics at the Tevatron: First Genuine NNLO QCD Corrections to $q\bar{q} \to t\bar{t} + X$*, Phys. Rev. Lett. **109** (2012) 132001, arXiv:1204.5201 [hep-ph].

[159] M. Czakon and A. Mitov, *NNLO corrections to top-pair production at hadron colliders: the all-fermionic scattering channels*, JHEP **12** (2012) 054, arXiv:1207.0236 [hep-ph].

[160] M. Czakon and A. Mitov, *NNLO corrections to top pair production at hadron colliders: the quark-gluon reaction*, JHEP **1301** (2013) 080, arXiv:1210.6832 [hep-ph].

[161] M. Czakon and A. Mitov, *Top++: A Program for the Calculation of the Top-Pair Cross-Section at Hadron Colliders*, Comput. Phys. Commun. **185** (2014) 2930, arXiv:1112.5675 [hep-ph].

[162] J. Gao, M. Guzzi, J. Huston, H.-L. Lai, Z. Li, et al., *The CT10 NNLO Global Analysis of QCD*, Phys. Rev. D **89** (2014) 033009, arXiv:1302.6246 [hep-ph].

[163] T. Gleisberg, S. Höche, F. Krauss, M. Schönherr, S. Schumann, et al., *Event generation with SHERPA 1.1*, JHEP **02** (2009) 007, arXiv:0811.4622 [hep-ph].

[164] S. Catani, F. Krauss, R. Kuhn, and B. R. Webber, *QCD matrix elements + parton showers*, JHEP **11** (2001) 063, arXiv:hep-ph/0109231.

[165] S. Höche, F. Krauss, S. Schumann, and F. Siegert, *QCD matrix elements and truncated showers*, JHEP **05** (2009) 053, arXiv:0903.1219 [hep-ph].

[166] C. Anastasiou, L. J. Dixon, K. Melnikov, and F. Petriello, *High precision QCD at hadron colliders: Electroweak gauge boson rapidity distributions at NNLO*, Phys. Rev. D **69** (2004) 094008, arXiv:hep-ph/0312266.

[167] ATLAS Collaboration, *Measurements of the W production cross sections in association with jets with the ATLAS detector*, Eur. Phys. J. C **75** (2015) 82, arXiv:1409.8639 [hep-ex].

[168] M. Bahr et al., *Herwig++ Physics and Manual*, Eur. Phys. J. C **58** (2008) 639, arXiv:0803.0883 [hep-ph].

[169] J. Bellm et al., *Herwig 7.0/Herwig++ 3.0 release note*, Eur. Phys. J. C **76** no. 4, (2016) 196, arXiv:1512.01178 [hep-ph].

[170] L. Harland-Lang, A. Martin, P. Motylinski, and R. Thorne, *Parton distributions in the LHC era: MMHT 2014 PDFs*, Eur. Phys. J. C **75** no. 5, (2015) 204, arXiv:1412.3989 [hep-ph].

[171] ATLAS Collaboration, G. Aad et al., *Electron and photon performance measurements with the ATLAS detector using the 2015-2017 LHC proton-proton collision data*, arXiv:1908.00005 [hep-ex].

[172] M. Cacciari, G. P. Salam, and G. Soyez, *FastJet User Manual*, Eur. Phys. J. **C72** (2012) 1896, arXiv:1111.6097 [hep-ph].

[173] ATLAS Collaboration, G. Aad et al., *Performance of pile-up mitigation techniques for jets in pp collisions at $\sqrt{s} = 8$ TeV using the ATLAS detector*, Eur. Phys. J. **C76** no. 11, (2016) 581, arXiv:1510.03823 [hep-ex].

[174] ATLAS Collaboration, G. Aad et al., *ATLAS b-jet identification performance and efficiency measurement with $t\bar{t}$ events in pp collisions at $\sqrt{s} = 13$ TeV*, arXiv:1907.05120 [hep-ex].

[175] ATLAS Collaboration, M. Aaboud et al., *Performance of missing transverse momentum reconstruction with the ATLAS detector using proton-proton collisions at $\sqrt{s}$ = 13 TeV*, Eur. Phys. J. **C78** no. 11, (2018) 903, arXiv:1802.08168 [hep-ex].

[176] M. Cacciari, G. P. Salam, and G. Soyez, *FastJet User Manual*, Eur. Phys. J. C **72** (2012) 1896, arXiv:1111.6097 [hep-ph].

[177] M. Cacciari, G. P. Salam, and G. Soyez, *The Catchment Area of Jets*, JHEP **04** (2008) 005, arXiv:0802.1188 [hep-ph].

[178] ATLAS Collaboration, "Data-Quality Requirements and Event Cleaning for Jets and Missing Transverse Energy Reconstruction with the ATLAS Detector in Proton–Proton Collisions at a Center-of-Mass Energy of $\sqrt{s} = 7$ TeV." ATLAS-CONF-2010-038, 2010. https://cds.cern.ch/record/1277678.

[179] P. Martinez Agullo, S. Cabrera Urbán, and C. Escobar Ibáñez, *Optimisation of selection criteria of t-channel single-top-quark events at $\sqrt{s}$ = 13 TeV for studies of anomalous couplings in the Wtb vertex.*, 2017. https://cds.cern.ch/record/2285874. Presented 20 Sep 2017.

[180] *Estimation of non-prompt and fake lepton backgrounds in final states with top quarks produced in proton-proton collisions at $\sqrt{s} = 8\ TeV$ with the ATLAS detector*, Tech. Rep. ATLAS-CONF-2014-058, CERN, Geneva, Oct, 2014. http://cds.cern.ch/record/1951336.

[181] ATLAS Collaboration, G. Aad et al., *Comprehensive measurements of t-channel single top-quark production cross sections at $\sqrt{s} = 7$ TeV with the ATLAS detector*, Phys. Rev. **D90** no. 11, (2014) 112006, arXiv:1406.7844 [hep-ex].

[182] G. D'Agostini, *A Multidimensional unfolding method based on Bayes' theorem*, Nucl. Instrum. Meth. A **362** (1995) 487–498.

[183] T. Adye, *Unfolding algorithms and tests using RooUnfold*, 2011. arXiv:1105.1160 [physics.data-an].

[184] ATLAS Collaboration, Z. Marshall, *Simulation of Pile-up in the ATLAS Experiment*, J. Phys. Conf. Ser. **513** (2014) 022024.

[185] ATLAS Collaboration, "Tagging and suppression of pileup jets with the ATLAS detector." ATLAS-CONF-2014-018, 2014. https://cds.cern.ch/record/1700870.

[186] ATLAS Collaboration, *Small-R ($R = 0.4$) jet energy scale and jet energy resolution uncertainties for full Run 2 analyses (release 21) twiki,*. https://twiki.cern.ch/twiki/bin/view/AtlasProtected/JetUncertaintiesRel21Summer2018SmallR.

[187] *Jet Calibration and Systematic Uncertainties for Jets Reconstructed in the ATLAS Detector at $\sqrt{s} = 13$ TeV*, Tech. Rep. ATL-PHYS-PUB-2015-015, CERN, Geneva, Jul, 2015. https://cds.cern.ch/record/2037613.

[188] J. Butterworth et al., *PDF4LHC recommendations for LHC Run II*, J. Phys. G **43** (2016) 023001, arXiv:1510.03865 [hep-ph].

[189] R. Bi, J. Boudreau, N. Bruscino, S. Cabrera Urban, M. J. Costa, M. De Beurs, C. Escobar, O. Estrada Pastor, J. E. García Navarro, G. R. Gonzalvo Rodriguez, J. Mueller, C. W. Ng, and M. Vreeswijk, *Complete measurement of the top-quark polarisation in t-channel single top-quark production using pp collisions at $\sqrt{s} = 13$ TeV with the ATLAS detector*, Tech. Rep. ATL-COM-PHYS-2019-326, CERN, Geneva, Apr, 2019. https://cds.cern.ch/record/2671941.